U.S. DEPARTMENT OF **ENERGY** | Energy Efficiency & Renewable Energy

QUANTIFYING EGS RESERVOIR COMPLEXITY WITH AN INTEGRATED GEOPHYSICAL APPROACH- IMPROVED RESOLUTION AMBIENT SEISMIC NOISE INTERFEROMETRY

Institution:

University of Nevada, Reno

Principal Investigators:

Phase I:
Ileana M. Tibuleac
PI from 2014 – 16 September 2016
Contact information:
Formerly at: Nevada Seismological Laboratory, University of Nevada, Reno, MS 0174, 1664 N. Virginia St., 89557, Tel. 781-258-3619, imtseismic@yahoo.com
Now at: Air Force Technical Application Center, Patrick AFB, Melbourne, FL, itibulea@aftac.gov

Phases I and II:
John Louie
PI from 16 September 2016 through 2018
Nevada Seismological Laboratory, University of Nevada, Reno, MS 0174, 1664 N. Virginia St., 89557, Tel. 775-229-3835, louie@seismo.unr.edu

Project Team:

Joe Iovenitti, Consulting Geoscientist
Bill Honjas, Optim Earth, Inc., 200 S. Virginia St., Suite 560, Reno, NV 89501
Zachary Young, Nevada Seismological Laboratory, University of Nevada, Reno;
William S. Honjas, Nevada Seismological Laboratory, University of Nevada, Reno;

Collaborators:

Keith Campbell, Geologist
Hank Ibser, University of California at Berkeley
Galen Kaip, University of Texas at El Paso
Mouse Reuch, Incorporated Research Institutions for Seismology
Alissa Scire, Incorporated Research Institutions for Seismology
Felix Ziwu, University of Texas at El Paso

Students:

Lianza Yap, University of Nevada, Reno
Ryley Hill, University of Nevada, Reno
Ray Lopez, University of Nevada, Reno
Brent Moore, University of Nevada, Reno
Andrew Rosenburg-Main, University of Nevada, Reno
Trent Snyder, University of Nevada, Reno
Josh Breen, University of Nevada, Reno

AUTHOR CONTRIBUTIONS:

PI Tibuleac designed, led and completed the field experiment and helped build the seismic database. Dr. Tibuleac performed all the seismic interferometry, and current seismic parameter analysis and is the lead author of both the Phase I Seismic report, and this Final Report. William S. Honjas helped with data processing and representation, is the author of Figure 10 in this report, and offered crucial support for figure representation and writing the Milestone Go/No Go and this Final report. As President of Optim Earth, Inc., Bill Honjas takes responsibility for all project work done by Optim, which includes all work by Joe Iovenitti, and all Phase I work done by Optim staff. Joe Iovenitti managed Phase I of the project overall, helped design, was an active participant in the field experiment, completed the updated geothermal favorability map (Task 5), and provided non-seismic geoscience support and review of reports. Optim staff completed the seismic waveform analysis during Phase I, shown in Appendix 4 and in Figure 11 of this report; offered important advice related to the field logistics, and later assisted with the completion of the Task 3, 4, and 5 reports during Phase II. Zachary Young performed the very difficult task of building the project seismic database, in collaboration with Mouse Reuch and Alyssa Scire. Galen Kaip, Zachary Young, Keith Campbell, William S. Honjas and Lianza Yap, together with Felix Ziwu, Mouse Reuch and Alyssa Scire were essential personnel in a very challenging field experiment. Keith Campbell helped manage the field experiment and the field personnel, and offered innovative solutions to overcome continuously changing field conditions and resource availability. Hank Ibser collaborated on the geostatistics in Phase II. Felix Ziwu offered important advice related to data acquisition. This project would have not been possible without the dedicated work of the UNR students, in extreme winter conditions. Every student who worked on this project contributed with ideas and solutions to the field experiment. PI John Louie managed the project at UNR starting in September 2016, presented Phase I seismic results at the GTO Peer Review Meeting in November 2017, completed a Cost Savings assessment for Task 6, submitted data and reports to the Geothermal Data Repository, and assembled this final report.

TABLE OF CONTENTS

EXECUTIVE SUMMARY

The primary goal of the project was met, as improved resolution (from kilometers to tens/hundreds of meters and to a depth of at least 3 km) was added to the seismic interferometry-estimated parameters relative to the work reported in AltaRock Energy Inc. (2014) for the Dixie Valley Geothermal Wellfield. A procedure for initial fault identification, using seismic interferometry, was developed. The project team further improved, and applied a new, cost-effective, and non-invasive exploration method, developed and validated since 2010, during two previous experiments, at Dixie Valley and Soda Lake, Nevada. The method, initially designed for hydrothermal exploration, was adapted to EGS exploration conditions, which require deeper crustal information. Regions of elevated energy for both the 2-7 Hz and 5-15 Hz frequency bands are located above intersections of multiple faults. Thus, an unprecedented, innovative seismic field deployment and ambient seismic noise and signal processing were successfully used to estimate crustal structure and to identify fault locations at depths up to 3 km, at a cost per kilometer of survey that in some cases may be as much as ten times less than the cost of a controlled-source survey.

Based on valid and useful seismic data collected and analyzed during Phase I, in Phase II the team has further quantified statistically the advantage of using seismic analysis, in combination with other geological and geophysical techniques, for EGS target identification. A power spectral density analysis of the passive-seismic empirical Green's functions reveals significantly higher power recorded over the exploration area at the power plant, and in the drilling area, near the BB station 10201, especially on the horizontal components.

In this study, the most important relationship observed during the prior report, namely the one between velocity and temperature was explored. The areas that show anomalously high predicted temperature in the geostatistics occur where multiple faults intersect. Not surprisingly, such areas span between the Dixie Valley range front fault and the basin-ward Piedmont faults, in the vicinity of numerous wells. These locations also fall in the area of high EGS favorability from the prior 2014 study. The anomalies also coincide with the high power spectral density values. The result of altering all favorability criteria for the new data reached a maximum of 1/8th of a point and were not large enough to change any favorability value reported in the 2014 study. The new data reinforce the results obtained from the previous 2014 study.

The current high-resolution ambient seismic noise project provided excellent results in defining faults in the wellfield. As such the identification of known faults by the project demonstrated the utility of this method for identifying faults at an exploration stage in geothermal development. Such fault identification, while extremely useful in exploration investigation, has not added sufficient new data for the generation of significantly different DVGW favorability maps in the current project.

We believe the cost savings of our passive-seismic technique for EGS, over common industry active-source survey techniques, may have a minimum of 30%, and a maximum of 90%. There are many significant non-cost benefits of passive seismic surveys. Our passive-source method provides an environmentally-friendly seismic survey with minimal to negligible impacts. The economic benefit is greater EGS project feasibility.

A.   PROJECT OBJECTIVES

The primary goal of this project is to add improved resolution (from kilometers to tens/hundreds of meters and to a depth of at least 3 km) seismic interferometry-estimated parameters relative to the work reported in AltaRock Energy Inc. (2014)[1] for the Dixie Valley Geothermal Wellfield (herein referred to as the project area), assess the possibility of using seismic analysis, in combination with other geological and geophysical techniques, for EGS target identification, and determine select native phase parameters described below. Improvements to the baseline technology are accomplished by (1) adapting and applying a non-invasive and cost-effective seismic exploration method based on ambient-seismic noise analysis and nuclear monitoring methods to EGS target area investigations; (2) estimating the benefits of adding supplementary seismic parameters, from analysis of seismic events recorded in the project area; and (3) validating high resolution seismic information, for the first time, against similar-resolution geological and geophysical findings reported in AltaRock Energy Inc. (2014).

Physical subsurface parameters measured directly in this project are (1) P- and S-wave seismic velocities and ratios, (2) seismic attenuation, and (3) stochastic heterogeneity. Subsurface parameters, measured indirectly are (1) temperature and pressure at depth, (2) location and geometry of features/faults, (4) stress and stress drop, (5) lithology/heterogeneity at target depth, and (6) potential EGS reservoir volume.

In this report we show that the project met critical success factors in achieving the above stated goals, and that the method, originally designed for conventional geothermal analysis, was successfully adapted to larger scale and different EGS requirements, while preserving the lower cost of the technique.

B.   TECHNICAL SCOPE SUMMARY

A new exploration technology was developed and tested at UNR by Tibuleac et al. (2015; DOE Soda Lake report, 2015, further referred to as DOE Final Report EE005518) and Iovenitti et al. (2014; DOE AltaRock report, further referred to as AltaRock Energy Inc., 2014), which included application of seismic interferometry and seismic array signal processing techniques developed for nuclear monitoring to conventional geothermal seismic reflection surveys. This technique was developed to evaluate the usefulness for EGS exploration of seismic parameter information in comparison with information from, and at the same scale as, other geophysical exploration methods deployed in the project area. For this purpose, the project (1) collected new data and (2) generated a higher resolution (tens/hundreds of meters versus ~ 5 kilometers) velocity models in a 25x25 km area, and along five seismic lines. These activities were successfully completed and constituted the Go-No Go milestone, after which DOE approved the project to continue with Phase II.

---

[1] AltaRock Energy, Inc., 2014, Exploration Methodology Project using the Dixie Valley Geothermal System, Nevada as a Calibration Site Part II—Final Scientific Report Enhanced Conceptual Model, US Department of Energy DOE Award: DE-EE0002778, submitted to the National Geothermal Data Repository, 2 January.

In Phase II, the subsequent steps included (1) the use of seismic event waveforms from AltaRock Energy Inc. (2014) seismic surveys to complete extraction of supplementary seismic parameter information, (2) generation of new EGS favorability/trust maps by factoring the proposed higher seismic resolution data to compliment and improve the previous investigations, and (3) generation of a new geostatistical analysis of the improved data set comparable to that provided in AltaRock Energy Inc. (2014).

An essential difference in exploration for EGS sites compared to hydrothermal sites is the degree of spatial resolution required to identify drilling targets. Hydrothermal production relies on an existing fracture network favorable for geothermal fluid production, thus localized high-resolution geological information is critical for well location. In contrast, EGS exploration seeks to identify relatively large targets of hot, competent rock, at depths of ≤3 km.

We addressed this challenge through (1) designing an innovative seismic deployment, including an unprecedented combination of broadband (BB), short period (SP) and high frequency sensors; (2) modifying the data processing technique to shorten the duration of the experiment from 21 days (Tibuleac et al., 2015) to 6-9 days, while obtaining the same resolution; (3) identifying and quantifying multiple seismic parameters (velocity, attenuation, waveform complexity, heterogeneity, stress drop, stress orientation) to improve characterization of lithology, temperature and fault location and orientation; (4) evaluating the best method to circumvent effects of the seismic noise directionality when assessing P/S velocity and attenuation; and (5) managing time and resources effectively to finish Phase I of the project on time and within scope, in extremely difficult weather conditions. At the Go/No Go Milestone after the completion of the Phase 1 Seismic Report, with the approval of DOE, we showed that the method is suitable for application at EGS sites, and gained approval for Phase II work. During Phase II of the project, we performed the statistical analyses on our results that allowed us to prepare a new EGS favorability map for the DVGW, and examine whether the new map presents any advantages over prior results.

C.   TECHNICAL APPROACH

The individual tasks to be performed are described below. Project milestones are presented in Table 1.

TASK 1 – PROJECT MANAGEMENT

US Bureau of Land Management (BLM) Form 3200-9, "Notice of Intent to Conduct Geothermal Resource Exploration Operations" (NOI) was submitted to the corresponding BLM office (Appendix 1) and the experiment was approved on November 10, 2015. Note that more locations were permitted than were used, as result of weather conditions, schedule and field work budget. All Quarterly Reports have been submitted. The project completed on budget.

Table 1. Project milestones

Recipient Name:	University of Nevada Reno						
Project Title:	Quantifying EGS Reservoir Complexity with an Integrated Geophysical Approach and Improved Resolution Ambient Seismic Noise Interferometry						
No.[1]	Task Title	Milestone Type (Milestone or Go/No-Go Decision Point)	Milestone No. (Go/No-Go Decision Point No.)	Milestone Description (Go/No-Go Decision Criteria)	Milestone Verification Process	Date[3] (Months from Start of the Project)	Quarter[2] (Quarters from Start of the Project)
1	Project Management	Milestone	1	Task 1 Completion		Month 1 (M1) –M2	Quarter 1 (Q1)
2	Seismic Field Data, Acquisition, Processing and Interpretation	Milestone	2	Task 2 Completion	E-mail notification to DOE point of contact (POC)	M1-M17	Q1 – Q6
		Go/No-go Decision Point	1	Significance of the derived seismic parameters.	Presentation of data significance and DOE	M17	Q6
3	Dixie Valley Conceptual Model	Milestone	3	Completion of Task 3	E-mail notification to DOE POC	M17 – M19	Q6 – Q7
4	Geostatistical Data Analysis	Milestone	4	Task 4 Completion		M20 – M23	Q7 – Q8
5	EGS Favorability/ Trust Maps	Milestone	5	Task 5 Completion	E-mail notification to DOE POC	M23	Q8
6	Project reporting	Milestone 6	6	Task 6 Completion		M24	Q8

[1] Number; [2] Anticipated

TASK 2 – SEISMIC FIELD DATA ACQUISITION, PROCESSING, AND INTERPRETATION

On February 2, 2016, an unprecedented seismic experiment was completed in Dixie Valley (DV), Nevada (Figure 1A). The experiment had a total duration of three months, and included a deployment of more than 550 three-component (3C) broadband (BB), short-period (SP) and vertical high-frequency geophone stations in an area of 25x25 km. Green's Functions (GFs) were extracted from stacks of cross correlations and autocorrelation of ambient seismic noise and signal. Independent shear wave models were extracted from inversion of fundamental-mode Rayleigh group and phase velocity dispersion curves, to be used as initial models on each line. A set of virtual shot gathers and initial, 500-m-grid side models at the site of each sensor were estimated and delivered to Optim, for further interpretation along each of the five ambient-noise reflection lines.

Subtask 2.1 Seismic Equipment Installation and Data Acquisition

Continuous data were collected during a two-month passive seismic survey in DV. The deployment, from November 12, 2015 to January 21, 2016, included two campaigns. The first campaign was during the whole period, from November 12, 2015 to January 21, 2016, and included BB (yellow pins in Figure 1A) and SP (blue pins in Figure 1A) sensor deployment in an area designated as the study area by AltaRock Energy Inc. (2014) during the 2014 experiment (Iovenitti et al., 2015). The second campaign, started for 6 days in November 2015, and continued from January 5-19 in 2016, consisting of passive recording with high frequency sensors deployed for 6 or 9 days along five lines (named Lines 2, 3, 4, 5 and 6, shown in gray in Figure 1A) with 100 ft (30 m) inter-station distance (on Line 4) or 200 ft (60 m) interstation distance (on Lines 2, 3, 5 and 6). These lines were deployed at the same locations as the locations on a 2010-2011 AltaRock geophysical study, as reported by Iovenitti et al. (2015). Documentation of the experiment conditions is shown in Appendix 2.

The deployment described in Appendix 3 included:

Part 1. Closely-spaced (34 to 68 m apart) sensors (vertical 4.5 Hz geophones with "Texan" digitizers) recording at 250 sps were deployed within five passive seismic reflection lines to obtain virtual shot gathers. These were permitted sensor locations as shown in Appendix 1. Replacement "Texan" digitizers with fresh batteries were switched with the ones in the field every three days. The sample rate was chosen to meet digitizer memory constraints, and allow optimal storage during the 3-4 days recording time of each "Texan". The sensors recorded for a total of 6 days, or in the case of lines 2, 3 and 6, for 9 consecutive days.

Experiment design modification– While the initial survey plans were very ambitious (Appendix 1), weather, field personnel availability, experiment location (travel to a site more than 2 hours from lodging) and budget constraints led to an experiment redesign in November 2015. The initial goals were ultimately achieved, within the total project budget. Based on interpretations in Iovenitti et al. (2014), only lines of utmost interest were deployed (Figure 1B). Limited battery life (maximum 4 days) and memory capacity made switching "Texan" digitizers necessary. Thus, the surveys included multiple "Texan" deployments (6 to 9 days) along one line, using sensors 34 m

apart (on Line 4, two three-day surveys) or 68 m apart (on all other lines).

Lines 2 and 3 were shorter than lines 4, 5 and 6 because the DV basin floor was covered with water at the time of the experiment (Appendix 2), a very rare occurrence in the area. The six-day Line 4 survey was completed in November 2015, and the remaining lines were completed from January 5 to 19, 2016. Delaying completion of Line 4 would have made the survey extremely difficult, as the Line 4 area was partially under water by mid-January 2016 (see Appendix 2). After processing, it was concluded that records on Line 4 were of the highest quality obtained during the experiment.

All the seismic lines were deployed perpendicular to a low-traffic road and the principle faults in the project area, which provided conditions which have been observed to be optimal for other ambient noise seismic surveys (Tibuleac et al., 2010, AGU abstract).

The total distance surveyed, including repetitive surveys along the same line, was greater than 72 km. Reduced costs for interpretation allowed an increased budget for the field experiment, to overcome weather-related difficulties. In comparison, the cost of a nearby 3-D active-source survey (Echols et al., 2011, at Soda Lake) was ~ $300,000 per kilometer. The cost of this 2-D DVWF field survey was less than $2000 per kilometer of reflection line.

Although recording during the winter significantly improved the quality of the data, extreme weather conditions, with temperatures less than 2° F overnight resulted in reduced "Texan" battery life, and thus loss of data. This was the reason three deployments were necessary on Line 6. The solution to avoid the low "Texan" battery life was to wrap the "Texan" digitizers in bubble wrap/paper towels and bury them at least one foot (30 cm) underground. These precautions significantly improved the field data recovery.

Part 2. Fifteen three-component (3C) L2 sensors (2 Hz corner frequency) with Reftek RT130 dataloggers, recorded continuously at 250 sps, equipped with solar panels and 12.8 V batteries (Appendix 1). The SP sensors, together with a set of 12 BB stations were added to the lines in an effort of enhancing the station coverage and the Green's Function (GF) amplitude. A map of the final deployment configuration is shown in Figure 1A.

Examples of waveforms from a real seismic event recorded by the deployed ambient noise 2015-2016 DV seismic deployment are shown in Figure 2. The experiment was designed to meet the challenges of low-cost, high resolution, deep seismic surveys using seismic interferometry and seismic noise and signal. Improved extraction of GFs has been observed when using combinations of sensors including BB velocity and acceleration sensor pairs in Reno, NV, (Tibuleac, 2017, in preparation), thus, for the first time in an ambient-noise geophysical survey, multiple types of sensors were used.

Subtask 2.2 Seismic Ambient Noise and Signal Acquisition and Processing

2.2.1 The seismic database

Zachary Young built the seismic Antelope (BRTT) database, with help from Mouse Reuch, Alyssa Scire, Ileana Tibuleac, Galen Kaip and Felix Ziwu (see cover page for affiliations at the time of the work). Building the database included first a thorough verification of thousands of sensor and digitizer numbers paired with station numbers. The waveforms were delivered to IRIS, who in turn provided the interface with a BRTT Antelope database, for which the UNR algorithms were written. A second step consisted of database building and data quality verification, as shown in Figure 2. The database is now available as "assembled dataset" *16-013* from http://ds.iris.edu/ds/nodes/dmc/forms/assembled-data/?dataset_report_number=16-013, or through https://service.iris.edu/ph5ws/, further documented by the International Federation of Digital Seismograph Networks at http://www.fdsn.org/networks/detail/ZS_2015/ with DOI https://doi.org/10.7914/SN/ZS_2015 .

2.2.2. Method

Existing and newly acquired seismic survey data was used to test the possibility of applying a cost-effective, non-invasive, seismic exploration method, based on seismic interferometry to EGS exploration. Interferometry is a seismic analysis technique (Campillo and Paul, 2003; Gouedard et al., 2008 and references herein) which is currently successfully applied to reflection surveys and small aperture (of the order of a kilometer) surveys (Draganov et al. 2009, 2013; Irie and Brown, 2010, Tibuleac et al., 2010, 2012, 2015, Iovenitti et al., 2014, Tibuleac et al., 2015). This technique is based on the theoretical result which states that, if A and B are two passive sensors (seismic sensors), the Green's Function (GF), or the signal that B would receive when A is given an impulsive excitation, can be recovered from the temporal cross-correlation of noise received at A and B. The impulse response or GF, with surface waves as the largest features is retrieved from crosscorrelation stacks of ambient seismic noise, at arrays or lines of sensors. This new seismic exploration method (Tibuleac et al., 2010, 2011, 2012) has had promising results when used for fault definition and P and S -velocity model estimation at the hydrothermal exploration site in Soda Lake, Nevada (Tibuleac et al., 2015, DOE Final Report EE005518).

Figure 1A
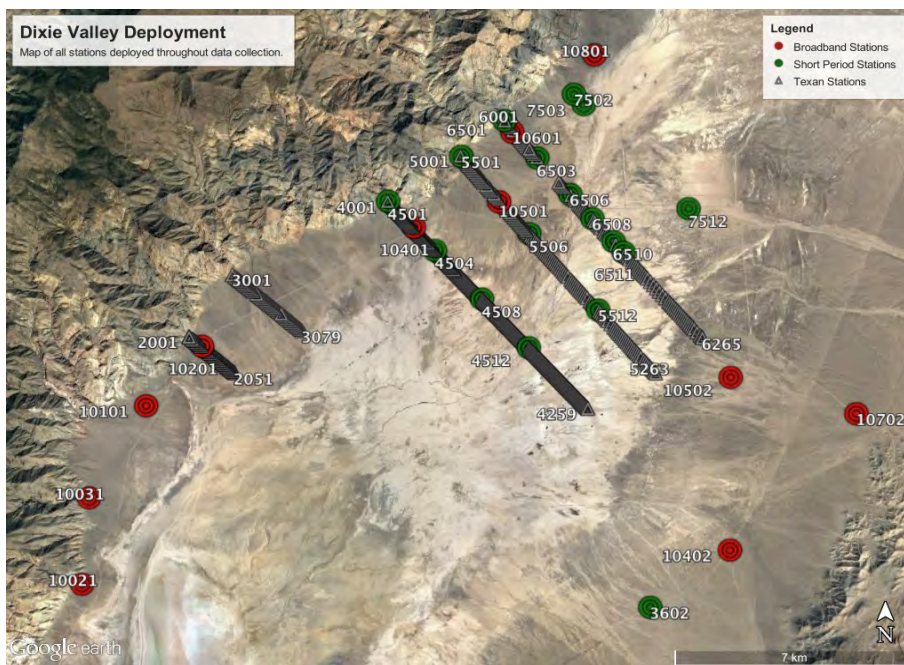
Figure 1B
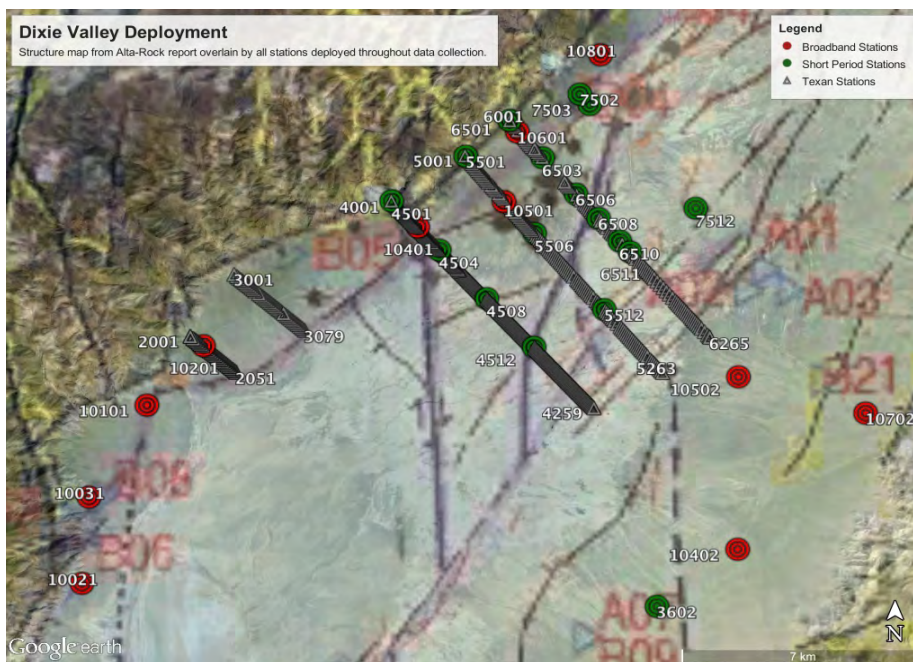
Figure 1. A. Map of the Dixie Valley ambient seismic noise survey deployment. The gray lines show, from left to right, lines 2, 3 4, 5 and 6. The red dots are BB sensor locations and the green dots show the SP locations. B. Deployed lines overlaid on structure and seismic location map for Dixie Valley Geothermal Wellfield (Iovenitti et al., 2015).

Figure 2 A
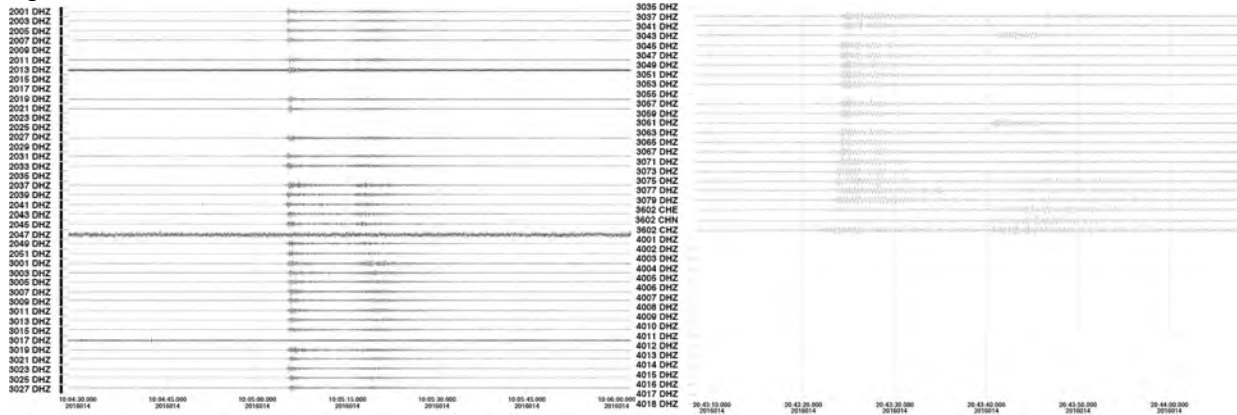
Figure 2 B

Figure 2 C

Figure 2 D

Figure 2. Sensor record quality is routinely verified by evaluation of the capability of recording earthquakes. It was assessed that the quality of the surveys was adequate, as earthquakes were recorded by high frequency sensors on every line. Plot A shows waveforms recorded on Lines 2 and 3, plot B shows waveforms recorded along Line 4, plot C shows records on Line 5, plot D shows records on line 6, plot E shows records recorded by broadband stations deployed throughout the Dixie Valley project area (Figure 1).

Unlike hydrothermal reservoirs, EGS reservoirs only require characterization at a resolution of hundreds of meters, to depths up to 3 km. Our previous studies in the same region (Iovenitti et al., 2014) estimated a P/S velocity model with a resolution of 5 km. The method was further developed at the Soda Lake Geothermal Field, NV (DOE Final Report EE005518), by analysis of ambient noise and signal along a seismic line, surrounded by a small aperture (< 4 km) two-dimensional array. A unique feature of this method is the use of a combination of sensors of the same, or different types, to first estimate at hundred-meter resolution an initial seismic S-velocity model using fundamental-mode Rayleigh waves. This initial model is crucial for P-velocity model estimation from virtual shot gathers along the line, also allowing sampling at depths up to 3 km.

GFs are extracted from stacks of ambient noise and signal crosscorrelations and autocorrelations from pairs of sensors and at the same sensor. Data were processed using ambient seismic noise and signal autocorrelation and crosscorrelation algorithms in a package of optimized analysis codes (Tibuleac et al., 2011; Tibuleac and Von Seggern, 2012). The algorithms employ spectral whitening for crosscorrelations and sign-bit normalization.

By applying <u>cross-correlation</u> to ambient noise data recorded at pairs of closely spaced (34 meters or 68 meters) seismic sensors along reflection lines, and stacking the results over several days or months (where available), we generated virtual shot gathers as if one of the sensors was producing seismic waves, i.e., we retrieved the earth's reflection response (Draganov et al., 2009).

Because the initial velocity model is crucial in any inversion, before interpretation, a set of 500 m resolution initial P/S models were generated. *Note that this resolution was the best resolution reached in the AltaRock Energy Inc. (2014) study.* These models were further constrained by information extracted from the new passive survey's fundamental mode Rayleigh phase velocities. A set of programs named CPS3.0 (Herrmann and Ammon, 2002) were used for fundamental mode Rayleigh group velocity analysis. The group velocity maps at each depth were inverted for P- and S-velocity models. The AltaRock Energy Inc. (2014)–derived P- and S-velocity models were used as baseline, initial models, at a resolution of 2.5-5 km.

Stacking the results over the recording time, virtual shot gathers were generated along each line as if one of the sensors would be generating seismic waves, i.e., the earth's reflection response was retrieved. This virtual reflection survey was interpreted in Task 3 for an updated conceptual earth model for the DVGWF.

Stacks of continuous waveform auto-correlations were used to image the individual station substructure by extracting the GF reflection component at each station (Claerbout, 1968). The ambient-noise autocorrelation at each station was interpreted as the collocated source–receiver elastic wave GF (i.e., the Earth's reflection response) and was used to distinguish reflecting layers beneath each station. Changes in the reflection GFs along the lines were investigated in association to known faults. The GF P-reflection component resulted from line and array autocorrelations was used for an independent verification of the Vp model. Based on the success of this analysis in identifying faults, we recommend that this analysis take precedence over alternatives, in future experiments.

Stochastic reservoir characteristics were estimated (Appendix 4). During Phase II, geothermal reservoir seismic spectral, entropy and attenuation characteristics, *which are mainly used as surface indicators of fault/EGS favorability presence*, as well as stress drop, were estimated and statistically evaluated, searching for the benefit for geothermal exploration of integrating seismic and other geological and geophysical results at Dixie Valley.

Subtask 2.2.3 Ambient noise preliminary P/S-wave velocity models of the study area

The reason for this first investigation is to obtain an accurate preliminary velocity model, to be used as initial/input model with the reflection survey. *Note that the preliminary S-velocity model estimated at this task, described below, is already at the minimum resolution of 0.5 km required by AltaRock Energy Inc. (2014).* This is an essential step for seismic survey interpretation, as in the past the lack of preliminary Vs models has proven to be a problem for geothermal exploration studies. The preliminary P/S model was estimated using a 25 km aperture seismic array and seismic interferometry and will be compared in Phase II with the geophysical measurements of the geothermal reservoir, to estimate whether it has the potential to provide cost-effective preliminary information in the study area.

The low-resolution P/S seismic velocity model was estimated from integration of a baseline seismic velocity model and models estimated from records of a 2D ambient noise seismic array.

2.2.3.1 Ambient – noise preliminary P/S seismic velocity model estimation (DV16_INITIAL MODEL_ARRAY)

A preliminary P/S model, DV16_INITIAL MODEL_ARRAY, was estimated as a combination of a model extracted using the 2015-2016 ambient-noise seismic array and line records (DV16_GVEL_MOD) and a baseline seismic velocity model (DV16_BPS_MODEL). The models estimated using array data were obtained by inversion of the fundamental Rayleigh (FR) wave group velocity dispersion curves. *This is the first estimate of a Vs velocity model using surface waves in the area, at the resolution of ~0.003 km^2 with depth resolution of 0.25 km, to a depth of 3 km.*

2.2.3.1.1 The baseline P/S-velocity model DV14_BPS_MODEL

An initial *P/S* velocity model, in the upper 19 km, at 2.5-5 km resolution was extracted in DV by Iovenitti et al. (2015) in AltaRock Energy Inc. (2014), from a combination of ambient noise interferometry information and earthquake and explosion tomography. This initial model was the basis for an adjusted mean model, shown in Table 2. The best mean model DVM in Table 2 was adjusted (through trial and error) in successive iterations to obtain the best fit of the surface wave dispersion curves described in Section 2.2.3.1.2.

2.2.3.1.2 The ambient noise Vs models DV16_INITIAL_MODEL estimated using array data

New seismic data from the passive, 550 vertical component geophone lines, from the 12 BB sensors and from the 15 SP sensors was used to estimate *preliminary, lower resolution (~100 m – 500 m)* 3D *Vs* models. The models were estimated by inverting the dispersion curves of the fundamental model Rayleigh component of the GFs, which usually is the largest phase (ground roll), often discarded in active-source industry reflection surveys. The GFs were extracted from beams of continuous waveform crosscorrelations. A successful outcome of this experiment was extraction of periods of 1-2 s using 5 Hz corner-frequency sensors, and 2 Hz corner SP frequency sensors, combined with BB sensors. This was achieved by modification of the instrument response to simulate a BB sensor when different sensors were used. The instrument response was not removed in the case of high-frequency geophone pairs.

DV16_GVEL_MOD Ambient Noise

A *Vs* model with grid cell side of 0.5 km (north-south) and 0.6 km (east-west) was extracted from inversion of fundamental mode Rayleigh dispersion curves and is named DV16_GVEL_MOD. Figure 3 shows the square root of the number of paths per grid cell used for group velocity estimation.

Figure 3. The square root of the number of inter-station ray paths for the ambient seismic survey station locations in the Dixie Valley Project Area used for FR group velocity estimation. A grid element side length was 0.5 km (N-S) and 0.6 km (E-W).
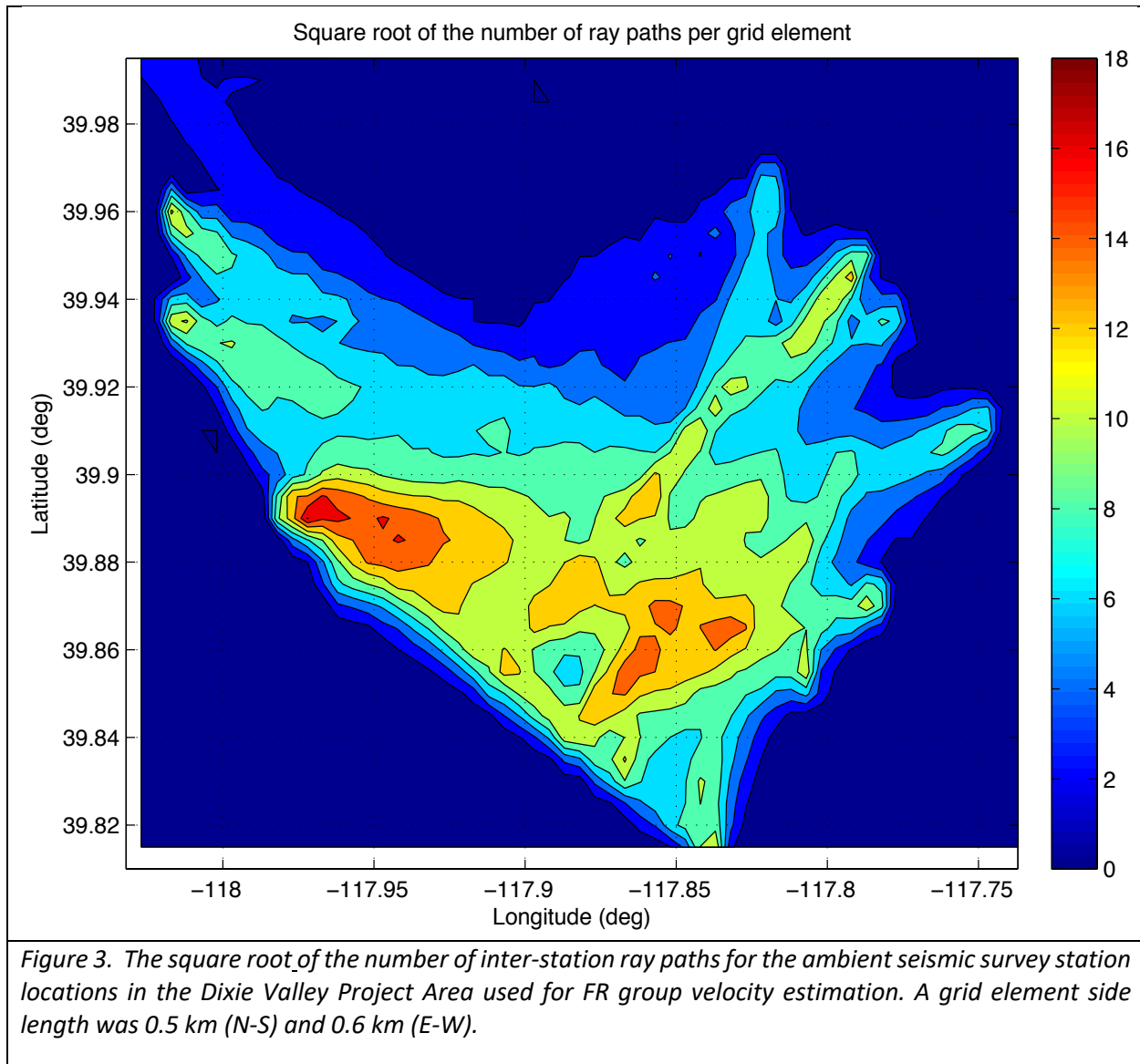
Using the CPS3.3 (Herrmann and Ammon, 2002) program *do_mft,* more than 14,300 fundamental Rayleigh group velocity dispersion curves were analyzed. While no pre-filters were applied to pairs of BB and SP sensors, the pairs of "Texans" and BB and SP sensors were filtered from 0.4 to 2 Hz prior to dispersion curve extraction. *do_mft* was applied twice, first to the raw waveform and the second time to the reconstructed waveform, which helped weed out waveforms with small signal to noise ratio. A total of 2625 good signal-to-noise GFs were chosen. Figure 4 shows examples of filtered GFs in record sections.

Figure 4 A (3602)
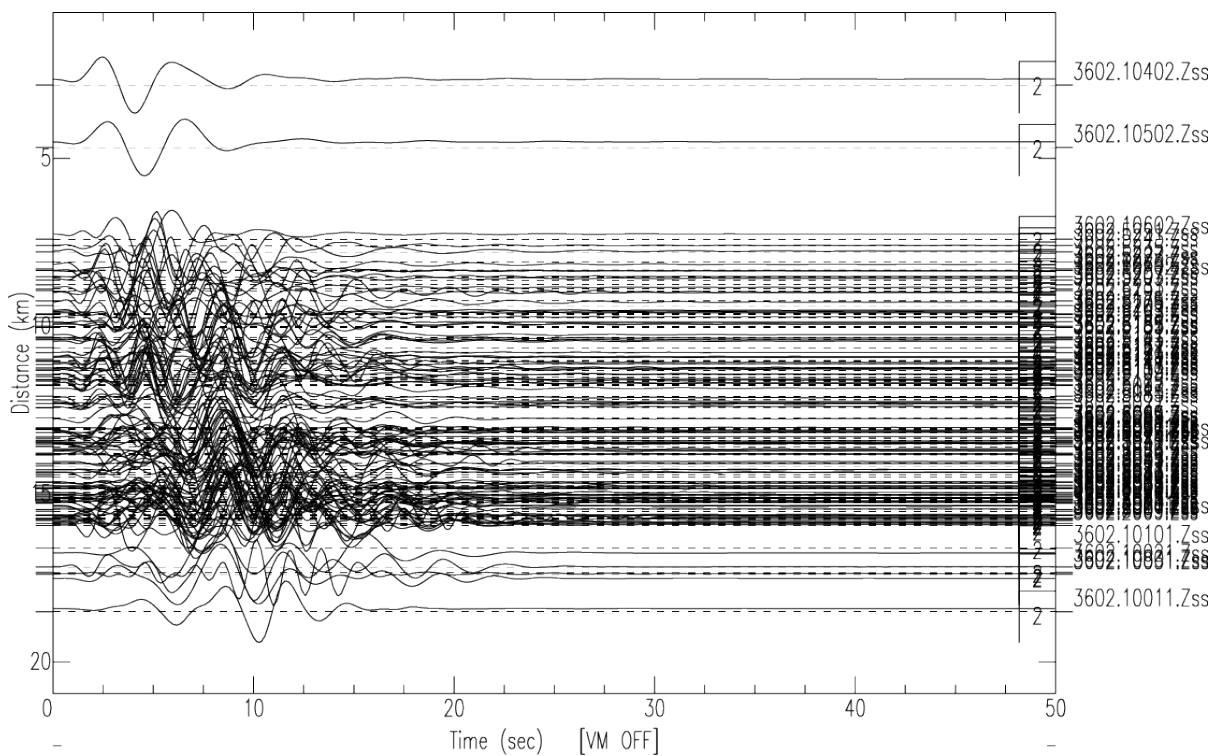
Figure 4 B (6506)
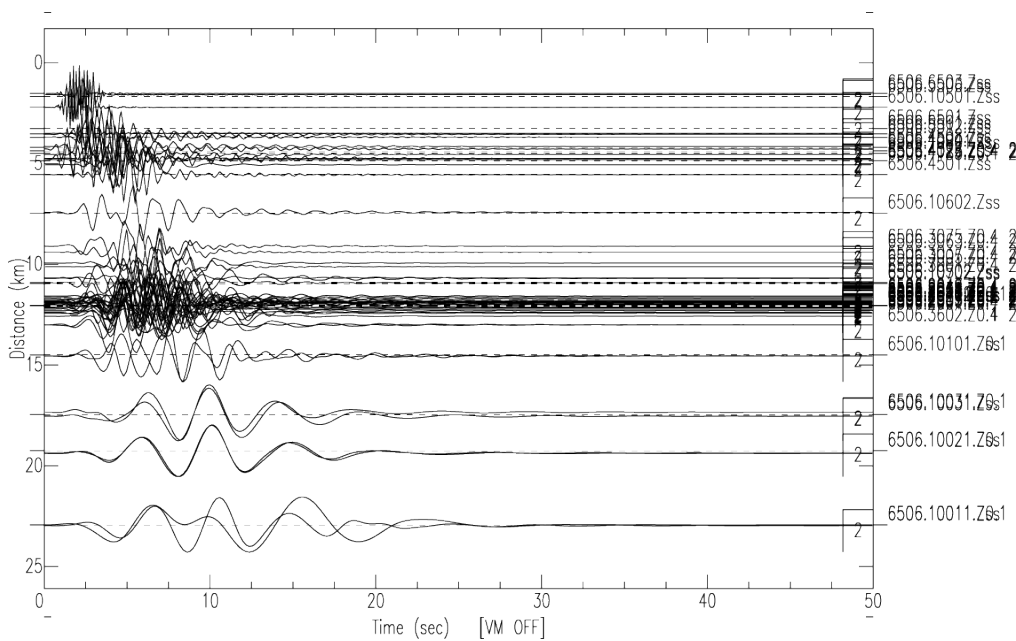
Figure 4 C (7502)
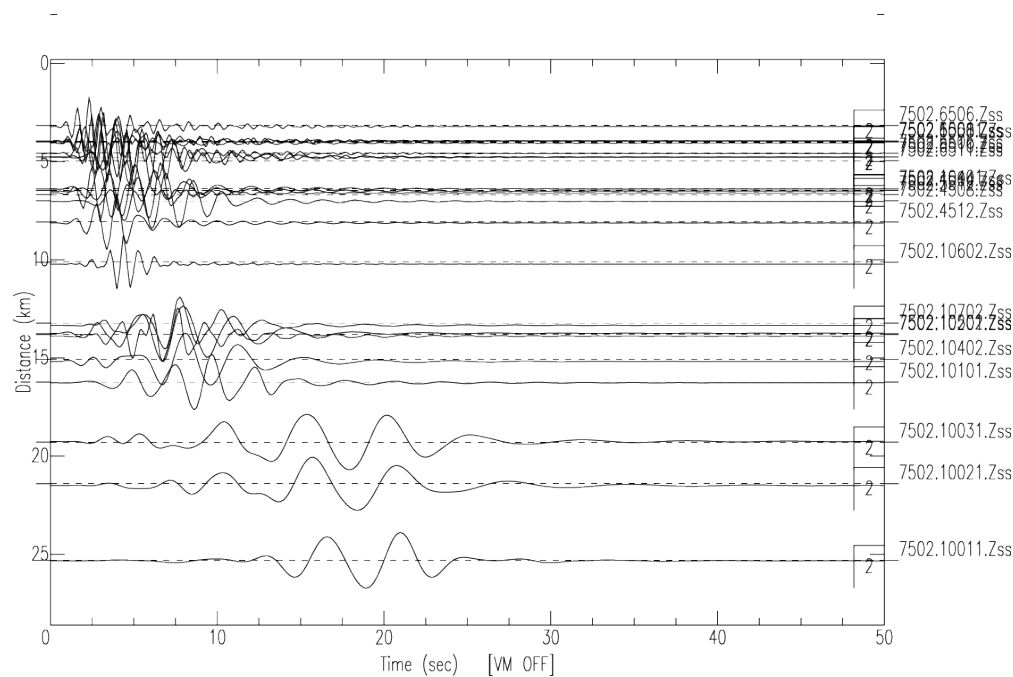
Figure 4. Record sections of GF waveforms extracted in the DV study area on paths from SP sensors to all other sensors, including high frequency geophones. All show the waveforms after applying Phase Match Filters (PMF) twice: once on the raw data, and once again on the reconstructed dispersion curves after the first-iteration. Figure 4A shows GFs extracted at station pairs including the SP station 3602. Figure 4B shows GFs extracted at station pairs including the SP station 6506. Figure 4C shows GFs extracted at station pairs including the SP station 7517. The vertical axis shows inter-station distance. We interpret the largest arrivals at all distances as the fundamental-mode Rayleigh wave.

Using the CPS3.3 program *surf96* the curves were inverted for shear wave velocity models. To estimate a group velocity model in each grid cell of the study area the code named *gridsp* was used (Dr. Hafidh Ghalib, personal communication). *gridsp* used stochastic inversion, following a method by Feng and Teng (1983). The propagations paths were assumed to be straight rays. The resulting fundamental mode Rayleigh group velocity maps at a set of chosen periods (1s, 1.5s, 2s, 2.5s, and 3s) are shown in Figure 5(A-E).

The surface of the DV study area was partitioned into a grid with elements 0.005˚ (0.5 km) on one side, in the north-south direction, and with elements of 0.006˚ (0.6 km) in the east-west direction. A dispersion curve has been estimated for each of the 1989 total grid elements in the DV study area. The inverted group velocity curves were estimated from inter-station dispersion curves which were used only if the wavelengths were less than half the interstation distance. The starting model DVM (Table 2) was used for each grid cell. The mean DV14_BPS_MODEL was modified by trial

and error during successive *surf96* runs, with the goal to obtain minimal difference between most of the observed and calculated dispersion curves. Another goal was to use the same DVM input model for the whole area, which was considered a best approach when assessing differences in the velocity model across grid cells.

Table 2. DVM, the starting model for Vs inversion in this study, is the modified mean Vp and Vs model used as initial model by Iovenitti et al., 2015.

DVM			
Layer Thickness	*Vp*	*Vs*	Rho
(km)	(km/s)		(g/cm^3)
0.2	1.3	0.7	2
0.15	1.647	0.8	2.53
0.15	2.	1	2.64
0.15	2.344	1	2.64
0.3	2.77	1.2	2.64
1	4.0	1.5	2.64
1	4.06	1.5	2.64
0.5	4.1	2	2.64
0.5	4.4	2.6	2.64
1.2	4.5	2.8	2.04
4	5.4	2.9	2.5
4	6	3.3	3.0
10	7.6	4	3.4
4	7.9	4.5	3.45
10	8.2	4.7	3.5
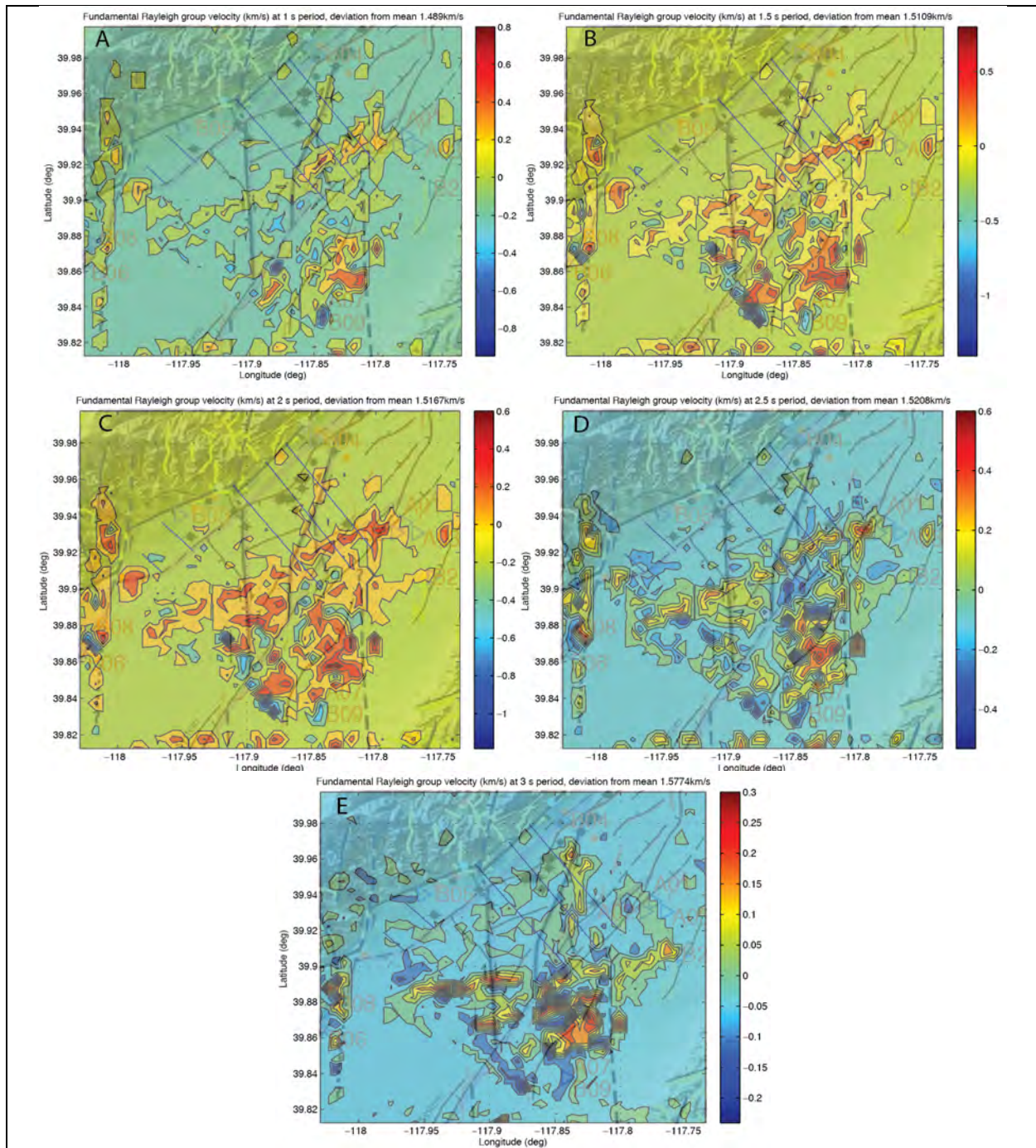
Figure 5. Maps of the deviation from the mean (at each period) of the fundamental Rayleigh group velocity at periods of 0.5 s (A), 1 s (B), 2 s (C) and 2.5 s (D) in the DV study area. The color scales on the right are in km/s. Lines 2, 3, 4, 5, and 6 are shown as blue lines in each plot and the surface projections of the fault zones are shown as gray lines. Note that the scale is not the same in A-D, because the group velocity is variable at different periods. Faults appear to be present near sign changes of the Vs difference from the mean sign at multiple depths.

The DV16_GVEL_MOD was the product of an inversion by CPS3.3 program *surf96*. The inversion took place for each grid cell and required two estimates: an input model (DVM, Table 2) and the dispersion curve. The program *surf96* estimated an output model to minimize the difference between the observed and calculated dispersion curves, for a given set of input parameters. The *surf96* input parameters, such as smoothing and damping values, were constant in this study and were as recommended by the CPS3.3 documentation. Variations of the smoothing and damping values may produce final model velocity variations on the order of tenths of km/s for *Vs*. For high smoothing the velocity discontinuities were less sharp between depth cells. The final output of the CPS3.3 algorithms was a velocity model with estimated values in *each depth slice i*. The number of depth slices was chosen by the analyst in the DVM input model. In this project, *surf96* first was applied first with constrained layer thickness looking for best layer velocity, and second, was applied with the previously estimated velocity fixed, however, looking for best layer thickness. The estimated layer thickness variations from DVM, however, were under 10 m.

The mean dispersion curve for the entire DV study area is shown in Figure 6. An example of inversion results and dispersion curve fit in one grid cell (39.8825N, 117.945W) is shown in Figure 7. Examples of the *Vs* models estimated by inversion of the velocity maps in Figure 5 at 1 km, 1.5 km, 2 km, 2.5 km and 3 km; depth *from the surface* are shown in Figure 8A (A-E). Because the input Vp was estimated in a different study, we considered Vp as an independent estimate and the Vp/Vs maps were shown in Figure 8A(D-E). Tibuleac et al. (2015) in a study at Soda Lake (SL), Fallon, NV (DOE Final Report EE005518) observed that changes in sign of the Vs anomalies were associated with fault projections on the surface, and this observation appears to be valid in DV, as shown in Figures 1 and 8.2 (A-F). The fundamental mode Rayleigh group velocity model extracted along each line is shown in Figure 10, with surface fault locations at "X" marks.

Trust factor estimation

Errors for each component model are expressed as "trust" factors (the "trust" is higher when the errors are smaller) and are the assessment of the analyst, based on the model resolution, as described below. In this section, we describe the empirical estimation of the DV16_GVEL_MOD trust factors (Figure 8B in each grid cell at each depth and Figure 10B along each line). Higher trust factors correspond to lower estimated errors. In each grid cell the input model has trust factors for *Vp, Vs, Rho* (density) and *Qp* and *Qs,* estimated at each depth *i* as the weighted mean of all the trust factors of all the models available at that depth.

The DV16_GVEL_MODEL errors can be associated with:
1) The input model, DVM (Table 1)
The DVM errors have been discussed in detail in our previous study, Altarock Energy Inc. 2014, when trust factors were evaluated at each depth and location. The *Vs* values in DVM were chosen by trial and error, with the goal to obtain the best fit for the dispersion curves in all the grid cells, and to use the same DVM values as an input model for all the grid cells. The DVM errors were not used in calculations.

2) The dispersion curve in each grid cell
In a grid cell, a dispersion curve was estimated using the CPSS3.3 program *do_mft* and had errors at each period. The main question to address was how these errors propagated into the inverted

model. An analyst picked the fundamental mode Rayleigh dispersion curve which was usually the largest amplitude arrival. Errors could occur when several Rayleigh modes were present in the time series and they were misidentified. Mode identification is easier when an array is used, and at distances larger than 1-2 km, and that was one of the advantages of the DV array (Figure 1A). A model (discussed below) of fundamental mode Rayleigh group velocity was estimated.

Errors in velocity estimates occur when the GFs have low SNR. The errors were inversely proportional to the amplitude of the picked arrival at each period. The maximum amplitudes at each period were recorded for each dispersion curve and were input in the inversion program (*surf96*).
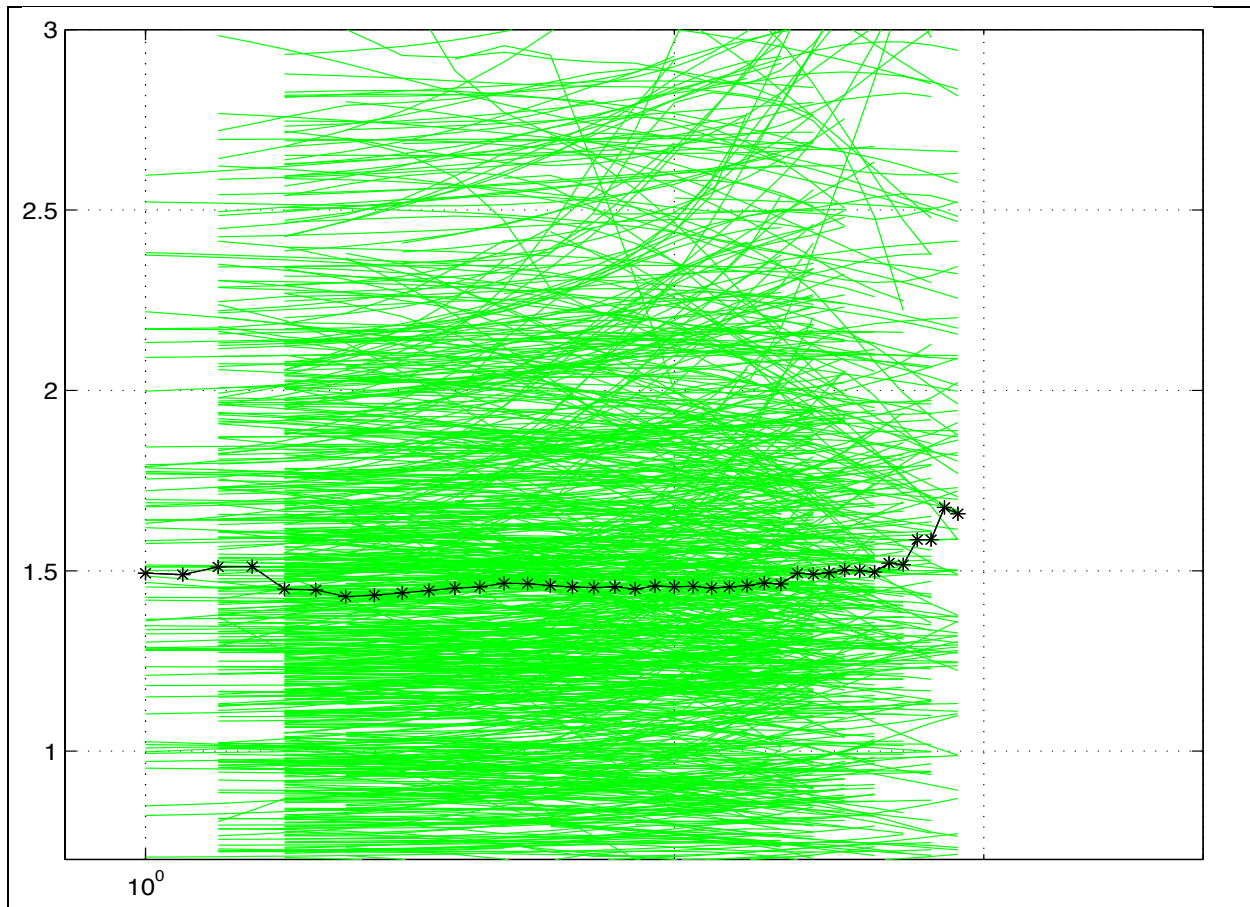
Figure 6. Estimated fundamental mode Rayleigh dispersion curves measured in Dixie Valley, and the calculated median dispersion curve (black line) used in this study. Horizontal scale is log period in seconds (with dispersion estimated from 1.0 s to just below 10 s); vertical scale is group velocity in km/s In this figure, the mean of the standard deviations at all periods is 0.55 km/s.

A plot of all the estimated group velocity dispersion curves in DV is shown in Figure 6. In this figure, the mean of the standard deviations at all periods is 0.55 km/s. These dispersion curves, however, are different most probably because of real crustal structure variations, *thus their variation at each period should not be used as an estimate of analysis errors or uncertainties.*

An experiment has been conducted using these curves, to evaluate how errors in the dispersion curves translate into the final model at each depth. Assuming these curves to be random realizations of the same measurement, we investigated how the variation of these curves was mapped into the estimated model. Using the mean observed model with random variations up to 0.5 km/s around a mean velocity at each period, 2425 dispersion curves were created, which were considered random realizations. With the same input model, realizations of the output model shown in Figure 9 were obtained. The normalized inverse standard deviation at each depth i was calculated as a trust vector $T_{surf96,i}/max(T_{surf96,i})$ used in all the grids at depths i. The results were that the input model variations mapped into the output model variations, with larger variations deeper in the crust.
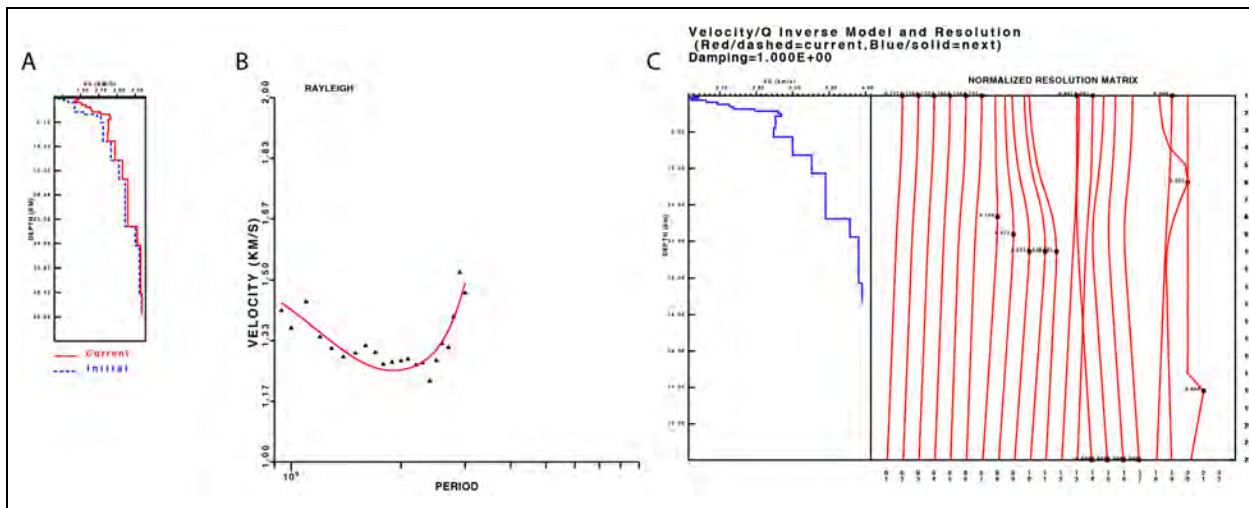
Figure 7. Example of velocity model inversion results, when using surf96. *Figure 7A shows the starting model (blue) and the final inverted model (red), after at ten iterations. Figure 7B: black dots show the observed fundamental-mode Rayleigh dispersion curve in Dixie Valley (black triangles) inverted to obtain the final model at the grid cell 15 (latitude) and 15 (longitude). The dispersion curve was estimated using the* gridsp *program. Figure 7C shows the resolution kernels (Hermann and Ammon, 2002) for the inversion. The model is resolved, although the kernels suggest that the layering was possibly too thin because the kernels are wider than the layer thickness. The layer thickness of the DV was chosen such that the inversion converged for the maximum number of cells.*

According to the CPS3.3 documentation, if the group velocity dispersion curves were perfect, a "true model" would have been the result of the inversion. However, because the dispersion curves were not perfect, the estimated model (a vector of parameters, for example velocities V, one parameter for each depth layer) was the resolution matrix (which was a square matrix) multiplied with the "true model". The resolution matrix is not symmetrical in the presence of smoothing and damping. In the following formula:

$$V_{i\,estimated} = \sum_{j} R_{ij} V_{j\,true}$$

where *i* is the depth interval number. The j column of the resolution matrix *Rij* showed how a unit perturbation in "Vj true" mapped into each of the elements of the Vj estimated. That means the true model was blurred by the inversion and the resolution matrix shows how this happens. Figure 7B shows an example of the estimated model and the observed (dots) and calculated (solid line) fundamental Rayleigh dispersion. Figure 7C shows an example of a resolution matrix representation for the same grid cell as in Figure 7A. For some of the layers, the resolution matrix value is largest at the layer depth, however, for some of the layers, a perturbation in the layer maps into perturbations in other depth layers, mostly when the depth resolution is lower than the depth interval of the model. Resolution matrices were calculated for each grid cell and a value was estimated for each depth layer. are the trust factors *TR*. Unlike in our previous studies, due to the amount of data (2425 x 20 estimates) and due to small (of the order of 0.01 trust factor differences in each grid cell) an empirical assessment was made by an analyst, based on values common to most of the grid cells.

Figure 8.1 Vs
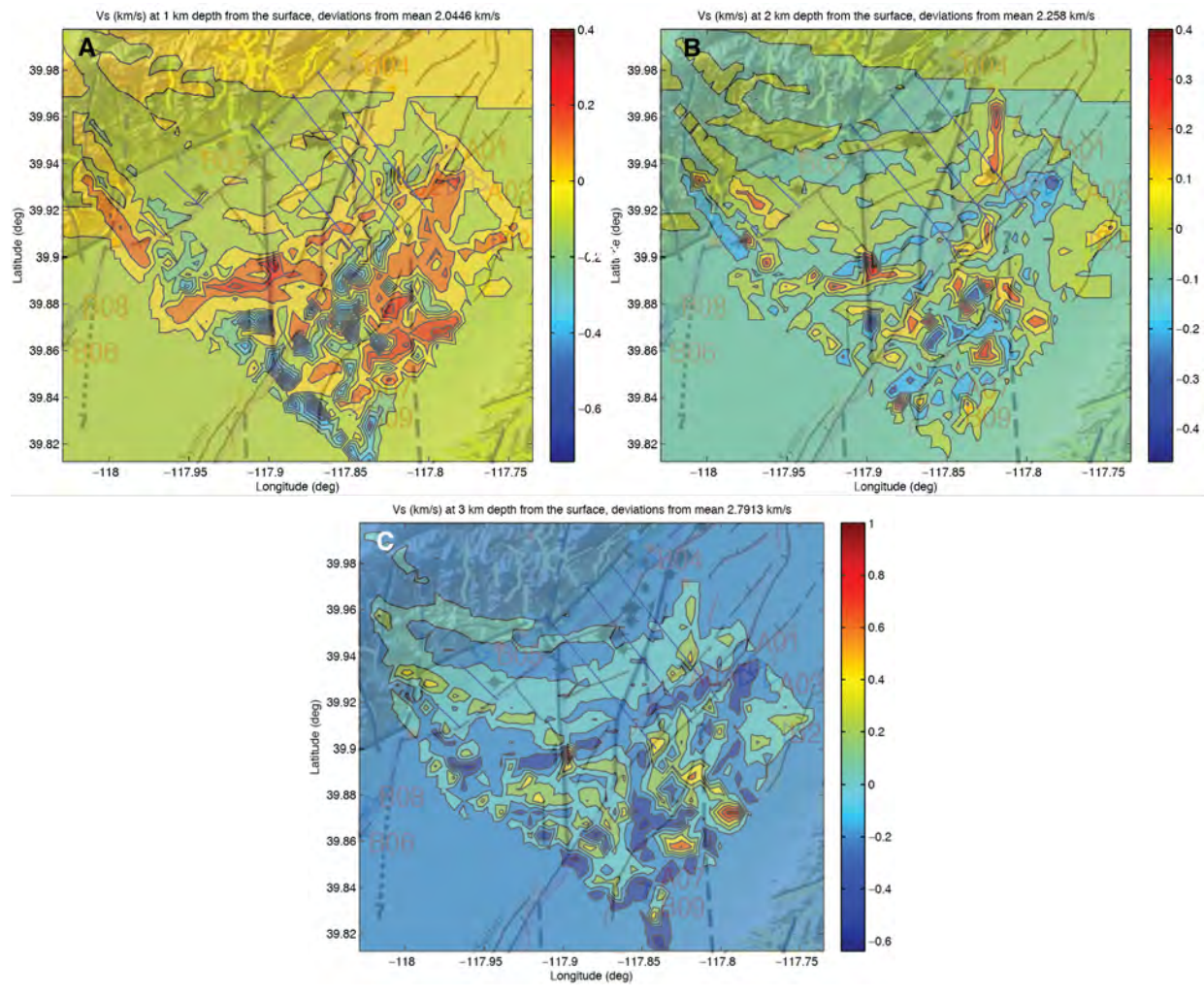
Figure 8.1 Vp
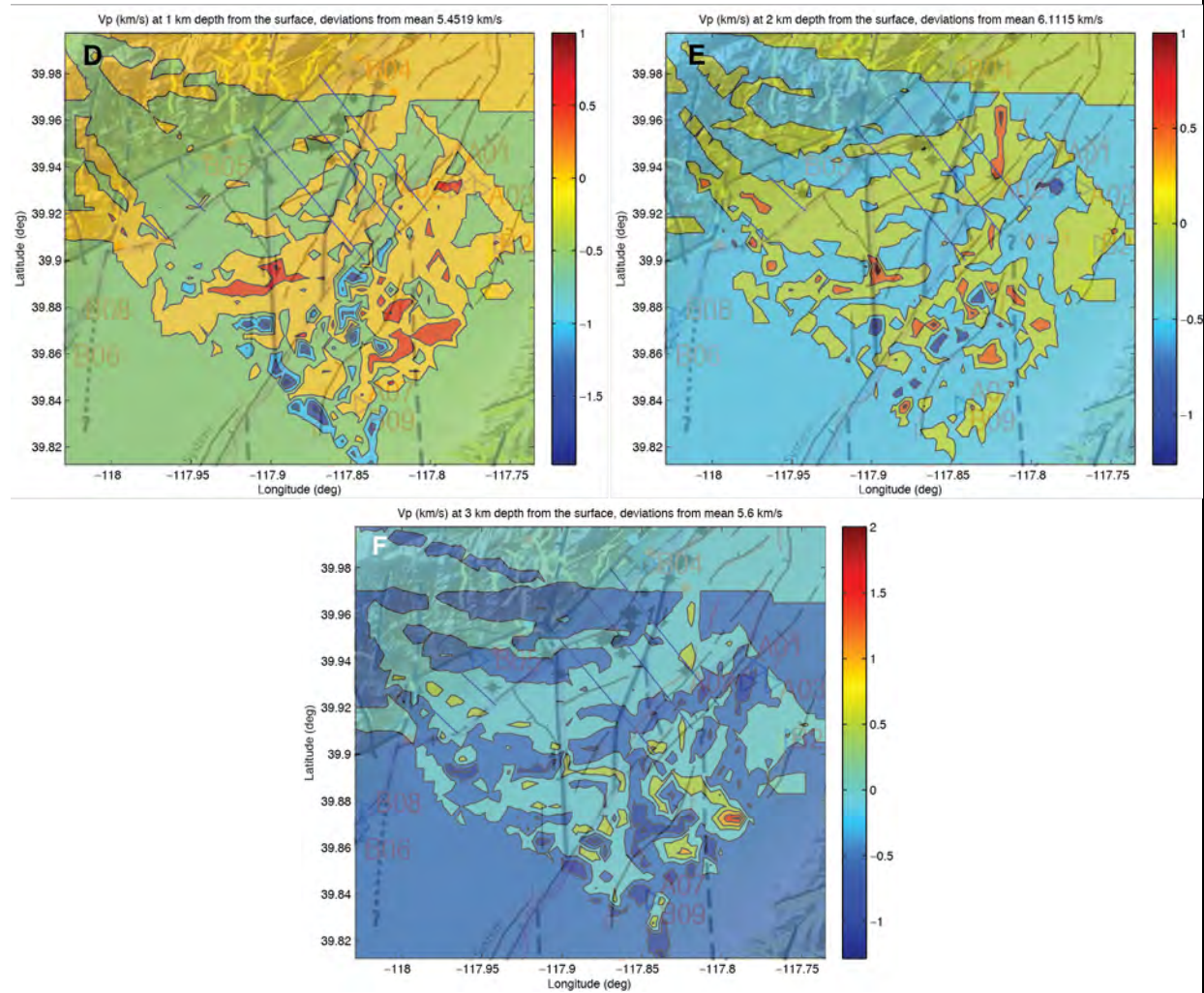
Figure 8.1 Vs maps (A-E) at depths of 1 km, 2 km, and 3 km (A-C). Lines 2, 3, 4, 5 and 6 are shown as blue lines in each plot. Vp maps (E-F) at the same depths are shown in plots F-J. Lines 2, 3, 4, 5 and 6 are shown as blue lines in each plot. The Vp/Vs maps (plots G-I) shown in subplots G, H, and I show changes near faults. These results provide important constraints for the DV16_INITIAL_MODEL and can, as they are, be used for comparison of the seismic experiment results with results of other geophysical methods.

Figure 8.2 Trust S Factors
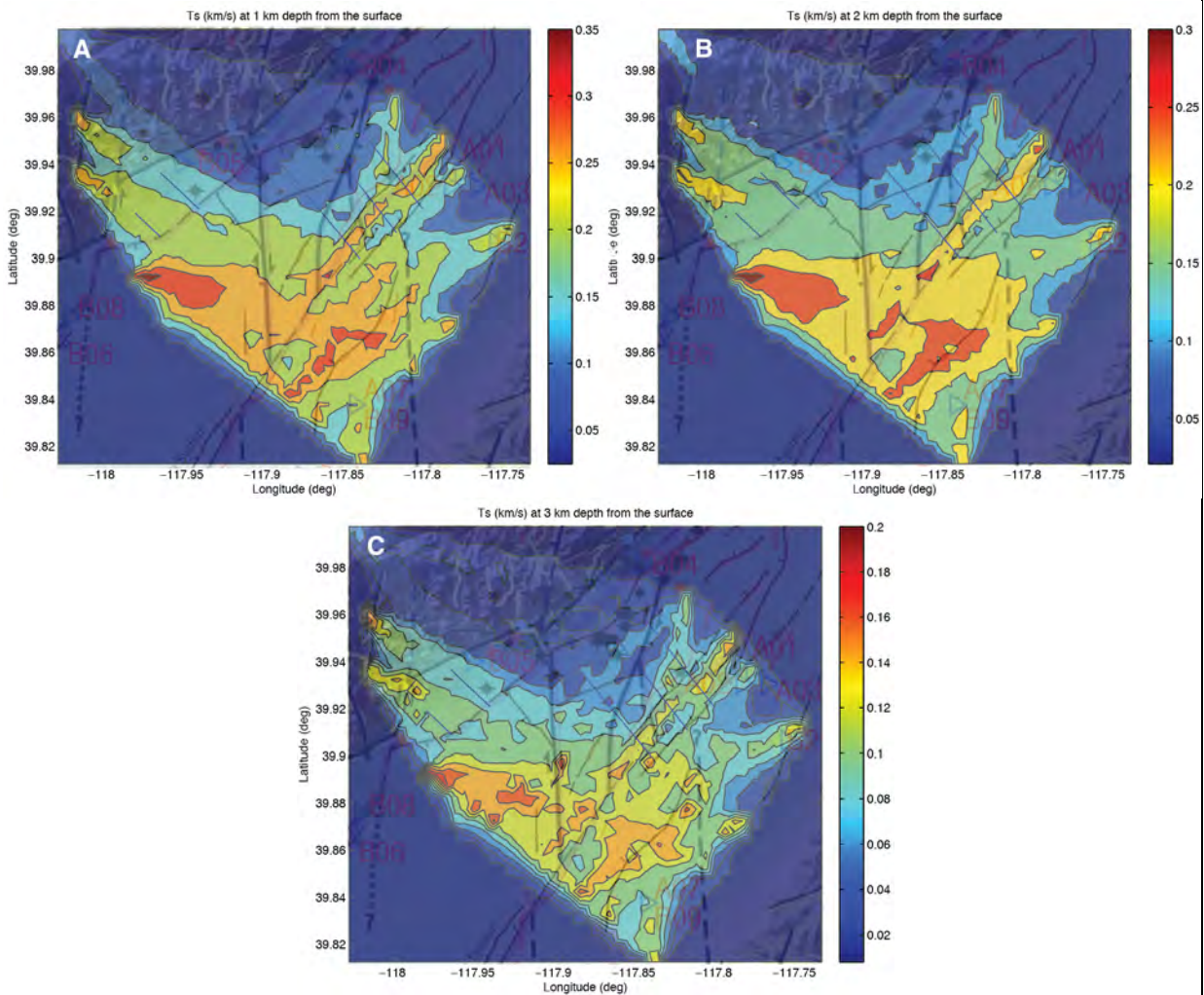
Figure 8.2. Plots A-C show the trust factors for Vs.

3) Ray-path-density

A dispersion curve in each grid cell was best resolved by the group velocity tomography code, *gridsp*, when more paths intersected the grid cell. This was why the number of paths per grid cell (for all depths) shown in Figure 3 was an important indicator of how well resolved the model was in the respective cell. Thus, a normalized trust factor matrix T_{gc} (*mn*) = 1/(Nr Paths in cell *mn*)/max(T_{gc}) was assigned to each grid cell *mn* (m and n are the number of rows and columns in the grid matrix projection on the surface). We acknowledged the limitations of this trust factor estimate, which were due to ignoring the path density at different depths.

Considering all the above errors, an empirical trust factor has been estimated for each layer i in a cell *mn* as:

$$T_{i, mn} = (TR * T_{surf96,i} * T_{gc,mn})^{1/3}$$
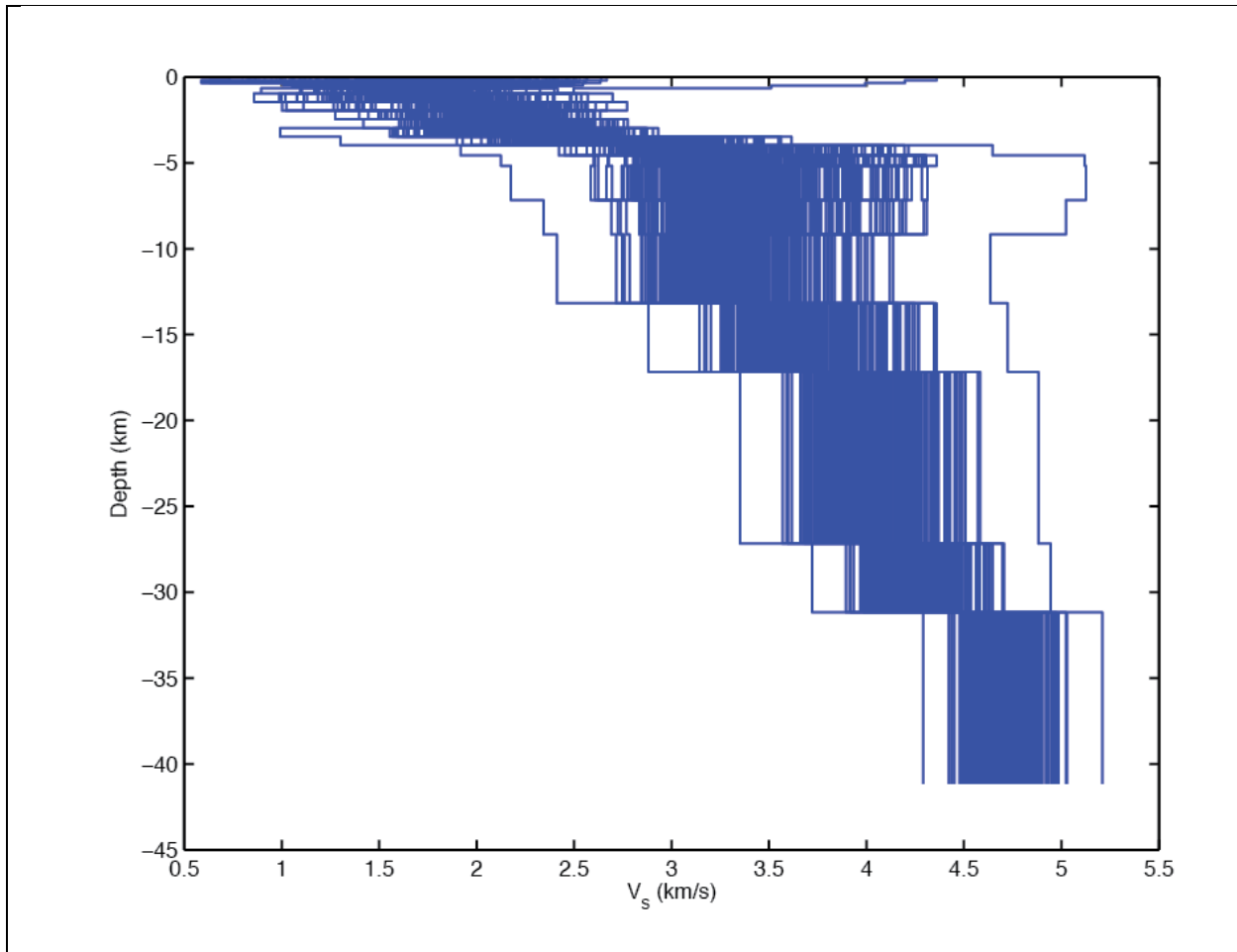
Figure 9. Realizations of the inverted shear-velocity models in Dixie Valley when the input model randomly varies 0.5 km/s around the mean velocity in Figure 6. The input model velocity variations produce output model variations of similar standard deviation relative to the mean. The uncertainty of the model is large from 5 to 10 km depth.

Figure 10.1
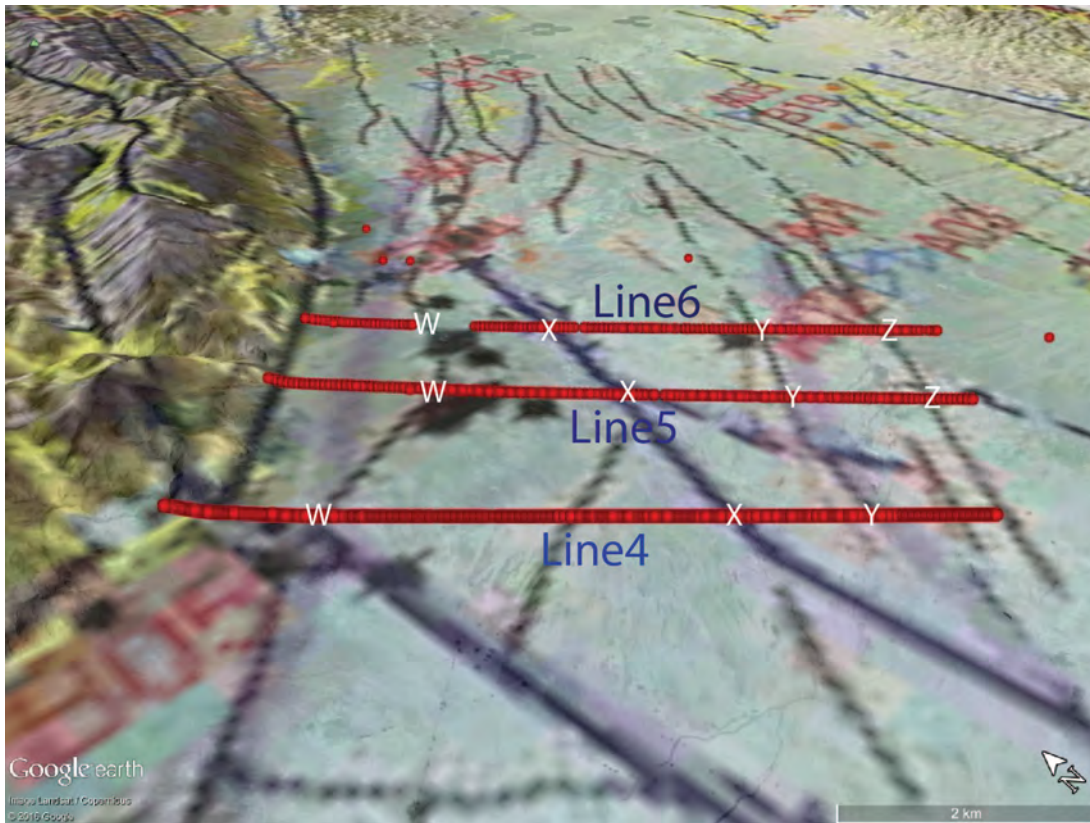
Figure 10.1. Google Earth oblique view of map of Dixie Valley deployment highlighting lines 4, 5, and 6. The large white letters (W-Z) identify an approximate fault location for each line. Each letter consistently identifies the same fault for each line. Note that fault "Z" does not cross line 4. The overlain structure map is derived from Iovenitti et al. (2015).

Figure 10.2 A
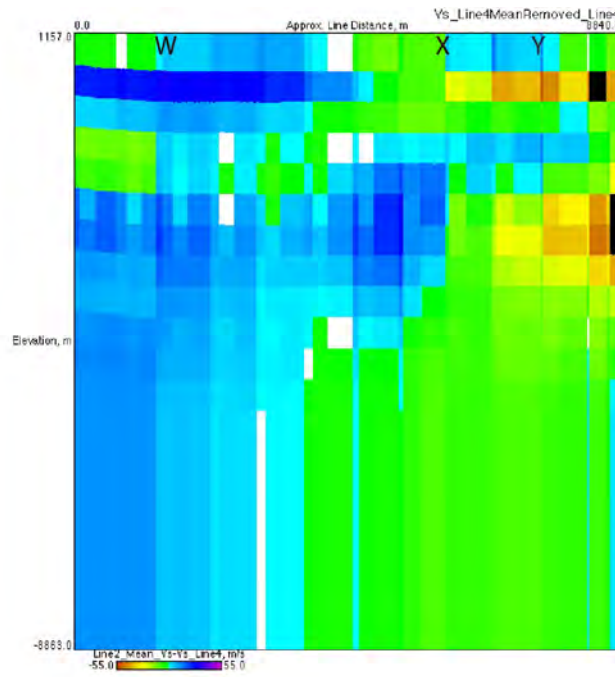
Figure 10.2 B
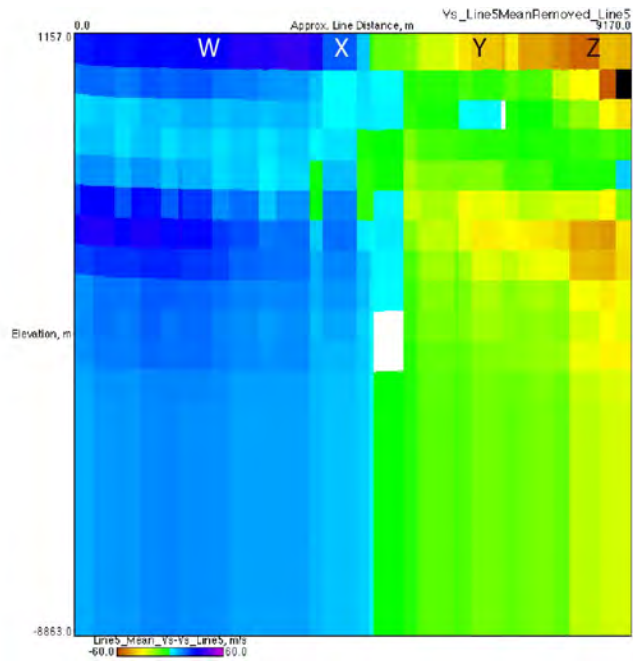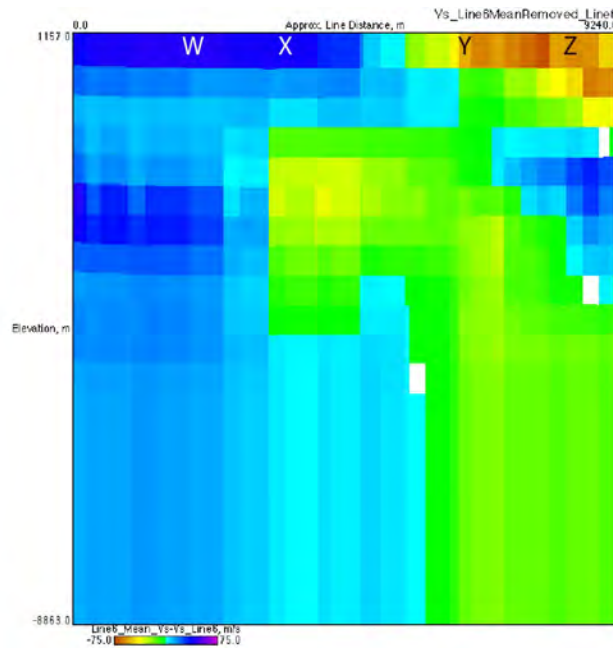
Figure 10.2 C

Figure 10.2. DV16_GVEL_MOD_LINE is the DV16_GVEL_MODEL along Line 4 (A), Line 5 (B), Line 6 (C), as a function of depth (m) for Vs. Sections have approximately no vertical exaggeration. The Vs values are in m/s. The mean Vs for each line at each depth is removed and approximate fault locations are added to the cross section (Figure 10.1). Slower than average Vs is represented by warmer colors while faster than average Vs is represented by cool colors. (A) Vs with the mean removed is shown from -55 m/s to 55 m/s. (B) Vs with the mean removed from removed from -60 m/s to 60 km/s. (C) Vs with mean removed velocities from -75 m/s to 75 km/s. Note changes in Vs near the major faults (green), although at the low resolution provided by measurements of the Vs anomalies appear vertical (see discussion in Section 3). The models removed at each depth are shown in Table 3. Plotted with JRG Viewmat from http://crack.seismo.unr.edu/jrg .
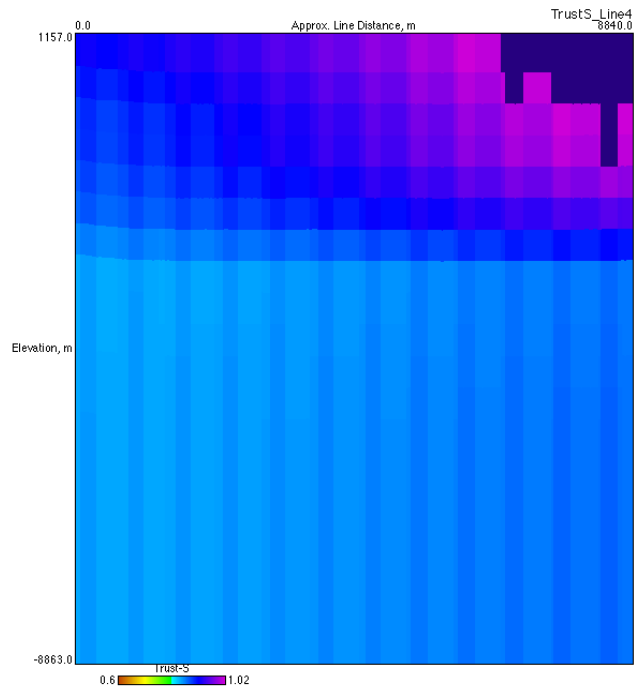
Figure 10.2 A
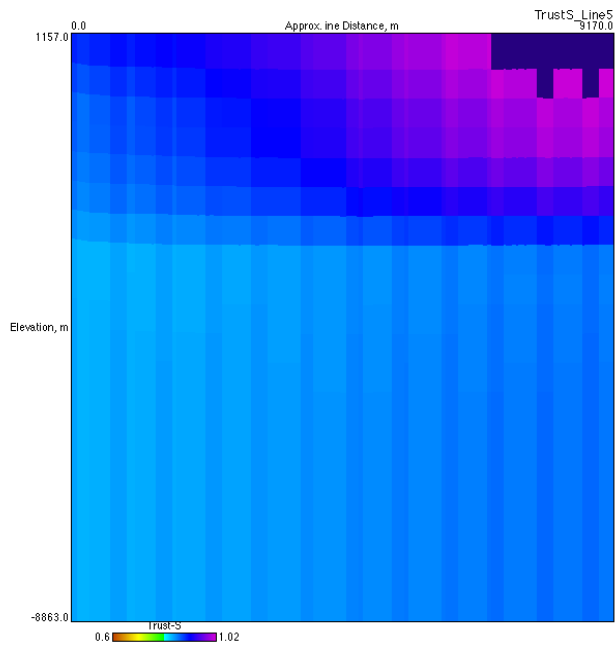
Figure 10.2 B
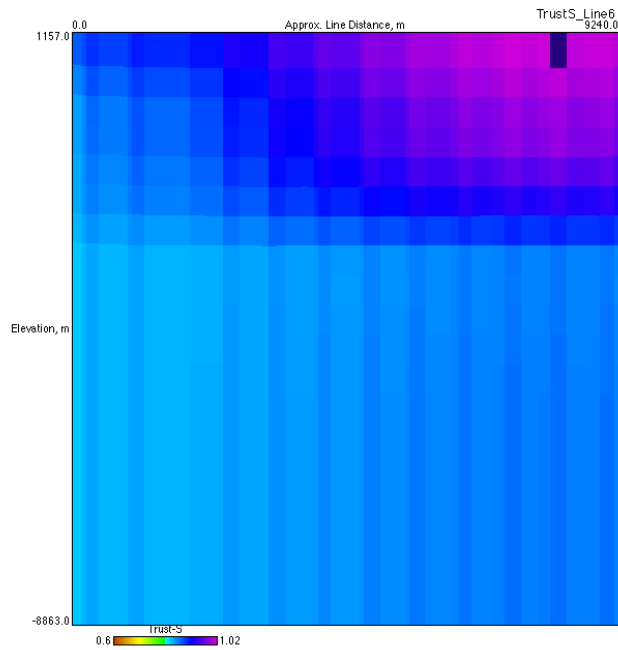
Figure 10.2 C

Figure 10.3. The S-trust factor is shown here as extracted from the DV16_GVEL_MOD along Line 4 (A), Line 5 (B), Line 6 (C), as a function of depth for S Trust Factor. All cross-section models are represented from 0.6 (lighter colors) to 1.02 (dark colors). Sections have approximately no vertical exaggeration. Plotted with JRG Viewmat from http://crack.seismo.unr.edu/jrg .

Table 3. Mean velocity models extracted from each depth on Lines 4, 5 and 6.

Depth (m)	Line 4 Vs mean (m/s)	Line 5 Vs mean (m/s)	Line 6 Vs mean (m/s)
0	1672	1638	1619
500	1765	1772	1769
1000	2072	2068	2061
1500	2195	2190	2183
2000	2300	2296	2293
2500	2513	2506	2506
3000	2920	2911	2911
3500	3256	3246	3244
4000	3300	3290	3286
4500	3252	3241	3237
5000	3261	3250	3246
5500	3245	3234	3230
6000	3229	3219	3214
10500	3600	3593	3590
15500	4037	4030	4027
20500	4326	4320	4317
25500	4556	4551	4549
30500	4766	4763	4761
35000	4429	4429	4429

2.2.4 Discussion of the low-resolution array-derived models

The DV16_GVEL_MOD estimated in Section 2.1.2-3 was integrated with *Vp* and *Vs* models estimated in the DV study area, DV14_BSL_MOD, using a set of algorithms named MAT_MOD. To give maxim weight to DV16_GVEL_MOD, 0.7 was added to the P velocity trust and 0.9 was added to the S-velocity trust. A final model was estimated in the study area, combining the DV16_GRVEL_MOD and the DV14_BSL_MOD, using MATMOD. At each depth, and in each grid cell, the resulting velocity value was a median of the velocity in each of the three models, weighted with the respective trust value. The resulting model, named DV16_INITIAL_MODEL and the virtual shot gathers, were delivered to Optim for further interpretation. The MAT_MOD algorithms were particularly suitable for this study, because they allowed integration of independent information from multiple sources.

2.2.4.1 MAT_MOD

Each model we collected or estimated was stored into a Matlab$^@$ structure. A "structure" is a named collection of data representing a single idea or "object". For anything in a computer more complicated than a list of numbers, structures can be used. The structure contains a list of fields,

each being a variable name for some subset of data. Structures are similar to arrays in that they contain multiple data, but the main difference is, instead of an index to each piece of data, we have a "name"; and instead of every piece of data being the same type, we can have a different type for each "field". The fields of a MAT_MOD structure were: the reference to the model; the model area (which is a square oriented North-South, East-West; and the model matrix. The model matrix had eleven columns: depth, P velocity in km/s, S velocity in km/s, density (g/cm^3), P and S attenuation factors Qp and Qs and five trust factors, one for P, S, density, Qp and Qs. For "no information" the matrix element value was set to -99. The "trust" factor (a value from 0 to 1) was, for example, set by the analyst as high as 0.9 for reflection/refraction lines and is set to 0.01 for general (non-local) models. Using the "trust" parameter, seismic lines and local data were given higher weights than the global model weights. A "slack" number (in this case 0.005˚) for each model represents the area where the model is considered valid. When, for example, the P and S-velocity model at a point characterized by (latitude, longitude) is requested by the user, MAT_MOD finds all the models including a square centered on the respective point, i.e., within a 0.005-degree distance from the respective point (based on one degree of latitude being 111.19 km). A side of the square is twice the slack number value. For example, the resulting P-velocity at the respective point is a "trust" - parameter weighted mean, after the "-99" estimates are discarded. The choice of the "slack" factor can "sharpen" or "smooth" the P/S extracted velocity models.

2.2.5 Array- estimated Ambient Noise S-velocity (Vs) Data Discussion

The preliminary velocity models have an average resolution of ~0.03 km^2. A remarkable achievement of this preliminary survey was obtaining fundamental Rayleigh wave information at periods longer than 1 second from sensors with a corner frequency of 5 Hz, and 2 Hz, for an analysis duration of 6-9 days. This was achieved through innovative adaptation of the seismic interferometry code to remove the instrument response of the geophones and replace it with a BB sensor response and through modifications of the processing algorithms to use overlapping windows. In this case, 15 minute windows with 50% overlap were used.

A number of *Vs* anomalies were observed at the depths of this investigation, 0.5 km to 3 km. In our previous study at Soda Lake, NV (Tibuleac et al., 2015, DOE final report), low *Vs* velocity anomalies were observed at the same locations as high temperature, low gravity and low resistivity anomalies estimated in previous geophysical studies. Also, according to Ramachandran (2011) "subsurface faults that are not clearly interpretable from velocity model plots can be identified by sharp contrasts in velocity gradient plots". Similar observations were reported in our previous study (Iovenitti et al., 2014, AltaRock DOE final report). In this study it was also observed that *Vs* gradients were associated to known fault locations (Figures 5, 8 and 10).

The resolution of the *Vs* models extracted from seismic array processing (Figures 5, 8 and 9) was lowest at depths greater than 5 km and in the upper 0.5 km below the surface.

2.3. Virtual shot gather Interpretation.

The activities to complete this task are described in Appendix 4, attached. Figure 11 below demonstrates several examples of how to locate faults in the virtual shot gathers, and in the corresponding high-resolution passive seismic reflection sections and their statistical renderings.

Figure 11.1 line 2	
Figure 11.1 line 3, threeseconds	
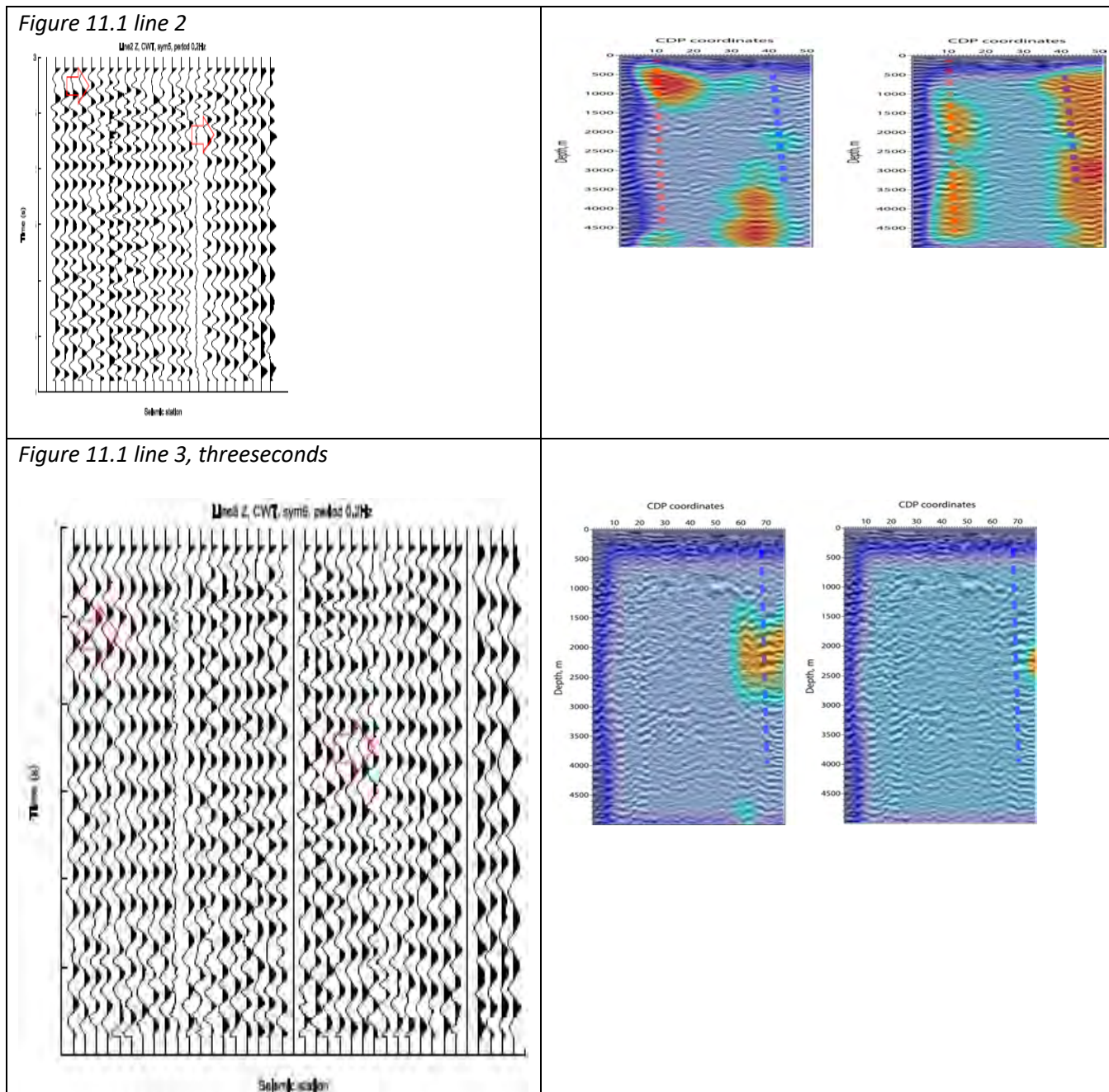
Figure 11.1 line 4, three seconds

Line 6, three seconds
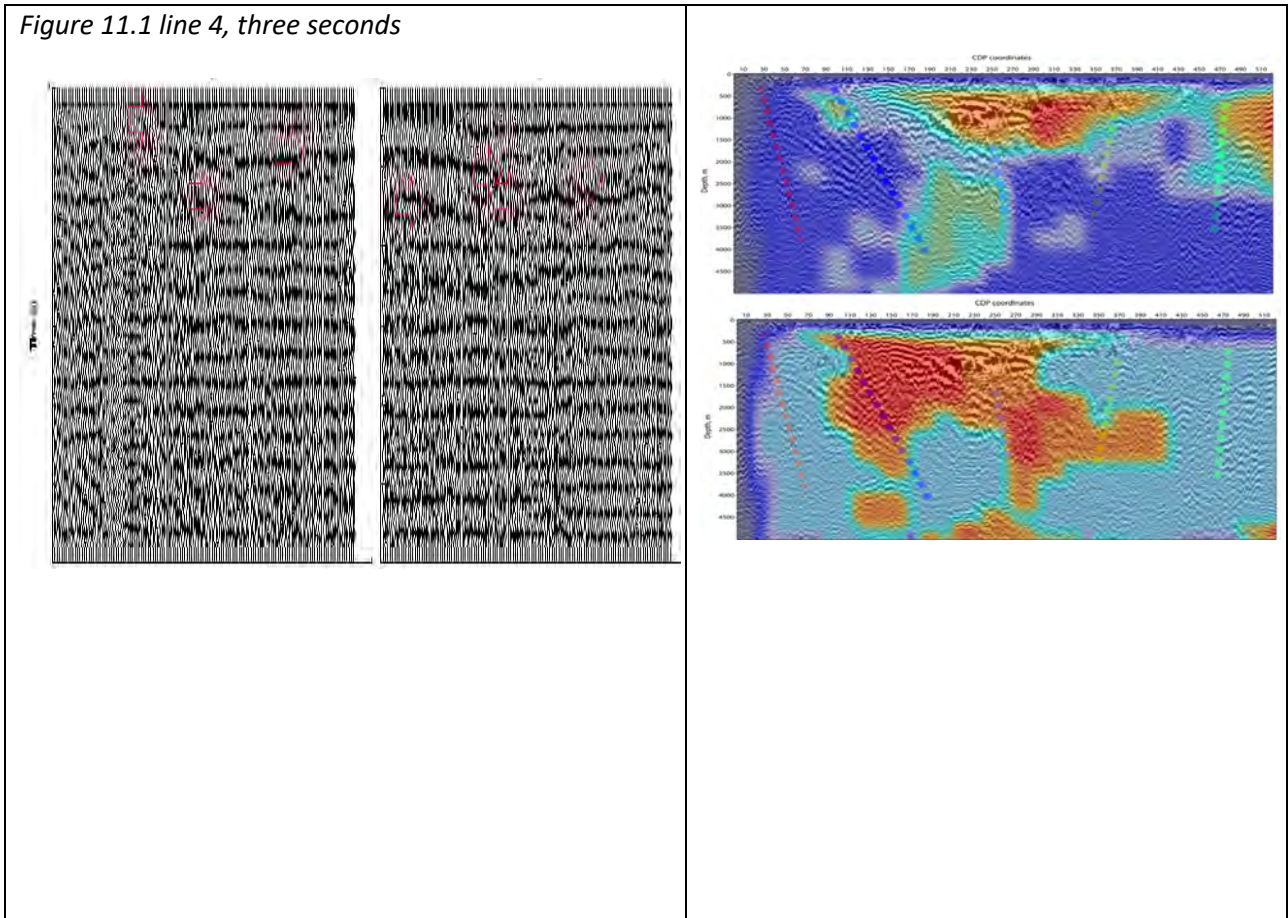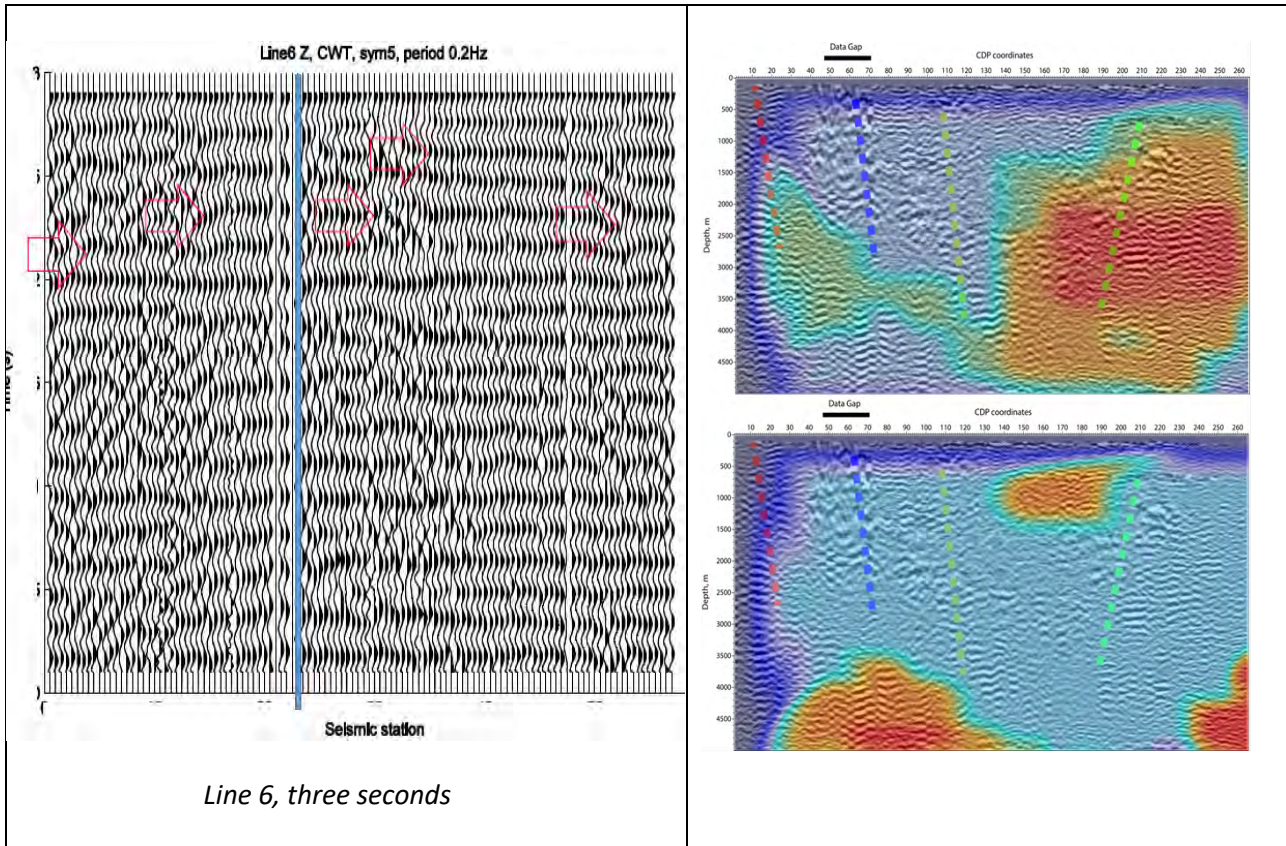
Six-second record sections on un-migrated autocorrelations on Lines 2-6, CWT sym5 at 0.36s center period

Line 2	*Line 3*
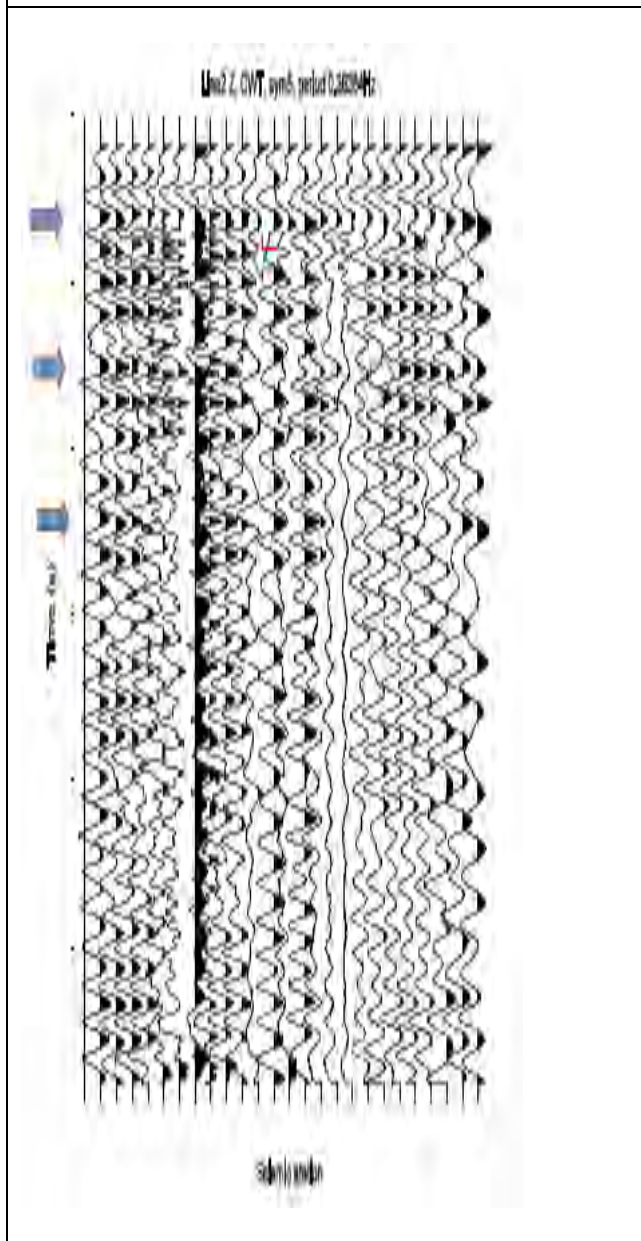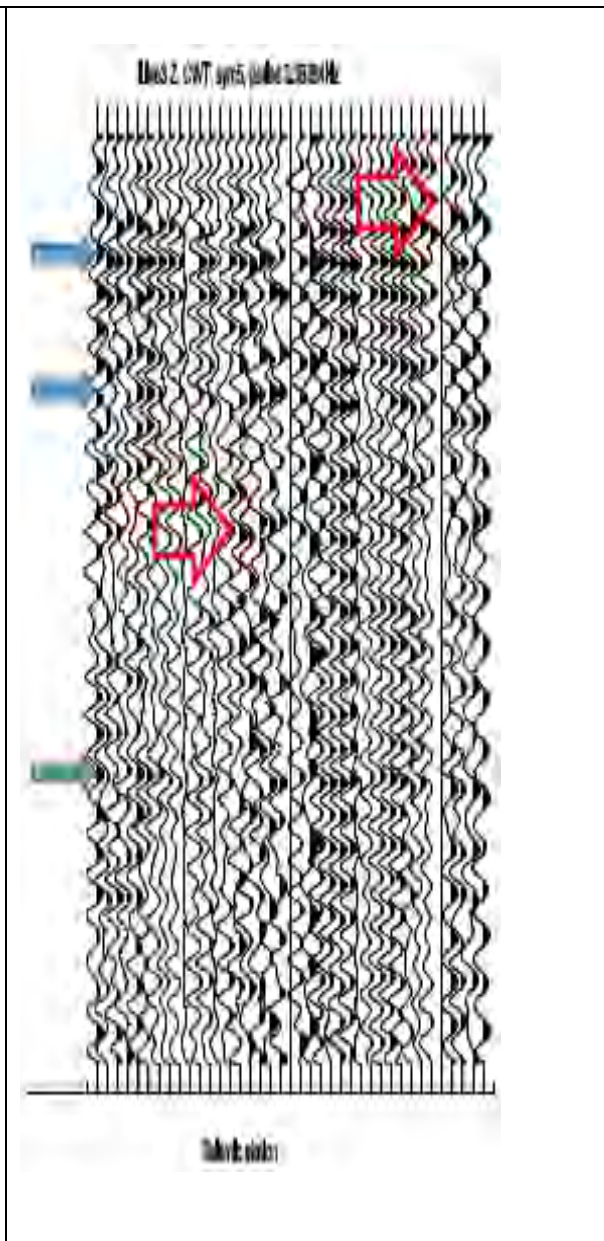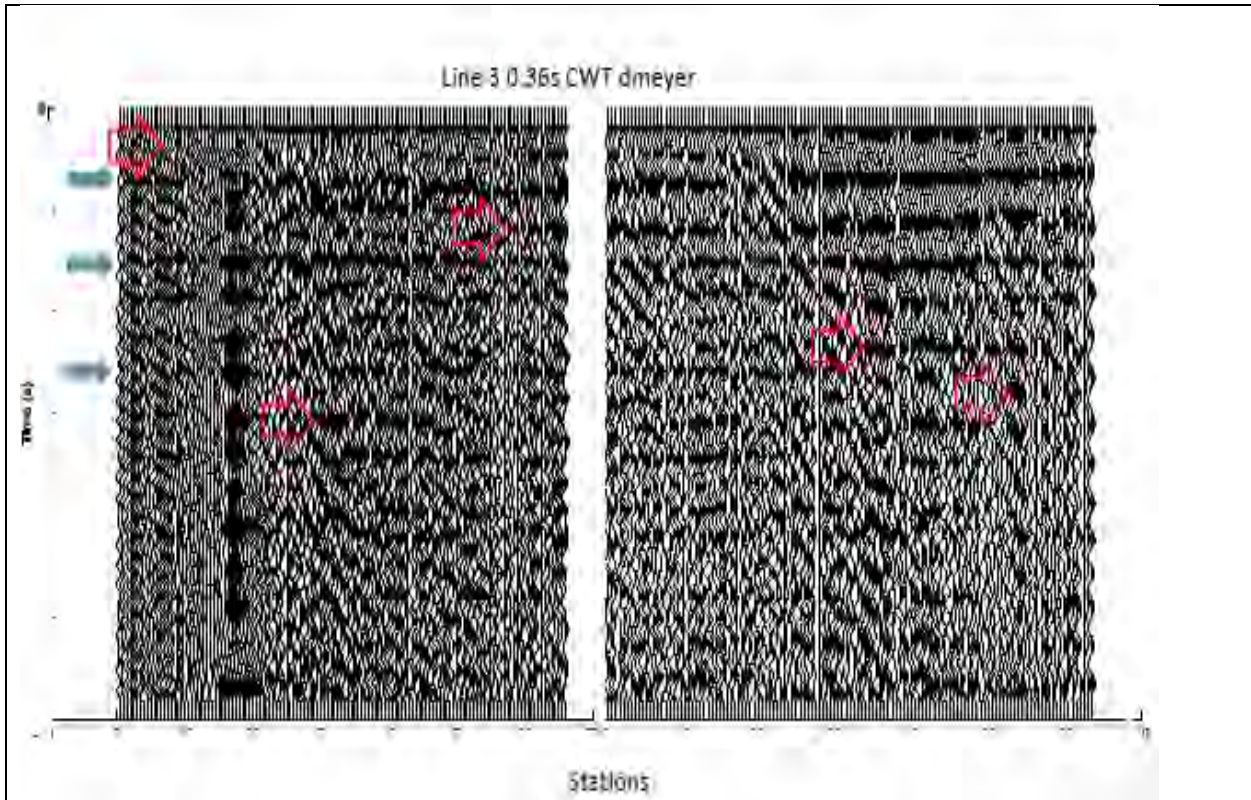
Line 4
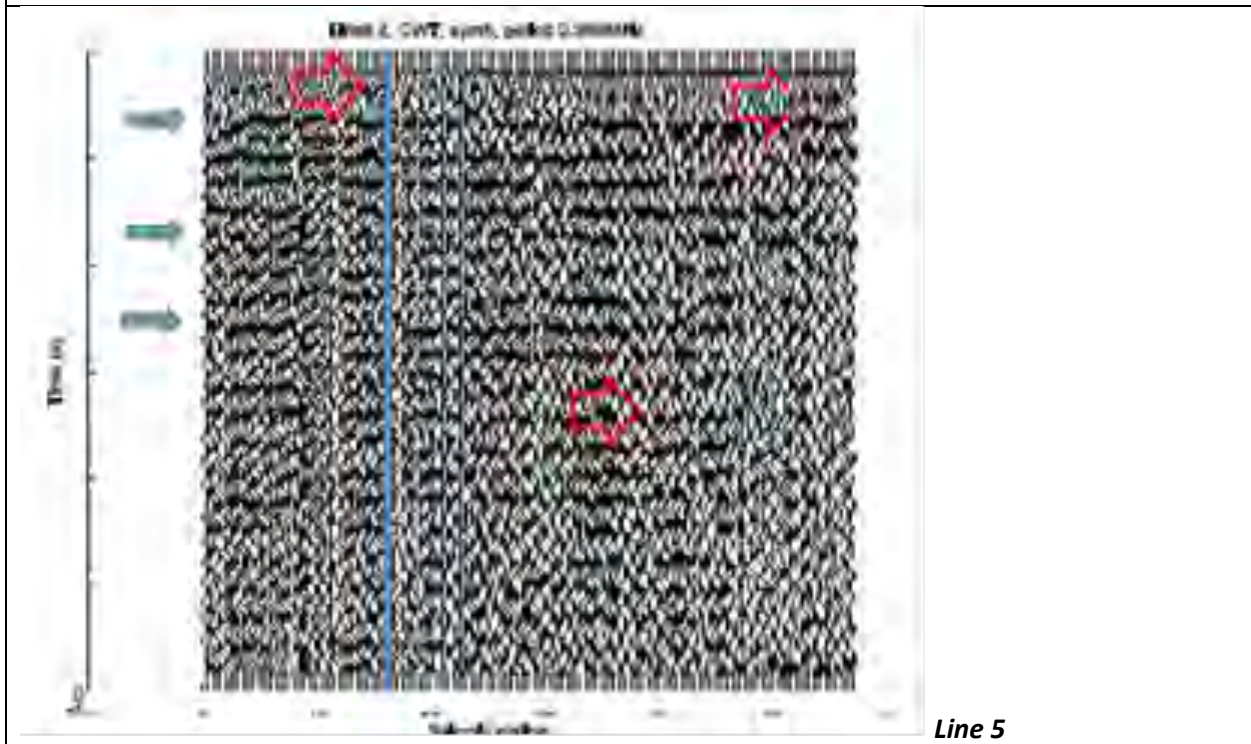
Line 5

Line 6
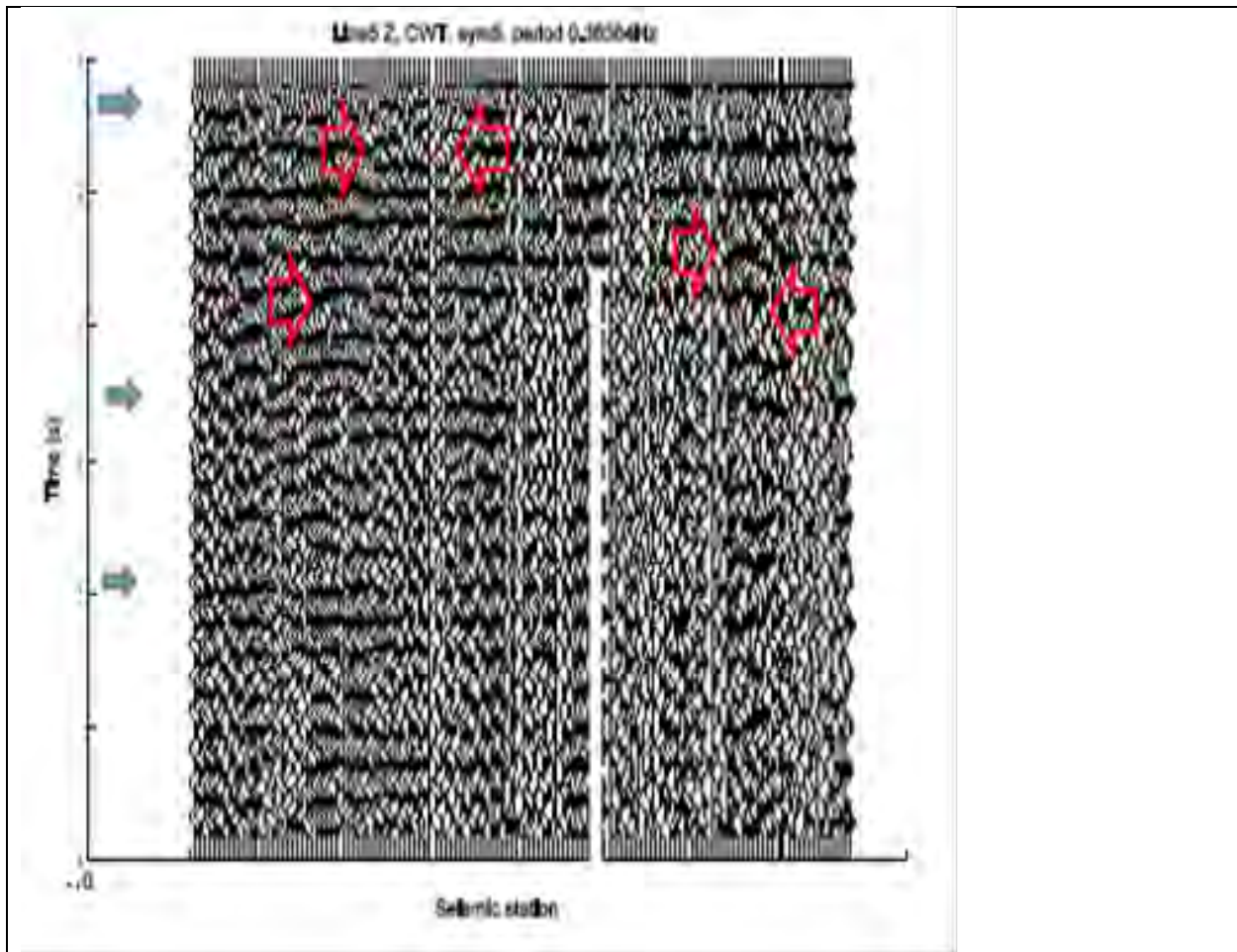
Figure 11. **A.** *Record sections of three second reflection GFs at CWT center frequency 0.2 Hz (Figure 11.1) show pattern changes at the fault locations and in the Dixie Valley Basin. Note that higher frequency filters applied to the autocorrelations enhance shallower reflections. Depth-migrated sections described in Appendix 4 are on the right side of each reflection GF record, on each line. The faults are as described at Figure 10A and in all the figures are located where the GFs change lateral pattern. Red arrows indicate changes in auto-correlation pattern, which are interpreted as possible fault zones. Blue arrows show arrivals identified as reflections from deeper layers. Note that the figures are aligned such that the time representation on the left corresponds to the depth in the depth-migrated sections.* **B.** *Six seconds of the reflection GFs are shown at each station, starting at the top of the figure. Possible faults are marked with red arrows. A reflection at 0.7 s corresponds to a layer 1.5 km deep, a 2.5 s arrival is from an ~8 km deep layer.*

TASK 3 — DIXIE VALLEY EGS CONCEPTUAL MODEL

This task involved updating the AltaRock Energy Inc. (2014)[2] Dixie Valley Conceptual Model with respect to the new seismic results. The new seismic values were integrated into the conceptual model and are presented as a spread-sheet form (Task3_Attachment.zip file). The seismic velocities were then used in Task 4 as part of a geostatistical analysis to explore relationship to measured temperature values in order to help identify anomalous zones with the project area.

In addition to these, we also explore the spectral properties of the reflection component of the Green's functions for the ambient noise survey and relationships with faults. These results are summarized below and output values provided as Task3_Attachment2.zip file.

Hydrothermal reservoirs include fragmented areas and migrating fluids. Here we research whether these fluids and their conduits along faults have any surface manifestation in terms of energy anomalies. The presence of spectral anomalies in the passive seismic wavefield, i.e., microtremors, has been found to have a high degree of correlation with the location of hydrocarbon reservoirs and hydrothermal exploration regions. For instance, Saenger et al. (2009) observed such an energy anomaly in the low-frequency band of passive seismic data between approximately 1 Hz and 6 Hz. These observations were explained as due to the partial saturation of the hydrocarbon reservoir with gas and water, whereas the surrounding rocks are fully saturated with water, such that the low- frequency resonant scattering and amplification effects only occur within the reservoir, modifying the background seismic wave field in a way characteristic of the reservoir. Another possibility would be a higher intensity of low-frequency fracturing and/or fluid migration processes within the reservoir compared to outside the reservoir. Additionally, any kind of body waves hitting the reservoir, with wavelength comparable to the reservoir dimensions, could contribute to the excitation of resonance effects.

Tibuleac *et al.*, 2012, in a study of a hydrothermal energy field at Soda Lake, NV, observed larger energy in the 5-15 Hz range on all seismic components in the production area, which was the most fragmented at the location of the faults, when compared to lower energy in other locations. This study also found significant anomalies in the Dixie Valley production well-field at frequencies between 5-15 Hz for a large aperture array deployment in 2010-2011.

Here the same methods as in Tibuleac *et al.*, 2012, are used to investigate whether similar energy anomalies can be observed using the data collected during the 2015-2016 experiment in Dixie Valley Wellfield. Reflection GFs were extracted from ambient seismic noise autocorrelation stacks (see Tibuleac and von Seggern, 2012; and Tibuleac et al., 2015) at each station in DV2016 deployment.

---

[2] AltaRock Energy Inc., 2014a, EGS Exploration Methodology Project using the Dixie Valley Geothermal System, Nevada as a Calibration Site Part I—Final Scientific Report Baseline Conceptual Model, US Department of Energy DOE Award: DE-EE0002778, submitted to the National Geothermal Data Repository.

Autocorrelations stacks at each station are the time domain expressions of mean ambient noise and signal spectra at each site and were stacked over 6-9 days at high frequency geophone stations along seismic lines, and over two months or less at SP and BB stations. The sign bit representation was applied prior to autocorrelation, however, spectral whitening was not applied. Each waveform has been denoised, using a Discrete Wavelet Transform (DWT) technique, with a *dmey*[3] wavelet. After decomposition at level eight, the approximation and details 5 – 8 were removed and the waveform was reconstructed. The effect of this procedure was equivalent to a high-pass filter, i.e., frequencies below Ny/16 were removed. The Nyquist frequency (Ny) is half of the sample rate, i.e., Ny = 125 Hz. The filter was not expected to significantly affect the waveforms recorded by the high- frequency geophones with corner frequency 5Hz. The *dmey* wavelet was also used for the Continuous Wavelet Transform (CWT) filtering.

Line analysis is shown in Figures 12-16. Vertical-component power spectral density (PSD) was estimated using Welch's method and normalized to the maximum value (and called "normalized PSD"). Using the normalized PSD of the GF's extracted at each of the DV2016 high-frequency geophone stations (Figure 11 and Figures 12-16), energy was estimated in four frequency intervals: 1- 6 Hz, 4-7 Hz, 5-10 Hz and 7-15 Hz. The 7-15 Hz (red) PSD and 5-10 Hz (black) variations along each line were best indicators of fault locations. The fault locations were the result of interpretations done during Phase I. The bottom plots in each of the Figures 12-16 are from Appendix 4 and represent the fault interpretation and the stochastic heterogeneity parameters, correlation length and Hurst number, found to be highly correlated with geothermal favorability presence (see Tibuleac et al., 2012).

The wavelet <u>entropy</u> carries information about the degree of order/disorder associated with a multi-frequency signal response. If all the reflection GFs along a line were similar, the entropy of the difference between two GFs at consecutive stations would be very low. If two successive GFs were completely different, the entropy of their difference at each time lag would be largest. The Matlab® function "wentropy"[4] was applied on reflection GFs extracted from autocorrelation beams with the option for "Shannon" or "Threshold" (with a threshold value of 0.15) entropy (Figures 12-16, plots C and G). For both types of entropy, it was found that high entropy generally corresponds to fault presence, as also found by Tibuleac et al. (2015) at Soda Lake.

Spectral analysis of the BB (Figure 17) and SP array three-component GF's (Figure 18) was applied at each of the DV2016 BB and SP stations. In Figures 17 and 18, GF record sections filtered using CWT at four center periods show remarkable reflector consistency in the study area. As discussed in each figure, stations at the location of exploration wells or fumaroles show different reflector layers, and anomalous normalized PSD values (lower plots in Figures 17 and 18). Similar to the study by Tibuleac et al. (2015) on all components, the 2-7 Hz and 5-15 Hz intervals are characterized by larger energy in the production area and lower energy otherwise.

---

3 Discrete Meyer Wavelet: An orthogonal function proposed by Yves Meyer Meyer, Yves (1990). Ondelettes et opérateurs: Ondelettes. Hermann. <u>ISBN</u> <u>9782705661250</u>.

[4] E = `wentropy(X,T)` returns the entropy E of the vector or matrix input X. In both cases, output E is a real number. The "T' stands for type and "Shannon", otherwise called "Threshold" with a value of 0.15 was used for the entropy calculations.

The frequency bands of 2-7 Hz and 5-15 Hz have been chosen to filter array data. Note significantly lower quality reflection GFs at the SP stations, mostly on the Z-components, when compared to the BB stations.

Array – estimated values of the PSD in the 2-7 Hz and 5-15 Hz intervals were represented in Figures 19-20 for each component. In these figures, the PSD values between 5 and 15 Hz were named POW515 for the BB (upper plots) and SP (lower plots) arrays. The ratio of the difference from the array mean and the array mean, expressed in percent, was represented in each figure, at each component (E, N and Z, in columns from left to right). Maps of known faults are shown in the background. Note significantly higher energy values in both bands in the exploration area at the power plant, and in the well area, especially on the horizontal components, for both frequency bands, which is encouraging, considering that the lower energy samples deeper. Regions of elevated 2-7 Hz and 5-15 Hz energy are located above areas with high fault density, and may be related to geothermal fluids having altered the shallow media. In Figure 21, the percentage BB and SP anomalies in Figures 19 and 20 were combined, and the results in the 2-7 Hz and 5-15 Hz intervals are shown in three columns for the E, N and Z components, from left to right. It is noted that, for both bands, the horizontal component energy is anomalously large in the fault area, however, the vertical energy is anomalously high only southwest of the study area, where active well drilling was going on during the DV2015-2016 experiment.

To summarize, the power spectral density analysis reveals significantly higher values in the exploration area at the power plant, and in the drilling area, near the BB station 10201, especially on the horizontal components. Regions of elevated energy for both the 2-7 Hz and 5-15 Hz frequency bands are located above intersections of multiple faults. The anomalously high BB anomalies in the SW could be due to drilling activities which are confined to the vertical direction.

Sum PSD amplitudes 7 to 15 Hz red, 4 to 7 Hz green, 1 to 6 Hz magenta, 5 to 10 Hz black

A

Line 2 Z, Normalized PSD

E

Z, CWT, dmey, period 0.090909Hz

B

Z, CWT, dmey, period 0.2Hz

F

CWT, dmey, per 0.090909s, Shannon Entropy (red), threshold entropy (black) 0.15, differentiated Line 2

C

CWT, dmey, per 0.2s, Shannon Entropy (red) threshold entropy (black) 0.15, Line 2

G

D

H
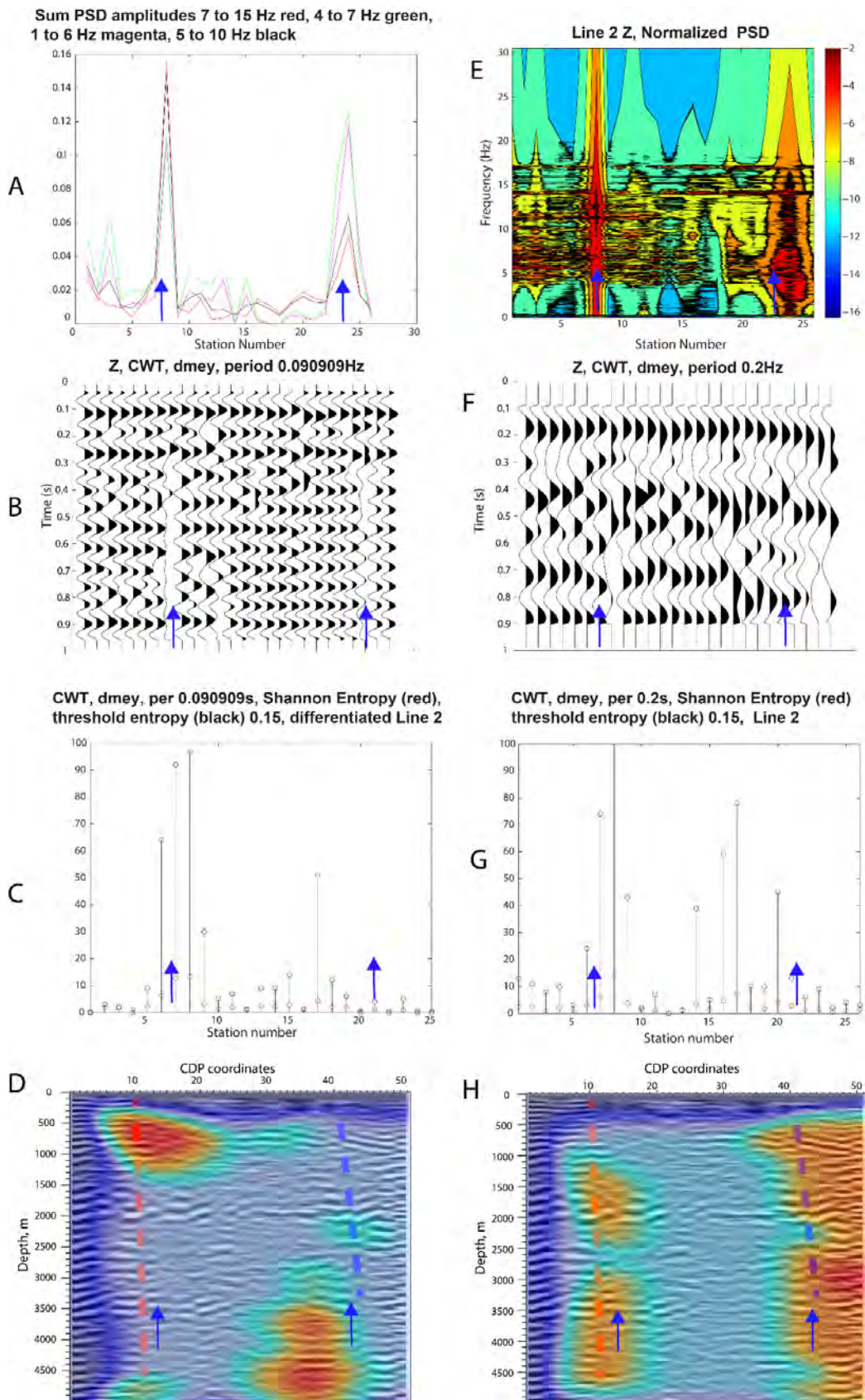
*Figure 12: **Line 2.** In plot A spectral energy at each station location (on the x-axis) is shown as follows: 1-6 Hz (magenta), 4-7 Hz (green), 5-10 Hz (black) and 7-15 Hz red for the Z-component. The E and N components were not available for the vertical (Z) high frequency geophones installed on Line 2. Plot E shows the normalized reflection GF power spectral density (PSD) in each frequency band, estimated using Welch's method. Plots B and F are showing GF record sections along the line, filtered using CWT centered on 0.1 s (plot B) and 0.2 s (plot F). Changes in the GF pattern are observed at the fault locations and marked by arrows. In plots C, respectively G, the Shannon (red) and Threshold (black) entropy of the GF (plots B, respectively F) differences between every two consecutive stations increase above faults, as shown at the arrow locations. If the structure along Line 2 would be uniform, all GFs would be similar and the entropy would be low. The fragmented areas, however, have significant differences in structure and the scattered energy makes the waveforms different. Shannon and Threshold entropy increases for stations on the faults identified along Line 2 by the Optim analysis in plots D and H. Care should to be taken in entropy interpretation, as one irregular station (such as station 17) may also result in an isolated increase in entropy, without a pattern change. The Phase I interpretation of the profile in terms of correlation length (plot D) and Hurst number (plot H) are shown for comparison.*

Sum PSD amplitudes 7 to 15 Hz red, 4 to 7 Hz green, 1 to 6 Hz magenta, 5 to 10 Hz black

Line 3 Z, Normalized PSD

Z, CWT, dmey, period 0.090909Hz

Z, CWT, dmey, period 0.2Hz

CWT, dmey, per 0.090909s, Shannon Entropy (red), threshold entropy (black) 0.15, differentiated Line 3

CWT, dmey, per 0.2s, Shannon Entropy (red) threshold entropy (black) 0.15, Line 3

CDP coordinates

CDP coordinates
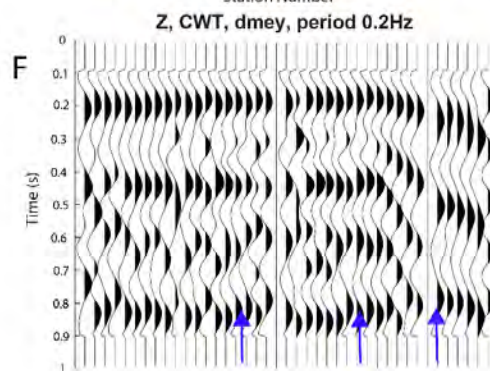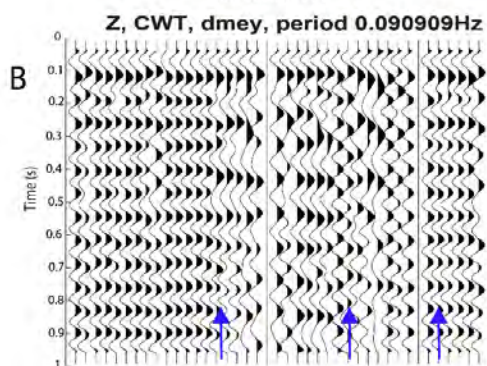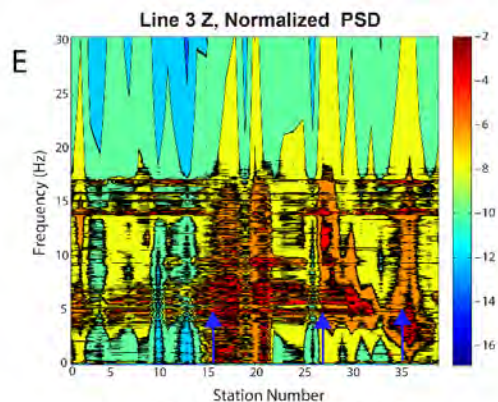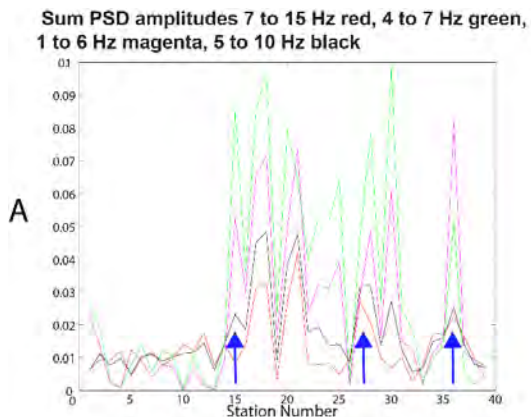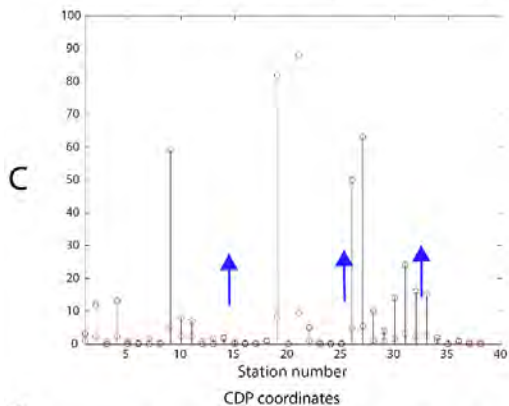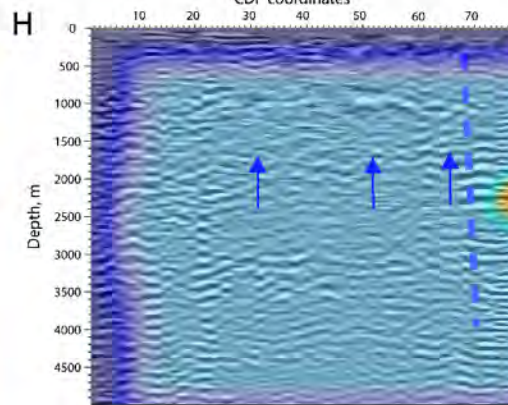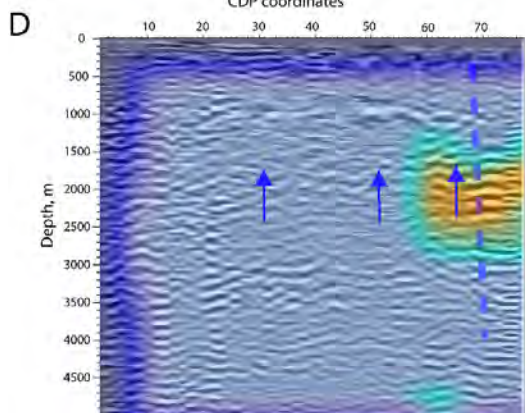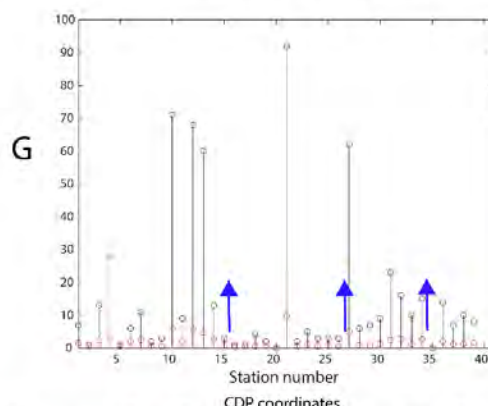
*Figure 13: **Line 3**. In plot A spectral energy at each station location (on the x-axis) is shown as follows: 1-6 Hz (magenta), 4-7 Hz (green), 5-10 Hz (black) and 7-15 Hz red for the Z-component. The E and N components were not available for the vertical (Z) high frequency geophones installed on Line 3. Plot E shows the normalized reflection GF power spectral density (PSD) in each frequency band, estimated using Welch's method. Plots B and F are showing GF record sections along the line, filtered using CWT centered on 0.1s (plot B) and 0.2s (plot F). Changes in the GF pattern are observed at the interpreted fault locations and marked by arrows. In plots C, respectively G, the Shannon (red) and Threshold (black) entropy of the GF (plots B, respectively F) differences between every two consecutive stations increase above faults, as shown at the arrow locations. If the structure along Line 3 would be uniform, all GFs would be similar and the entropy would be low. The fragmented areas, however, have significant differences in structure and the scattered energy makes the waveforms different. Shannon and Threshold entropy increases for stations on the faults identified along Line 3 by the reflection analysis in plots D and H. Care should to be taken in entropy interpretation, as one irregular station (such as station 17) may also result in an isolated increase in entropy, without a pattern change. The Phase I interpretation of the profile in terms of correlation length (plot D) and Hurst number (plot H) are shown for comparison.*

Sum PSD amplitudes 7 to 15 Hz red, 4 to 7 Hz green, 1 to 6 Hz magenta, 5 to 10 Hz black

A

Line 4 Z, Normalized PSD

E

Z, CWT, dmey, period 0.090909Hz

B

Z, CWT, dmey, period 0.2Hz

F

CWT, dmey, per 0.090909s, Shannon Entropy (red), threshold entropy (black) 0.15, differentiated Line 4

C

CWT, dmey, per 0.2s, Shannon Entropy (red) threshold entropy (black) 0.15, Line 4

G

D

H
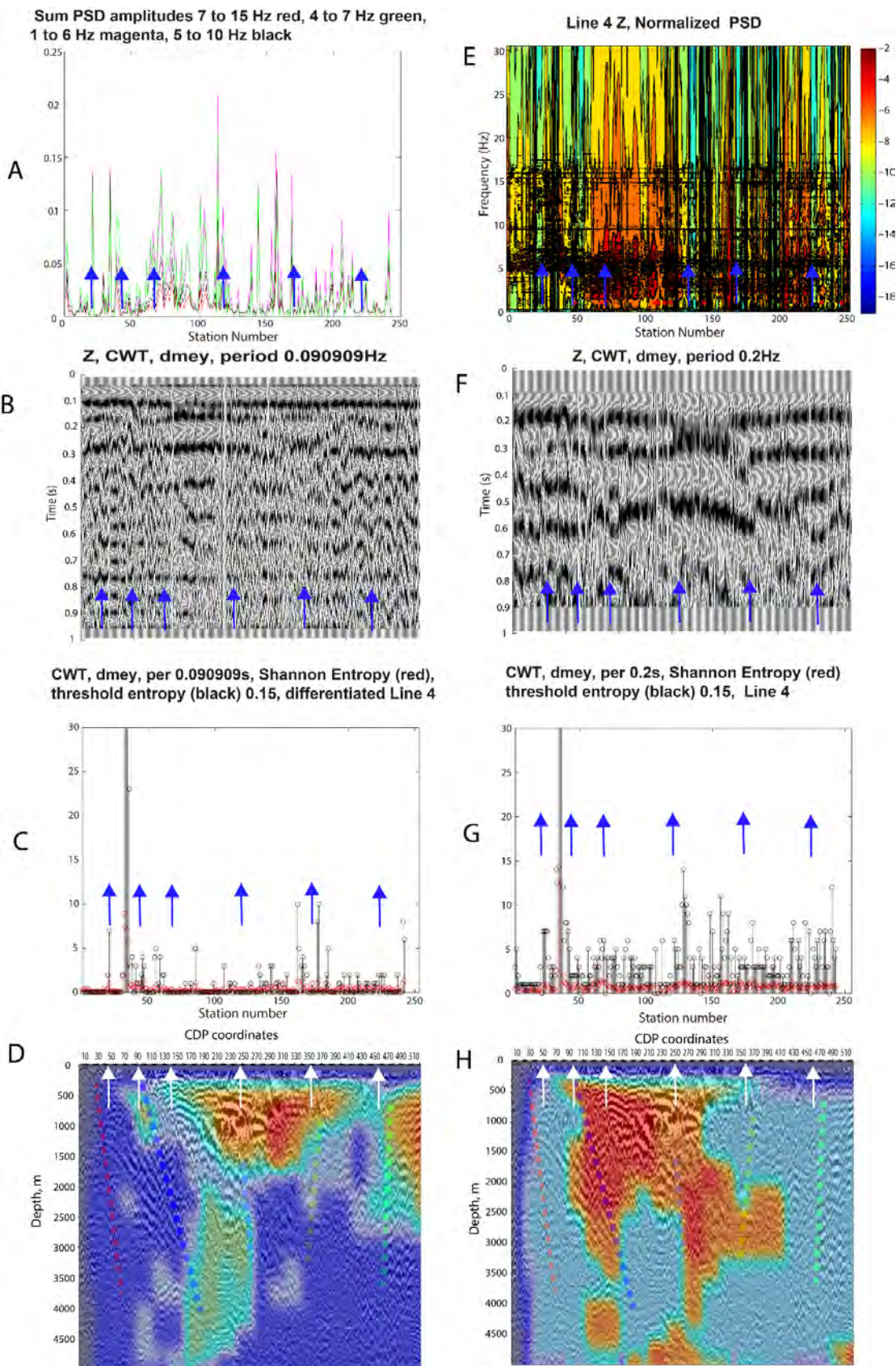
*Figure 14: **Line 4**. In plot A spectral energy at each station location (on the x-axis) is shown as follows: 1-6 Hz (magenta), 4-7 Hz (green), 5-10 Hz (black) and 7-15 Hz red for the Z-component. The E and N components were not available for the vertical (Z) high frequency geophones installed on Line 4. Plot E shows the normalized reflection GF power spectral density (PSD) in each frequency band, estimated using Welch's method. Plots B and F are showing GF record sections along the line, filtered using CWT centered on 0.1s (plot B) and 0.2s (plot F). Changes in the GF pattern are observed at the interpreted fault locations and marked by arrows. In plots C, respectively G, the Shannon (red) and Threshold (black) entropy of the GF (plots B, respectively F) differences between every two consecutive stations increase above faults, as shown at the arrow locations. If the structure along Line 4 would be uniform, all GFs would be similar and the entropy would be low. The fragmented areas, however, have significant differences in structure and the scattered energy makes the waveforms different. Shannon and Threshold entropy increases for stations on the faults identified along Line 4 by the reflection analysis in plots D and H. Care should to be taken in entropy interpretation, as one irregular station (such as station 17) may also result in an isolated increase in entropy, without a pattern change. The Phase I interpretation of the profile in terms of correlation length (plot D) and Hurst number (plot H) are shown for comparison.*

Sum PSD amplitudes 7 to 15 Hz red, 4 to 7 Hz green, 1 to 6 Hz magenta, 5 to 10 Hz black

A

Line 5 Z, Normalized PSD

E

Z, CWT, dmey, period 0.090909Hz

B

Z, CWT, dmey, period 0.2Hz

F

CWT, dmey, per 0.090909s, Shannon Entropy (red), threshold entropy (black) 0.15, differentiated Line 5

C

CWT, dmey, per 0.2s, Shannon Entropy (red) threshold entropy (black) 0.15, Line 5

G

CDP coordinates

D

CDP coordinates

H
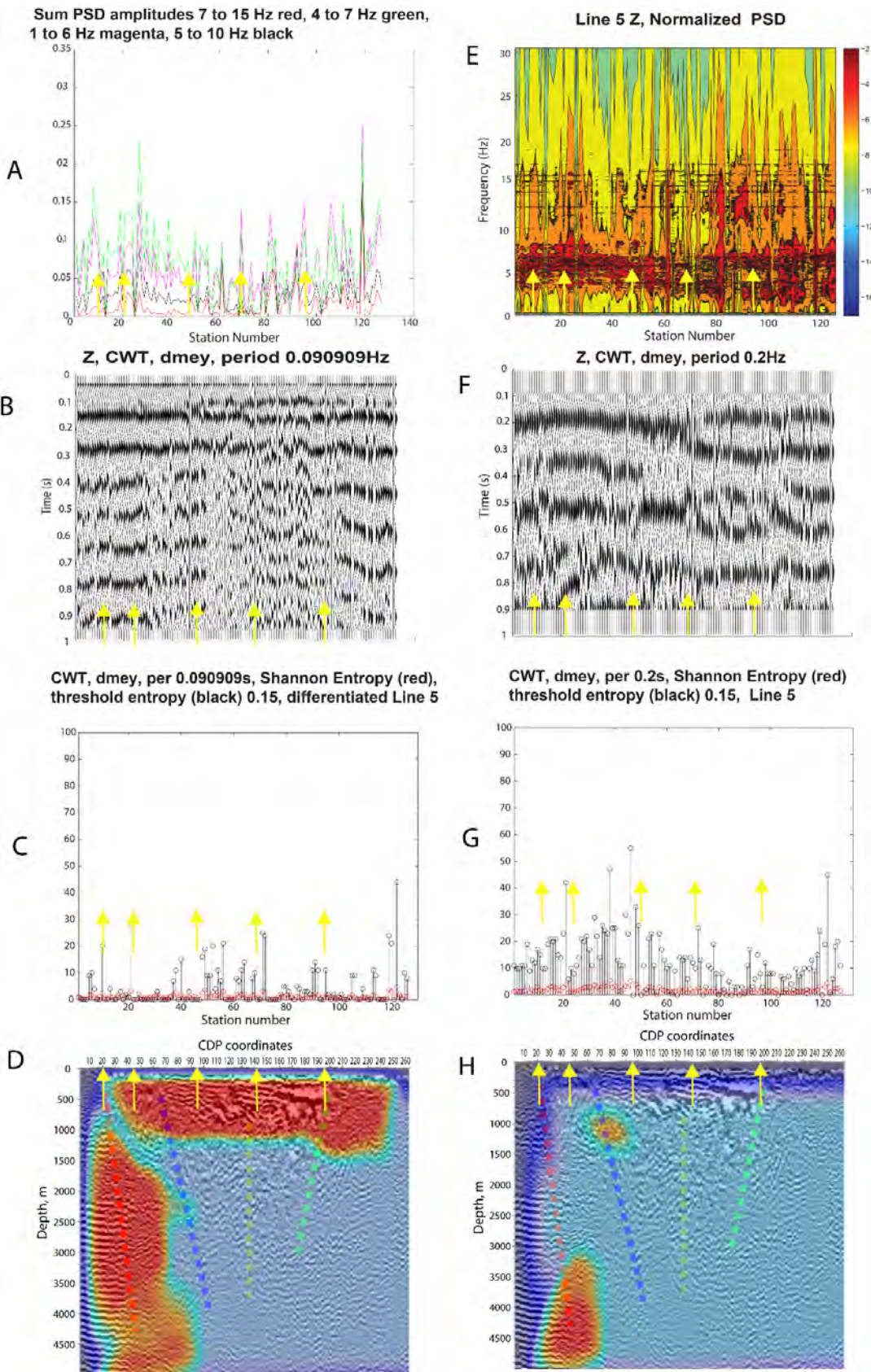
*Figure 15. **Line 5**. In plot A spectral energy at each station location (on the x-axis) is shown as follows: 1-6 Hz (magenta), 4-7 Hz (green), 5-10 Hz (black) and 7-15 Hz red for the Z-component. The E and N components were not available for the vertical (Z) high frequency geophones installed on Line 5. Plot E shows the normalized reflection GF power spectral density (PSD) in each frequency band, estimated using Welch's method. Plots B and F are showing GF record sections along the line, filtered using CWT centered on 0.1s (plot B) and 0.2s (plot F). Changes in the GF pattern are observed at the interpreted fault locations and marked by arrows. In plots C, respectively G, the Shannon (red) and Threshold (black) entropy of the GF (plots B, respectively F) differences between every two consecutive stations increase above faults, as shown at the arrow locations. If the structure along Line 5 would be uniform, all GFs would be similar and the entropy would be low. The fragmented areas, however, have significant differences in structure and the scattered energy makes the waveforms different. Shannon and Threshold entropy increases for stations on the faults identified along Line 5 by the reflection analysis in plots D and H. Care should to be taken in entropy interpretation, as one irregular station (such as station 17) may also result in an isolated increase in entropy, without a pattern change. The Phase I interpretation of the profile in terms of correlation length (plot D) and Hurst number (plot H) are shown for comparison.*

Sum PSD amplitudes 7 to 15 Hz red, 4 to 7 Hz green, 1 to 6 Hz magenta, 5 to 10 Hz black

Line 6 Z, Normalized PSD

Z, CWT, dmey, period 0.090909Hz

Z, CWT, dmey, period 0.2Hz

CWT, dmey, per 0.090909s, Shannon Entropy (red), threshold entropy (black) 0.15, differentiated Line 6

CWT, dmey, per 0.2s, Shannon Entropy (red) threshold entropy (black) 0.15, Line 6
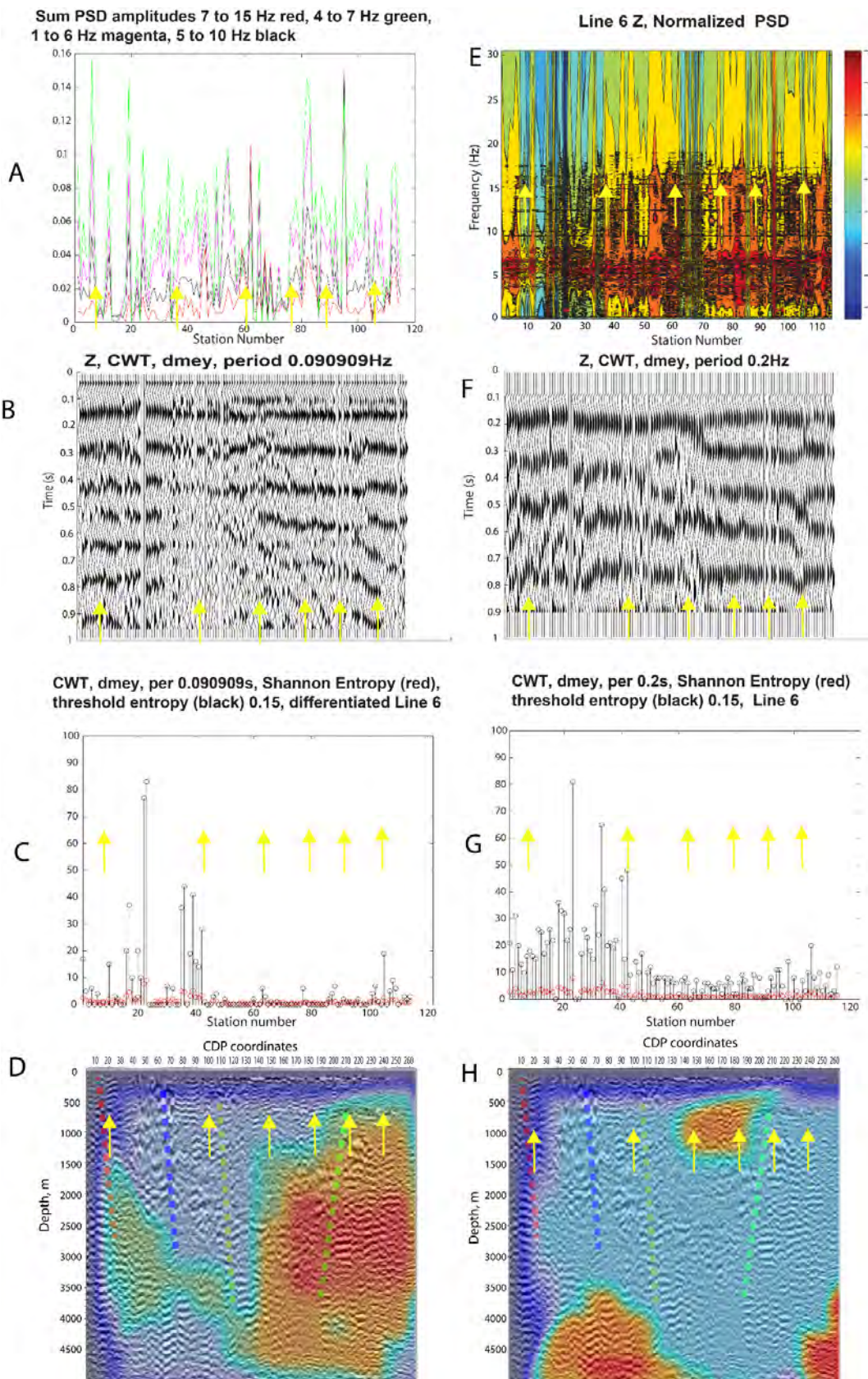
*Figure 16. **Line 6**. In plot A spectral energy at each station location (on the x-axis) is shown as follows: 1-6 Hz (magenta), 4-7 Hz (green), 5-10 Hz (black) and 7-15 Hz red for the Z-component. The E and N components were not available for the vertical (Z) high frequency geophones installed on Line 6. Plot E shows the normalized reflection GF power spectral density (PSD) in each frequency band, estimated using Welch's method. Plots B and F are showing GF record sections along the line, filtered using CWT centered on 0.1s (plot B) and 0.2s (plot F). Changes in the GF pattern are observed at the interpreted fault locations and marked by arrows. In plots C, respectively G, the Shannon (red) and Threshold (black) entropy of the GF (plots B, respectively F) differences between every two consecutive stations increase above faults, as shown at the arrow locations. If the structure along Line 6 would be uniform, all GFs would be similar and the entropy would be low. The fragmented areas, however, have significant differences in structure and the scattered energy makes the waveforms different. Shannon and Threshold entropy increases for stations on the faults identified along Line 6 by the reflection analysis in plots D and H. Care should to be taken in entropy interpretation, as one irregular station (such as station 17) may also result in an isolated increase in entropy, without a pattern change. The Phase I interpretation of the profile in terms of correlation length (plot D) and Hurst number (plot H) are shown for comparison. Note that some of the arrows show deeper interpreted faults.*
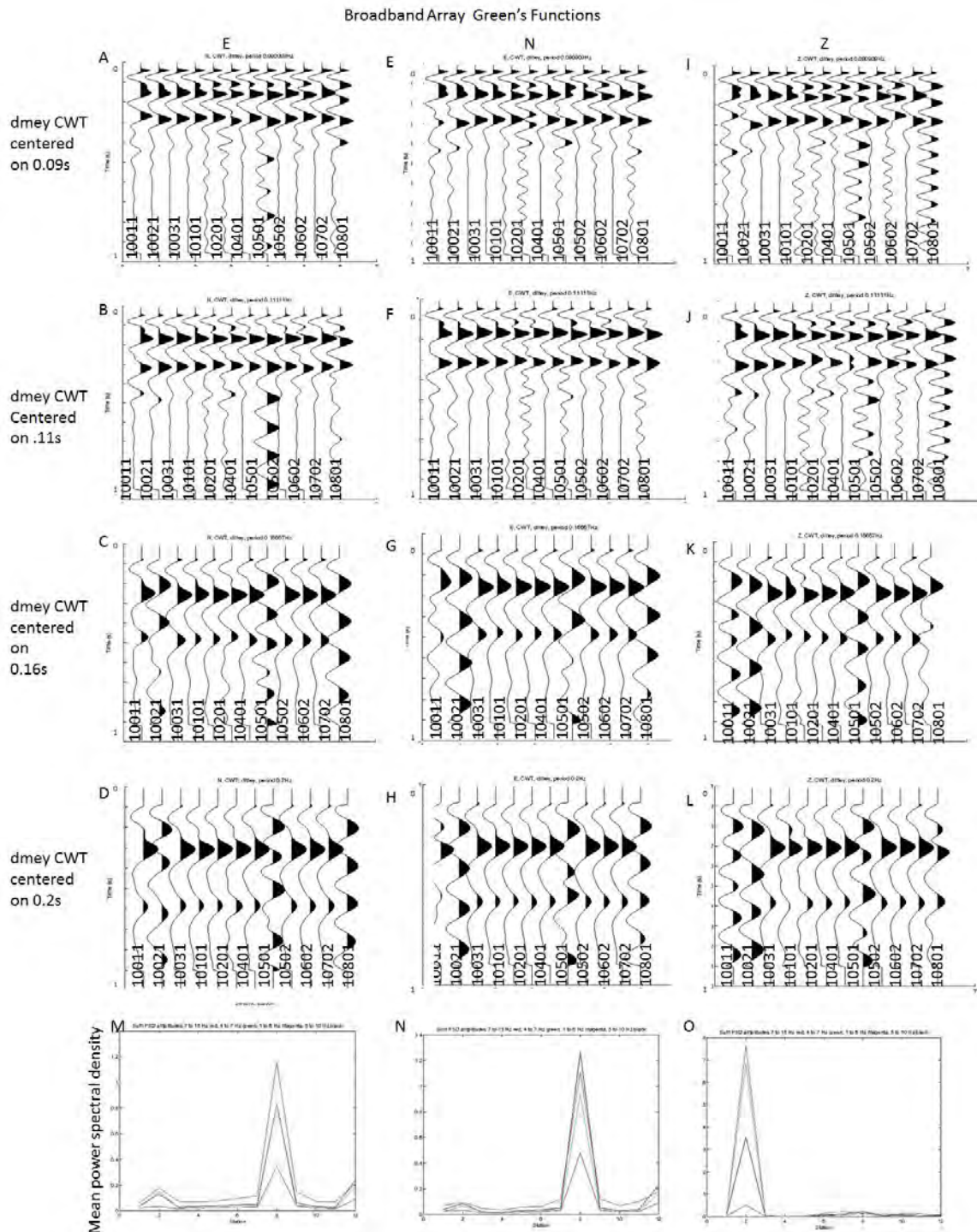
Figure 17. The BB CWT-filtered GFs are shown in plots A-L, for three center periods:0.09 s, 0.11 s and 0.16 s. The E, N, Z components are shown in each column from left to right. Stations 10101, 10201, 10501 and 10801 have different GFs and relatively higher mean PSDs, on all components. Drilling was taking place near stations 10101 and 10201 over the duration of the experiment, which resulted in significantly higher seismic noise.

Short Period Array Green's Functions
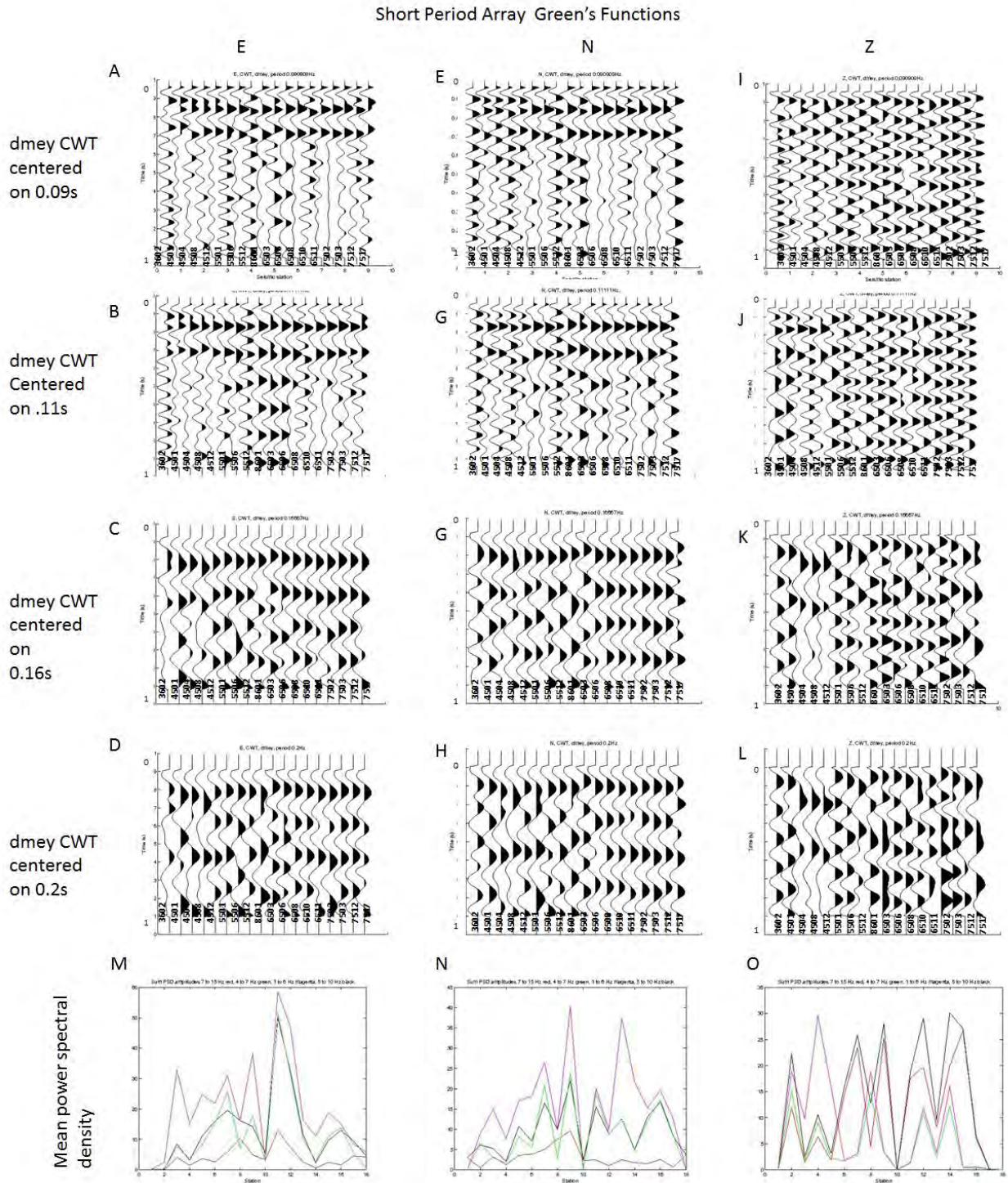
Figure 18. The SP CWT-filtered GFs are shown in plots A-L, for three center periods:0.09 s, 0.11 s and 0.16 s. The E, N, Z components are shown in each column from left to right. Stations 4501, 5506, 6506 and 7507 have different GFs and higher normalized PSD, on all components. All these stations are located above faults or close to production wells.
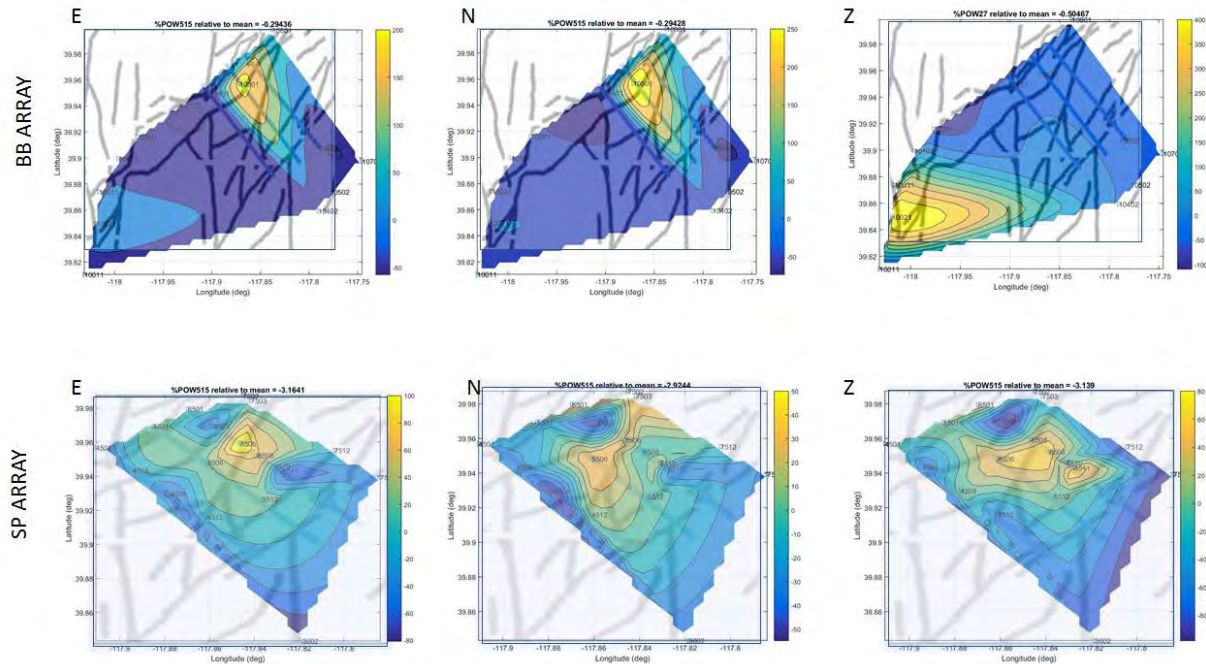
Figure 19. The PSD values between 5 and 15 Hz named POW515 were estimated at the BB (upper plots) and SP (lower plots) arrays. The ratio of the difference from the array mean and the array mean, expressed in percent, was represented in each figure, at each component (E, N and Z, in columns from left to right). Maps of known faults are shown in the background. Note significantly higher values in the exploration area at the power plant, and in the drilling area, near the BB station 10201, especially on the horizontal components. Regions of elevated 5-15 Hz energy are located above intersections of multiple faults.
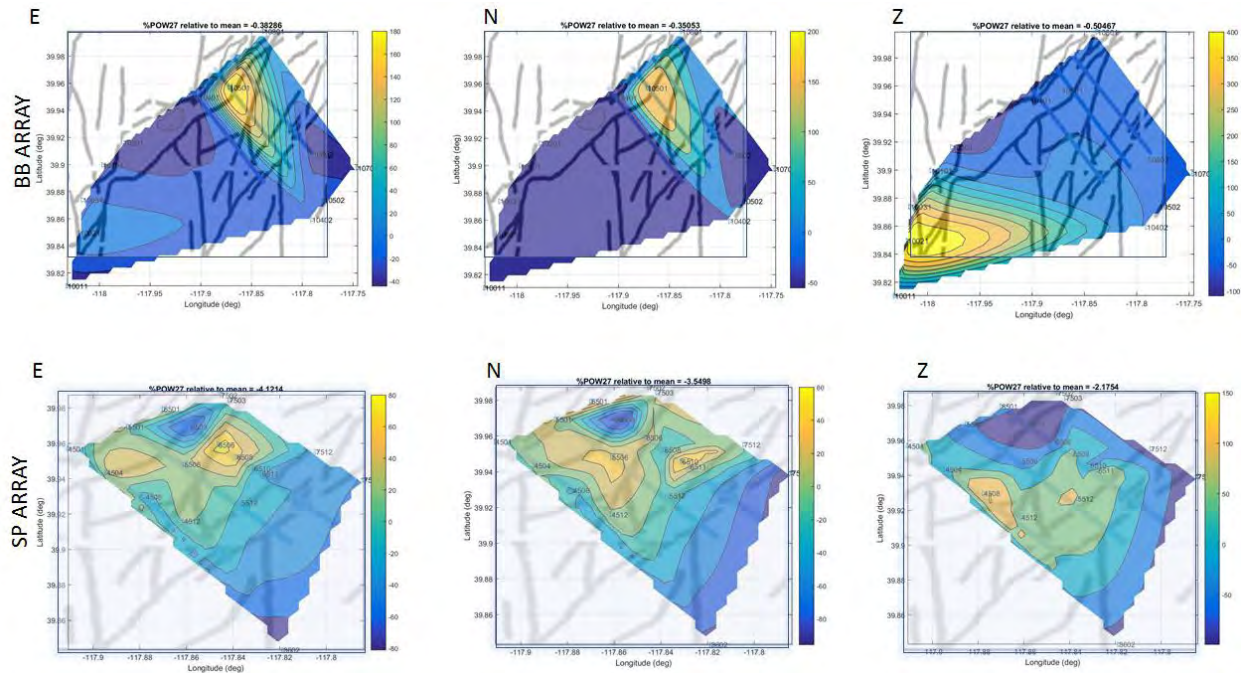
Figure 20. The PSD values between 2 and 7 Hz named POW27 were estimated at the BB (upper plots) and SP (lower plots) arrays. The ratio of the difference from the array mean and the array mean, expressed in percent, was represented in each figure, at each component (E, N and Z, in columns from left to right). Maps of known faults are shown in the background. Note significantly higher values in the exploration area at the power plant, and in the drilling area, near the BB station 10201, especially on the horizontal components. Regions of elevated 2-7 Hz energy are located above intersections of multiple faults.
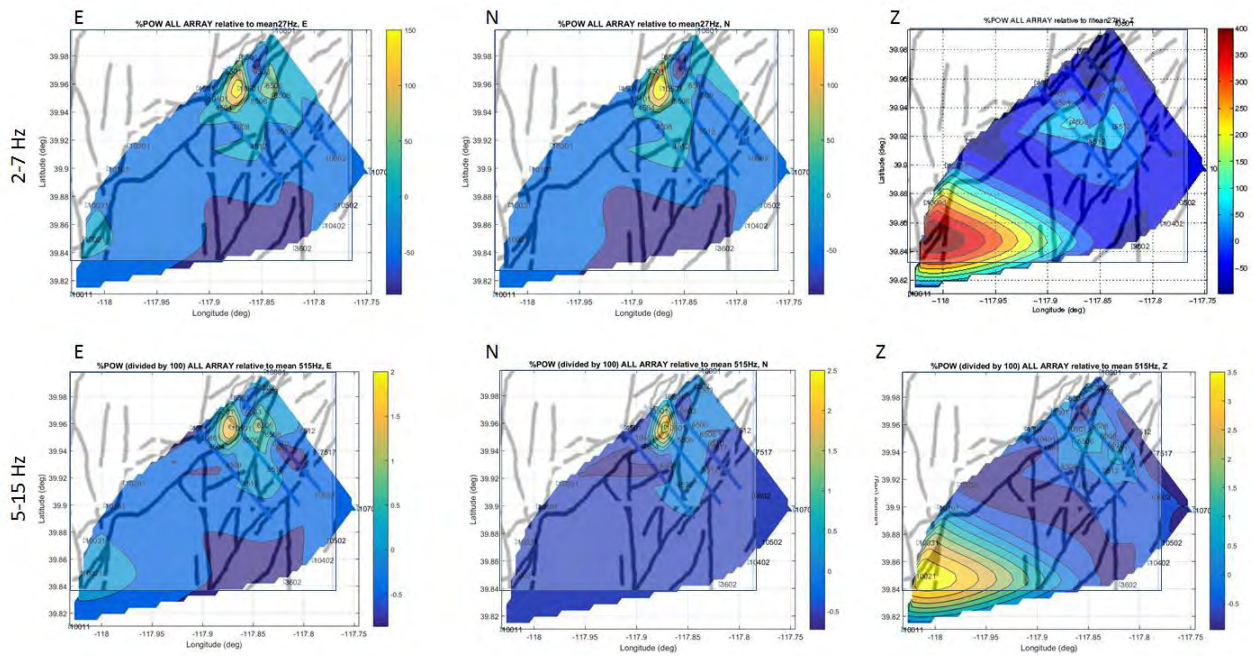
Figure 21. The percentage BB and SP anomalies in Figures 19 and 20 were combined, and the results in the 2-7 Hz and 5-15 Hz intervals are shown in three columns for the E, N and Z components, from left to right.

TASK 4 — GEOSTATISTICS

During this task, we investigated, especially modeling of temperature and fault location using the new seismic velocity values as well as the power spectral density (PSD) values derived during Task 3. Results are discussed below and values predicted from the analysis provided in the file Task4_Attachment.zip

The geostatistical analysis used was similar to described in AltaRock Energy Inc. (2013) DOE Award: DE-EE0002778 report. A fundamental assumption applied there was that while the exploration data set is statistically not ideal, and some parameters are more reliable than others, the data can be used to determine statistical significance. The validity of this assumption rests on the notion that whatever uncertainty exists in the different parameters can be thought of as a measurement error, and is at least from a practical standpoint, unbiased. The objective in this study was to include the new velocity information and repeat the analysis done during the prior work to explore whether the additional data revealed any patterns or correlations.

In this study, the most important relationship observed during the prior report, namely the one between velocity and temperature was explored. Both Vp and Vs were used for the prediction. Figure 22 shows the locations of the old and new data. Tests were done using both new and old data and just with the new data. The results presented here are using the new Vp and Vs values since those gave the best results. Since temperature is limited to the old locations (Figure 23), only new data near the temperature locations was used. Figure 24 shows where the data used is located. Figure 25 shows a map with these points with the overlay of faults and well locations for reference. The profiles along which cross-sections of various parameters is also shown.
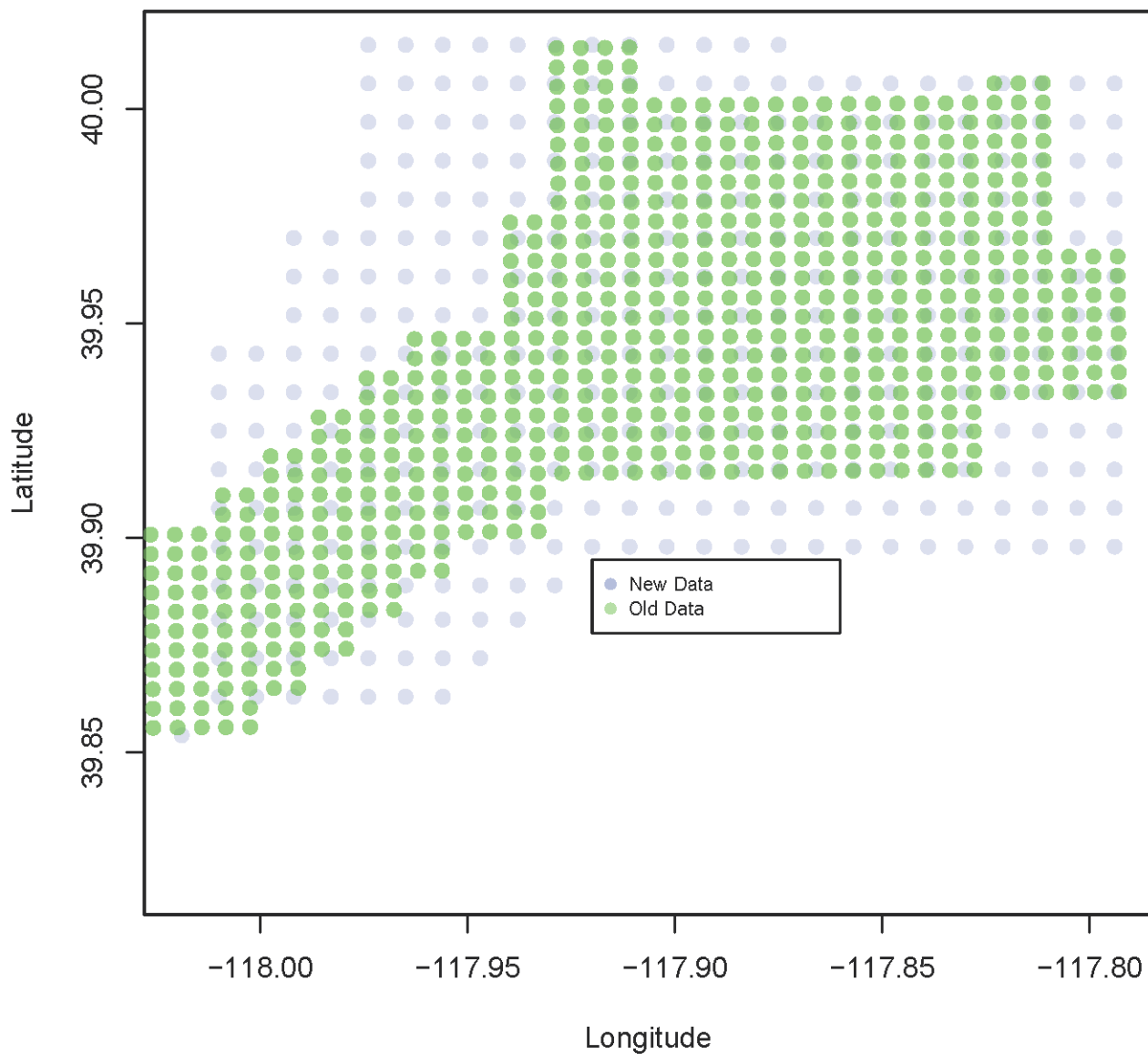
Figure 22: Map showing gridded location of the new data set (grey dots). Shown in green are prior locations where temperature estimates exist.
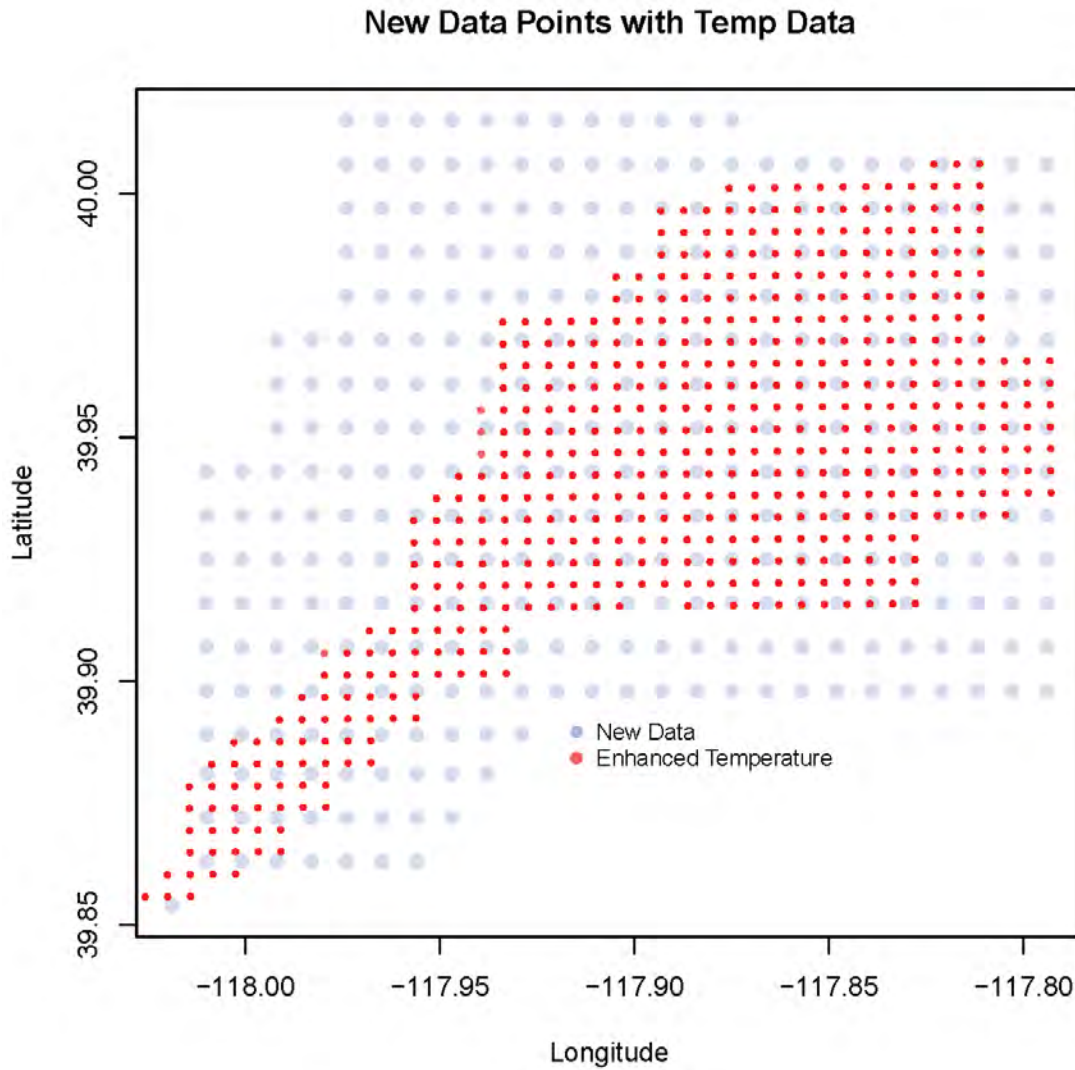
Figure 23: Map showing gridded location of the new data set (grey dots). Shown in red are points where prior temperature estimates exist.

Data Locations Used
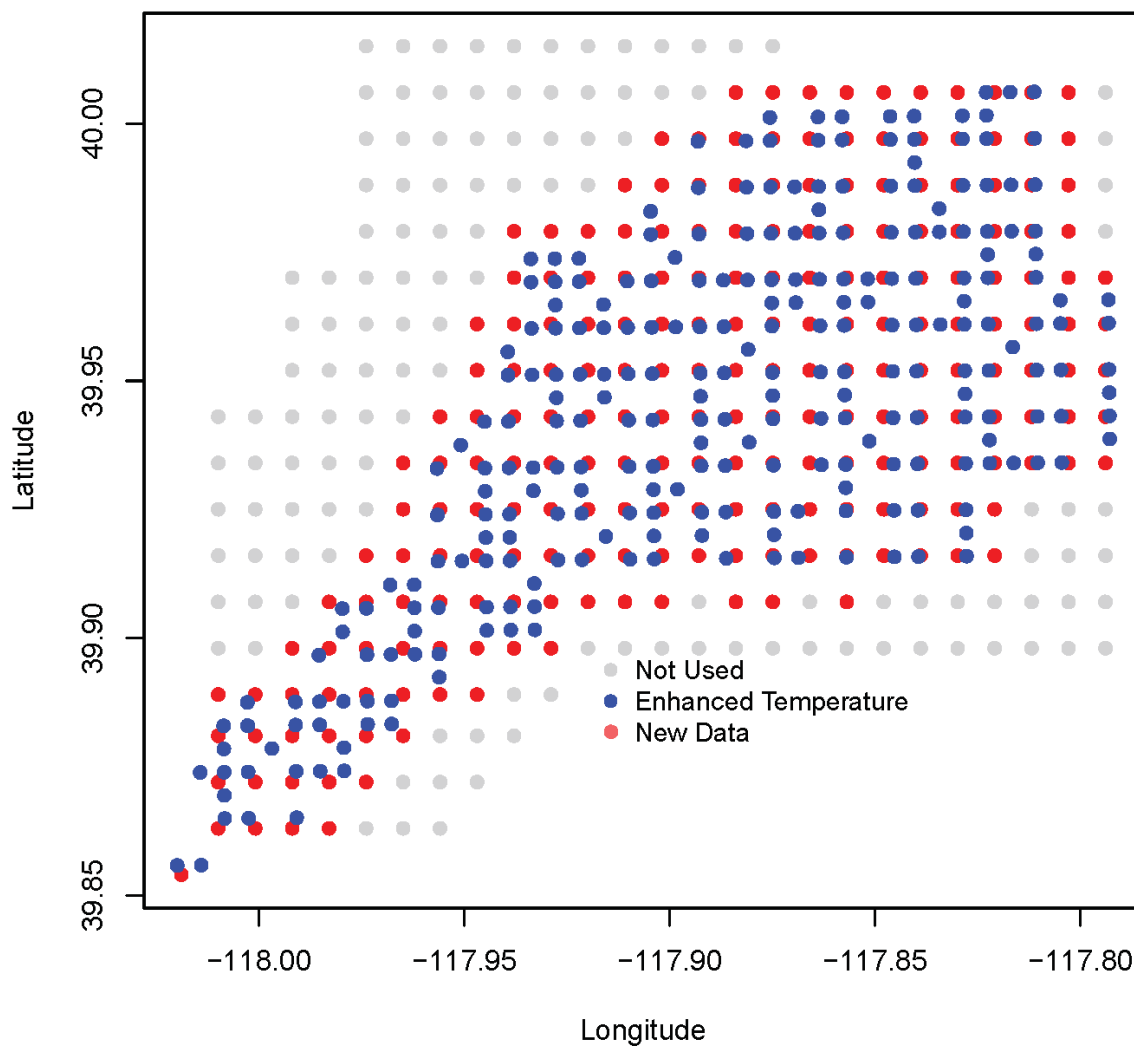
Figure 24: Only data that were close to the available temperature estimates (red dots) were used for the geostatistical analysis.
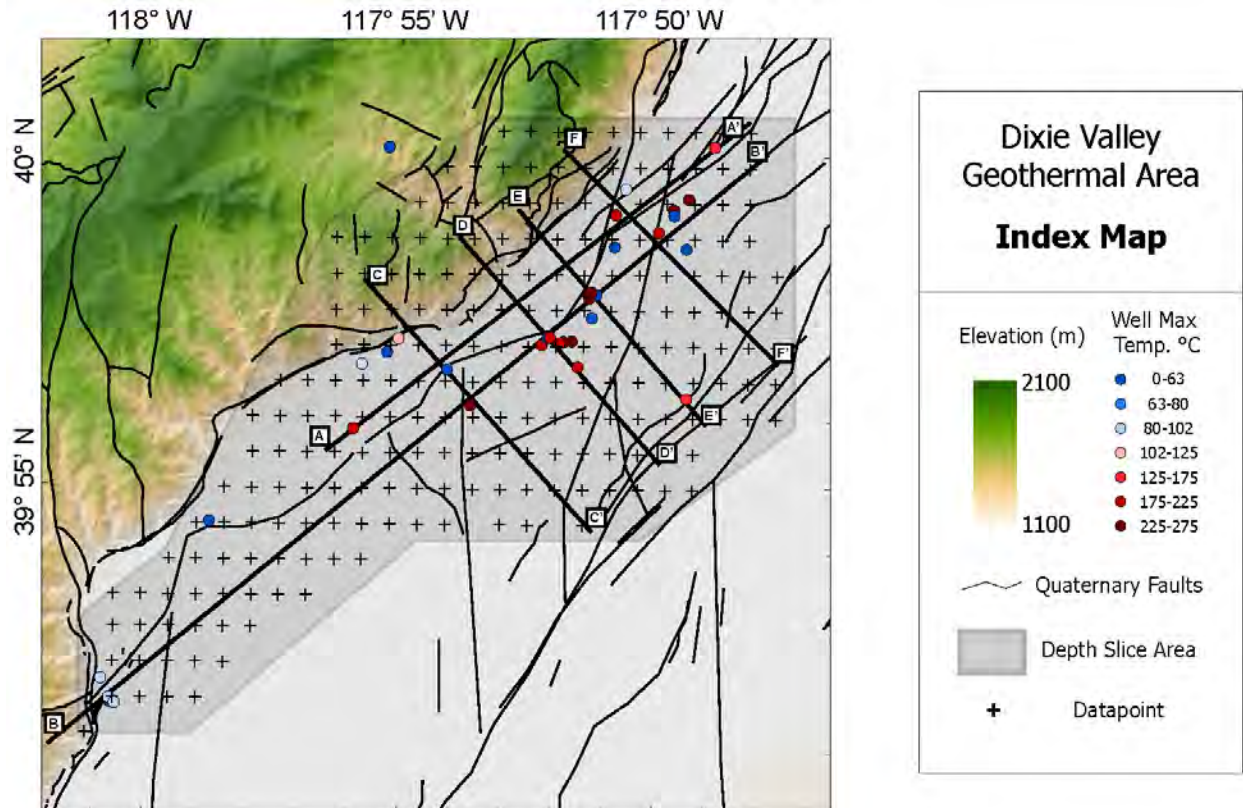
Figure 25: Index map showing location of the data points used for the geostatistical analysis (cross), Quaternary faults (from Iovenitti et al., 2012), and wells. The lines A to F denote profiles along with profiles of the geostatistical parameters are calculated from the depth volume.

In trying to figure out what variables predict temperature, the high level of correlation between depth and temperature must be dealt with. Since temperatures increase with depth, and the variables we are considering have a great deal of correlation with depth, we first predict temperature based on depth, essentially figuring out the average temperature for each depth. This is shown in Figure 26. The blue line is a linear fit. Since the relationship seems to be slightly nonlinear (high temperatures seem to plateau at greater depths) we used the green curve (quadratic) in the prediction of temperature. The correlation coefficients are very similar and so this is a qualitatively determination.
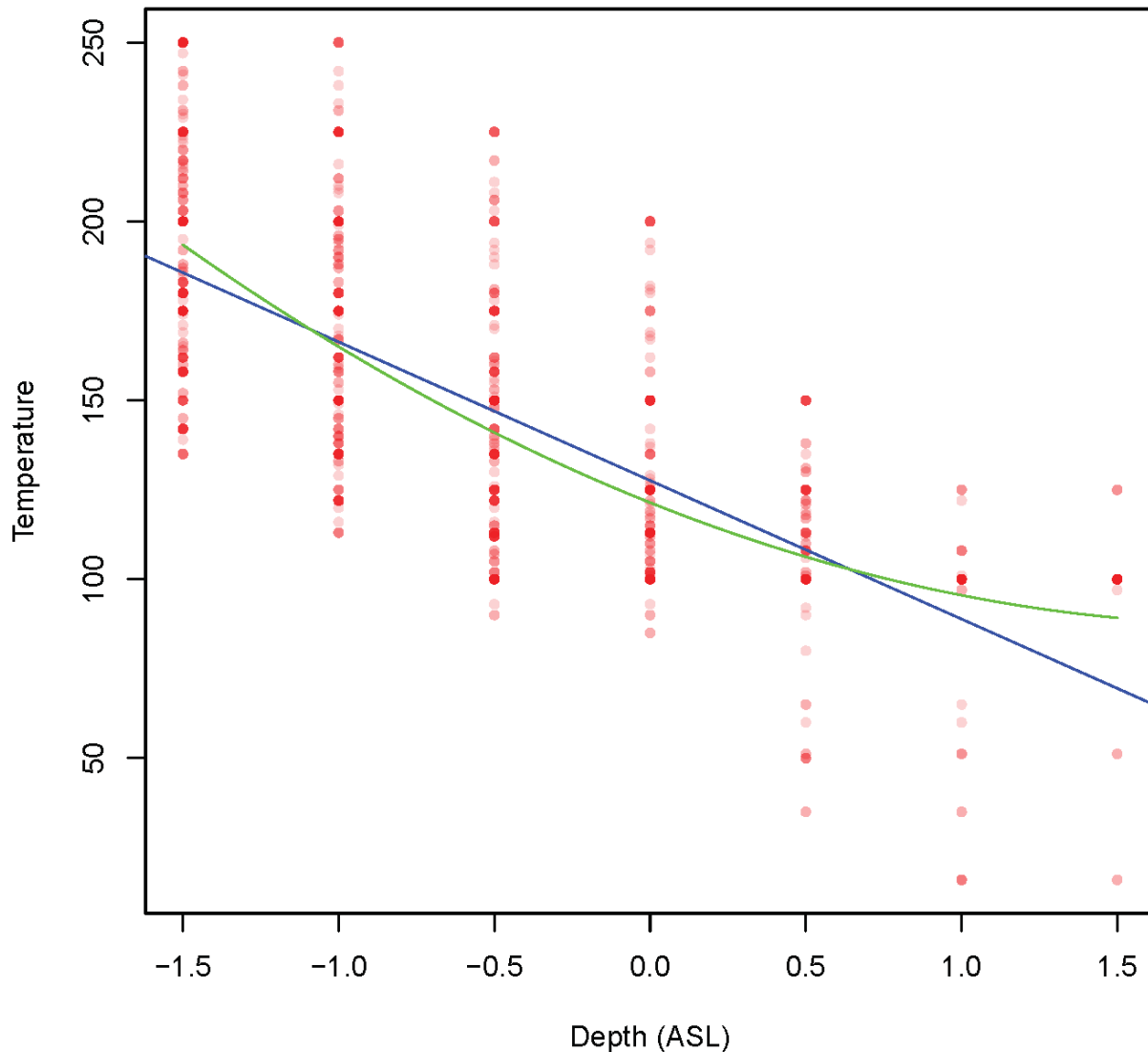
Figure 26: Predicted temperature as a function of depth. A quadratic relationship (green line) was found to be a better predictor compared to a linear fit (blue line).

The difference is between the actual temperature and the predicted temperature at a particular depth is called a residual – an unusually high temperature at a particular temperature has a large residual; a low temperature at a particular depth has a low (negative) residual. These residuals have an average of 0° C by construction, and a standard deviation of about 29° C. They range between

-84° C to 73° C. We are particularly interested in whether the variables we have can do a good job of predicting the higher temperature values. Unfortunately, the correlations between these residuals and the variables Vp, Vs, Rho, Qp, and Qs are all pretty low (less than 0.1 in absolute value) when data from both datasets is considered. Slightly more promising is looking at the data just from the new dataset, with temperatures estimated based on the closest values from the old dataset. Based on residuals from this subset of the data, the correlation between the residuals and Vp is -0.12, between the residuals and Vs is 0.14, and for the other variables the correlation remains small, still less than 0.1. Predicting these residuals is essentially predicting where the temperature will be unusually high for a particular depth. Using Vp and Vs, we made predictions, the values of the predictions are shown in Figure 27. By visual inspection, there is a cluster of unusually high predictions, implying hotter than normal areas, starting around the red line at 11. The points to the right of that line are at least 11 degrees hotter than would be predicted at their depth. The locations corresponding to those values are shown Figure 28 for various depth ranges.
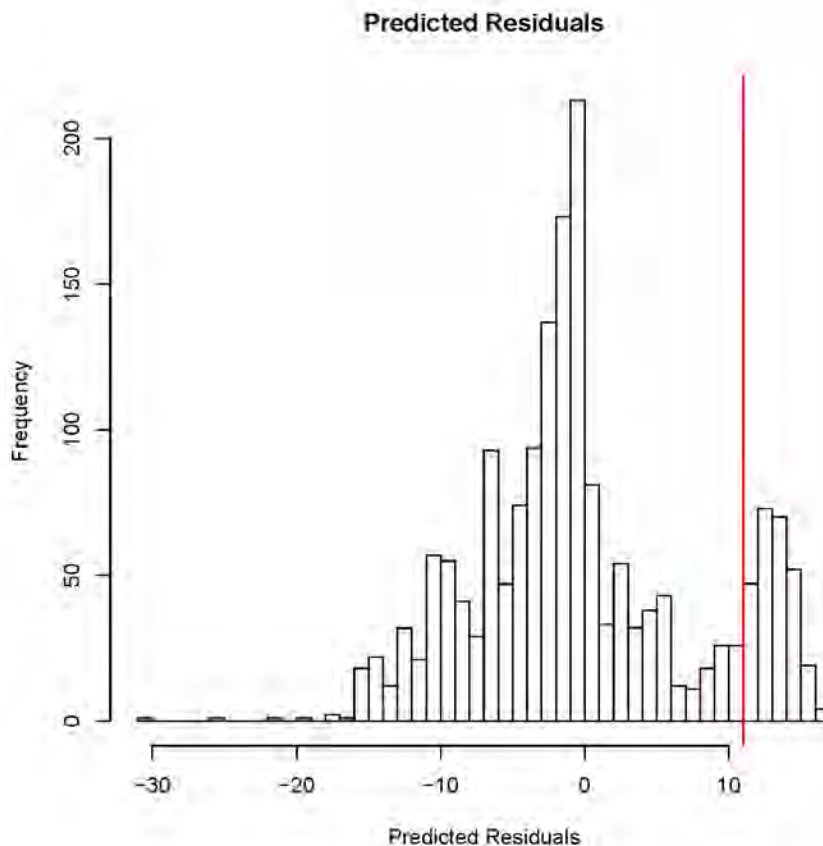
Figure 27: Residual temperature distribution (observed – predicted) over the study area showing a bimodal character. Since our objective is to look for anomalous hot zones, focus is on positive residuals. A residual of 11° C (red line) is picked rather arbitrarily. The location of these anomalies is shown in Figure 28.

Dixie Valley Geothermal Area
Predicted Residuals
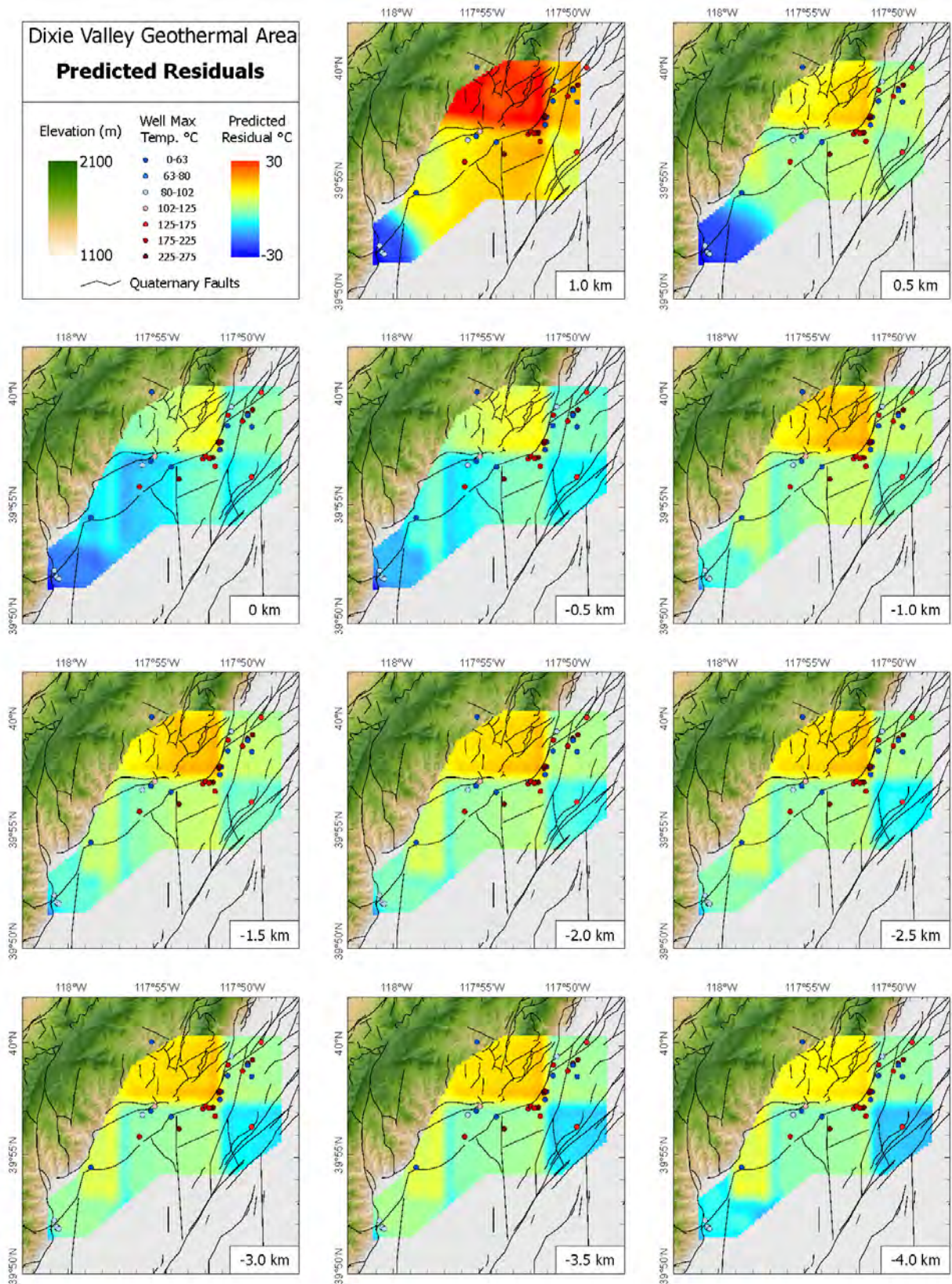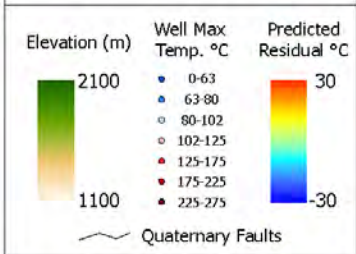
Figure 28: Depth maps of the predicted temperature residuals from geostatistical analysis. Slices go from 1.0 km to -4.0 km ASL in increments of 0.5 km. The high positive anomaly (yellow to red) is seen between the Dixie Valley range front fault and the basin ward Piedmont fault and near the intersection of multiple faults. This occurs in the vicinity of wells that reached high temperatures during drilling.

The areas that show anomalous high predicted temperature occur where multiple faults intersect (Figure 28). Not surprisingly, it spans an area between the Dixie Valley Range Front Fault and the basin-ward Piedmont faults and in the vicinity of numerous wells that have high maximum temperature. It also falls in the area of high EGS favorability from the prior study. This anomaly also coincides with the high PSD values (Figure 22). It does not change the favorability ratings but the new data seem to reinforce the results obtained from the previous study.

To further illustrate the high predicted temperature residuals, we constructed cross sections, Figure 29, along six linear profiles, AA to FF (located by Figure 25) that were chosen during the previous study (AltaRock, 2014).

Cross sections AA and BB are parallel to the faults while CC to FF traverse perpendicular to the faults (Figure 25). As shown in Figure 29 the high temperature residuals fall at the intersection of profiles AA, BB, DD, and FF, which as seen in Figure 28 is between the Dixie Valley Range Front and Piedmont Faults and in the vicinity of wells that hit high maximum temperatures. The zone extends in depth from surface to the bottom of the model (-4 km ASL).

Dixie Valley Geothermal Area
Predicted Residuals
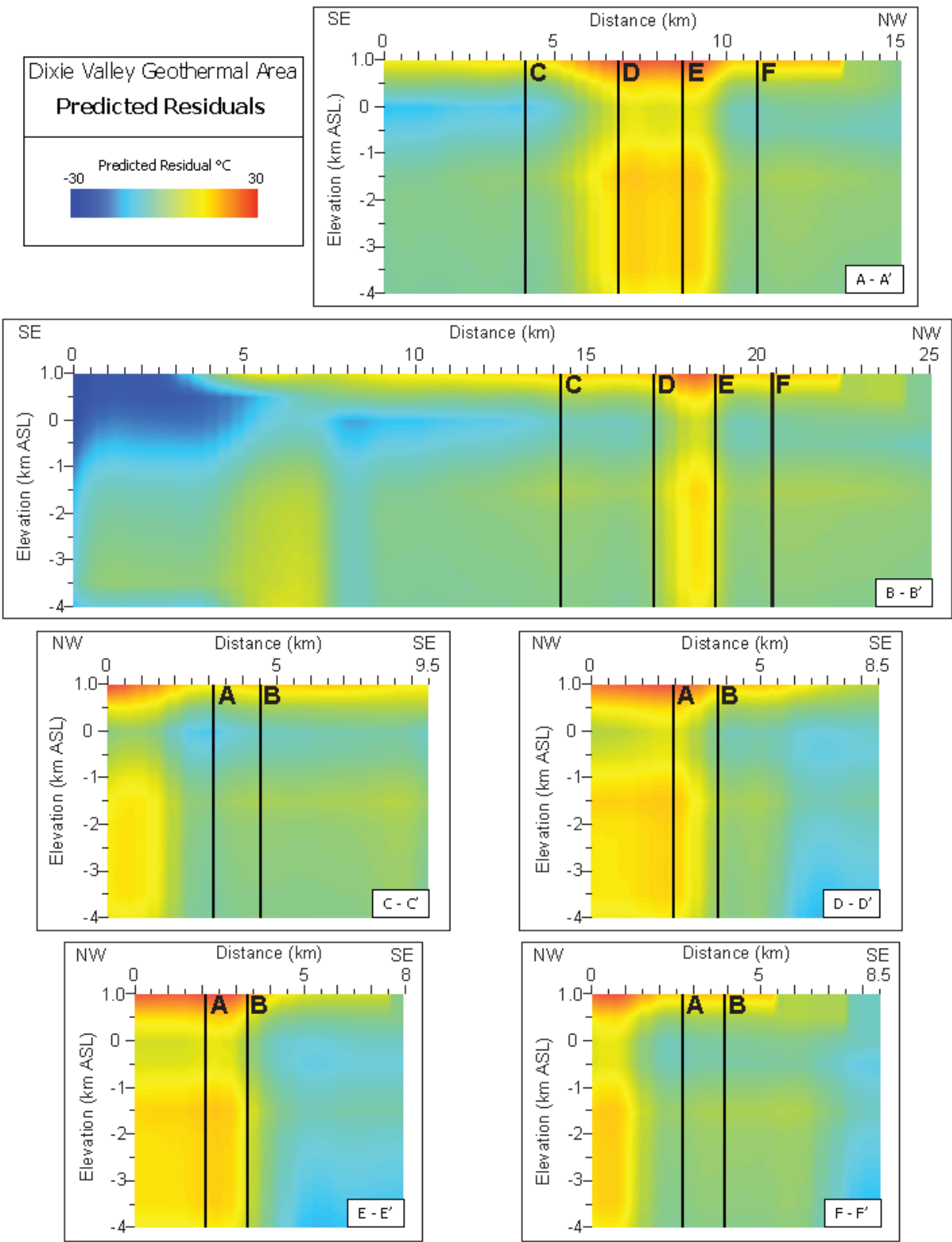
Figure 29: Cross sections along AA, BB, CC, DD, EE and FF. Please refer to Figure 25 for location of these profiles. The intersection of profiles AA, BB, DD, and FF, which as seen in Figure 25 is between the Dixie Valley Range Front and Piedmont Faults and in the vicinity of wells that hit high maximum temperatures. The zone extends in depth from surface to the bottom of the model (-4 km ASL). There is a slightly lower amplitude anomaly to the SE along BB, which can also be discerned in the depth maps (Figure 28).

We also explored correlations between PSD values and two other parameters, namely Coulomb stress change (CSC) and dilatational strain. Both these parameters are indicators of fault and fracture characteristics. Additionally, we investigated the nature of the PSD values within and outside a mapped fault zone.

Empirical Green's function PSD values derived from broad band (BB) and short period (SP) seismometers were analyzed separately. For each, all three components (E, N and Z) were examined individually. For each dataset, we looked at correlations between E, N, and Z and CSC and dilatation. These results are shown in the Table 4 below. Red-highlighted values were larger than 0.15 in absolute value, to highlight some of the more unusual cases. Data from broad band and in particular the horizontal components seem to exhibit higher correlation to stress changes compared to the short period data. Correlations are generally poor to dilatational strain.

PSD 5-15 Hz SP		
Component Analyzed	Coulomb Stress Change Correlation Coefficient	Dilatational Strain Correlation Coefficient
E	-0.07	0.04
N	-0.02	-0.11
Z	-0.24	0.09

PSD 5-15 Hz BB		
Component Analyzed	Coulomb Stress Change Correlation Coefficient	Dilatational Strain Correlation Coefficient
E	0.36	0.10
N	0.36	0.12
Z	-0.15	0.01

PSD 2-7 Hz SP		
Component Analyzed	Coulomb Stress Change Correlation Coefficient	Dilatational Strain Correlation Coefficient
E	-0.25	0.00
N	-0.17	-0.18
Z	-0.35	0.21

PSD 2-7 Hz BB		

Component Analyzed	Coulomb Stress Change Correlation Coefficient	Dilatational Strain Correlation Coefficient
E	0.38	0.21
N	0.38	0.22
Z	-0.05	0.08

Table 4: Correlation coefficients from analyses of PSD values against stress change (CSC) and dilatational strain, for short period (SP) and broad band (BB) data for the two frequency ranges. Larger correlation coefficients are highlighted in red. The horizontal components for BB seem to exhibit better correlation to stress changes compared to dilatational strain and to SP.

In addition, for each dataset we looked at whether the PSD value (for each of E, N, and Z) was significantly different between values in fault zones and outside of fault zones. Here the values correspond to standard normal (z) values. About 95% of the time we would expect to see a value between -2 and +2, and the more extreme values are highlighted red in Table 5. Once again data from broad band instruments and specifically the horizontal components reveal high (z) values indicating they are better indicator of presence or absence of faults.

PSD 5 – 15 Hz SP	
Component Analyzed	Normal (z) values
E	-0.95
N	-0.36
Z	-0.03
PSD 5 – 15 Hz BB	
Component Analyzed	Normal (z) values
E	-2.69
N	-2.68
Z	-0.47
PSD 2 - 7 Hz SP	
Component Analyzed	Normal (z) values
E	0.43
N	1.75
Z	0.08
PSD 2 - 7Hz BB	
Component Analyzed	Normal (z) values
E	1.84
N	1.54
Z	2.53

Table 5: Normal (z) statistical parameter from analysis of PSD values sampled into two sets – one within fault zone and another outside fault zone. A value that falls outside the range (-2, 2) indicates a strong difference between to two samples. In other words, the PSD values indicate a change in character. These are highlighted in red. It is clear data from broad band instruments are more sensitive to presence or absence of faults, especially the horizontal components.

TASK 5—EGS FAVORABILITY/TRUST MAPPING

Using the planned seismic results of this project, new EGS favorability and trust maps for the Dixie Valley Geothermal Wellfield (DVGW) were to be developed using the AltaRock Energy Inc. (2014a) favorability and trust map approach as a base case. The base case maps used a grid scale of 0.5 km by 0.5 km, for 0.5 km from +1 km to -4 km above sea level. Three principal parameters were determined to be most important for EGS. These are, in their order of importance, *temperature* (T, 350° C < T > 200° C), *rock type* (competent rock that can form fractures), and *stress condition* (extension being more favorable than compression). Given that the DVGW lies in an extensional terrane, the Basin and Range geologic province, the stress parameter was sub-divided into four stress sub-elements (1) fault orientation, (2) presence or absence of a fault, (3) Coulomb stress change or CSC, and (4) occurrence of a structural zone including compression, dilatation, or neither.

The favorability values of the individual parameters being considered and the final weighting to calculate overall EGS favorability value determined based on the polling od the project team's Subject Matter Experts. Favorability values each grid cell were calculated using the following equation:

$$F_v = (d_0 * w_0) + (d_1 * w_1) + ... (d_n * w_n)$$

where F_v is the favorability value for a grid cell, d_0 through d_n is the favorability value of a cell's geoscience parameter (e.g., temperature) data, and w is the weight for a particular data set. Table 6 presents the favorability weights and values used.

Table 6. Weights and values used in generated the favorability maps reported in AltaRock Energy Inc. (2014a) and presented below.

Temp[1] (.51 w[5])	Fav Value[2]	Lith-ology[6] (.31 w)	Fav Value	Stress Sub-parameters (.18 w)								
				C/D[3] (.03 w)	Fav Value	Fault Orientation (.07 w)	Fav Value	Structure Present (.05 w)	Fav Value	CSC[4] (.03 w)	Fav Value
< 100	1	QTbf	1	Compression	4	30-60°	7	Stucture	7	<-22	2
100	1	Tmb	5	Dilation	7	Other	4	None	5	-22	3
125	2	Jz	7	Neither	5	Neither	5			–14	3
150	2	Tr	3							-6	4
175	4	Kgr	9							0	5
200	7	Tv	3							6	6
225	7	Jbr	8							14	7
250	8	Jznm	4							22	8
275	9									> 22	9
300	8										
325	7										
350	5										
> 374	3										

[1] Temperature in °C
[2] Favorability Value
[3] Zones of Compression/Dilation
[4] Coulomb Stress Change
[5] Favorability weights
[6] Lithology formations included the QTbf (Quaternary-Tertiary basin fill), Tmb (Miocene basalt), Jz (Jurassic mafic rocks), Kgr (Cretaceous granodiorite), Tv (Tertiary silicic volcanics), Jbr (Jurassic Boyer Ranch Fm), Jznm (Jurassic non-magnetic mafic rocks)

The current high-resolution ambient seismic noise project provided excellent results in defining major faults in the wellfield. As such the identification of know faults by this methodology demonstrated its utility in identifying faults at an exploration stage in geothermal development. Expected seismic-derived parameters that were to be developed in this current project that could potential have affected the manner in which EGS favorability/trust maps was determined were:

1. Stress
2. Attenuation structure
3. Seismic attenuation
4. Temperature and pressure at depth
5. Earthquake focal mechanism

Given project constraints these seismic-derived parameters were not determined.

The fault identification by ambient seismic noise, while extremely useful in exploration, investigation has not added any sufficient new data for the generation of new DVGW favorability maps in the current project, other than increase confidence in their location. The discussion below evaluates the effect of this fault identification by ambient seismic noise on EGS favorability.

Methodology

The linearity of favorability calculations allows direct updating of model results by calculating the change associated with changing a factor and adding it to the previous favorability rating. However, the practice of truncating favorability values makes small updates insignificant.

The change in favorability F for a parameter z is given by

$$\Delta F_z = \frac{\Delta z}{9}(w)$$

where w is the weight function assigned to a particular variable. An example calculation of the change in favorability for the changing the weight of zones of dilatation from 7 to 9 is shown below.

$$\Delta \text{Fz} = \Delta F_{DIL} = \frac{(9 - 7)}{9}(0.03) = 0.007$$

Results

Changes in favorability parameters for two analyses are shown Table 4. In the first pass weights were increased for the yellow highlighted cells in Table 4 with red text. On the second pass the values for the yellow highlighted cells with black text were altered.

Table 6: Parameter modifications used in the current project's favorability analysis.

| Temp[1] (.51 w[5]) | Fav Values[2] | Lith[6] (.31 w) | Fav Value | Stress Sub-parameters (.18 w) | | | | | | | |
				C/D[3] (.03 w)	Fav Value	Fault Orientation (.07 w)	Fav Value	Structure Present (.05 w)	Fav Value	CSC[4] (.03 w)	Fav Value
<100	1	QTbf	1	Compressio	4→9	30-60	7→9	Stucture	7→9	< -22	2
100	1	Tmb	5	Dilation	7→9	Other	4→9	None	5→0	-22	3
125	2	Jz	7	Niether	5→0	Neither	5→0			-14	3
150	2	Tr	3							-6	4
175	4	Kgr	9							0	5
200	7	Tv	3							6	6
225	7	Jbr	8							14	7
250	8	Jzm	7							22	8
275	9									> 22	9
300	8										
325	7										
350	5										
> 374	3										

[1]Temperature in °C
[2]Favorability Value
[3]Zones of Compression/Dilation
[4]Coulomb Stress Change
[5]Favorability weights

| 4→9 | Values altered for first pass |
| 5→0 | Values altered for second pass |

The results of favorability calculations are tabulated below. The units are favorability points, such that a value of 1 would increase the favorability rating by one point.

		ΔF_z	ΔF_z
C/D[3]	Compression	0.016	0.013
	Dilation	0.007	
Orientation	30°-60°	0.015	0.038
	Other	0.039	
	Structure	0.011	0.022
	TOTAL Pass 1	0.088	
	TOTAL Pass 2		0.073
Total			**0.161 Fav pts.**

Up-weighting the stress state, fault orientation, and binary structure indicators produced an increase of 0.088 of a favorability point. Down-weighting cells with a null result in these categories increases the relative weight of the other factors, by 0.073 points. The result of altering all favorability criteria reached a maximum of 1/8th of a point and were not large enough to change any favorability value reported in AltaRock Energy Inc. (2014a). This is graphically shown in Figure 30.
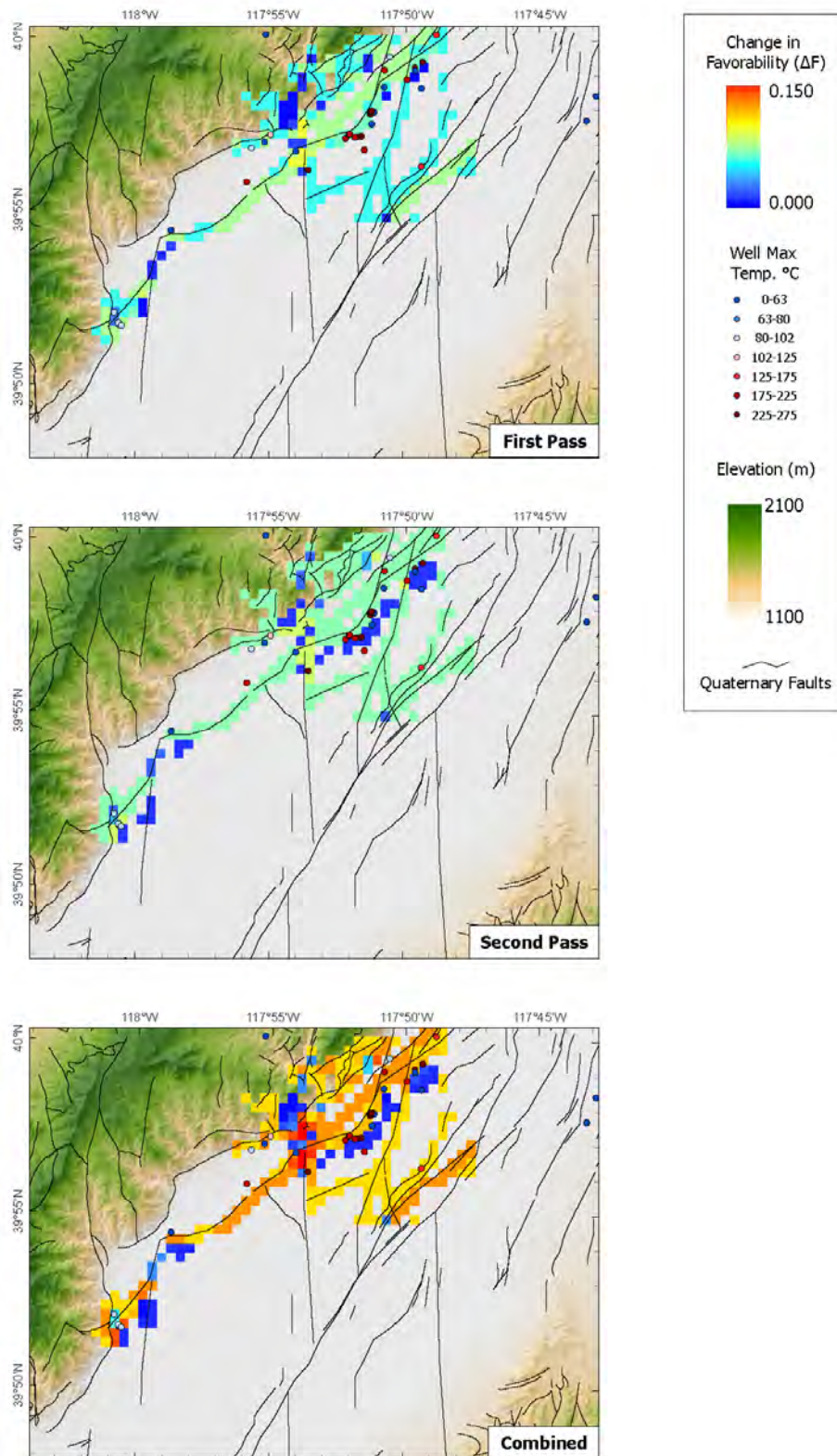
Figure 30: Map showing change in favorability value as a result of observations made during the current project. The result of altering all favorability criteria reached a maximum of 1/8th of a point and were not large enough to change any favorability value from the previous study (AltaRock, 2014).

For the sake of completeness, the favorability/trust maps generated in the AltaRock report are reproduced here as Figures 31 through 41.
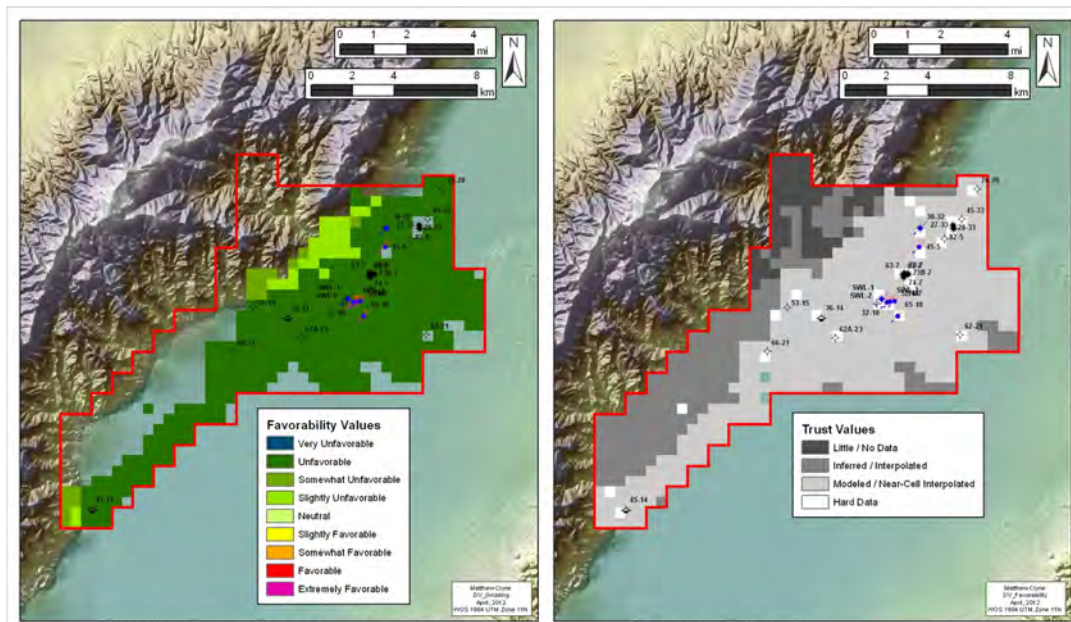
EGS Favorability-Trust Maps: Averaged Data and Weighting
Depth: 1.0km Above Sea Level

Figure 31. EGS Favorability map (left) and associated trust map (right) at 1.0 km ASL, the elevation of valley floor using average values based on Subject Matter Expertise input and weighting factors for temperature, lithology, and stress of 0.51, 0.31, and 0.18, respectively.
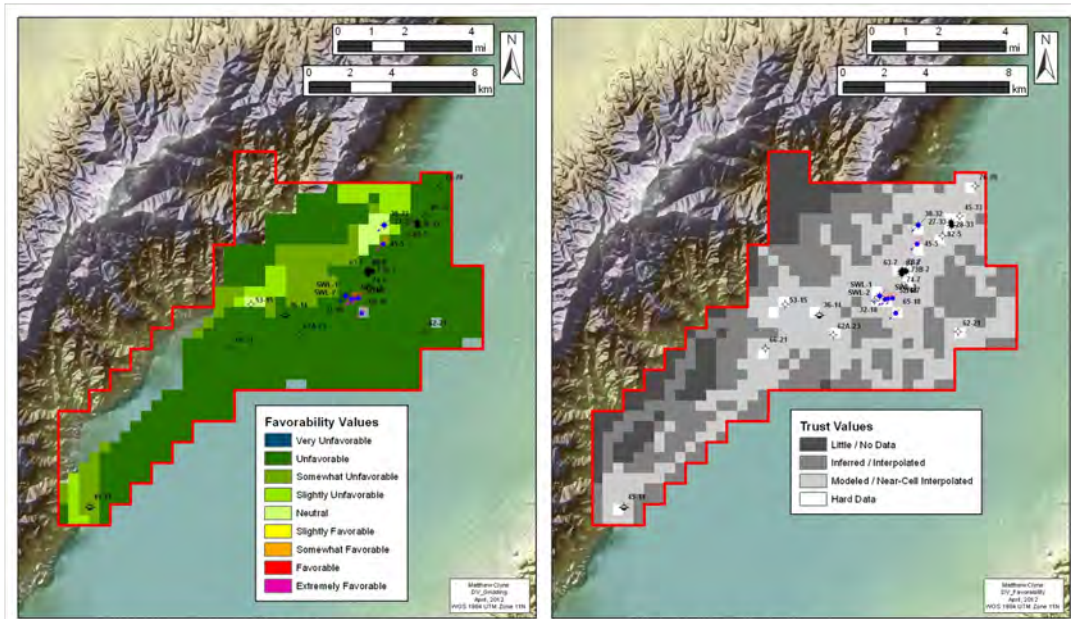
EGS Favorability-Trust Maps: Averaged Data and Weighting
Depth: 0.5km Above Sea Level

Figure 32. EGS Favorability map (left) and associated trust map (right) at 0.5 km ASL using average values based on Subject Matter Expertise input and weighting factors for temperature, lithology, and stress of 0.51, 0.31, and 0.18, respectively.
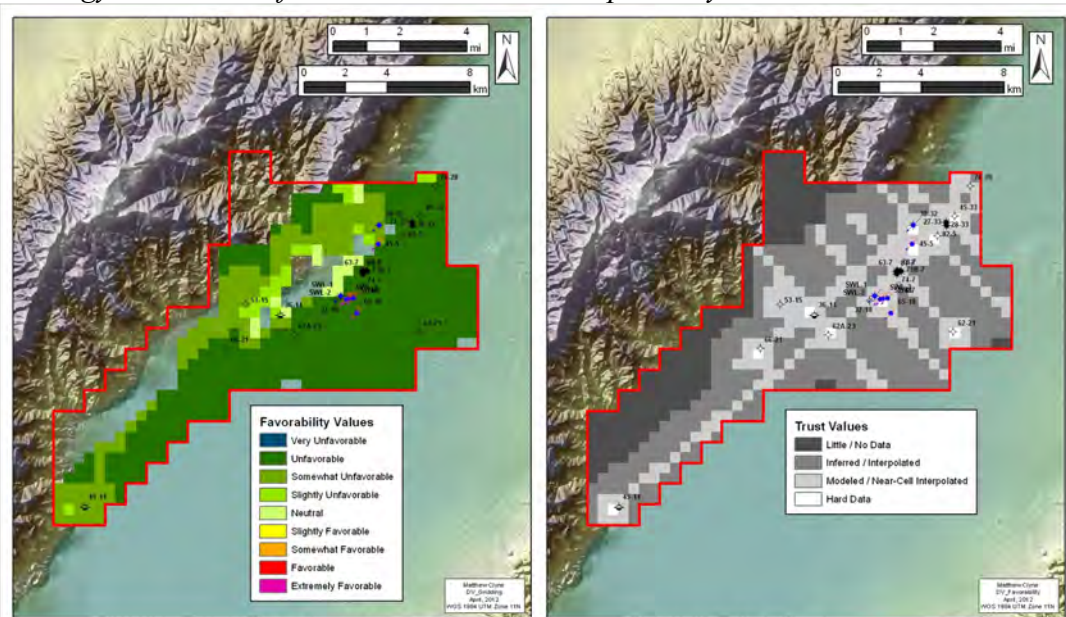
EGS Favorability-Trust Maps: Averaged Data and Weighting
Depth: 0.0km At Sea Level

Figure 33. EGS Favorability map (left) and associated trust map (right) at sea level (0 km ASL) using average values based on Subject Matter Expertise input and weighting factors for temperature, lithology, and stress of 0.51, 0.31, and 0.18, respectively.
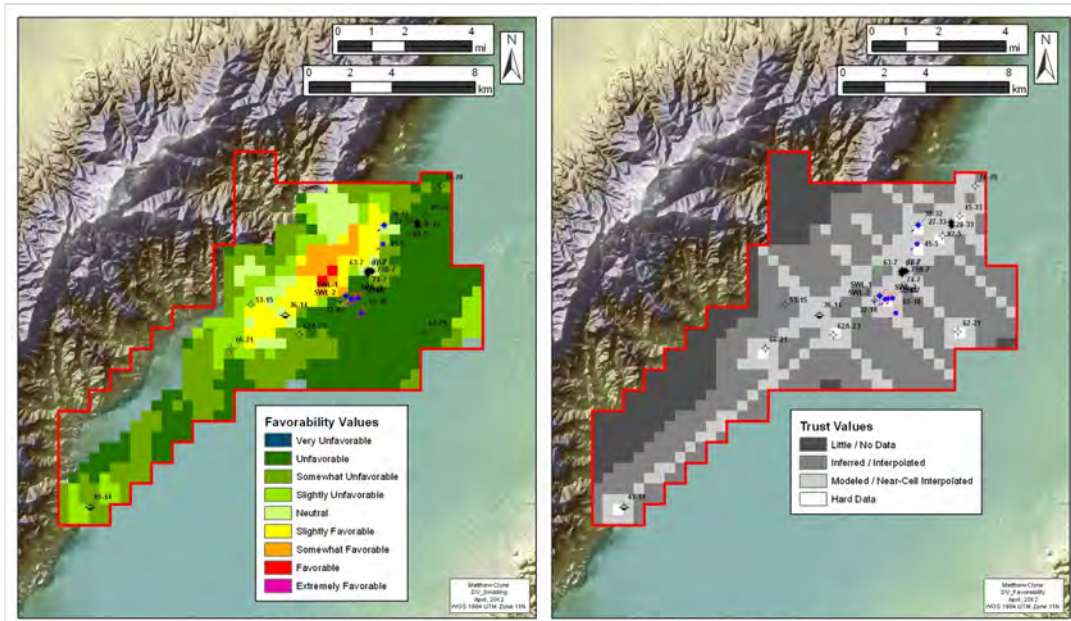
EGS Favorability-Trust Maps: Averaged Data and Weighting
Depth: 0.5km Below Sea Level

Figure 34. EGS Favorability map (left) and associated trust map (right) at -0.5 km ASL using average values based on Subject Matter Expertise input and weighting factors for temperature, lithology, and stress of 0.51, 0.31, and 0.18, respectively.
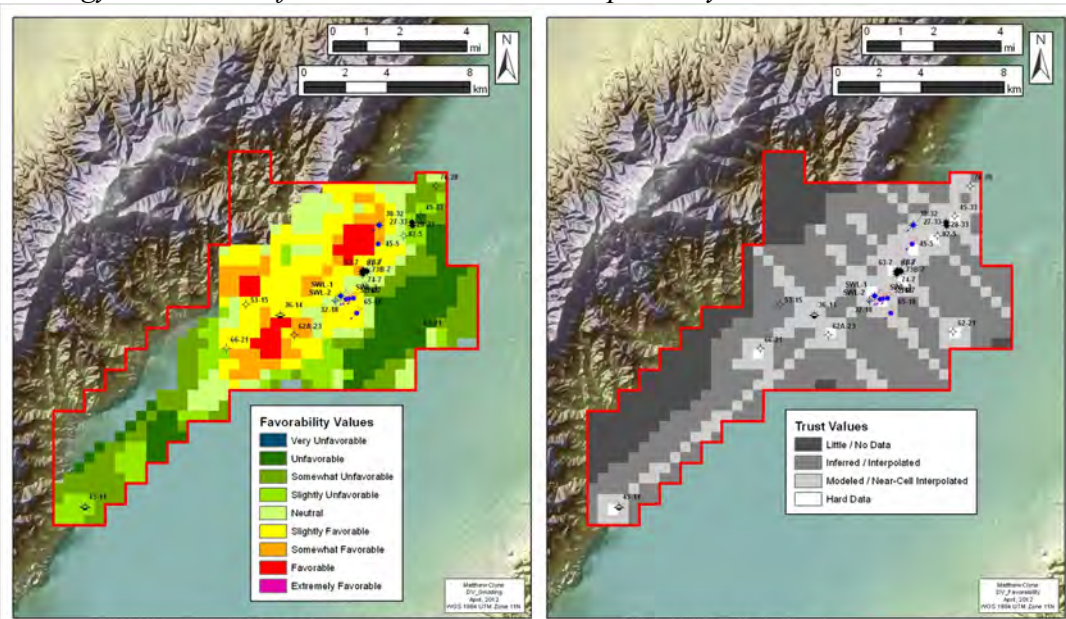
EGS Favorability-Trust Maps: Averaged Data and Weighting
Depth: 1.0km Below Sea Level

Figure 35. EGS Favorability map (left) and associated trust map (right) at -1.0 km ASL using average values based on Subject Matter Expertise input and weighting factors for temperature, lithology, and stress of 0.51, 0.31, and 0.18, respectively.

Page 79 of 234
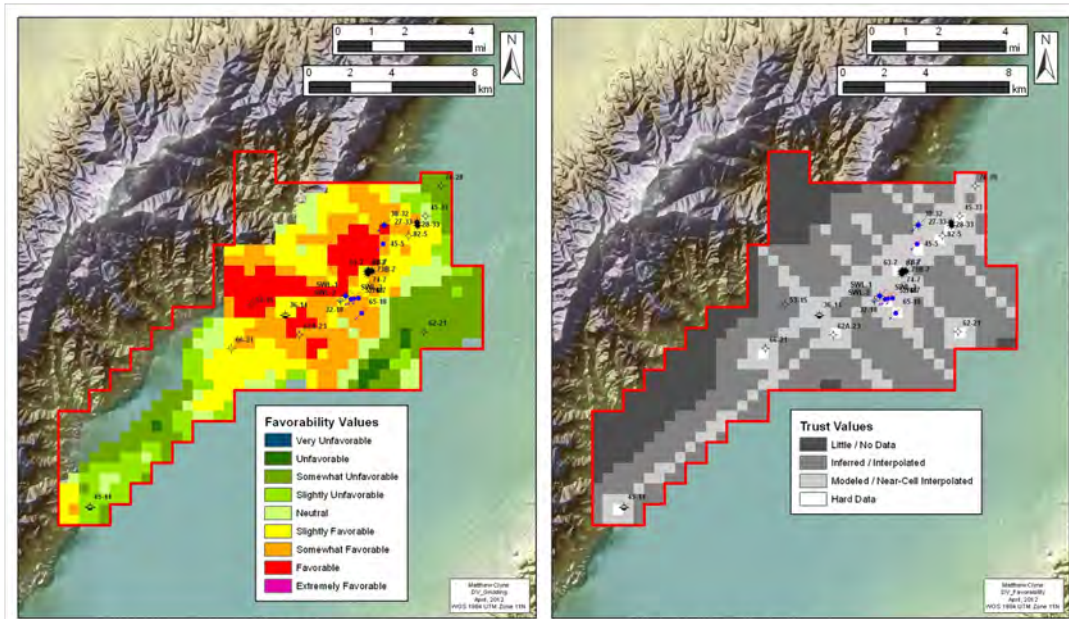
EGS Favorability-Trust Maps: Averaged Data and Weighting
Depth: 1.5km Below Sea Level

Figure 36. EGS Favorability map (left) and associated trust map (right) at -1.5 km ASL using average values based on Subject Matter Expertise input and weighting factors for temperature, lithology, and stress of 0.51, 0.31, and 0.18, respectively.
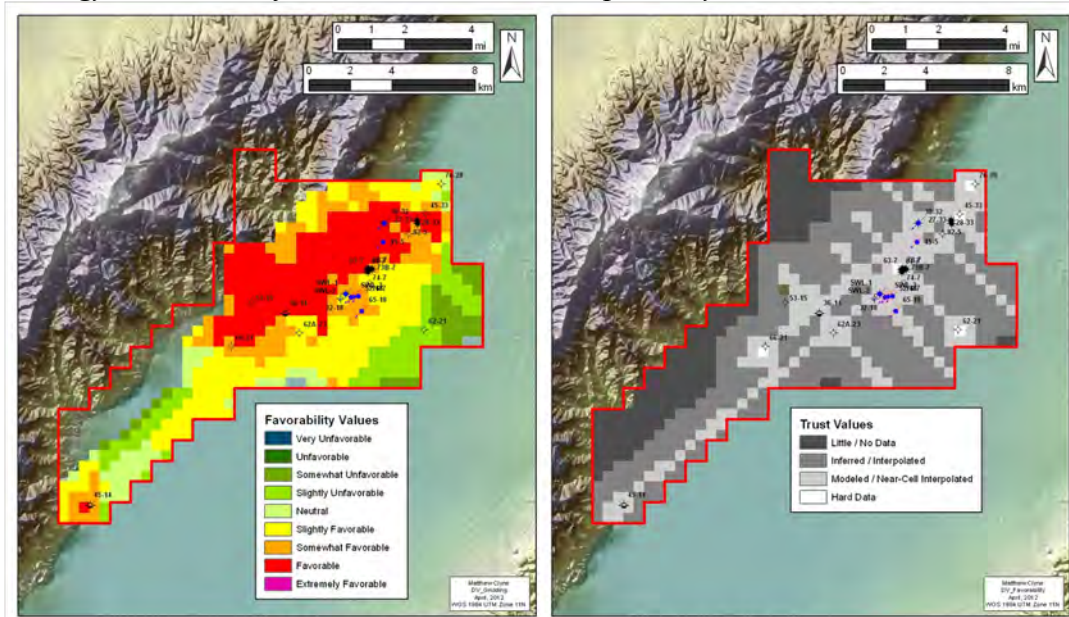
EGS Favorability-Trust Maps: Averaged Data and Weighting
Depth: 2.0km Below Sea Level

Figure 37. EGS Favorability map (left) and associated trust map (right) at -2.0 km ASL using average values based on Subject Matter Expertise input and weighting factors for temperature, lithology, and stress of 0.51, 0.31, and 0.18, respectively.
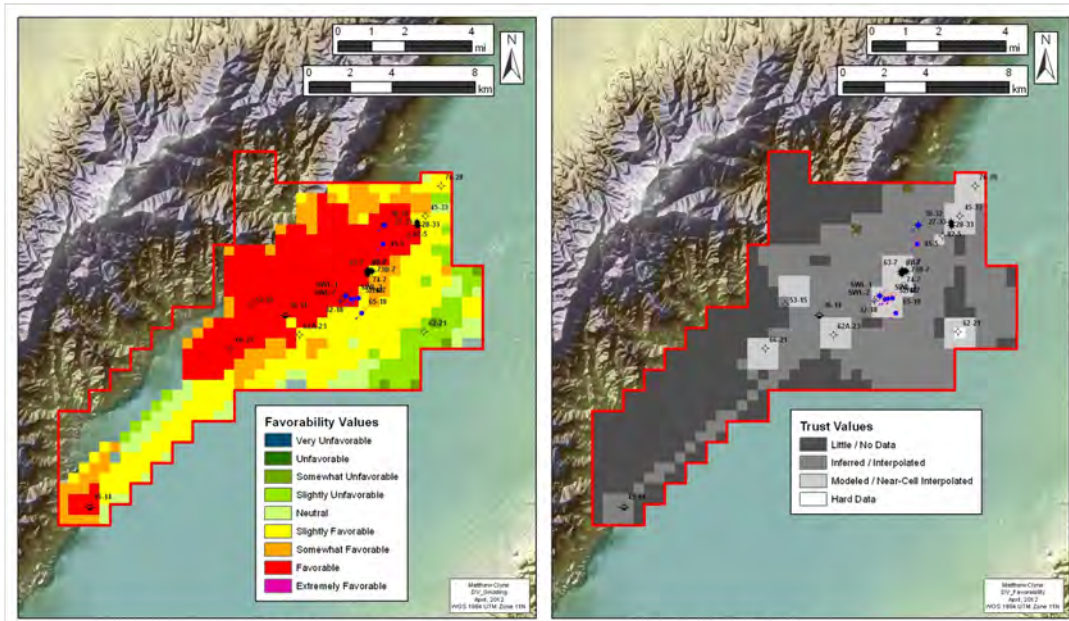
EGS Favorability-Trust Maps: Averaged Data and Weighting
Depth: 2.5km Below Sea Level

Figure 38. EGS Favorability map (left) and associated trust map (right) at -2.5 km ASL using average values based on Subject Matter Expertise input and weighting factors for temperature, lithology, and stress of 0.51, 0.31, and 0.18, respectively.
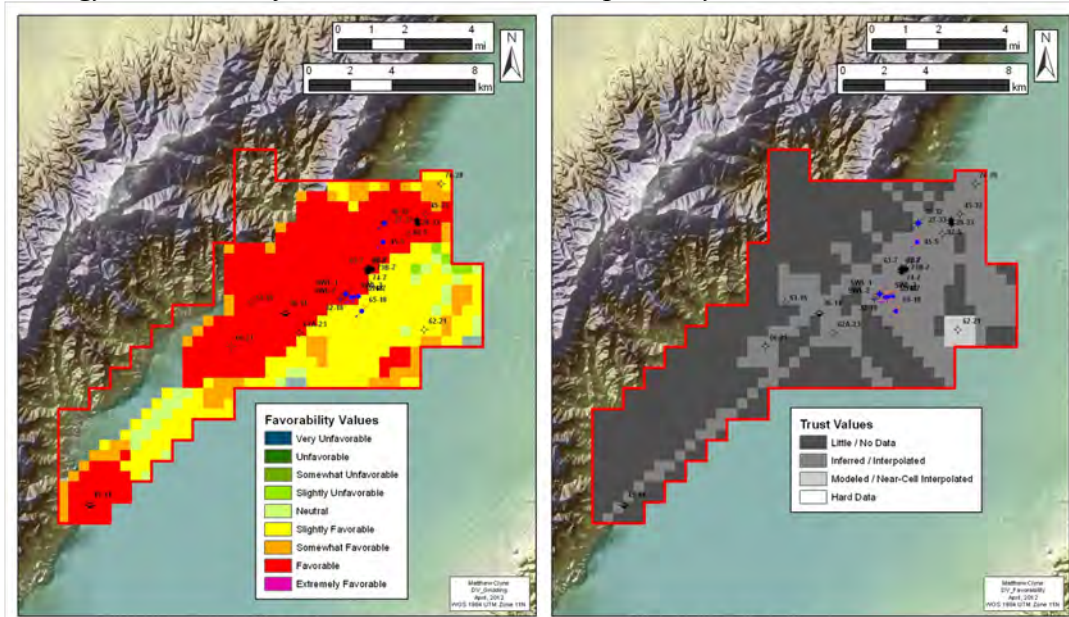
EGS Favorability-Trust Maps: Averaged Data and Weighting
Depth: 3.0km Below Sea Level

Figure 39. EGS Favorability map (left) and associated trust map (right) at -3.0 km ASL using average values based on Subject Matter Expertise input and weighting factors for temperature, lithology, and stress of 0.51, 0.31, and 0.18, respectively.
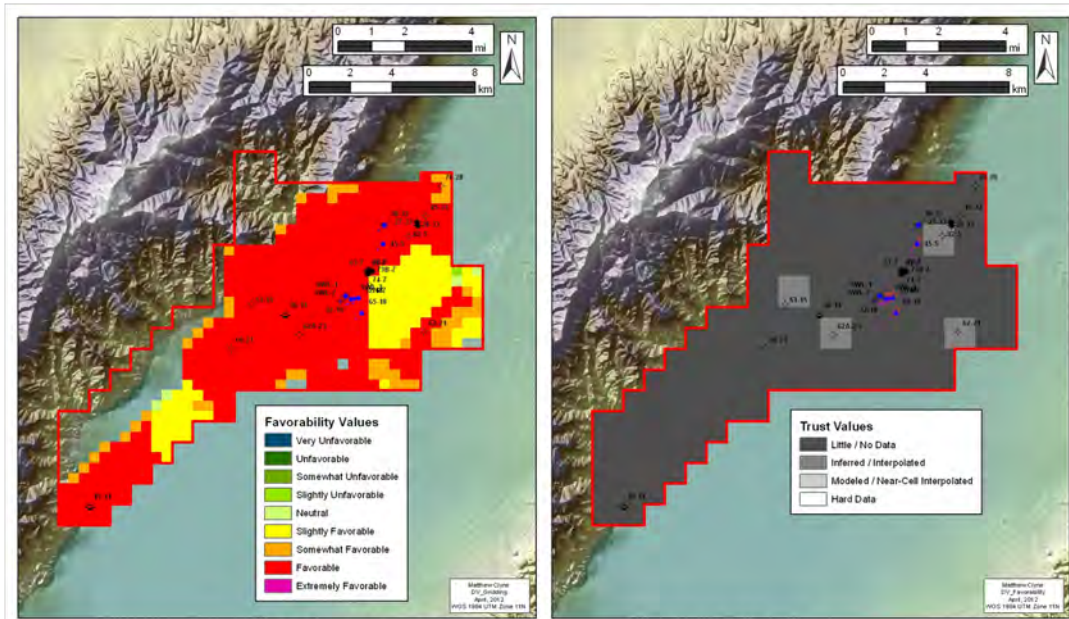
EGS Favorability-Trust Maps: Averaged Data and Weighting
Depth: 3.5km Below Sea Level

Figure 40. EGS Favorability map (left) and associated trust map (right) at -3.5 km ASL using average values based on Subject Matter Expertise input and weighting factors for temperature, lithology, and stress of 0.51, 0.31, and 0.18, respectively.
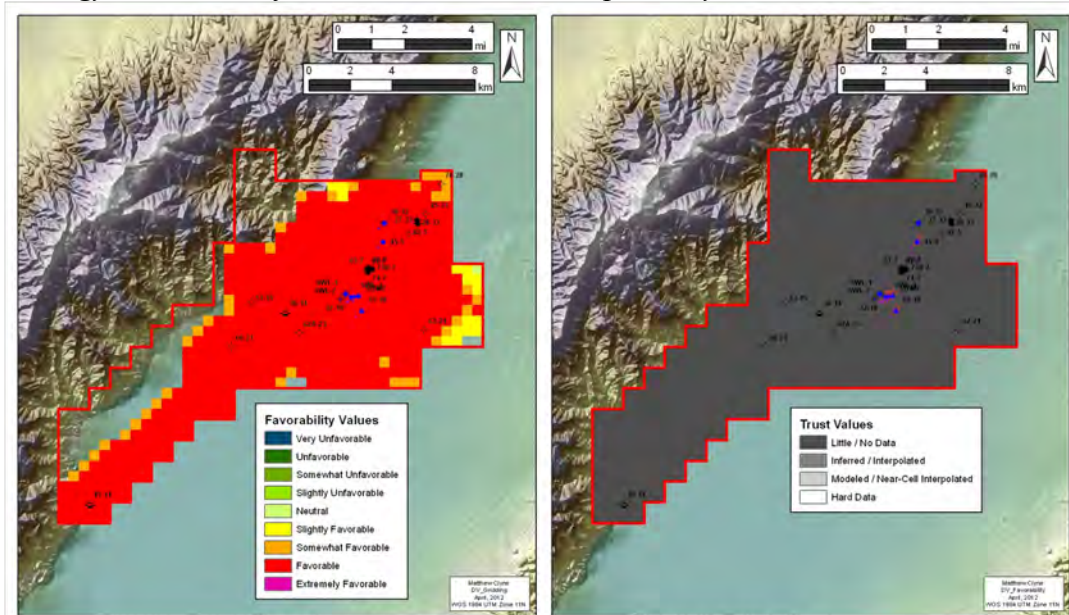
EGS Favorability-Trust Maps: Averaged Data and Weighting
Depth: 4.0km Below Sea Level

Figure 41. EGS Favorability map (left) and associated trust map (right) at -4.0 km ASL using average values based on Subject Matter Expertise input and weighting factors for temperature, lithology, and stress of 0.51, 0.31, and 0.18, respectively.

TASK 6 — COST-SAVINGS ANALYSIS

Louie and Pullammanappallil conducted a cost-savings analysis of the passive-source seismic imaging technique for EGS-favorability mapping, as used in this project. This project successfully conducted 31 km of passive-source seismic imaging in Dixie Valley. The cost to DOE was definitely less than what a standard active-source survey by the geophysical industry would cost. We explored several ways of assessing the savings:

A. *Gross project cost* comparison: $900,000 vs. $250,000, contrasting two DOE-funded surveys at Soda Lake;

B. *Per-kilometer gross cost* comparison: $300,000 vs. $9677, contrasting two different surveys-Soda Lake vs. Dixie Valley; and

C. *Industry estimate*: $420,000 vs. $300,000, estimate for industry to duplicate Dixie Valley passive surveys with standard active-source seismic surveys.

These assessments are very preliminary and mostly point to the need for a complete life-cycle cost element analysis. However, there are a number of very significant non-cost benefits of passive seismic surveys that will motivate the commercialization of this technique, explored at the end of this section.

For A, the *Gross Project Cost* comparison of $900,000 vs. $250,000 was presented in our April 2017 Seismic Report and Go/No Go meeting. It compares two DOE-funded research surveys along the Line 2 at Soda Lake, Nevada – both 3 km long. The $900,000 was the gross cost of just Line 2, from the active-source survey by Echols of Magma Energy. The passive-source survey along Line 2 was by Tibuleac and Pullammanappallil, our team. Gross project costs in each case included permitting, data acquisition, data processing, data interpretation, reporting, other research activities, and indirect costs of project management. The source of Magma's survey cost was personal communication with Echols in 2013. The two surveys covered the same ground but had significant differences in design and objectives. The *Gross Project Cost* comparison suggests 72% cost savings for passive.

For B, the *Per-Kilometer Gross Cost* comparison of $300,000 vs. $9677 was presented in our 2017 Seismic Report and Go/No Go meeting conservatively as "90%" cost savings. This compares two different DOE-funded research surveys, in different locations with different objectives and methods. The active-source survey was Line 2 from the Soda Lake survey by Echols at Magma energy, 3 km long in total. The passive survey was all Dixie Valley lines of this current project, 31 km total surveyed length. Gross project costs in each case included permitting, data acquisition, data processing, data interpretation, reporting, other research activities, and indirect costs of project management. The source of Magma's survey cost was personal communication with Echols in 2013. This *Per-Kilometer Gross Cost* comparison suggests 96% cost savings per kilometer. The 96% savings is not likely to be realistic, since differences in fixed costs per project were not taken into account.

For C, the *Industry Estimate* of $420,000 vs. $300,000, is an estimate for industry to duplicate this project's Dixie Valley surveys with standard active-source seismic surveys, given the same survey

layout and objectives. This comparison was estimated by Pullammanappallil following the Go/No Go meeting; it was included in our SOPO under "Commercialization Activities." The industry estimate was for a high-quality active-source survey of all Dixie Valley lines of this project, 31 km total. The passive-source estimate was also for all Dixie Valley lines of this project, 31 km total. The active-source cost estimate only included data acquisition, data processing, and data interpretation. The passive-source gross project costs included permitting, data acquisition, data processing, data interpretation, reporting, other research activities, and indirect costs of project management. This *Industry Estimate* comparison suggests 28% cost savings for our passive-source technique. This savings estimate may represent a minimum savings.

The wide range of the cost savings estimates point to the need for a complete life-cycle cost element analysis. Such an analysis was not part of this project's SOPO. We believe the cost savings of this passive technique for EGS may have a minimum of 30%, and a maximum of 90%. The complete life-cycle analysis would involve modeling costs for 10-12 project scenarios with varying EGS objectives and settings. The model scenarios could range from a commercial survey on an oilfield in Texas, to an academic DOE study in a swampy mountainous wilderness. We would obtain the cost savings percentage of our passive-source procedure for each scenario. These results would feed into a full life-cycle cost element analysis of the various components needed for a seismic survey and resulting report. The identification of the various cost elements should focus our attention on where the potential cost savings are and how significant they may be.

There are many very significant **Non-Cost Benefits** of passive seismic surveys. Our Dixie Valley results suggest that, when locating faults deep within basement, more than 1 km below the basin floor, passive-source surveys may perform as effectively for EGS studies as active-source surveys. Active-source seismic surveys require that heavy vibrator or drill trucks access the entire length of each survey line, and survey lines often must extend outside prospect or lease areas. Passive source surveys can be completed across areas inaccessible to heavy trucks, such as steep topography. Only drill pads for wells need be permitted for truck access. Many environmentally sensitive areas such as wetlands and reserves for sensitive species (e.g., sage grouse) could never be permitted for active-source surveys. Where active-source surveys may be allowed, stringent permit conditions can make active-source surveys cost prohibitive. Our passive-source method provides an environmentally-friendly seismic survey with minimal to negligible impacts. The economic benefit is greater project feasibility.

7. SUMMARY

7.1 Challenges and Lessons Learned

1) **Deployment logistics.** Although ideal ambient noise conditions exist in Dixie Valley, NV during the winter months, extreme temperatures (50° F during the day down to 2° F during the night) are a challenge. We found that significant insulation, and deep sensor burial was necessary to preserve battery power. Having to change the batteries and no information on the data quality in the field were significant logistics problems. Proposed solutions are processing in overlapping windows, enhancing data quality using hammer hits and in-field processing, and thus, reducing the duration of the field experiment.

1) **Sample rate.** It is our experience that a higher sample rate increases the accuracy of the GFs, because it increases the ambient noise bandwidth. Thus, although using 500 sps (250 Hz Nyquist frequency, i.e., 0-250 Hz frequency band) is best, it is shown below that the high end of the useable frequency band for the extracted GFs was 125 Hz in this study.

2) **Waveform pre-filtering**. Ambient seismic noise GFs often have narrow frequency bands, mostly when extracted at short distances (Tibuleac, in preparation for BSSA). This is why CWT was used in this case, thus avoiding the "ringing" typical for Fourier filtered signals when the filter is too narrow in frequency.

3) Changes in the reflection GFs along the lines were investigated in association to known faults, which makes this technique a strong candidate as a **first step in future surveys**, as the experiment design could be changed to imagine faults. The GF P-reflection component resulted from line and array autocorrelations should be used for an independent first order estimation of the Vp model.

4) **Inter-station distance**. Line 4, perpendicular to a road, with 34 m inter-station distance, a length of 9 km and 6 days of records was found to provide the best information for shot gather interpretation.

8) To mitigate cultural noise effects, the sensors deployed near the power plant were **buried deeper, and deployed farther from the well-field pipelines and from the road**. Some of the best data were obtained using deeply buried high frequency geophones in a quiet setting, even if the total recording time was as short as 6 days.

9) **Extended tests of the field conditions** and analysis of the ambient noise composition are recommended before any deployment.

7.2 Recommendations

We successfully tested and evaluated a novel seismic exploration method based on analysis of body-waves and surface-waves extracted from ambient seismic noise and concluded that the method has capability of resolving crustal structure up to 3 km depth with a resolution of tens to hundreds of meters. We recommend comparison of the seismic analysis with the AltaRock (2014)-

derived geophysical parameters along the seismic lines and assessment of favorability predictability separately, and in combination with other geophysical techniques. We recommend further assessment of additional seismic parameters such as attenuation, stress drop, spectral and complexity properties, in relation to other geophysical parameters. A power spectral density analysis of the passive-seismic empirical Green's functions reveals significantly higher power recorded over the exploration area at the power plant, and in the drilling area, near the BB station 10201, especially on the horizontal components. These estimates are made only at the surface, were found useful in hydrothermal reservoir characterization, and were not required to prove that the capability of the technique to characterize crustal properties up to 3 km depth. This technique allows first-order geothermal reservoir characterization, comparable, however, of lower resolution than the active survey results, through statistical integration of inexpensive seismic analysis results with information from other geological and geophysical data.

The Vs analysis showed promise for fault identification. A successful outcome of this experiment was extraction of periods of 1-2 seconds using 5 Hz corner frequency sensors. This was achieved by modification of the instrument response to simulate a BB sensor. A first-approximation model can be provided by the autocorrelations, however, this possibility needs more testing, and comparisons must be made between the E, N and Z components, to correctly identify all the reflection GF arrivals. Reflection GF's extracted from waveform autocorrelations were promising for fault identification.

The areas that show anomalously high predicted temperature in the geostatistics occur where multiple faults intersect. Not surprisingly, such areas span between the Dixie Valley Range Front fault and the basin-ward Piedmont faults, in the vicinity of numerous wells. These locations also fall in the area of high EGS favorability from the prior 2014 study. The anomalies also coincide with the high power spectral density values. These anomalies do not change the favorability ratings, but the new data reinforce the results obtained from the previous 2014 study.

The current high-resolution ambient seismic noise project provided excellent results in defining faults in the wellfield. As such the identification of known faults by the project demonstrated the utility of this method for identifying faults at an exploration stage in geothermal development. Such fault identification, while extremely useful in exploration investigation, has not added sufficient new data for the generation of new and different DVGW favorability maps in the current project.

We believe the cost savings of our passive-seismic technique for EGS may have a minimum of 30%, and a maximum of 90%. There are many very significant non-cost benefits of passive seismic surveys. Our passive-source method provides an environmentally-friendly seismic survey with minimal to negligible impacts. The economic benefit is greater EGS project feasibility.

ACKNOWLEDGEMENTS

REFERENCES

AltaRock Energy Inc., 2014a. EGS Exploration Methodology Project using the Dixie Valley Geothermal System, Nevada as a Calibration Site Part I—Final Scientific Report Baseline Conceptual Model, US Department of Energy DOE Award: DE-EE0002778, submitted to the National Geothermal Data Repository.

AltaRock Energy Inc., 2014b. Exploration Methodology Project using the Dixie Valley Geothermal System, Nevada as a Calibration Site Part II—Final Scientific Report Enhanced Conceptual Model, US Department of Energy DOE Award: DE-EE0002778, submitted to the National Geothermal Data Repository, 2 January.

Campillo M. and A. Paul, 2003., Long-range correlation in the diffuse seismic coda, Science, 299, p. 547–549.

Claerbout J.F., 1968. Synthesis of a layered medium from its acoustic transmission response, Geophysics 35, p. 264-269.

Draganov D., Campman, X., Thorbecke, J., Verdel, A., and Wapenaar, K., 2009. Geophysics 74, p. A63–A67, 10.1190/1.3193529.

Draganov, D., Campman, X., Thorbecke, J., Verdel, A., 2013. Seismic exploration-scale velocities and structure from ambient seismic noise (> 1 Hz), Journal of Geophysical Research: Solid Earth, 118, p. 4345-4360.

Echols, J., Benoit, D., Ohren, M., Oppliger, G., and T. Van Gundy, 2011. Integration of a 3D-3C reflection seismic survey over a known geothermal resource: Soda Lake, Churchill County, Nevada, GRC Transactions, 35.

Feng, C. and Teng, T., 1983. Three-dimensional crust and upper mantle structure of the Eurasian continent. Journal of Geophysical Research 88: doi: 10.1029/JB088iB03p02261. issn: 0148-0227.

Gouedard P., Stehly, L., Brenguier, F., Campillo, M., Colin de Verdiere, Y., Larose, E., Margerin, L., Roux, P., Sanchez-Sesma, P.J., Shapiro, N.M. and Weaver, R.L., 2008. Cross-correlation of random fields: mathematical approach and applications, Geophysical Prospecting, 56, p. 375–393.

Herrmann, R.B., Ammon, C.J., 2002. Computer Programs in Seismology, http://www.eas.slu.edu/People/RBHerrmann/ComputerPrograms.html.

Iovenitti, J., Tibuleac, I.M., Blackwell, D., Cladouhos, T., Karlin, R., Mack Kennedy, B., Issaks, E., P. Wannamaker, M. Clyne, O. Callahan (2010). Development of Exploration Methods for Engineered Geothermal Systems (vol. 33). Geothermal Resources Council Transactions, v. 33, p. 437-440.

Irie, K. and L. Brown, 2009. Extraction and analysis of seismic body waves from ambient noise recorded for crustal imaging in Montserrat, American Geophysical Union, Paper # V23D-2106, abstract and poster.

Tibuleac, I.M., Pullammanappallil, S., von Seggern, D. H., Pancha, A., Louie, J. N., 2010. Retrieval of Earth's reflection response from ambient seismic noise - a Nevada experiment, American Geophysical Union Fall Meeting, abstract #S33A-2071.

Tibuleac, I.M., von Seggern, D.H., Anderson, J.G., and Louie, J.N., 2011. Computing Green's Functions from Ambient Noise Recorded by Narrow-Band Seismometers, Accelerometers, and Analog Seismometers, doi: 10.1785/gssrl.82.5.661 Seismological Research Letters, September/October, v. 82, no. 5, p. 661-675.

Tibuleac, I., and Eneva, M., 2011. Seismic Signature of the Geothermal Field at Soda Lake, Nevada, from Ambient Noise Analysis, Geothermal Reservoir Council Transactions, 35, p. 1767-1772.

Tibuleac, I.M. and von Seggern, D.H., 2012, Crust-mantle boundary reflectors in Nevada from noise auto-correlations, Geophys. J. Int., v189, issue 1, p. 493-500.

Tibuleac, I. M., von Seggern, D. H, Faulds, J., Shaw, D., McLahaln, H., Iovenitti, J., Pullmmanappallil, S., Ibser, F. H., and Morrison, M., 2015. Development of a low cost method to estimate the seismic signature of a geothermal field from ambient seismic noise analysis, Final report, DOE Project DE-EE0005518.

List of Appendices

Appendix 1
BLM Notice of Intent

Carla James
U.S. Bureau of Land Management Stillwater Field Office
5665 Morgan Mill Road
Carson City, NV 89701

Dear Ms. James:
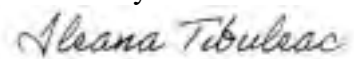
The University of Nevada Reno (UNR) and the U.S. Department of Energy (DOE) have funded a high resolution ambient seismic noise survey in the Dixie Valley Geothermal Wellfield (DVGW) area in Dixie Valley, Nevada (Figure 1). Attachment 1 provides Federal Form 3200-9 NOTICE OF INTENT TO CONDUCT GEOTHERMAL RESOURCE EXPLORATION OPERATIONS. The DVGW extends from well 45-14 at the southwestern portion of the wellfield to approximately well 76-28 at the northeastern portion of the wellfield and well 62-21 on the southeastern side of the wellfield. Attachment 1—Figure 1 presents the specific ambient seismic noise survey lines in the DVGW and the locations of the individual seismic sensors on those lines are provided in Attachment 1—Table 1. A description of the ambient seismic noise survey along with the field work associated with the installation and demobilization of the seismic sensors is presented in Attachment 2.

This permit application is being submitted to both the U.S. Bureau of Land Management Stillwater Field Office only. We are thought we would have some stations in the Humboldt River Field Office area of responsibility, but in the final survey design this is not the case. Attachment 1—Figure 1 presents the survey lines and seismic stations in the DVGW. Three types of sensors will be deployed (1) geophones with a Texan digitizers, (2) short-period sensors and (3) broadband sensors. Details on the deployment of these sensors is presented in Attachment 2. Attachment 1—Table 1A through 1L present the GPS coordinates for the seismic stations to be permitted.

As an aside, you may recall that you and Joe Iovenitti who was the Principal Investigator for a DOE/AltaRock Energy Inc. and now a team member in this current project, were involved in permitting a broadband seismic survey (but with a much lower resolution) in Dixie Valley in 2010. Locations of the 2010 permit-approved seismic stations are shown in Attachment 2—Figure 2 for comparative purposes.

If you have any comments or questions regarding this NOI, please contact me by telephone at 775-784-6256 or by e-mail at imtseismic@yahoo.com. Or, if I am not available, please contact Joe Iovenitti at 510-290-9247 and/or joeiovenitti@comcast.net. Mr. Iovenitti is assisting me on this project.

Sincerely,
University of Nevada Reno

Ileana Tibuleac

Ileana, Tibuleac, Ph.D.
Research Scientist and Principal Investigator for the Dixie Valley Project

Cc: Daniel Atkinson, Humboldt River Field Office David Schroeder, Stillwater Field Office
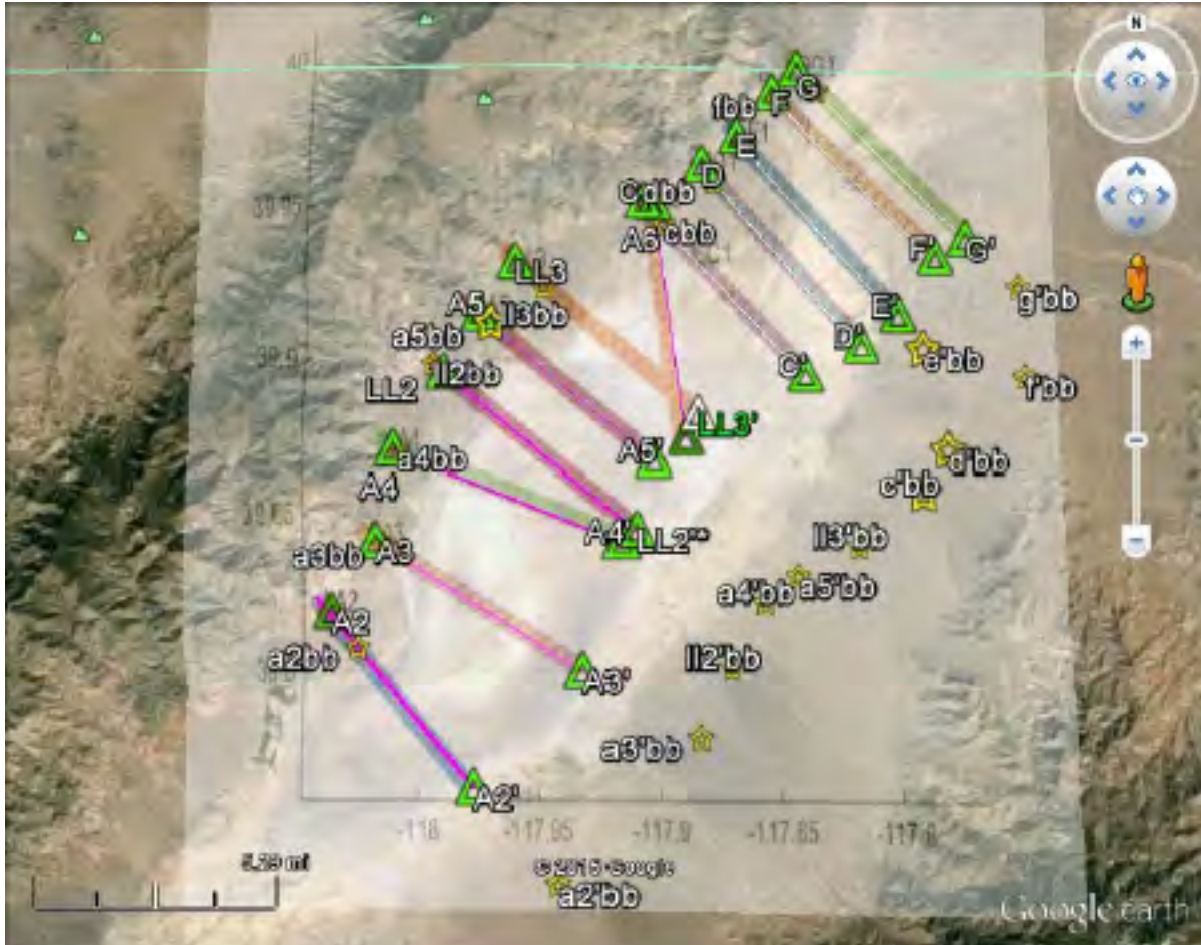
Figure 1. Location of the new ambient seismic noise survey (ANS) which are the subject of this permit application. Stars are broadband sensor locations, the survey lines (e.g., A2-A2') include geophone/Texan geophones about every 34m (100ft) locations and circles are centered on short period sensor locations located along the survey lines about every 500m. The green line above survey line G-G' is the county line. All seismic stations are located in Churchill County, Nevada.

2.2.1.1 Geophones and Texan Digitizers

Figures 5A and 5B show the geophone and Texan digitizer, respectively. The 3-inch spike on the geophone (Figure 5A) is pushed in the ground. The geophone and digitizer are positioned a few inches below the surface of the earth and covered by a few inches of soil (Figure 5C) for a period of 6-12 days per survey line. Data will be harvested every 3 days by replacing the Texan digitizers. These geophones will be spaced at ~34m ±10m along each line in Figure 3.

A

B

C

Figure 5. (A) Typical installation of a geophone, provided by IRIS, to be used in the Dixie Valley Geothermal Wellfield new ANS project. (B) Texan digitizer whose size is 3-inches in diameter by 7.7-inches long. (C) The geophone and digitizer is deployed a few inches below the ground surface and covered with soil. Note that the digitizer is covered by a clear plastic bad and taped closed.

Appendix 2
Documentation of Experiment Conditions

November 12-24 Installation of the BB, SP and Line 4

December -January 2015. Deployed field stations were serviced

January 2016 Line 3 installation

UNR vehicle at the Line 6 location

Preparing Texan insulation for Line 6.

Thumper shots at Line 5 January 2017

Line 5, near station 105

Collecting geophones on Line 5, January 2016

Geophone collection Line 6

Geophone collection Line 6

Field conditions, January 2016

Collecting Lines 2 and 3

Collecting geophones on Line 6

Along lines 2 and 3, Feb 2016: The lake on the valley floor has advanced to Line 4.

Along Line 4, Feb 2016

Calcified grass on Line 5

Pictures of Shipment to Fallon, NV from IRIS

Copy of Fallon Shed Inventory

Texan Inventory

Box number

PTC75	1516	Pallet 1
PTC75	3597	Pallet 1
PTC75	1673	Pallet 1
PTC75	2335	Pallet 1
PTC75	3658	Pallet 1
PTC75	4038	Pallet 1
PTC75	1511	Pallet 1
PTC75	2341	Pallet 1
PTC75	1057	Pallet 1
PTC75	2128	Pallet 1
PTC75	2424	Pallet 1
PTC75	1691	Pallet 1
PTC75	1663	Pallet 1
PTC75	1214	Pallet 1
PTC75	2841	Pallet 1
FTC56	1211	Pallet 1
FTC56	2231	Pallet 1
FTC56	2881	Pallet 1
FTC56	1066	Pallet 1
FTC56	1732	Pallet 1
FTC56	2143	Pallet 1
FTC56	1305	Pallet 1
FTC56	1122	Pallet 1
FTC56	746	Pallet 1
FTC56	2909	Pallet 1
FTC56	1814	Pallet 1
FTC56	2029	Pallet 1
FTC56	1899	Pallet 1
FTC56	1310	Pallet 1
FTC56	2401	Pallet 1
FTC25	2863	Pallet 1
FTC25	3910	Pallet 1
FTC25	2535	Pallet 1
FTC25	2688	Pallet 1
FTC25	3767	Pallet 1
FTC25	729	Pallet 1
FTC25	2553	Pallet 1

FTC25	3639	Pallet 1
FTC25	2315	Pallet 1
FTC25	2891	Pallet 1
FTC25	3740	Pallet 1
FTC25	3662	Pallet 1
FTC25	791	Pallet 1
FTC25	1931	Pallet 1
FTC25	3945	Pallet 1
FTC29	1716	Pallet 1
FTC29	1065	Pallet 1
FTC29	3602	Pallet 1
FTC29	2366	Pallet 1
FTC29	2409	Pallet 1
FTC29	1831	Pallet 1
FTC29	2262	Pallet 1
FTC29	3935	Pallet 1
FTC29	1973	Pallet 1
FTC29	3766	Pallet 1
FTC29	3997	Pallet 1
FTC29	2711	Pallet 1
FTC29	3641	Pallet 1
FTC29	2516	Pallet 1
FTC29	2898	Pallet 1
FTC86	1787	Pallet 1
FTC86	870	Pallet 1
FTC86	690	Pallet 1
FTC86	1191	Pallet 1
FTC86	2513	Pallet 1
FTC86	1072	Pallet 1
FTC86	3672	Pallet 1
FTC86	2006	Pallet 1
FTC86	2720	Pallet 1
FTC86	711	Pallet 1
FTC86	2583	Pallet 1
FTC86	860	Pallet 1
FTC86	1705	Pallet 1
FTC86	2614	Pallet 1
FTC86	1080	Pallet 1
PTC8	1830	Pallet 1
PTC8	1718	Pallet 1
PTC8	1847	Pallet 1

PTC8	1526	Pallet 1
PTC8	2572	Pallet 1
PTC8	2416	Pallet 1
PTC8	2941	Pallet 1
PTC8	2126	Pallet 1
PTC8	2539	Pallet 1
PTC8	2412	Pallet 1
PTC8	2653	Pallet 1
PTC8	2664	Pallet 1
PTC8	3909	Pallet 1
PTC8	1520	Pallet 1
PTC8	3864	Pallet 1
PTC87	2086	Pallet 1
PTC87	1844	Pallet 1
PTC87	3751	Pallet 1
PTC87	3783	Pallet 1
PTC87	1856	Pallet 1
PTC87	1185	Pallet 1
PTC87	2225	Pallet 1
PTC87	2101	Pallet 1
PTC87	2163	Pallet 1
PTC87	3757	Pallet 1
PTC87	2256	Pallet 1
PTC87	2634	Pallet 1
PTC87	2162	Pallet 1
PTC87	4054	Pallet 1
PTC87	1622	Pallet 1
FTC46	2498	Pallet 1
FTC46	4088	Pallet 1
FTC46	3809	Pallet 1
FTC46	2233	Pallet 1
FTC46	4078	Pallet 1
FTC46	4035	Pallet 1
FTC46	3834	Pallet 1
FTC46	3638	Pallet 1
FTC46	1612	Pallet 1
FTC46	1940	Pallet 1
FTC46	1634	Pallet 1
FTC46	1557	Pallet 1
FTC46	1879	Pallet 1
FTC46	2045	Pallet 1

FTC46	2033	Pallet 1
FTC1	2303	Pallet 1
FTC1	2681	Pallet 1
FTC1	2356	Pallet 1
FTC1	1802	Pallet 1
FTC1	1618	Pallet 1
FTC1	2895	Pallet 1
FTC1	1694	Pallet 1
FTC1	815	Pallet 1
FTC1	2125	Pallet 1
FTC1	1859	Pallet 1
FTC1	3947	Pallet 1
FTC1	742	Pallet 1
FTC1	3588	Pallet 1
FTC1	4086	Pallet 1
FTC1	724	Pallet 1
FTC65	2833	Pallet 1
FTC65	2579	Pallet 1
FTC65	847	Pallet 1
FTC65	2888	Pallet 1
FTC65	2072	Pallet 1
FTC65	2656	Pallet 1
FTC65	2495	Pallet 1
FTC65	2547	Pallet 1
FTC65	3870	Pallet 1
FTC65	3813	Pallet 1
FTC65	2944	Pallet 1
FTC65	1857	Pallet 1
FTC65	1262	Pallet 1
FTC65	2934	Pallet 1
FTC65	812	Pallet 1
FTC117	4073	Pallet 1
FTC117	1969	Pallet 1
FTC117	4041	Pallet 1
FTC117	4045	Pallet 1
FTC117	1575	Pallet 1
FTC117	3849	Pallet 1
FTC117	2235	Pallet 1
FTC117	2473	Pallet 1
FTC117	2063	Pallet 1
FTC117	2444	Pallet 1

FTC117	3661	Pallet 1
FTC117	2221	Pallet 1
FTC117	3797	Pallet 1
FTC117	1629	Pallet 1
FTC117	2577	Pallet 1
FTC83	4044	Pallet 1
FTC83	1770	Pallet 1
FTC83	1828	Pallet 1
FTC83	2241	Pallet 1
FTC83	3838	Pallet 1
FTC83	3816	Pallet 1
FTC83	2750	Pallet 1
FTC83	2708	Pallet 1
FTC83	1665	Pallet 1
FTC83	3869	Pallet 1
FTC83	1897	Pallet 1
FTC83	1755	Pallet 1
FTC83	1126	Pallet 1
FTC83	2051	Pallet 1
FTC83	2395	Pallet 1
PTC55	2767	Pallet 2
PTC55	4015	Pallet 2
PTC55	2119	Pallet 2
PTC55	1896	Pallet 2
PTC55	2884	Pallet 2
PTC55	2663	Pallet 2
PTC55	3734	Pallet 2
PTC55	1698	Pallet 2
PTC55	1620	Pallet 2
PTC55	2011	Pallet 2
PTC55	741	Pallet 2
PTC55	3747	Pallet 2
PTC55	1583	Pallet 2
PTC55	1650	Pallet 2
PTC55	2558	Pallet 2
PTC84	836	Pallet 2
PTC84	1933	Pallet 2
PTC84	2643	Pallet 2
PTC84	2440	Pallet 2
PTC84	2880	Pallet 2
PTC84	1058	Pallet 2

PTC84	1779	Pallet 2
PTC84	3707	Pallet 2
PTC84	1799	Pallet 2
PTC84	2511	Pallet 2
PTC84	1062	Pallet 2
PTC84	692	Pallet 2
PTC84	797	Pallet 2
PTC84	2736	Pallet 2
PTC84	3723	Pallet 2
TC80	3669	Pallet 2
TC80	2372	Pallet 2
TC80	2018	Pallet 2
TC80	3628	Pallet 2
TC80	1651	Pallet 2
TC80	1726	Pallet 2
TC80	2769	Pallet 2
TC80	1784	Pallet 2
TC80	3750	Pallet 2
TC80	4159	Pallet 2
TC80	2753	Pallet 2
TC80	704	Pallet 2
TC80	2261	Pallet 2
TC80	1160	Pallet 2
TC80	2676	Pallet 2
FTC109	1822	Pallet 2
FTC109	1821	Pallet 2
FTC109	1554	Pallet 2
FTC109	3618	Pallet 2
FTC109	3599	Pallet 2
FTC109	1190	Pallet 2
FTC109	2248	Pallet 2
FTC109	3738	Pallet 2
FTC109	3777	Pallet 2
FTC109	2518	Pallet 2
FTC109	2245	Pallet 2
FTC109	2811	Pallet 2
FTC109	2219	Pallet 2
FTC109	1739	Pallet 2
FTC109	2982	Pallet 2
FTC88	858	Pallet 2
FTC88	4096	Pallet 2

FTC88	835	Pallet 2
FTC88	799	Pallet 2
FTC88	2851	Pallet 2
FTC88	820	Pallet 2
FTC88	2359	Pallet 2
FTC88	1002	Pallet 2
FTC88	2679	Pallet 2
FTC88	4157	Pallet 2
FTC88	1181	Pallet 2
FTC88	2194	Pallet 2
FTC88	2867	Pallet 2
FTC88	1717	Pallet 2
FTC88	1307	Pallet 2
FTC41	1823	Pallet 2
FTC41	1047	Pallet 2
FTC41	3802	Pallet 2
FTC41	2935	Pallet 2
FTC41	821	Pallet 2
FTC41	1637	Pallet 2
FTC41	1053	Pallet 2
FTC41	1186	Pallet 2
FTC41	1753	Pallet 2
FTC41	762	Pallet 2
FTC41	2180	Pallet 2
FTC41	809	Pallet 2
FTC41	1114	Pallet 2
FTC41	2321	Pallet 2
FTC41	2499	Pallet 2
FTC82	1934	Pallet 2
FTC82	2560	Pallet 2
FTC82	3933	Pallet 2
FTC82	2929	Pallet 2
FTC82	1817	Pallet 2
FTC82	1675	Pallet 2
FTC82	1676	Pallet 2
FTC82	3671	Pallet 2
FTC82	2319	Pallet 2
FTC82	2223	Pallet 2
FTC82	2466	Pallet 2
FTC82	1793	Pallet 2
FTC82	3653	Pallet 2

FTC82	2857	Pallet 2
FTC82	2671	Pallet 2
NTC29	2759	Pallet 2
NTC29	740	Pallet 2
NTC29	1518	Pallet 2
NTC29	1712	Pallet 2
NTC29	2680	Pallet 2
NTC29	2878	Pallet 2
NTC29	2171	Pallet 2
NTC29	2048	Pallet 2
NTC29	2868	Pallet 2
NTC29	2195	Pallet 2
NTC29	3609	Pallet 2
NTC29	3703	Pallet 2
NTC29	3975	Pallet 2
NTC29	3833	Pallet 2
NTC29	2065	Pallet 2
FTC114	4063	Pallet 2
FTC114	3820	Pallet 2
FTC114	3995	Pallet 2
FTC114	2846	Pallet 2
FTC114	2203	Pallet 2
FTC114	2907	Pallet 2
FTC114	2695	Pallet 2
FTC114	2004	Pallet 2
FTC114	3744	Pallet 2
FTC114	1051	Pallet 2
FTC114	4091	Pallet 2
FTC114	3743	Pallet 2
FTC114	2727	Pallet 2
FTC114	1594	Pallet 2
FTC114	3841	Pallet 2
FTC66	1954	Pallet 2
FTC66	2214	Pallet 2
FTC66	2622	Pallet 2
FTC66	2367	Pallet 2
FTC66	998	Pallet 2
FTC66	3695	Pallet 2
FTC66	3762	Pallet 2
FTC66	2141	Pallet 2
FTC66	4037	Pallet 2

FTC66	1027	Pallet 2
FTC66	2307	Pallet 2
FTC66	2311	Pallet 2
FTC66	2326	Pallet 2
FTC66	1606	Pallet 2
FTC66	735	Pallet 2
FTC93	2324	Pallet 2
FTC93	3775	Pallet 2
FTC93	3635	Pallet 2
FTC93	3646	Pallet 2
FTC93	1139	Pallet 2
FTC93	2159	Pallet 2
FTC93	3925	Pallet 2
FTC93	2612	Pallet 2
FTC93	2843	Pallet 2
FTC93	1120	Pallet 2
FTC93	1552	Pallet 2
FTC93	2015	Pallet 2
FTC93	1635	Pallet 2
FTC93	1129	Pallet 2
FTC93	1617	Pallet 2
FTC63	1681	Pallet 2
FTC63	2294	Pallet 2
FTC63	685	Pallet 2
FTC63	3853	Pallet 2
FTC63	1923	Pallet 2
FTC63	3752	Pallet 2
FTC63	2919	Pallet 2
FTC63	4066	Pallet 2
FTC63	763	Pallet 2
FTC63	975	Pallet 2
FTC63	2939	Pallet 2
FTC63	1715	Pallet 2
FTC63	2755	Pallet 2
FTC63	3706	Pallet 2
FTC63	3814	Pallet 2
PTC11	2904	Pallet 3
PTC11	2514	Pallet 3
PTC11	995	Pallet 3
PTC11	3750	Pallet 3

PTC11	2790	Pallet 3
PTC11	767	Pallet 3
PTC11	3889	Pallet 3
PTC11	1935	Pallet 3
PTC11	2649	Pallet 3
PTC11	2098	Pallet 3
PTC11	3852	Pallet 3
PTC11	798	Pallet 3
PTC11	2330	Pallet 3
PTC11	3644	Pallet 3
PTC11	2075	Pallet 3
NTC25	1662	Pallet 3
NTC25	4080	Pallet 3
NTC25	3883	Pallet 3
NTC25	3666	Pallet 3
NTC25	2879	Pallet 3
NTC25	830	Pallet 3
NTC25	1588	Pallet 3
NTC25	1064	Pallet 3
NTC25	2462	Pallet 3
NTC25	3713	Pallet 3
NTC25	2682	Pallet 3
NTC25	1657	Pallet 3
NTC25	1955	Pallet 3
NTC25	1880	Pallet 3
NTC25	2618	Pallet 3
FTC105	3827	Pallet 3
FTC105	2154	Pallet 3
FTC105	2749	Pallet 3
FTC105	726	Pallet 3
FTC105	1639	Pallet 3
FTC105	2375	Pallet 3
FTC105	2208	Pallet 3
FTC105	2905	Pallet 3
FTC105	1032	Pallet 3
FTC105	3878	Pallet 3
FTC105	3642	Pallet 3
FTC105	1957	Pallet 3
FTC105	2121	Pallet 3
FTC105	2362	Pallet 3
FTC105	3908	Pallet 3

FTC18	1852	Pallet 3
FTC18	1867	Pallet 3
FTC18	4023	Pallet 3
FTC18	4161	Pallet 3
FTC18	2345	Pallet 3
FTC18	1304	Pallet 3
FTC18	2540	Pallet 3
FTC18	3720	Pallet 3
FTC18	1963	Pallet 3
FTC18	2987	Pallet 3
FTC18	2342	Pallet 3
FTC18	1772	Pallet 3
FTC18	2181	Pallet 3
FTC18	1985	Pallet 3
FTC18	963	Pallet 3
FTC35	2651	Pallet 3
FTC35	3765	Pallet 3
FTC35	1598	Pallet 3
FTC35	4087	Pallet 3
FTC35	1981	Pallet 3
FTC35	1701	Pallet 3
FTC35	3737	Pallet 3
FTC35	965	Pallet 3
FTC35	1200	Pallet 3
FTC35	2210	Pallet 3
FTC35	2089	Pallet 3
FTC35	1512	Pallet 3
FTC35	667	Pallet 3
FTC35	721	Pallet 3
FTC35	4047	Pallet 3
FTC67	2110	Pallet 3
FTC67	3793	Pallet 3
FTC67	2713	Pallet 3
FTC67	2123	Pallet 3
FTC67	3861	Pallet 3
FTC67	1600	Pallet 3
FTC67	2698	Pallet 3
FTC67	1572	Pallet 3
FTC67	2554	Pallet 3
FTC67	2398	Pallet 3
FTC67	2135	Pallet 3

FTC67	774	Pallet 3
FTC67	2567	Pallet 3
FTC67	2715	Pallet 3
FTC67	1812	Pallet 3
FTC3	2175	Pallet 3
FTC3	3805	Pallet 3
FTC3	3881	Pallet 3
FTC3	1060	Pallet 3
FTC3	3784	Pallet 3
FTC3	2211	Pallet 3
FTC3	1271	Pallet 3
FTC3	3608	Pallet 3
FTC3	4034	Pallet 3
FTC3	1151	Pallet 3
FTC3	701	Pallet 3
FTC3	1113	Pallet 3
FTC3	1646	Pallet 3
FTC3	683	Pallet 3
FTC3	1111	Pallet 3
TC74	2624	Pallet 3
TC74	1156	Pallet 3
TC74	748	Pallet 3
TC74	3621	Pallet 3
TC74	1719	Pallet 3
TC74	1914	Pallet 3
TC74	2097	Pallet 3
TC74	1569	Pallet 3
TC74	1825	Pallet 3
TC74	2263	Pallet 3
TC74	2127	Pallet 3
TC74	1663	Pallet 3
TC74	2165	Pallet 3
TC74	1733	Pallet 3
TC74	2479	Pallet 3
PTC64	1941	Pallet 3
PTC64	3818	Pallet 3
PTC64	3940	Pallet 3
PTC64	1873	Pallet 3
PTC64	1586	Pallet 3
PTC64	2861	Pallet 3
PTC64	2428	Pallet 3

PTC64	1943	Pallet 3
PTC64	2751	Pallet 3
PTC64	2534	Pallet 3
PTC64	3763	Pallet 3
PTC64	1720	Pallet 3
PTC64	1632	Pallet 3
PTC64	1970	Pallet 3
PTC64	3770	Pallet 3
FTC62	2886	Pallet 3
FTC62	2494	Pallet 3
FTC62	2385	Pallet 3
FTC62	2900	Pallet 3
FTC62	1101	Pallet 3
FTC62	1075	Pallet 3
FTC62	1573	Pallet 3
FTC62	2636	Pallet 3
FTC62	1033	Pallet 3
FTC62	2747	Pallet 3
FTC62	2742	Pallet 3
FTC62	2991	Pallet 3
FTC62	2854	Pallet 3
FTC62	2835	Pallet 3
FTC62	2477	Pallet 3
FTC37	3692	Pallet 3
FTC37	3604	Pallet 3
FTC37	3627	Pallet 3
FTC37	1180	Pallet 3
FTC37	2512	Pallet 3
FTC37	2585	Pallet 3
FTC37	3780	Pallet 3
FTC37	2310	Pallet 3
FTC37	1625	Pallet 3
FTC37	1519	Pallet 3
FTC37	2483	Pallet 3
FTC37	2830	Pallet 3
FTC37	2943	Pallet 3
FTC37	2731	Pallet 3
FTC37	2220	Pallet 3
TC54	1699	Pallet 3
TC54	3822	Pallet 3

TC54	2804	Pallet 3
TC54	2243	Pallet 3
TC54	2109	Pallet 3
TC54	1040	Pallet 3
TC54	2348	Pallet 3
TC54	4036	Pallet 3
TC54	2070	Pallet 3
TC54	4057	Pallet 3
TC54	2859	Pallet 3
TC54	1832	Pallet 3
TC54	1789	Pallet 3
TC54	1929	Pallet 3
TC54	2561	Pallet 3
FTC60	2526	Pallet 4
FTC60	1864	Pallet 4
FTC60	1654	Pallet 4
FTC60	2044	Pallet 4
FTC60	4025	Pallet 4
FTC60	2173	Pallet 4
FTC60	1840	Pallet 4
FTC60	810	Pallet 4
FTC60	1508	Pallet 4
FTC60	3952	Pallet 4
FTC60	1580	Pallet 4
FTC60	1975	Pallet 4
FTC60	2474	Pallet 4
FTC60	2740	Pallet 4
FTC60	2486	Pallet 4
FTC5	2472	Pallet 4
FTC5	1308	Pallet 4
FTC5	2414	Pallet 4
FTC5	1312	Pallet 4
FTC5	1885	Pallet 4
FTC5	1034	Pallet 4
FTC5	2217	Pallet 4
FTC5	2289	Pallet 4
FTC5	3009	Pallet 4
FTC5	3003	Pallet 4
FTC5	2484	Pallet 4
FTC5	1986	Pallet 4

FTC5	2921	Pallet 4
FTC5	2133	Pallet 4
FTC5	5160	Pallet 4
FTC50	2844	Pallet 4
FTC50	2595	Pallet 4
FTC50	1992	Pallet 4
FTC50	1974	Pallet 4
FTC50	1686	Pallet 4
FTC50	3596	Pallet 4
FTC50	2418	Pallet 4
FTC50	3972	Pallet 4
FTC50	4027	Pallet 4
FTC50	2450	Pallet 4
FTC50	2568	Pallet 4
FTC50	864	Pallet 4
FTC50	3771	Pallet 4
FTC50	1070	Pallet 4
FTC50	1585	Pallet 4
FTC13	2249	Pallet 4
FTC13	2242	Pallet 4
FTC13	3867	Pallet 4
FTC13	1882	Pallet 4
FTC13	2223	Pallet 4
FTC13	2467	Pallet 4
FTC13	1785	Pallet 4
FTC13	3674	Pallet 4
FTC13	2860	Pallet 4
FTC13	2146	Pallet 4
FTC13	1889	Pallet 4
FTC13	2403	Pallet 4
FTC13	1553	Pallet 4
FTC13	1818	Pallet 4
FTC13	1909	Pallet 4
FTC59	702	Pallet 4
FTC59	4083	Pallet 4
FTC59	1987	Pallet 4
FTC59	766	Pallet 4
FTC59	2763	Pallet 4
FTC59	2550	Pallet 4
FTC59	966	Pallet 4
FTC59	2491	Pallet 4

FTC59	1631	Pallet 4
FTC59	1758	Pallet 4
FTC59	1894	Pallet 4
FTC59	3823	Pallet 4
FTC59	1116	Pallet 4
FTC59	5221	Pallet 4
FTC59	2291	Pallet 4
FTC72	1865	Pallet 4
FTC72	3636	Pallet 4
FTC72	2240	Pallet 4
FTC72	3709	Pallet 4
FTC72	1866	Pallet 4
FTC72	2212	Pallet 4
FTC72	3748	Pallet 4
FTC72	3617	Pallet 4
FTC72	1979	Pallet 4
FTC72	2913	Pallet 4
FTC72	3899	Pallet 4
FTC72	2237	Pallet 4
FTC72	1595	Pallet 4
FTC72	4089	Pallet 4
FTC72	3643	Pallet 4
PTC13	3606	Pallet 4
PTC13	1661	Pallet 4
PTC13	811	Pallet 4
PTC13	1196	Pallet 4
PTC13	1757	Pallet 4
PTC13	723	Pallet 4
PTC13	2363	Pallet 4
PTC13	1303	Pallet 4
PTC13	3879	Pallet 4
PTC13	2586	Pallet 4
PTC13	1803	Pallet 4
PTC13	4011	Pallet 4
PTC13	1000	Pallet 4
PTC13	2722	Pallet 4
PTC13	1202	Pallet 4
FTC11	4010	Pallet 4
FTC11	2239	Pallet 4
FTC11	2660	Pallet 4
FTC11	2831	Pallet 4

FTC11	2509	Pallet 4
FTC11	3848	Pallet 4
FTC11	3633	Pallet 4
FTC11	2320	Pallet 4
FTC11	3847	Pallet 4
FTC11	2914	Pallet 4
FTC11	2408	Pallet 4
FTC11	2460	Pallet 4
FTC11	1608	Pallet 4
FTC11	2814	Pallet 4
FTC11	1858	Pallet 4
FTC95	1525	Pallet 4
FTC95	2198	Pallet 4
FTC95	1989	Pallet 4
FTC95	2052	Pallet 4
FTC95	2489	Pallet 4
FTC95	1035	Pallet 4
FTC95	2693	Pallet 4
FTC95	2411	Pallet 4
FTC95	2316	Pallet 4
FTC95	1138	Pallet 4
FTC95	2999	Pallet 4
FTC95	4158	Pallet 4
FTC95	1067	Pallet 4
FTC95	3863	Pallet 4
FTC95	1183	Pallet 4
FTC103	1077	Pallet 4
FTC103	2569	Pallet 4
FTC103	1584	Pallet 4
FTC103	730	Pallet 4
FTC103	924	Pallet 4
FTC103	2768	Pallet 4
FTC103	1571	Pallet 4
FTC103	4065	Pallet 4
FTC103	882	Pallet 4
Missing	714	last at 2013
	1210	last at 6223
	2560	last at 3067
	2521	last at 5179
	1790	last at 3039

Page 122 of 234

2232 not deployed?

Appendix 3
Deployment Documentation

Station Number	Phase 1							Notes
	In			Notes	Out			
	Date: Jan 07, 2016				Date: Jan 10, 2016			
	Geophone	Time (hh:mm:ss)	Light Color		Geophone	Time (hh:mm:ss)	Light Color	
3001	2460	13:30	G		2460	12:49	N	
3003	2731	13:37	G		2731	12:54	G	
3005	3747	13:45	G		3747	12:58	G	
3007	3863	13:50	G		3863	12:01	G	
3009	4158	13:55	G		4158	13:06	G	
3011	1583	14:00	G		1583	13:10	G	
3013	2060	14:04	G		2060	13:15	G	
3015	1963	14:08	G		1963	13:20	G	
3017	1053	14:13	G		1053	13:23	N	
3019	1987	14:19	G		1987	13:27	N	
3021	1111	14:24	G		1111	13:30	G	
3023	1060	14:30	G		1060	13:33	G	
3025	2359	14:35	G		2359	13:38	G	
3027	1821		G		1821	13:41	G	
3029	701	15:15	G		701	13:45	G	
3031	2198	15:28	G		2198	14:13	G	
3033	1151	15:16	G		1151	14:10	G	
3035	1989	15:05	G		1989	14:08	G	
3037	1271	15:00	G		1271	14:06	G	
3039	683	15:00	G		683	14:02	G	
3041	1067	12:34	G		1067	14:21	G	
3043	2999	12:42	G		2990	14:24	G	
3045	2411	12:48	G		2411	14:27	N	
3047	2693	12:52	G		2693	14:31	G	

Station Number	Geophone	Time	Light Color	Notes	Geophone	Time	Light Color	Notes
3049	1035	12:59	G		1035	14:36	G	
3051	2316	12:05	G		2316	14:40	G	
3053	1138	13:10	G		1138	14:42	G	
3055	2489	13:16	G		2489	14:45	G	
3057	2052	13:22	G		2052	14:50	G	
3059	2075	13:27	G		2075	14:46	G	
3061	4034	13:33	G		4034	14:43	N	
3063	1812	13:37	G		1812	14:38	G	
3065	1113	13:43	G		1113	14:32	G	
3067	2560	13:46	G		2560	14:26	N	
3069	1646	13:56	G		1646	14:24	N	
3071	3608	14:01	G		3608	14:14	N	
3073	3802	14:05	G		3802	14:10	G	
3075	1525	14:09	G		1525	14:05	N	
3077	2935	14:13	G		2935	14:01	G	
3079	1753	14:18	G		1753	13:56	G	

Station Number	Phase 2							Notes
	In			Notes	Out			
	Date: Jan 10, 2016				Date: Jan 13, 2016			
	Geophone	Time (hh:mm:ss)	Light Color		Geophone	Time (hh:mm:ss)	Light Color	
3001	821	12:49	G		821	13:36	G	
3003	3766	12:54	G		3766	13:44	G	
3005	3723	12:58	G		3723	13:49	G	
3007	2934	13:02	G		2934	13:55	G	
3009	1650	13:06	G		1650	14:09	G	
3011	2736	13:11	G		2736	14:18	G	
3013	2511	13:16	G		2511	14:27	G	
3015	3707	13:21	G		3707	14:40	N	
3017	2880	13:24	G		2880	14:49	G	
3019	2944	13:28	G		2944	14:59	G	
3021	1823	13:31	G		1823	15:08	G	
3023	2843	13:34	G		2643	15:20	G	

Page 125 of 234

Station Number	Geophone (In)	Time (In)	Light Color (In)	Notes	Geophone (Out)	Time (Out)	Light Color (Out)	Notes
3025	1799	13:38	G		1799	15:33	N	
3027	3641	13:42	G		3641	15:39	G	
3029	1516	13:46	G		1516	16:12	G	
3031	1634	14:14	G		1634	16:17	G	Geophone at surface
3033	3752	14:11	G		3752	16:17	N	Geophone at surface
3035	975	14:08	G		975	16:24	G	Disconnected
3037	2547	14:07	G		2547		G	
3039	2939	14:02	G		2939		G	
3041	2440	14:22	G		2440	12:57	G	
3043	3809	14:24	G		3809		G	
3045	4078	14:28	G		4078		G	
3047	2045	14:33	G		2045		G	
3049	1557	14:37	G		1557		G	
3051	2033	14:40	G		2033	13:07	G	
3053	3834	14:43	G		3834	13:14	G	
3055	2830	14:45	G		2830	13:22	G	
3057	1625	14:50	G		1625	13:25	G	
3059	1940		G		1940	13:41	G	
3061	4088		G		4088	13:50	G	
3063	4035		G		4035	13:57	N	
3065	1612		G		1612	14:06	G	
3067	3815		G		3814	14:11	G	
3069	2072		G		2072	14:23	G	
3071	3635		G		3635	14:35	N	
3073	1681		G		1681	14:43	G	
3075	2325		G		2324	14:48	G	
3077	3706		G		3706	14:53	G	
3079	2233		G		2233	14:58	G	

Station Number	Phase 3			Notes				Notes
	In				Out			
	Date: Jan 13, 2016				Date: Jan 16, 2016			
	Geophone	Time (hh:mm:ss)	Light Color		Geophone	Time (hh:mm:ss)	Light Color	

3001	2214	13:37	G		2214	G	
3003	2622	13:45	G		2622	G	
3005	998	13:50	G		998	G	
3007	1954	13:56	G		1954	N	
3009	3695	14:15	G		3695	G	
3011	2141	14:19	G		2141	G	
3013	3762	14:33	G		3762	G	
3015	2311	14:40	G		2311	N	
3017	2307	14:53	G		2307	N	
3019	1027	15:00	G		1027	N	
3021	2326	15:13	G		2362	G	
3023	1606	15:20	G		1606	G	
3025	735	15:34	G		735	G	
3027	4037	15:40	G		4037	G	
3029	3852	16:12	G		3852	G	
3031	3644	16:17	G		3644	G	
3033	2367	16:26	G		2307	G	
3035	1935	16:30	G		1935	G	
3037	2514	16:53	G		2514	G	
3039	1790		G			G	Couldn't read note on sheet
3041	1803	12:59	G		1803	G	Possible bad connection
3043	2740		G		2740	G	
3045	4011		G		4011	G	
3047	810		G		810	G	
3049	2486		G		2486	G	
3051	3952	13:11	G		3952	G	
3053	2474	13:15	G		2474	G	
3055	1975	13:23	G		1975	N	
3057	1000	13:30	G		1000	N	
3059	2173	13:42	G		2173	G	
3061	2722	13:51	G		7222	G	
3063	2904	13:58	G		2904	N	

3065	1580	14;07	G		1580		N	
3067	1202	14:14	G		1202		N	
3069	1840	14:24	G		1840		R	
3071	1508	14:36	G		1508		N	
3073	2330	14:44	G		2330		G	
3075	2098	14:50	G		2098		G	
3077	3889	14:54	G		3889		G	
3079	3750	14:59	G		3750	16:00	G	

Line 5

Station Number	Phase 1							Notes
	In			Notes	Out			
	Date:				Date: Jan 11, 2016			
	Geophone	Time (hh:mm:ss)	Light Color		Geophone	Time (hh:mm:ss)	Light Color	
5001	2211	13:00	G		2211		N	
5003	2755	13:04	G		2755		G	
5005	1831	13:12	G		1831		G	
5007	2123	13:19	G		2123		G	
5009	1785	13:26	G		1785		N	
5011	3881	13:32	G		3881		G	
5013	3867	13;34	G		3867		N	
5015	3674	13:41	G		3674		G	
5017	2146	13:46	G		2146		G	
5019	2403	14:07	G		2403		N	
5021	3602	14:24	G		3602		G	
5023	2698	14:31	G		2698		G	
5025	3784	14:39	G		3784		N	
5027	1973	14;43	G		1973		G	
5029	2483	14:50	G		2483		N	
5031	2898	14;56	G		2898		N	
5033	2398	15:04	G		2398		N	
5035	3775	15:10	G		3775		N	

5037	2585	15:14	G		2585		N	
5039	2512	15:23	G		2512		G	
5041	3780	15:28	G		3780		N	
5043	1720	15:32	G		1720		G	
5045	2711	15:36	G		2711		G	
5047	2846	15:41	G		2846		N	
5049	2110	15:47	G		2110		G	
5051	3669	15:54	G		3669		N	
5053	1822	15:57	G		1822		G	
5055	2065	16:03	G		2065		G	
5057	2195	16:08	G		2195		N	
5059	2217	16:12	G		2217		N	
5061	2175	16:16	G		2175		G	
5063	2212	16:20	G		2212		N	
5065	1684	16:25	G		1864			
5067	2414	16:30	G		2414		G	
5069	1308	16:34	G		1308		N	
5071	1866	16:41	G		1866		G	
5073	2011	16:44	G		2011			
5075	1885	16:48	G	Moved 8m NW of line	1885		G	
5077	2472	16:54	G		2472			
5079	2310	11:55	G		2310			
5081	2713	12:00	G		2713			
5083	2769	12:06	G		2769		N	
5085	3705	12:10	G		3705		N	
5087	3638	12:17	G		3638			
5089	2135	12:24	G		2135			
5091	2248	12:29	G		2248			
5093	1726	12:33	G		1726		N	
5095	1929	12:37	G		1929			
5097	704		G		704			
5099	1600		G		1600		N	

Page 129 of 234

5101	2567		G		2567			
5103	3861		G		3861			
5105	2249		G		2249			
5107	2811		G		2811	12:07	G	
5109	2554		G		2554	12:13	G	
5111	3177		G	paper damaged	3777	12:20	G	
5113	2740		G		2740	12:29	N	
5115	1790		G		1790	12:35	G	
5117	2486		G		2486	12:42	N	
5119	3738		G		3738	12:46	G	
5121	1608		G		1608	12:50	G	
5123	3813		G		3813	12:55	G	
5125			G	ground frozen	2245	13:00	G	
5127	2242		G		2242	13:10	G	
5129	1739		G		1739	13:16	G	
5131	2867		G		2867	13:20	G	
5133	2982		G		2982	13:25	G	
5135	1909		G		1909	13;30	G	
5137	2467	14:59	G		2467	13;37	G	
5139	1882	14:51	G		1882	13:41	G	
5141	2518	14:45	G		2518	13:50	G	
5143	2656	14:39	G		2656	13:55	N	
5145	2219	14:33	G		2219	14:03	G	
5147	2223	14:26	G		2223		R	
5149	1784	14:21	G		1784		G	
5151	1160	14:16	G		1160		G	
5153	2180	14:09	G		2180		G	
5155	2753	18:29	G		2753		G	
5157	3549	18:27	G		3599		G	
5159	2372	18:23	G		2372		G	
5161	2860	18:21	G		2860		G	
5163	3628	18:19	G		3628		G	

5165	2018	18:15	G		2018		N	
5167	1572	18:13	G		1572		G	
5169	1561	18:10	G		1651		G	
5171	4159	18:07	G		4159		N	
5173	4086	18:05	G		4086		N	
5175	4057	18:03	G		4057		N	
5177	2809	18:00	G		2804		G	
5179	2833	17:58	G		2833		N	
5181	2676	17:50	G		2676		G	
5183	2109	17:46	G		2109		N	
5185	3822	17:49	G		3822		G	
5187	1859	17:44	G		1859		G	
5189	1040	17:42	G		1040		G	
5191	1789	17:41	G		1789		G	
5193	2895	17:39	G		2895		G	
5195	1836	17:30	G		1832		G	
5197	2348	17:34	G		2348		G	
5199	4036	17:25	G		4036		G	
5201	2125	17:24	G		2125		G	
5203	3627	17:21	G		3627		G	
5205	2943	17:19	G		2943		G	
5207	809	17:16	G		809		G	
5209	4010	17:13	G		4010		G	
5211	1896	17:12	G		1896		G	
5213	1620	17:10	G		1620		N	
5215	1141	17:05	G		1114		G	
5217	1186	17:03	G		1186		G	
5219	2408	17:00	G		2408		G	
5221	2914	16:58	G		2914		G	
5223	2401	16:56	G		2401		G	
5225	3622	16:53	G		3633		G	
5227	2119	16:51	G		2119		G	

Station Number	Geophone	Time	Light Color	Notes	Geophone	Time	Light Color	Notes
5229	2239	16:47	G		2239		G	
5231	4831	16:44	G		3841		N	
5233	3695	16:42	G		2695		G	
5235	3975	16:37	G		3975		G	
5237	2727	16:35	G		2727		N	
5239	3820	16:31	G		3820		G	
5241	2004	16:25	G		2004		G	
5243	2203	16:20	G		2203		G	
5245	1951	16:24	G		1951		N	
5247	3995	16:14	G		3995		G	
5249	1744	16:11	G		3744		G	
5251	2907	16:10	G		2907		G	
5253	3743	16:06	G		3743		G	
5255	4091	16:03	G		4091		G	
5257	4063	15:57	G		4063		G	
5259	1594	16:00	G		1594		G	
5261	1637	15:55	G		1637		N	
5263	3853	15:50	G		3853		G	

Station Number	Phase 2							Notes
	In			Notes	Out			
	Date: Jan 11, 2016				Date:			
	Geophone	Time (hh:mm:ss)	Light Color		Geophone	Time (hh:mm:ss)	Light Color	
5001								
5003	1270		G		1720		G	
5005	2751		G		2751		G	
5007	2734		G		2534		G	
5009	3770		G		3770		G	
5011	3763		G		3762		N	
5013	1632		G		1632		G	
5015	1970		G		1970		G	
5017	3818		G		3818		G	
5019	3940		G		3940		G	

Page 132 of 234

5021	1941		G		1941		G
5023	2844		G		2844		G
5025	1974		G		1974		G
5027	2450		G		2450		G
5029	2668		G		2668		G
5031	2418		G		2418		G
5033	864		G		864		G
5035	2972		G		3972		N
5037	1886		G		1686		G
5039	1992		G		1992		G
5041	4027		G		4027		G
5043	2595		G		2595		G
5045	3596		G		3596		G
5047	2479		G		2479		G
5049	3717		G		3717		G
5051	1070		G		1070		N
5053	1585		G		1585		R
5055	3762		G		3762		N
5057	2651		G		2651		G
5059	1598		G		1598		N
5061	1701		G		1707		G
5063	2087		G		4087		G
5065	1981		G		1981		G
5067	3737		G		3737		N
5069	1200		G		1200		G
5071	965		G		965		G
5073	721		G		721		G
5075	3672		G		3672		N
5077	667		G		667		G
5079	2210		G		2210		G
5081	2089		G		2089		G
5083	4047		G		4047		N

5085	1943		G		1943		G	
5087	2006		G		2006		R	
5089	2861		G		2861		G	
5091	1586		G		1586		N	
5093	2513		G		2513		R	
5095	1733		G		1733		G	
5097	2165		G		2165		G	
5099	1645		G		1645		G	
5101	1589		G		1589		G	
5103	1825		G		1825		G	
5105	2127		G		2127		N	
5107	1719	12:07	G		1719		G	
5109	2624	12:13	G		2624		G	
5111	2263	12:21	G		2263		G	
5113	748	12:30	G		748		G	
5115	3621	12:36	G		3621		G	
5117	1901	12:43	G		1901		G	
5119	1156	12:48	G		1156		G	
5121	1032	12:51	G		1032		G	
5123	3642	12:56	G		3642		G	
5125	1957	13:07	G		1957		N	under water
5127	1639	13:11	G		1639		G	
5129	2744	13:18	G		2744		G	
5131	726	13:21	G		726		G	
5133	3827	13:26	G		3827		G	
5135	2375	13:31	G		2375		G	
5137	2618	13:39	G		2618		N	
5139	1867	13:42	G		1867		N	
5141	2154	13:51	G		2154		G	
5143	1873	13:56	G		1873		G	
5145	1512	14:04	G		1512		G	
5147				too wet			G	

5149	2097		G		2097		G	
5151	1852		G		1852		G	
5153	4023		G		4023		G	
5155	4161		G		4161		G	
5157	1304		G		1304		G	
5159	2540		G		2540		G	
5161	219		G		219		G	
5163	3720		G		3720		G	
5165	2181		G		2181		N	
5167	2342		G		2342		N	
5169	963		G		963		G	
5171	2345		G		2345		G	
5173	1772		G		1772		G	Not connected?
5175	1985		G		1985		N	Not connected?
5177	1116		G		1116		G	
5179	2521		G		95		G	
5181	95		G		2512		N	
5183	1758		N		1758		N	
5185	3823		G		3823		G	
5187	966		G		966		G	
5189	2491		G		2491		G	
5191	1631		G		1631		G	
5193	2763		G		2763		G	
5195	766		G		766		G	
5197	702		G		702		G	
5199	4083		G		4083		G	
5201	120		G		120		G	
5203	185		G		185		N	
5205	158		G		158		G	
5207	171		G		171		G	
5209	147		G		147		N	
5211	172		G		172		N	Not connected?

Station Number	Geophone	Time	Light Color	Notes	Geophone	Time	Light Color	Notes
5213	611		G		611		G	
5215							G	
5217	394		G		394		G	
5219	113		G		113		N	
5221	470		G		470		G	
5223	392		G		392		G	
5225	181		G		181		G	
5227	153		G		153		G	
5229	421		N		421		N	
5231	144		G		144		N	Not connected?
5233	591		G		591		G	
5235	428		G		428		G	
5237	2682		G		2682		G	
5239	1455		G		1455		N	
5241	1880		G		1880		N	
5243	2720		G		2720		R	
5245	1657		G		1657		G	
5247	1588		G		1588		G	
5249	3666		G		3666		N	
5251	1064		G		1064		G	
5253	2462		G		2462		G	
5255	2879		G		2879		G	
5257	830		G		830		G	
5259	3883		G		3883		G	
5261	4080		G		4080		G	
5263	1662		G		1662		N	

Line 6

Station Number	Phase 1								Notes
	In			Notes	Out				
	Date: Jan 12, 2016				Date:				
	Geophone	Time (hh:mm:ss)	Light Color		Geophone	Time (hh:mm:ss)	Light Color		

6001	1716		G		1716	16:56	G		
6003	1717		G		1717	17:08	G		
6005	2409		G		2409	17:19	N		
6007	3997		G		3997	17:29	G		
6009	2679		G		2679	17:37	G		
6011	1307		G		1307	17:47	G		
6013	4157		G		4157	17:53	G		
6015	812		G		812		G		
6017	811		G		811		G		
6019	723		G		723		G		
6021	3748		G		3748		G		
6023	1002		G		1002		G		
6025	2363		G		2363		N		
6027	1303		G		1303		G		
6029	2320		G		2320		G		
6031	1757		G		1757		N	Geophone sideways on surface	
6033	1181		G		1181		G		
6035	3879		G		3879		G		
6037	2330		G		2330		G		
6039	1196		G		1196		G		
6041	4025		G		4025		G		
6043	4089		G		4089		G		
6045	1190		G						
6047									
6049									
6051									
6053									
6055									
6057									
6059									
6061									
6063									

6065							
6067							
6069							
6071							
6073				2715		N	
6075				1180		G	
6077	2098		G	4098		G	
6079	3848		G	3848		G	
6081	3606		G	3606		N	
6083	1661		G	1661		G	
6085	3604		G	3604		G	
6087	3852		G	3852		G	
6089	2831		G	2831		G	
6091	1894		G	1894		G	
6093	2814		G	2814		N	
6095	3870		G	3870		G	
6097	1240		G	1240		G	
6099	4066		G	4066		N	
6101	1712		G	1712		G	
6103	2614		G	2614		G	
6105	847		G	847		G	
6107	860		G	860		G	
6109	740		G	740			
6111	1518		G	1518			
6113	2509		G	2509			
6115			G				
6117	1080		G	1080		G	
6119	2759		G	2759		G	
6121	3833		G	3833		G	
6123	2868		G	2868		G	
6125	2171		G	2171			geophone problem
6127	1857		G	1857		N	

6129	3609		G		3609		G
6131	3646		G		3646		G
6133	2612		G		2612		G
6135	1617		G		1617		G
6137	2843		G		2843		G
6139	1635		G		1635		N
6141	2015		G		2015		G
6143	1552		G		1552		G
6145	2261		G		2261		G
6147	3925		G		3925		G
6149	1879		G		1879		G
6151	3709		G		3709		N
6153	3003		G		3003		N
6155	2498		G		2498		N
6157							
6159	2680		G		2690		
6161	1560		G		1560		
6163	2159		G		2159		G
6165	1698		G		1698		
6167	3073		G		3703		G
6169							
6171	2878		G		2878		N
6173	2048		G		2048		N
6175	3847		G		3847		N
6177	1935		G		1935		G
6179	1011		G		4011		G
6181	998		G		995		G
6183	810		G		910		G
6185	3750		G		3750		G
6187	2294		G		2294		R
6189	3611		G		3644		G
6191	1508		G		1508		G

6193						
6195	2326		G		2326	N
6197						
6199	3793		G		3793	N
6201						
6203	2622		G		2622	N
6205						
6207	4039		G		4037	G
6209						
6211	2514		G		2514	G
6213						
6215	1954		G		1954	N
6217						
6219	1840		G		1840	G
6221	3695		G		3695	G
6223	2904		G		2904	N
6225	1202		G		1202	G
6227	2214		G		2214	G
6229	1581		G		1581	G
6231	3762		G		3762	G
6233	2722		G		2722	G
6235	1027		G		1027	N
6237	1122		G		1122	G
6239	1211		G		1211	G
6241	2921		G		2921	G
6243	2231		G		2231	G
6245	746		G		746	G
6247	1066		G		1066	G
6249	2881		G		2881	G
6251	1310		G		1310	G
6253	1305		G		1305	G
6255	2029		G		2029	G

Station Number	6257	2143		G		2143		N	
	6259	1899		G		1896		R & G	
	6261	1814		G		1814		G	
	6263	1732		G		1732		N	
	6265	2909		G		2909		N	

Station Number	Phase 2								Notes
	In			Notes	Out				
	Date: Jan 10, 2016				Date: Jan 15, 2016				
	Geophone	Time (hh:mm:ss)	Light Color		Geophone	Time (hh:mm:ss)	Light Color		
6001	3738	16:59	G		3738		G		
6003	2811		G		2811		G		
6005	2245	17:19	G		2245		G		
6007	1739	17:31	G		1739		G		
6009	2219	17:38	G		2219		G		
6011	2518	17:47	G		2518		G		
6013	2982	17:54	G		2982		G		
6015									
6017									
6019									
6021									
6023									
6025									
6027									
6029									
6031									
6033									
6035									
6037									
6039									
6041					3599				
6043	462		G		462				
6045					1190				

Page 141 of 234

6047							
6049							
6051							
6053							
6055							
6057							
6059							
6061							
6063							
6065							
6067							
6069							
6071							
6073							
6075							
6077							
6079							
6081							
6083							
6085							
6087							
6089							
6091							
6093							
6095							
6097	2248		G		2248		G
6099	3777		G		3777		G
6101	1822		G		1822		G
6103	47		G		47		G
6105	50		G		50		G
6107	562		G		562		G
6109	163		G		163		G

6111	2065		G		2065		G	
6113	2509		G		597		G	in water
6115			G					
6117	204		G		204		G	
6119	596		G		596		N	
6121	2195		G		2195		G	
6123	2175		G		2175		N	
6125	556		G		556		G	
6127	224		G		224		G	
6129	484		G		484		G	
6131	3881		G		3881		G	
6133	3784		G		3784		N	
6135	2211		G		2211		G	
6137	3975		G		3975		N	
6139	1785		G		1785		N	
6141	1909		G		1909		G	
6143	2242		G		2242		G	
6145	2663		G		2403		N	
6147	3847		G		3867		N	
6149	2467		G		2467		G	
6151	3674		G		3674		G	
6153								
6155	2498		G		1818		G	
6157								
6159	2249		G		2249		G	
6161	1889		G		1889		G	
6163								
6165	1882		G		1882		G	
6167	2146		G		2146		G	
6169								
6171	1553		G		1553		G	
6173	3638		G		3638		G	

6175	1608		G		1608		G	
6177	2846		G				skipped
6179	2180		G		2180		G
6181	4159		G		4159		G
6183	2769		G		2769		G
6185	704		G		704		G
6187	3705		G		3705		N
6189	1726		G		1726		G
6191	1651		G		1615		G
6193							
6195	3628		G		3628		G
6197							
6199	3669		G		3669		G
6201							
6203	2372		G		2372		G
6205							
6207	2018		G		2018		G
6209							
6211	2223		G		2223		N
6213							
6215	2860		G		2860		G
6217							
6219	1784		G		1784		G
6221							
6223	1929		G		1929		G
6225							
6227	1160		G		1160		G
6229							
6231	2753		G		2753		G
6233							
6235	2676		G		2676		G
6237							

Station Number	Geophone	Time (hh:mm:ss)	Light Color	Notes	Geophone	Time (hh:mm:ss)	Light Color	Notes
6239	1789		G		1789		N	
6241	2561		G		2561		N	
6243	4057		G		4057		N	
6245	2859		G		2859		G	
6247	1832		G		1832		N	
6249	2348		G		2348		G	
6251	4036		G		4036		N	
6253	2070		G		2070		G	
6255	2243		G		2243		G	
6257	2109		G		2109		G	
6259	1040		G		1040		N	
6261	1699		G		1699		G	
6263	3822		G		3822		G	
6265	2804		G		2804		G	

Station Number	Phase 3							Notes
	In			Notes	Out			
	Date: Jan 15, 2016				Date:			
	Geophone	Time (hh:mm:ss)	Light Color		Geophone	Time (hh:mm:ss)	Light Color	
6001	4089		G		4089		G	
6003	2240		G		2240		G	
6005	2526		G		2526		G	
6007	865		G		865		G	
6009	3643		G		3643		G	
6011	3636		G		3636		G	
6013	1979		G		1979		G	
6015	2484		G		2484		N	
6017	1312				1312		G	
6019	2133				2133		G	
6021	1986				1986		G	
6023	1120				1120		N	
6025	192				192		G	
6027	1654				1654		G	

Page 145 of 234

6029	2044				2044		G	
6031	3899				3899		G	
6033				none				
6035	2289		G		2289		G	
6037	1884		G		1884		G	
6039	1595		G		1595		G	
6041	2237		G		2237		G	
6043	3009		G		3009		G	
6045	2913		G		2913		G	
6047								
6049								
6051								
6053								
6055								
6057								
6059								
6061								
6063								
6065								
6067								
6069								
6071	2217		G		2217		G	
6073	1034		G		1034		G	
6075	1866		G		1866		G	
6077	1885		G		1885		G	
6079	2212		G		2212		G	
6081	2414		G		2414		G	
6083	1308		G		1308		G	
6085	2472		G		2472		G	
6087	1552		G		1552		G	
6089	3709		G		3709		G	
6091	1560		G		1560		N	

6093	2612		G		2612		G	
6095	3003		G		3003		N	
6097	3646		G		3646		G	
6099	3925		G		3925		G	
6101	1617		G		1617		G	
6103	2843		G		2843		G	
6105	2159		G		2159		G	
6107	2919		G		2919		G	
6109	2401		G		2401		G	
6111	2755		G		2755		N	
6113	3780		G		3780		G	
6115								
6117	2310		G		2310		N	
6119	2585		G		2585		N	
6121	2483		G		2483		G	
6123	2512		G		2512		G	
6125	3775		G		3775		G	
6127	1180		G		1180		G	
6129	3604		G		3604		G	
6131	3692		G		3692		G	
6133	2220		G		2220		G	
6135	3627		G		3627		G	
6137	2731		G		2731		N	
6139	2943		G		2943		G	
6141	1519		G		1519		G	
6143	2830		G		2830		G	
6145	1625		G		1625		G	
6147	3809		G		3809		G	
6149	2045		G		2045		G	
6151	1634		G		1634		G	
6153	4078		G		4078		G	
6155	2233		G		2233		G	

6157	1612		G		1612		G	
6159	4088		G		4088		G	bad connection
6161	1557		G		1557		G	
6163	4035		G		4035		G	
6165	140		G		1940		G	
6167	3834		G		3834		G	
6169	2033		G		2033		G	
6171	2498		G		2498		N	
6173	2261		G		3638		G	left from phase 2
6175	1879		G		1879		G	
6177					2846		N	left from phase 2 and possible bad connection
6179	2695		G		2695		G	
6181	2727		G		2727		G	
6183	3820		G		3830		N	
6185	2004		G		2004		G	
6187	2203		G		2203		N	
6189	1951		G		1951		G	
6191	2907		G		2907		G	
6193	3995		G		3995		G	
6195	3744		G		3744		N	
6197	3743		G		3743		G	
6199	4091		G		4091		G	
6201	4063		G		4063		G	
6203	1594		G		1594		G	
6205	3841		G		3841		G	
6207	3853		G		3853		G	
6209	1932		G		1932		N	
6211	2939		G		2939		N	
6213	685		G		685		N	
6215	975		G		975		N	
6217	3752		G		3752		N	
6219	4066		G		4066		N	

Page 148 of 234

6221	2294		G		2294		G	
6223	1210		G					geophone/texan wasn't picked up
6225	3706		G		3706		G	
6227	1715		G		1715		G	
6229	3635		G		3635		N	
6231	1681		G		1681		G	
6233	2324		G		2324		G	
6235	3814		G		3814		G	
6237	763		G		763		G	
6239	1122		G		1122		G	
6241	1211		G		1211		G	
6243	2231		G		2231		G	
6245	746		G		746		G	
6247	1066		G		1066		G	
6249	2881		G		2881		G	
6251	1310		G		1310		G	
6253	1305		G		1305		G	
6255	2029		G		2029		N	
6257	1899		G		1899		N	
6259	1713		G		1732		N	
6261	2143		G		2143		N	
6263	1814		G		1814		G	
6265	2909		G		2909		N	

Active Source Locations and Times

shotLine	ShotID	Strike		Time (UTC)	Lattitude	Longitude	Elevation (m)
	1	71771	1	2016:016:20:55:00.000	39.955626	-117.804632	1061
	1	71772	2	2016:016:20:55:07.500	39.955626	-117.804632	1061
	1	71773	3	2016:016:20:55:12.600	39.955626	-117.804632	1061
	1	71774	4	2016:016:20:55:17.600	39.955626	-117.804632	1061

Page 149 of 234

1	71775	5	2016:016:20:55:22.600	39.955626	-117.804632	1061
1	61751	2	2016:016:21:12:07.600	39.939476	-117.82312	1051
1	61752	3	2016:016:21:12:12.400	39.939476	-117.82312	1051
1	61753	4	2016:016:21:12:17.200	39.939476	-117.82312	1051
1	61754	5	2016:016:21:12:22.000	39.939476	-117.82312	1051
1	61756	6	2016:016:21:12:26.800	39.939476	-117.82312	1051
1	61051	1	2016:016:21:25:09.600	39.955543	-117.841791	1048
1	61052	2	2016:016:21:25:14.300	39.955543	-117.841791	1048
1	61053	3	2016:016:21:25:19.200	39.955543	-117.841791	1048
1	61054	4	2016:016:21:25:23.800	39.955543	-117.841791	1048
1	61055	5	2016:016:21:25:28.400	39.955543	-117.841791	1048
1	60591	1	2016:016:21:36:05.200	39.965928	-117.853971	1061
1	60592	2	2016:016:21:36:09.800	39.965928	-117.853971	1061
1	60593	3	2016:016:21:36:14.500	39.965928	-117.853971	1061
1	60594	4	2016:016:21:36:19.100	39.965928	-117.853971	1061
1	60595	5	2016:016:21:36:23.900	39.965928	-117.853971	1061
1	60461	1	2016:016:21:43:09.600	39.968779	-117.857211	1064
1	60462	2	2016:016:21:43:14.400	39.968779	-117.857211	1064
1	60463	3	2016:016:21:43:19.000	39.968779	-117.857211	1064
1	60463	4	2016:016:21:43:23.700	39.968779	-117.857211	1064
1	60464	5	2016:016:21:43:28.300	39.968779	-117.857211	1064
1	50831	1	2016:016:21:55:09.600	39.950426	-117.863396	1054
1	50832	2	2016:016:21:55:14.100	39.950426	-117.863396	1054
1	50833	3	2016:016:21:55:18.800	39.950426	-117.863396	1054
1	50834	4	2016:016:21:55:23.500	39.950426	-117.863396	1054
1	50835	5	2016:016:21:55:28.100	39.950426	-117.863396	1054
1	40351	1	2016:016:22:05:09.300	39.949278	-117.901342	1056
1	40352	2	2016:016:22:05:14.000	39.949278	-117.901342	1056
1	40353	3	2016:016:22:05:18.700	39.949278	-117.901342	1056
1	40354	4	2016:016:22:05:23.400	39.949278	-117.901342	1056
1	40355	5	2016:016:22:05:28.100	39.949278	-117.901342	1056
1	30411	1	2016:016:22:24:08.600	39.928449	-117.95305	1080

1	30412	2	2016:016:22:24:13.300	39.928449	-117.95305	1080
1	30413	3	2016:016:22:24:17.900	39.928449	-117.95305	1080
1	30414	4	2016:016:22:24:22.500	39.928449	-117.95305	1080
1	30415	5	2016:016:22:24:27.000	39.928449	-117.95305	1080
1	30001	1	2016:014:19:04:02.800	39.928449	-117.95305	1080
1	30002	2	2016:014:19:04:07.360	39.928449	-117.95305	1080
1	30003	3	2016:014:19:04:11.990	39.928449	-117.95305	1080
1	30004	4	2016:014:19:04:16.710	39.928449	-117.95305	1080
1	30005	5	2016:014:19:04:21.390	39.928449	-117.95305	1080

Appendix 4
Optim Seismic Imaging Report

Technical Report in Support of

Quantifying EGS reservoir complexity with an integrated geophysical approach- improved resolution ambient seismic noise interferometry

Prepared for

Ileana Tibuleac, Ph.D. and Prof. John N. Louie, Ph.D.
University of Nevada, Reno
1664 N. Virginia St., MS 174
Reno, NV, 89557

Purchase Order No: 115GC000044
Subaward No: UNR-15-40
UNR Account No: 1320-114-11KV

By

Optim, Inc.
Bill Honjas, President
200 South Virginia Street
Suite 560
Reno, NV 89501
Current Contact: bill.honjas@optimsoftware.com

March 2017

Appendix 4 Table of Contents

1.0 INTRODUCTION

Optim participated and completed the work described in this report as part of the UNR's DOE funded project entitled, "Quantifying EGS reservoir complexity with an integrated geophysical approach- improved resolution ambient seismic noise interferometry". Tasks involved generating P-wave velocity model from virtual shot gathers generated using seismic interferometry and using the model to perform a pre-stack depth migration in an attempt to image faults and fractures.

The study area is the well-characterized Dixie Valley Geothermal Wellfield in central Nevada (Figure 1, Blackwell et al. 2005). Between November 2015 and January 2016 UNR personnel completed ambient noise data acquisition along five seismic profiles (Figure 2). The deployment used vertical, 4.5 Hz geophones with a nominal spacing of 64 m, except along Line 4 which had sensors spaced more closely at 34 m.

Optim was provided with the virtual shot gathers generated from the recorded ambient noise and an initial P-wave velocity model obtained by analyzing fundamental mode Rayleigh phase velocity information extracted from the noise recordings. These models had a 500-m resolution and served as the initial model for the subsequent velocity analyses.
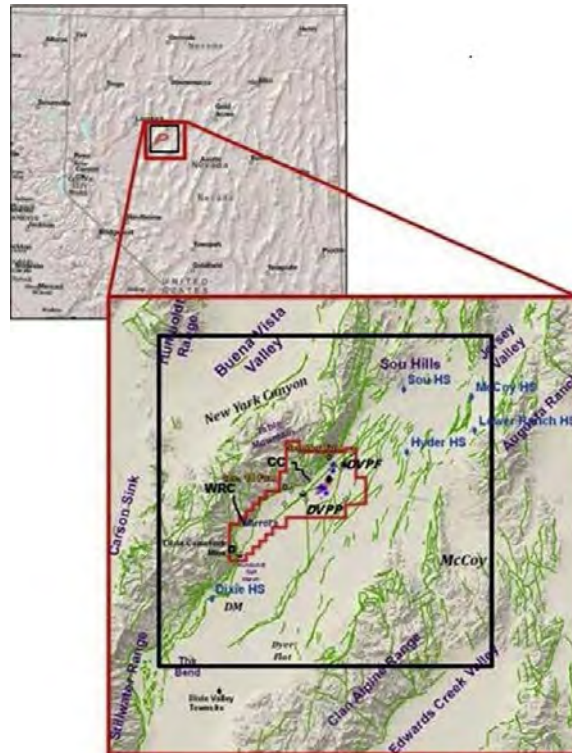
Figure 1: General location map showing the Dixie Valley Geothermal Wellfield (from Blackwell et al., 2005). The seismic profiles analyzed were acquired within this geothermal resource area (Figure 2).

Figure 2: Google Earth images showing orientation of the five seismic profiles along which ambient noise was acquired. The numbers shown are station numbers. They have a spacing of about 64 m for Lines 2, 3, 5 and 6 and 34 m for Line 4.

2.0 DATA PROCESSING

The five seismic profiles varied in length between 1,730 m (Line 2) and 9,010 m (Line 6). The nominal sensor spacing was 68 m for Lines 2, 3, 5 and 6 while it was closer spaced 34 m for Line 4. The virtual short gathers were generated following the methods elaborated in previous studies (e.g. Tibuleac et al., 2010, 2011). The virtual source location was at each sensor location and each shot gather consisted of a trace at every sensor. This resulted in data with good coverage at depth especially for the longer lines 4, 5 and 6. Each seismic trace was 10 second long sampled every 4 millisecond. The total number of traces analyzed was a follows: Line 2: 676; Line 3: 1,521; Line 4: 67,081; Line 5: 17,424; and Line 6: 17,689.

Velocity modeling was done using and coherency optimization approach (Pullammanappallil and Louie, 1997). The flow chart shown in Figure 3 explains the process. The virtual shot gathers along

with the source and receiver information is fed into the algorithm. The modeling starts with the initial, 500 m resolution, velocity models derived from Rayleigh wave dispersion analysis recorded during the deployment. The objective of the optimization is to maximize the semblance or coherency of the reflections contained in the raw data. The resulting velocity models for each profile are shown in Figures 6, 8, 10, 12 and 14.
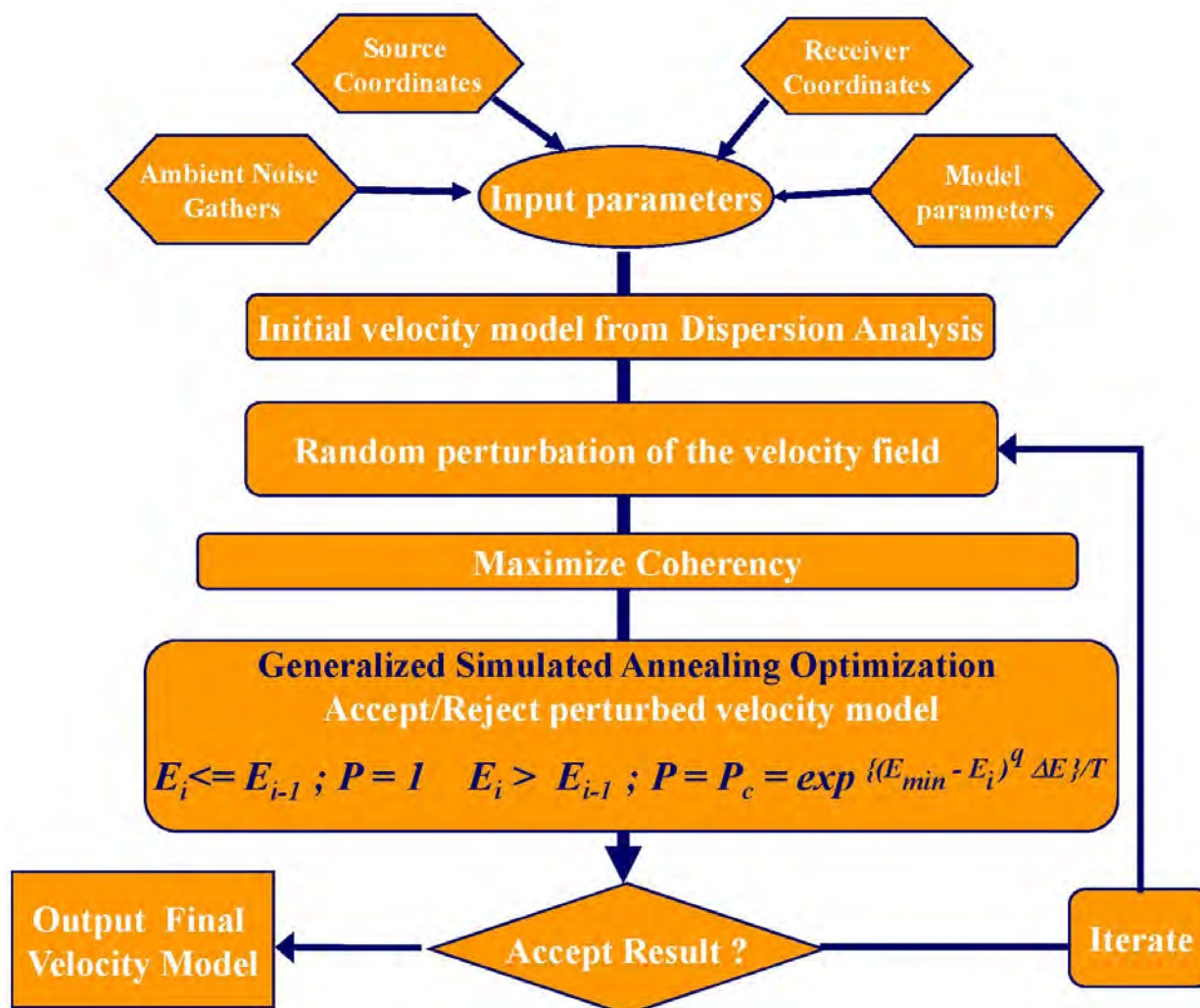
Figure 3: Flow chart showing the velocity optimization process used to derived models used for the pre-stack depth migration

We then use this velocity model in a depth migration to place the reflection amplitudes in their correct position in the subsurface. It is important to note that the accuracy and resolution of the velocity model is a dependent on the acquisition parameters, specifically the geophone spacing. In this case the reliability is +/- 34 m the nominal geophone spacing used for three of the lines and slightly better +/- 17 m for Line 4.

Velocity models obtained by the above process are then used as input for the Kirchhoff pre-stack depth migration algorithm, which is the second processing technique. The pre-stack migration algorithm uses the velocity models for accurate calculation of travel times down to and up from every point within the reflection data volume.

It produces images by summing the value of seismograms within the data volume at discrete points of time, based on travel-time calculations through the velocity model. Given a model that characterizes the velocity structure, the pre-stack migration can produce images from seismic data that has no visible signs of reflective coherency. Because pre-stack migration is free of assumptions about dip of bedding and structure, it will create images that reveal the true-depth location and geometry of permeable features in any orientation (Louie and Qin, 1991).
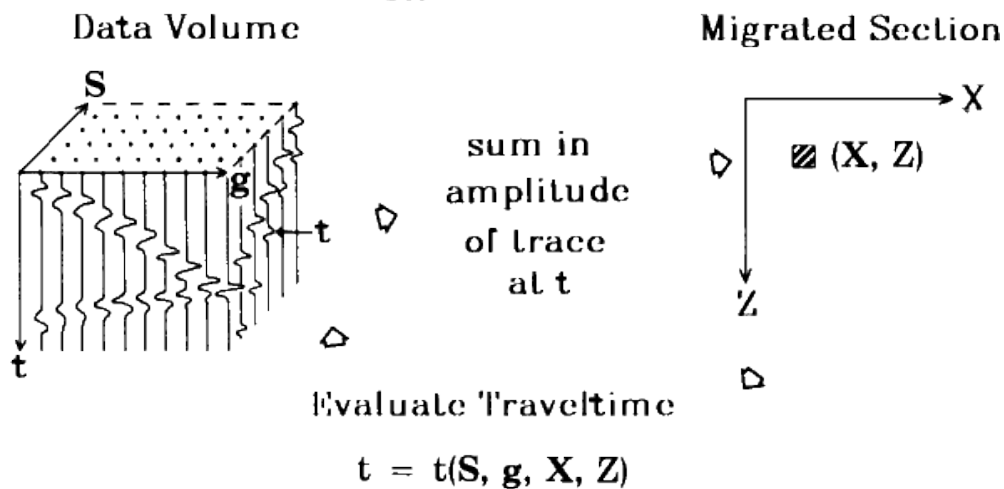
Figure 4: Schematic showing the Kirchhoff pre-stack depth migration (PSDM) process.
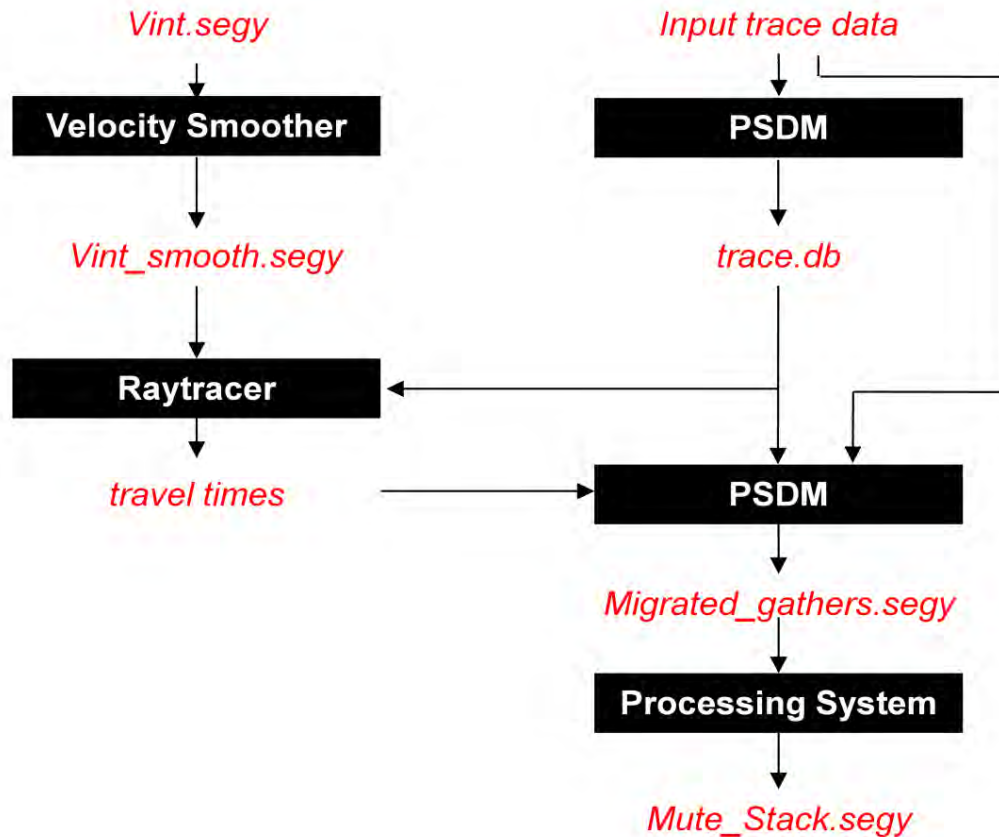
Figure 5: Flow chart showing the PSDM process.

The combined approach utilizing velocity optimization and depth migration objectively evaluates the subsurface velocity structure, which may include significant horizontal velocity gradients, to accurately image permeable features within geothermal fields.

3.0 RESULTS

Figures 6 to 15 show the P-wave velocity model and the final depth migration image produced by the processing steps enumerated in Section 2.0. The velocity models are all plotted with a range that varies from 2,500 m/s to 5,500 m/s with the cooler colors (blue/purple) representing the higher velocities. The depth axes for all models go from 0 to 5,000 m. The top of the models is at an elevation of 1,157 m. The horizontal axis is labeled in CDP (common depth points). In general there are two CDP's between two station or sensor locations. Hence, spacing between the CDP's is half the sensor spacing. Thus it is approximately 34 m for lines 2, 3, 5, and 6 and 17 m for line 4. Appending following this report provides tables listing CDP number and their UTM coordinates and distance along the line. Tables also list the station /sensor number, UTM coordinates and distances for each line as well so the reader can orient themselves with the map shown in Figure

2. The lower CDP's are to the northwest and the higher CDP's extend into the valley to the southeast.

All velocity models show lateral and vertical variations with them being more pronounced along the longer lines 4, 5, and 6. The lack of long offsets for the shorter lines 2 and 3 probably resulting in the models being smooth. In spite of this the models along these lines show the variations associate with basin fill and underlying basalt layers. The maximum depth of resolution varies between 1,000 m for the shorter lines 2 and 3 to about 3,500 m for the longer lines 4, 5, and 6.

The depth migrated images (Figures 7, 9, 11, 13 and 15) show several sub-horizontal reflections with truncations and loss of reflectivity in the lateral directions which we interpret as due to presence of faults or fractures (Section 4.0)
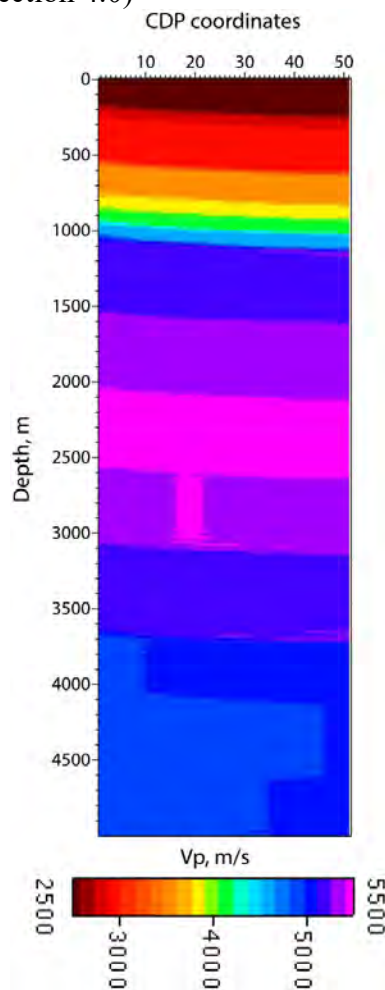
Figure 6: P-wave velocity model derived using velocity optimization along Line 2. The top of the model is at elevation of 1,157 m and the spacing between CDP's is 34 m. Tables following the report provide UTM coordinates for each CDP.
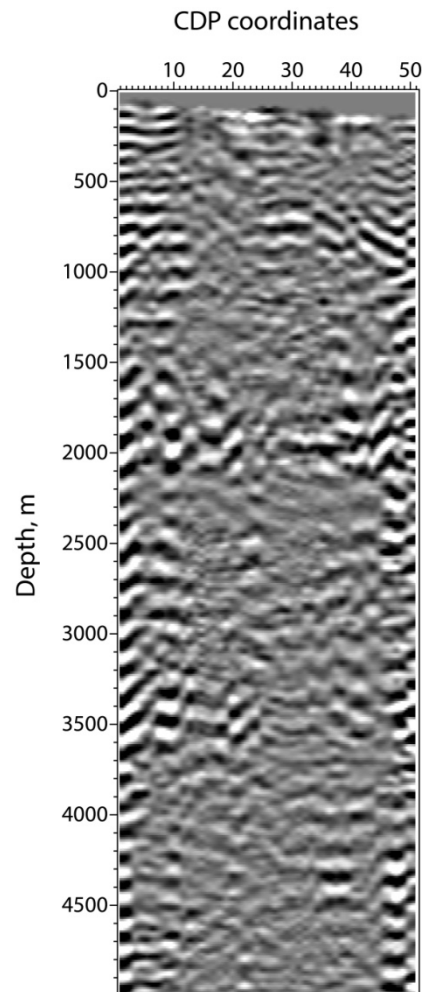
Figure 7: Pre-stack depth migrated image along Line 2 using the velocity model shown in Figure 6. The top of the model is at elevation of 1,157 m and the spacing between CDP's is 34 m. Tables following the report provide UTM coordinates for each CDP.
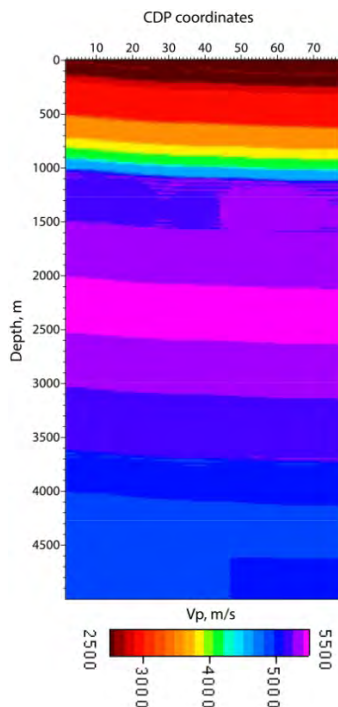
Figure 8: P-wave velocity model derived using velocity optimization along Line 3. The top of the model is at elevation of 1,157 m and the spacing between CDP's is 34 m. Tables following the report provide UTM coordinates for each CDP.
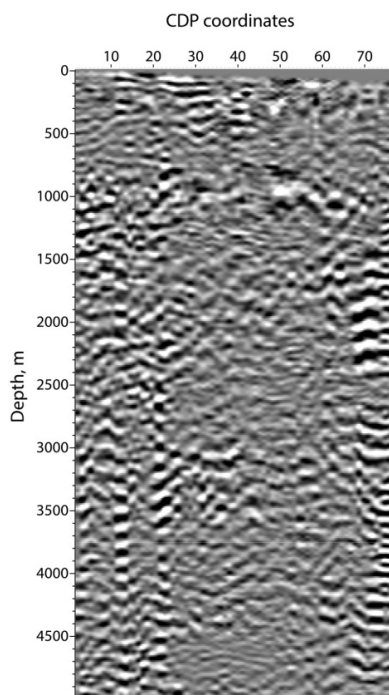
Figure 9: Pre-stack depth migrated image along Line 3 using the velocity model shown in Figure 8. The top of the model is at elevation of 1,157 m and the spacing between CDP's is 34 m. Tables following the report provide UTM coordinates for each CDP.

Page 161 of 234
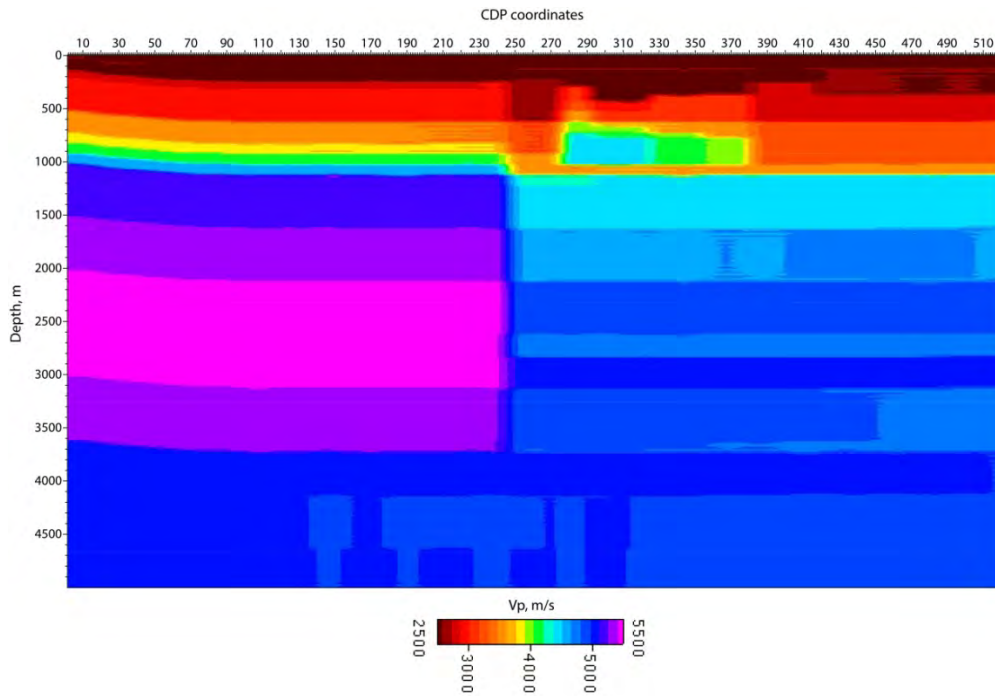
Figure 10: P-wave velocity model derived using velocity optimization along Line 4. The top of the model is at elevation of 1,157 m and the spacing between CDP's is 17 m. Tables following the report provide UTM coordinates for each CDP.
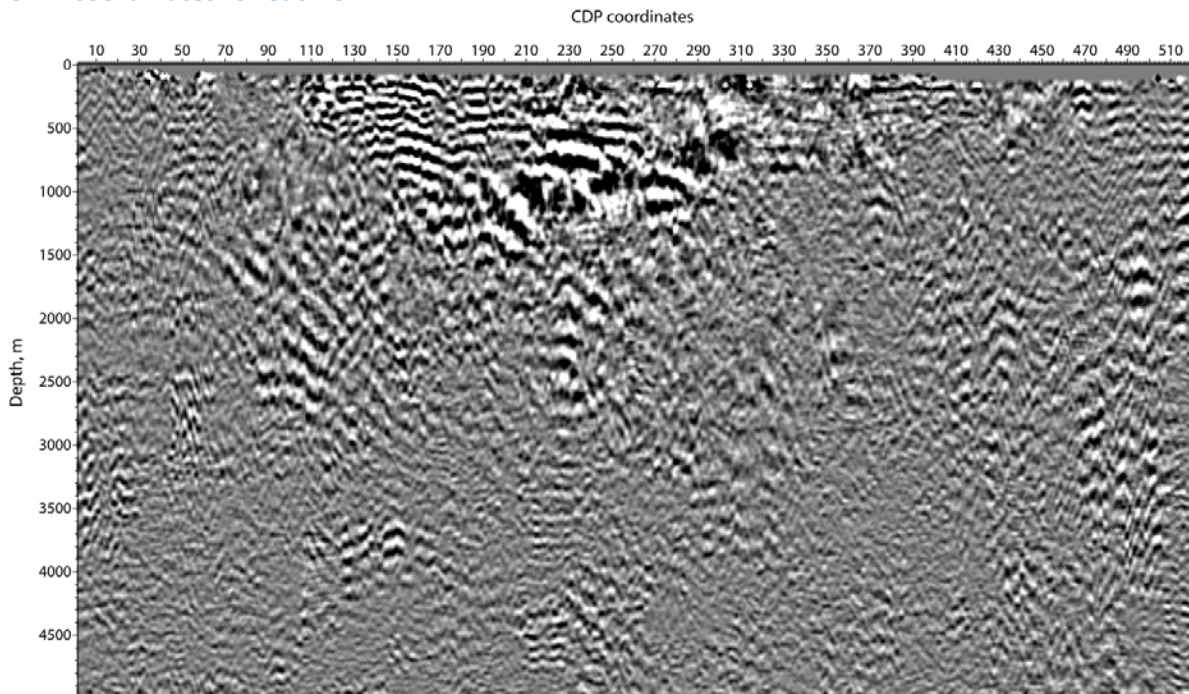
Figure 11: Pre-stack depth migrated image along Line 4 using the velocity model shown in Figure 10. The top of the model is at elevation of 1,157 m and the spacing between CDP's is 17 m. Tables following the report provide UTM coordinates for each CDP.
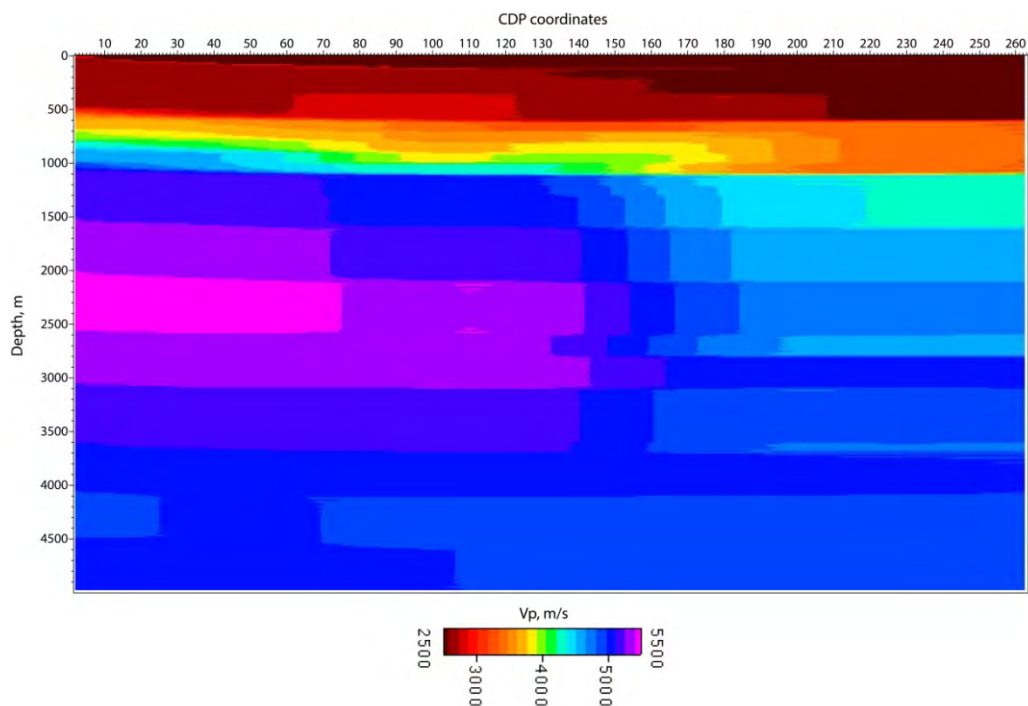
Figure 12: P-wave velocity model derived using velocity optimization along Line 5. The top of the model is at elevation of 1,157 m and the spacing between CDP's is 34 m. Tables following the report provide UTM coordinates for each CDP.
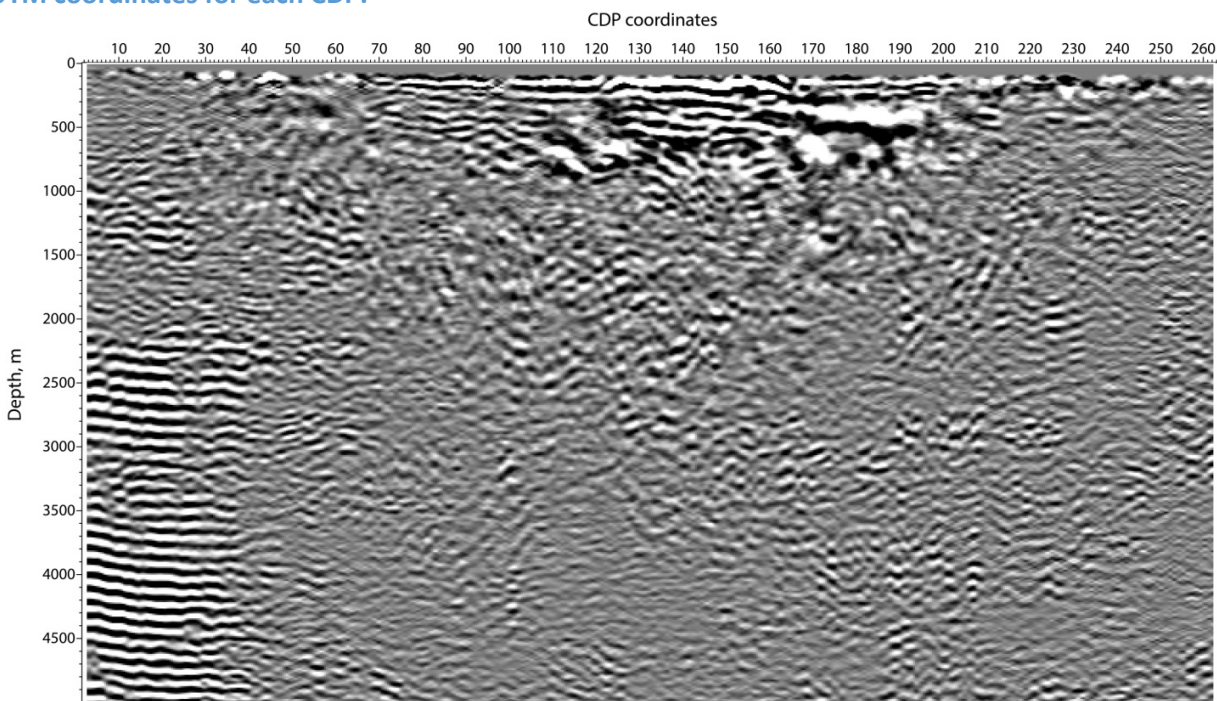
Figure 13: Pre-stack depth migrated image along Line 5 using the velocity model shown in Figure 12. The top of the model is at elevation of 1,157 m and the spacing between CDP's is 34 m. Tables following the report provide UTM coordinates for each CDP.
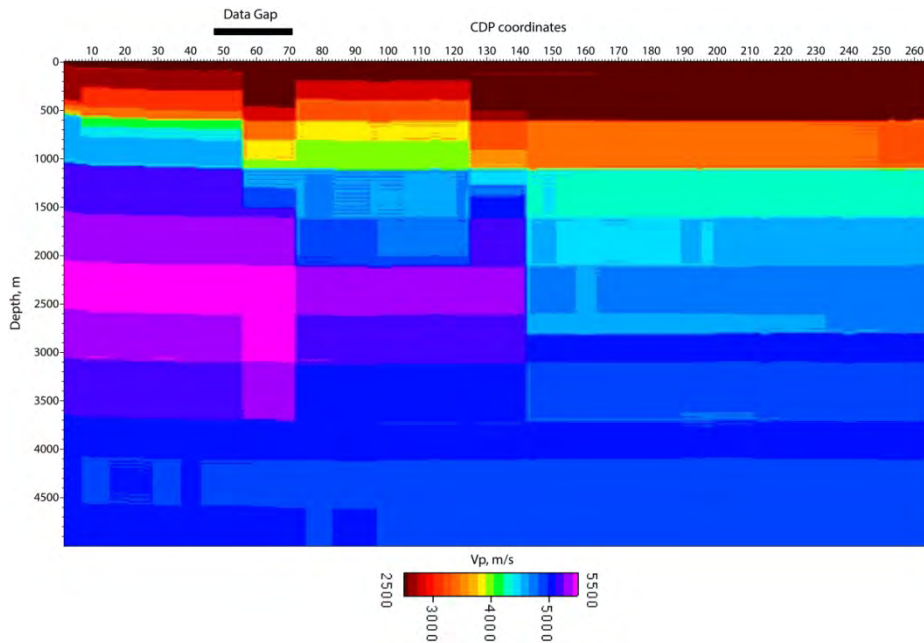
Figure 14: P-wave velocity model derived using velocity optimization along Line 6. The top of the model is at elevation of 1,157 m and the spacing between CDP's is 34 m. Tables following the report provide UTM coordinates for each CDP. The 'Data Gap' indicates the length along which no sensors were deployed due to the presence of obstacles related to the presence of the geothermal power plant.
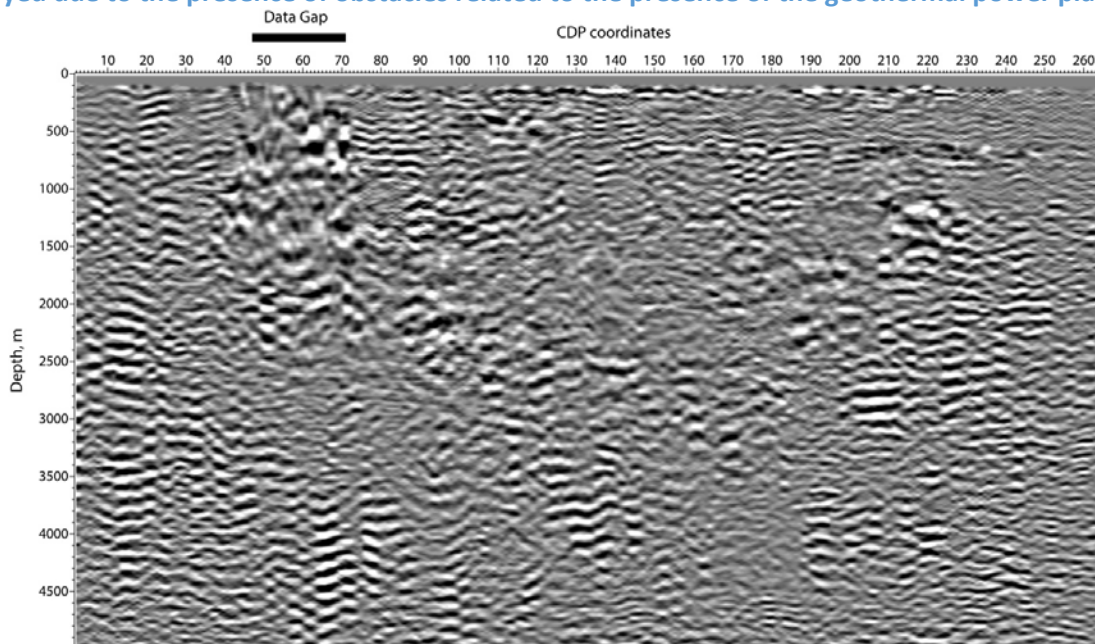
Figure 15: Pre-stack depth migrated image along Line 6 using the velocity model shown in Figure 14. The top of the model is at elevation of 1,157 m and the spacing between CDP's is 34 m. Tables following

the report provide UTM coordinates for each CDP. The 'Data Gap' indicates the length along which no sensors were deployed due to the presence of obstacles related to the presence of the geothermal power plant.

4.0 INTERPRETATION

The interpretations shown in Figures 16 to 25 were based on the pre-stack depth migrated images along each line. The objective was to identify fault and fracture zones which are the primary conduits for movement of thermal fluids. The effective permeability of these zones controls the EGS potential of the wellfield. In keeping with the objective of this project which is to quantify EGS reservoir complexity, identifying the projected location and down dip geometry is critical to assess the success of the integrated innovative approach.

In general the longer lines 4, 5, and 6 reveal features that can be correlated to faulting and fracturing. The quality and amplitude of reflections recorded from the interferometry were not sufficient for direct imaging of dipping faults. The fault plane reflections are hard to reconstruct in the best of conditions and so it is not surprising we failed to recover them from the ambient noise data set. However the pre-stack depth migrations reveal truncations of packet of reflectors and loss of reflectivity that can be interpreted to be caused by faulting and fracturing.

One observation that is valuable for future experiments and commercial application of this approach is the need for closer geophone spacing. Line 4 with a sensor spacing of 34 m yielded well constrained velocity and depth migrated images.

The interpretation made using the pre-stack depth images were then superimposed on the velocity models. In general the following features were identified:

- Southeast dipping Dixie Valley Range Front Fault (orange color in Figures 16 to 25)
- Southeast dipping Piedmont Fault (blue color in Figures 16 to 25)
- Intra basin faults, most likely a northeast-southwest trending strike-slip fault (olive green color in Figures 16 to 25)
- Possible strands of the Northwest dipping Buckbrush Fault System (green color in Figures 16 to 25).

The intra basin features line up with regions that exhibit lateral velocity variations but that is not necessarily true of the interpreted location of the Dixie Valley Range Front fault which lies at the edge of the models.

The error in the location (strike) of the fault is the order of +/- 68 m for all lines except for line 4 where the error decreases to +/- 34 m due to the short sensor spacing. The constraints on the dip are not very high. Since we are unable to identify fault plane reflections dips could be shallow compared to what has been inferred.

Figure 16 and 17 show Line 2 models. Faults are inferred from truncation of reflection bands and significant break or offset in the sub-horizontal layering. The orange line is interpreted as a strand of the Dixie Valley Range Front fault and the blue line is inferred to be the subsurface trace of the Piedmont fault. No significant lateral change occurs across the interpreted faults except at

depths greater than 2,500 m. The short offsets associate with a short line probably results in smoothing of any changes associated with faulting.
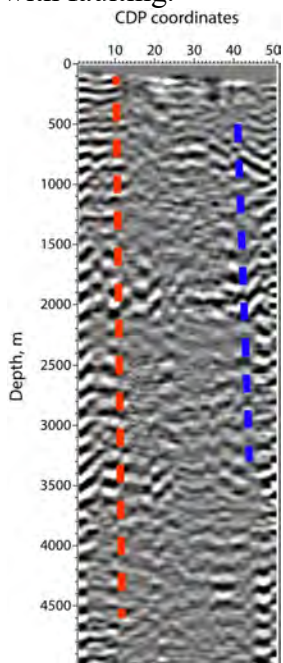
Figure 16: Interpreted pre-stack depth migrated image along Line 2.
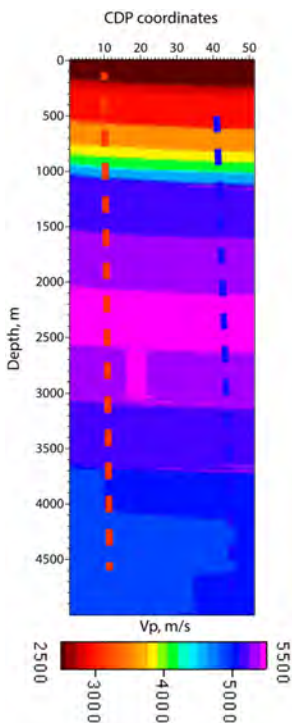
Figure 17: Interpretations made in Figure 16 are superimposed on to the velocity model.

Page 166 of 234

Line 3 interpretations are shown in Figure 18 and 19. Only the possible location of the Piedmont fault (blue) is inferred from the truncations of reflectors in this section. There are some lateral velocity variations in the middle of the section (around CDP 40) that can be inferred as being caused by effect of the Dixie Valley Range Front fault to the northwest (lower CDP) and the Piedmont fault to the south east (higher CDP).
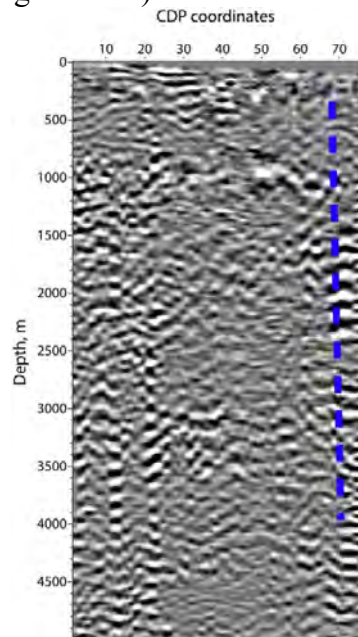
Figure 18: Interpreted pre-stack depth migrated image along Line 3.
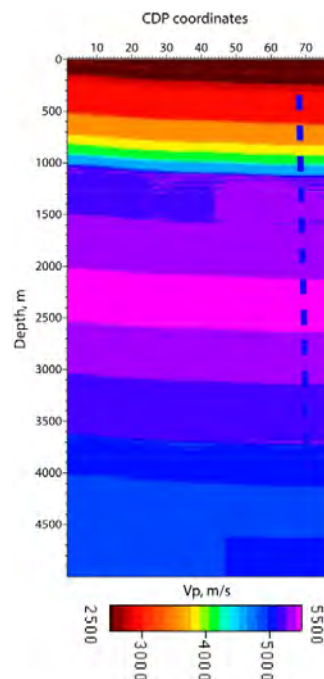
Figure 19: Interpretations made in Figure 18 are superimposed on the velocity model along Line 3.

Figure 20 shows interpreted pre-stack depth migrated image along Line 4. The closer sensor spacing (34 m) provided a better image along this line, in particular the Piedmont fault (blue line). Several features were identified including the Piedmont fault (blue) intra basin features (light blue and olive green) and the northeast dipping strand of the Buckbrush fault (green). The orange line indicates the possible strand of the Dixie Valley Range Front fault inferred mostly sudden loss of reflectivity as one moves to the lower CDP's. The light blue line around CDP 230 indicates the axis of what could be intra-basin strike slip faults This also correlates with a significant lateral velocity change (Figure 21)
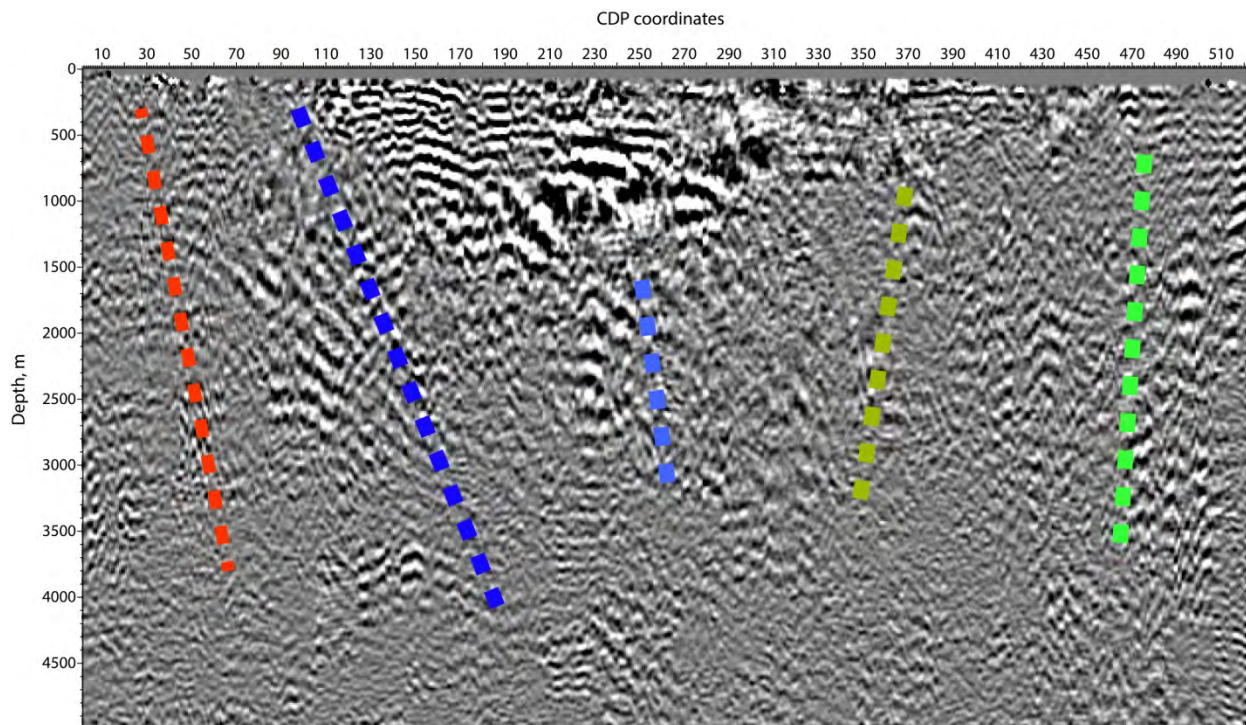
Figure 20: Interpreted pre-stack depth migrated image along Line 4.
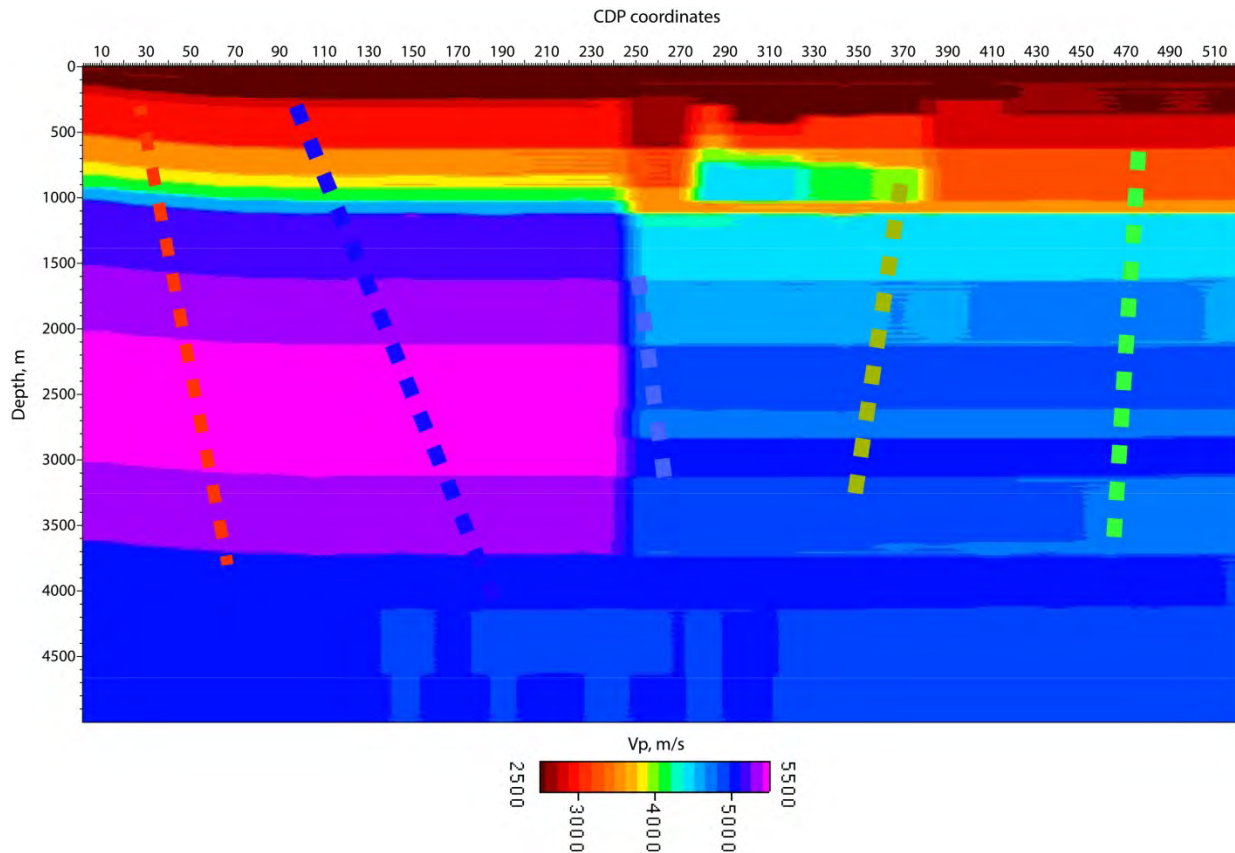
Figure 21: Interpretations from Figure 20 are superimposed on the velocity model along Line 4, The intra-basin strike slip fault in the center of the image manifests as a strong lateral velocity change. Velocity changes are also observed along the northwest dipping faults.

Figures 22 and 23 show interpreted pre-stack depth migrated image along Line 5 and the same interpretations superimposed on the corresponding velocity model. The Dixie Valley Range Front fault (orange line) to the northwest (lower CDP's) seem best inferred from this line. There is a prominent break in the sub-horizontal reflectors along a trend that can be inferred as the subsurface trace of the fault. The pinching out of bright reflections around CDP 60 could be due to the presence of the Piedmont fault (blue). Similarly there is an abrupt truncation of the horizontal band of reflectors at CDP 200 that is interpreted to be caused due to the northeast dipping strand of the Buckbrush Fault System. Velocity changes are associated with both these faults (Figure 23). Between these two faults you have intra-basin features most prominent is the northeast-southwest trending strike-slip fault (olive green line) that manifests as a velocity change around CDP 135 (Figure 23).
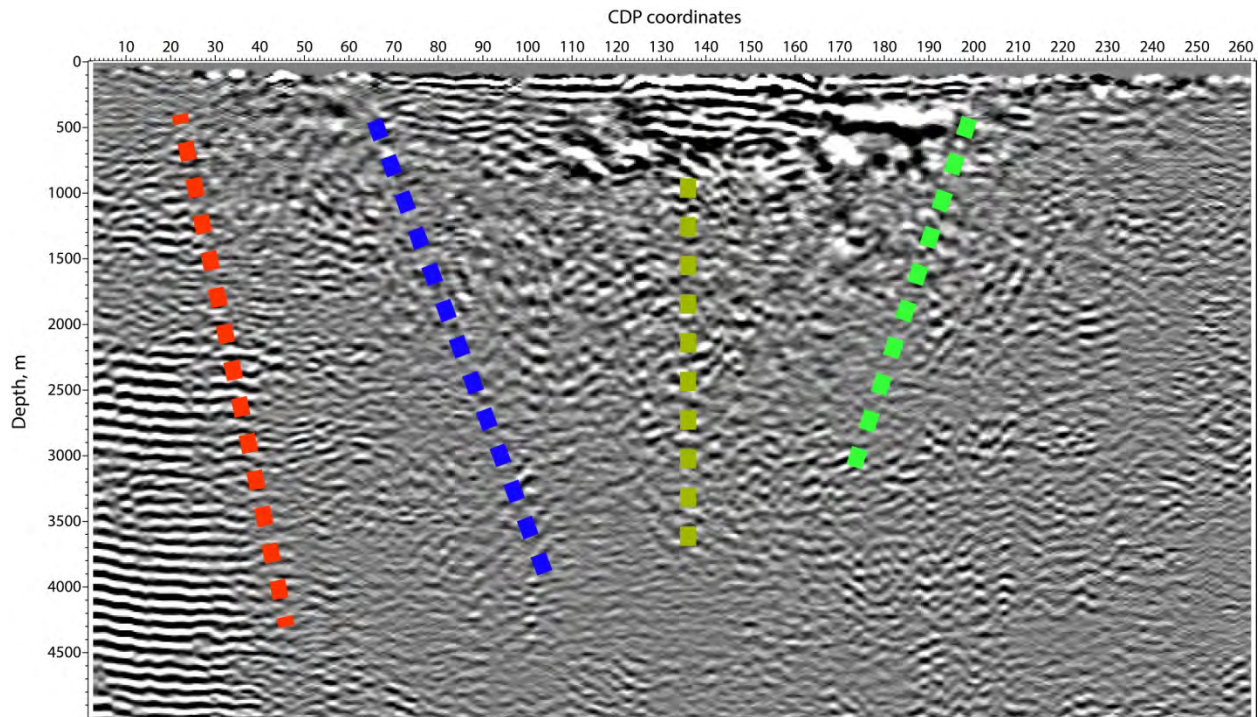
Figure 22: Interpreted pre-stack depth migrated image along Line 5.
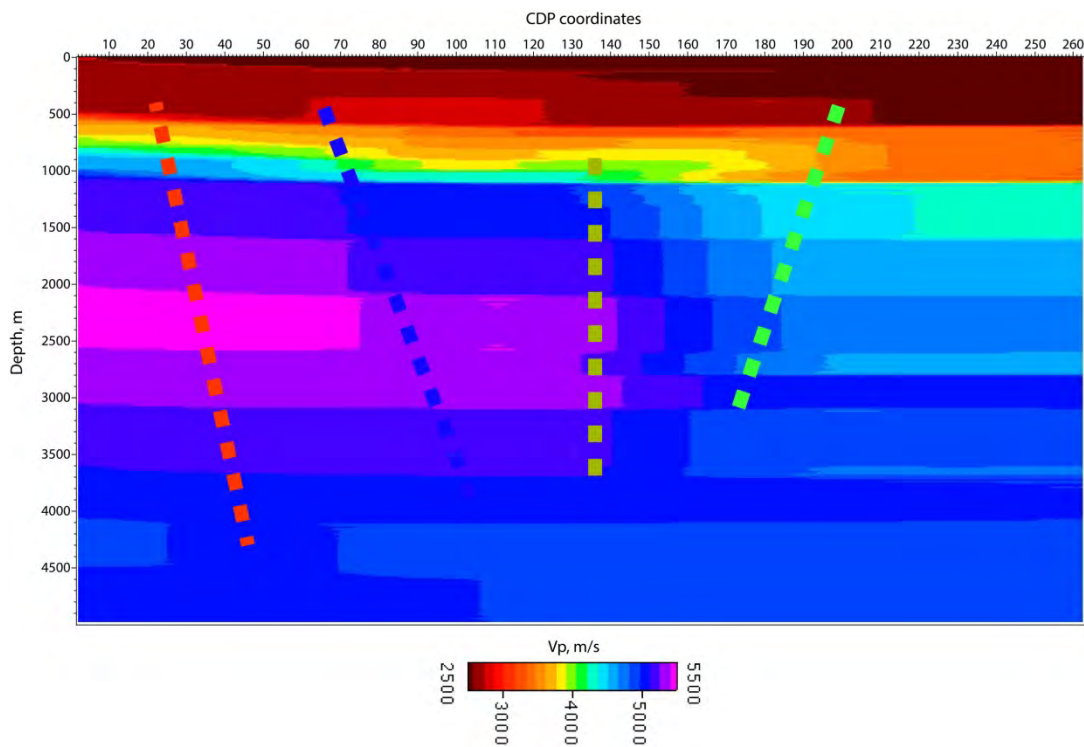
Figure 23: Interpreted faults from Figure 22 superimposed on the velocity model. Lateral velocity changes are associated most of the inferred fault systems.

Page 170 of 234

Interpretations of images obtained along Line 6 are shown in Figures 24 and 25. The data gap between CDP's 47 and 71 is where no sensors were deployed due to presence of the geothermal power plant. As with Line 5, truncation of sub-horizontal reflectors lateral velocity changes allow us to infer the Range Front fault (orange), Piedmont fault (blue) and the Buckbrush fault (green).
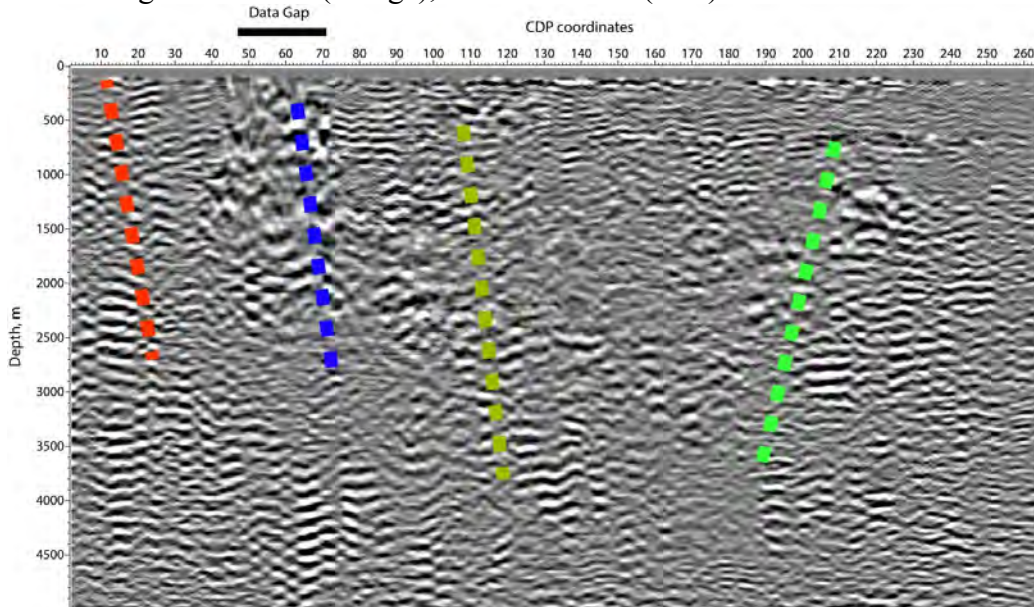
Figure 24: Interpreted pre-stack depth migrated image along Line 6.
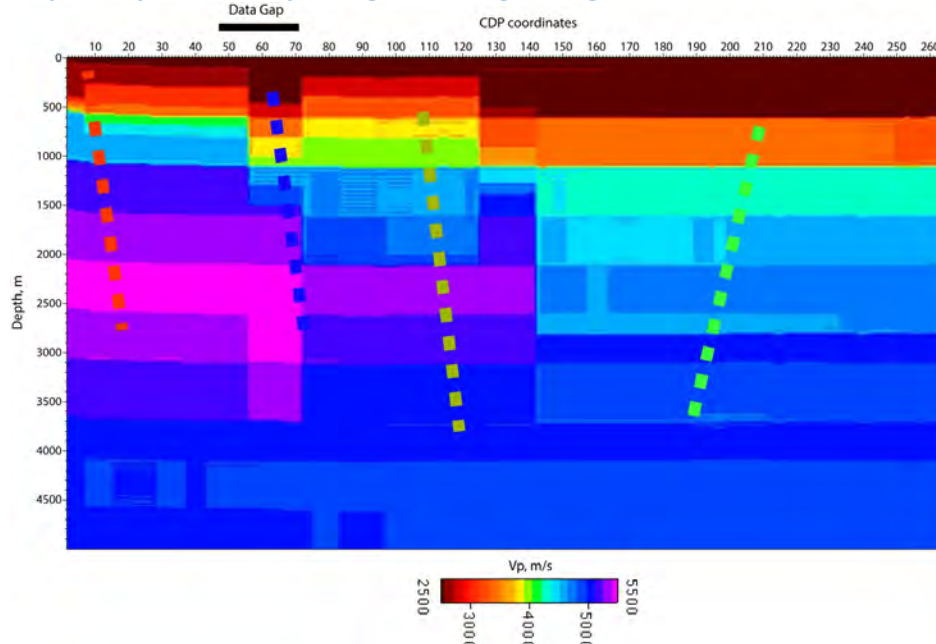
Figure 25: Interpreted faults from Figure 24 superimposed on the velocity model. Lateral velocity changes are associated most of the inferred fault systems.

Figure 26 shows traces of faults plotted on the seismic line map in Google Earth. The colors correlate with the colors in the interpreted images (Figure 16 to 25. Figure 27 shows the same map with the overlay from Iovenitti et al., 2012. The match with the previous imaged features is very consistent.
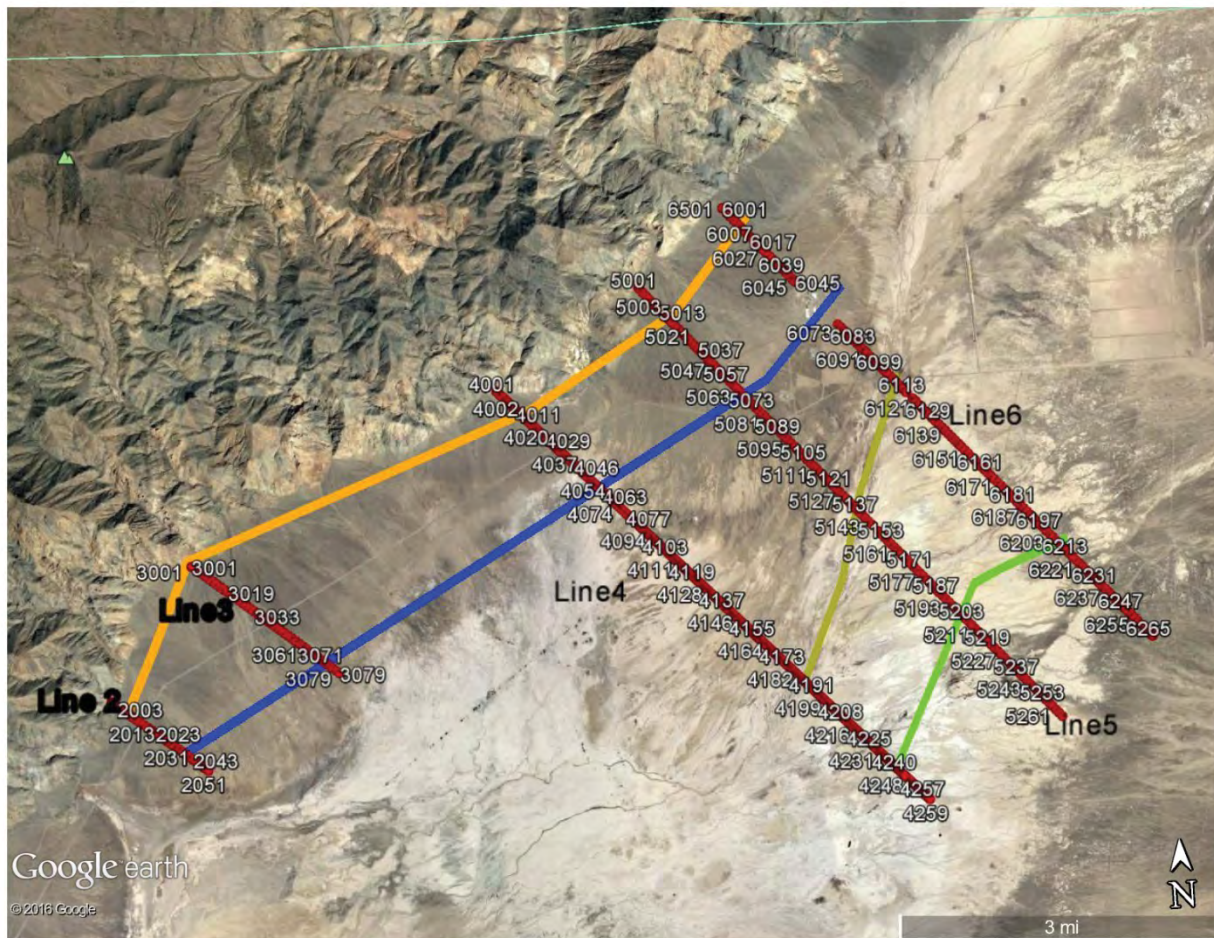
Figure 26: Surface projection of inferred fault traces (Figures 16 to 25) plotted on the seismic line map. The color codes are as follows: Orange – Dixie Valley Range Front Fault, Blue – Piedmont Fault, Olive Green – intra basin strike slip fault, Green – Buckbrush Fault system.
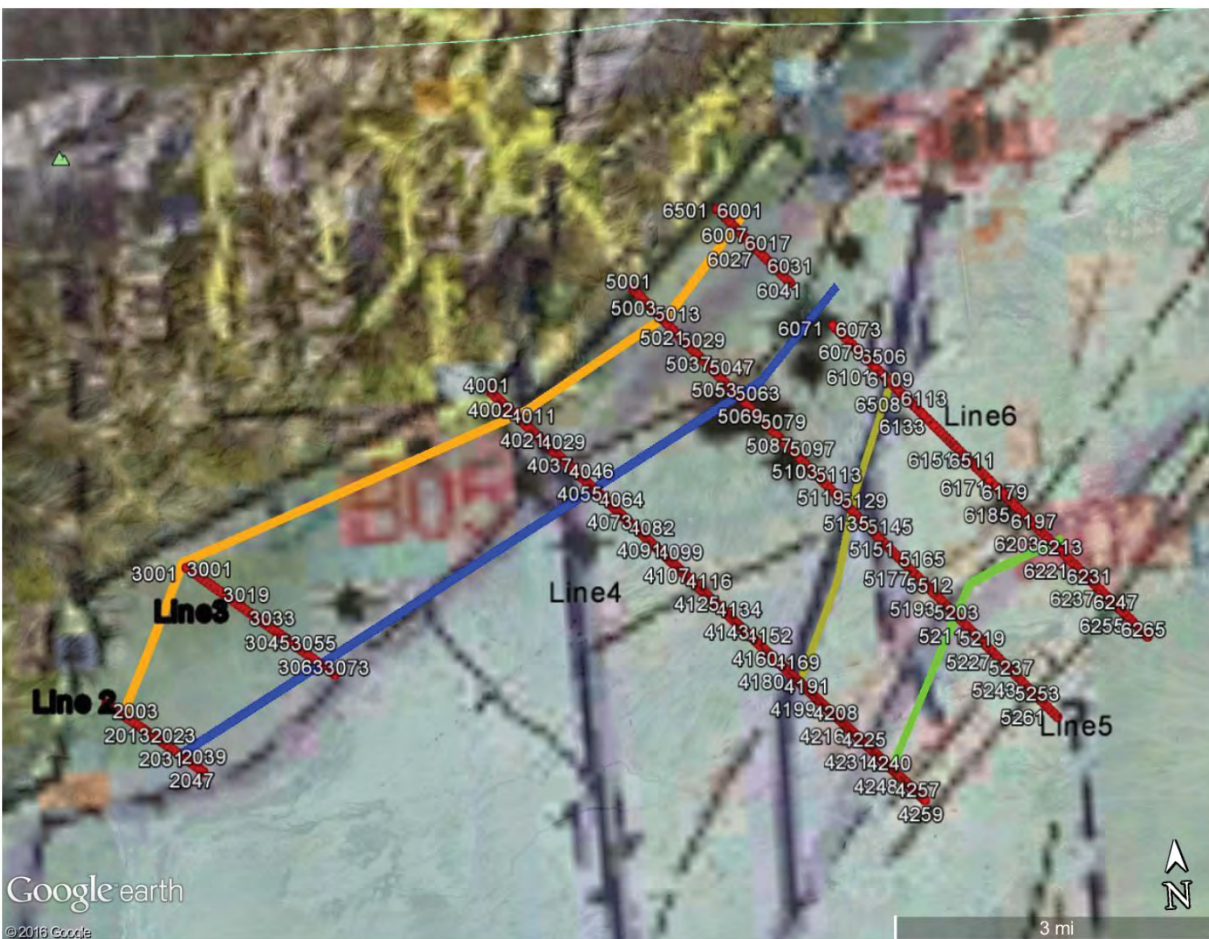
Figure 27: Fault traces with the interpretation map overlay from Iovenitti et al., 2012. There is a strong correlation between the inferred traces from the current processing effort and the previous interpretations.

5.0 ESTIMATING OF STOCHASTIC PARAMETERS

We estimate stochastic parameters from the depth migrated sections shown in Section 3.0. The estimated parameters include correlation length and Hurst number. The objective is to see if these provide additional information that could be used as indicators of permeability within the subsurface and to determine if any of the mapped structures could be good drill target.

We start with the assumption the depth migrated images reveal heterogeneities that represent a von Karman heterogeneity distribution (Carpentier et al., 2010). The process begins by loading the migrated depth section. Once loaded, a normalized 2D autocorrelation function is computed in an N x M window, using user provided window parameters. The windows are shifted by 25 percent of the window height and width to produce an array of overlapping autocorrelation matrices. To aid in selecting the proper window size, the program provides a spectrum analyzer function.

U.S. DEPARTMENT OF **ENERGY** | Energy Efficiency & Renewable Energy

Given the proper window size, the following 2D autocorrelation function is computed.

$$\Phi(l, \tau) = \frac{\sum_{j=1}^{M} \sum_{i=1}^{N} p\left(x_i, z_j\right) p\left(x_{i+l}, z_{j+\tau}\right)}{\sum_{j=1}^{M} \sum_{i=1}^{N} p\left(x_i, z_j\right) \sum_{j=1}^{M} \sum_{i=1}^{N} p\left(x_i, z_j\right)}$$

Where $p(x_i, z_j)$ is a 2D seismic field in common midpoint (CMP) and time, l is the horizontal lag and τ is the vertical or time lag. From the resulting 2D autocorrelation array, $\Phi(l,0)$ is selected as the average lateral autocorrelation function for the entire 2D matrix.

The next step is an optional dip correction to the average lateral autocorrelation functions. This is done by interpolating along a line rotated by an incremental dip angle. The line at the dip angle producing a maximum amount of elongation is selected as representing the dip-corrected autocorrelation function (Hurich, 2003).

The lateral correlation functions are used to estimate the von Karman parameters, correlation length and Hurst number. The misfit function for the parameters is assumed to be:

$$LSQ(a_x, v) = \sum_{i=1}^{N} \left(\Phi(l, 0) - C_i(r)\right)^2$$

where $LSQ(a_x, v)$ is the least-squares misfit as a function of a_x and v. $\Phi_i(l,0)$ are the observed datapoints of $\Phi(l,0)$ and $C_i(r)$ is (from Goff and Jordan, 1988):

$$C(r) = \frac{G_v(r)}{G_v(0)}$$

where $G_v(r) = r^v K_v(r)$, $K_v(r)$ is the second modified Bessel function of fractional order, and r the weighted lateral autocorrelation lag, defined as x/a_x. $G_v(0)$ is defined as:

$$G_v(0) = 2^{v-1} \Gamma(v)$$

and $\Gamma(v)$ is the gamma function.

A grid-search is used to determine the 1D von Karman function that minimizes the misfit function. Once the von Karman parameters are estimated for each lateral autocorrelation window, the

parameters are assigned to the center of the window. This produces a 2D parameter array that can be used as input to a gridding routine to fill in the remainder of the 2D seismic line. The gridding is accomplished with a 2D cubic-spline interpolation with no smoothing.

Figure 28 to 32 show results from the analysis. For all plots the correlation length varies from 0 which are shown blue colors to the maximum of 150 shown in orange colors. Similarly the Hurst number varies from 0 (blue) to 0.2 (orange).
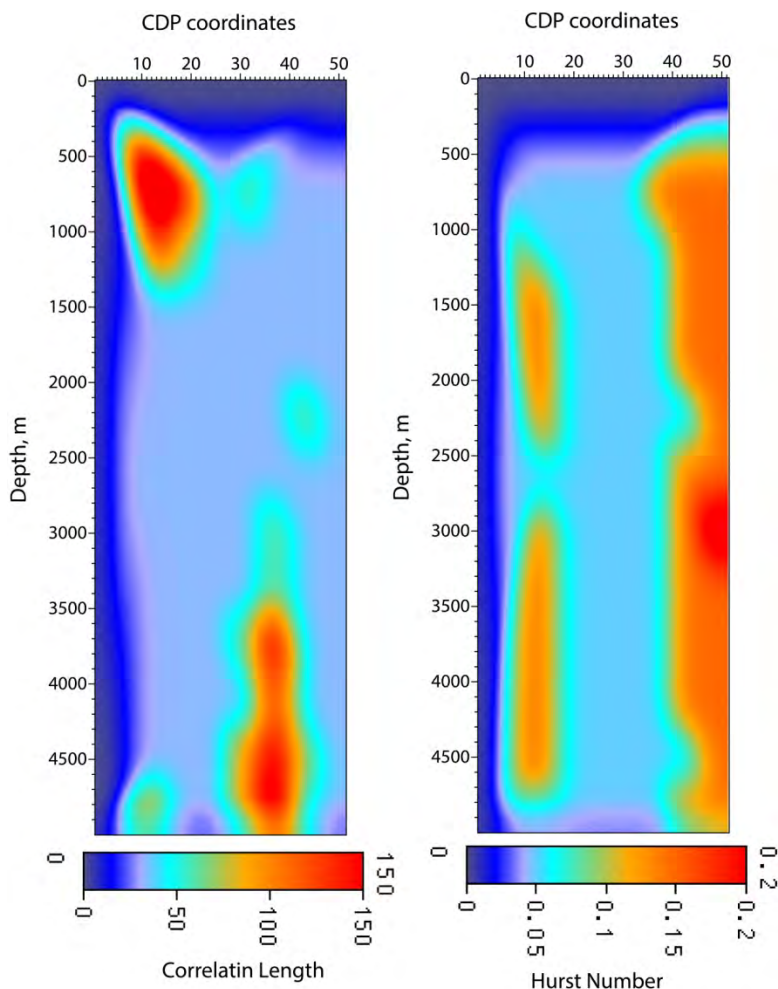
Figure 28: Results from stochastic analysis of Line 2. Figure shows correlation length on the left and Hurst number on the right.
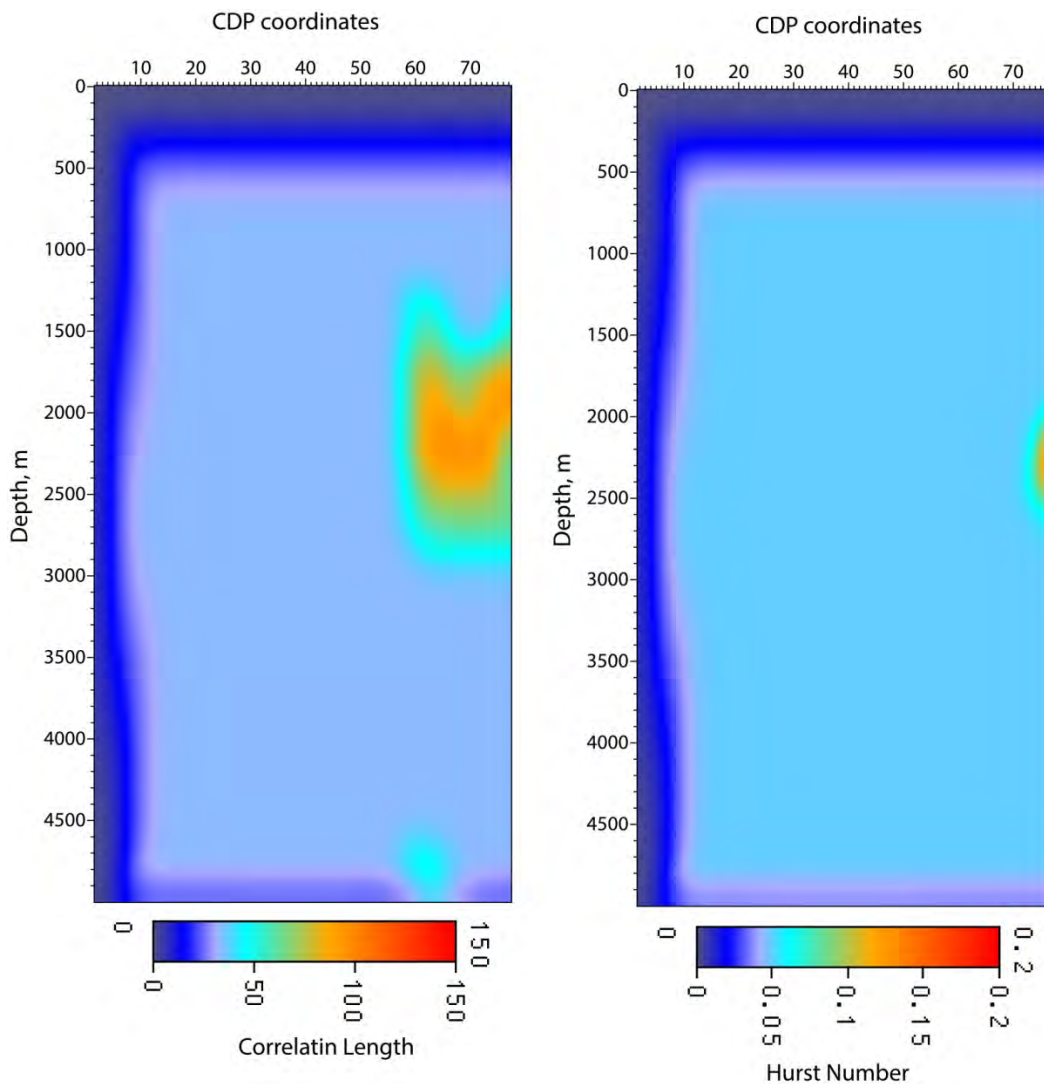
Figure 29: Results from stochastic analysis of Line 3. Figure shows correlation length on the left and Hurst number on the right.
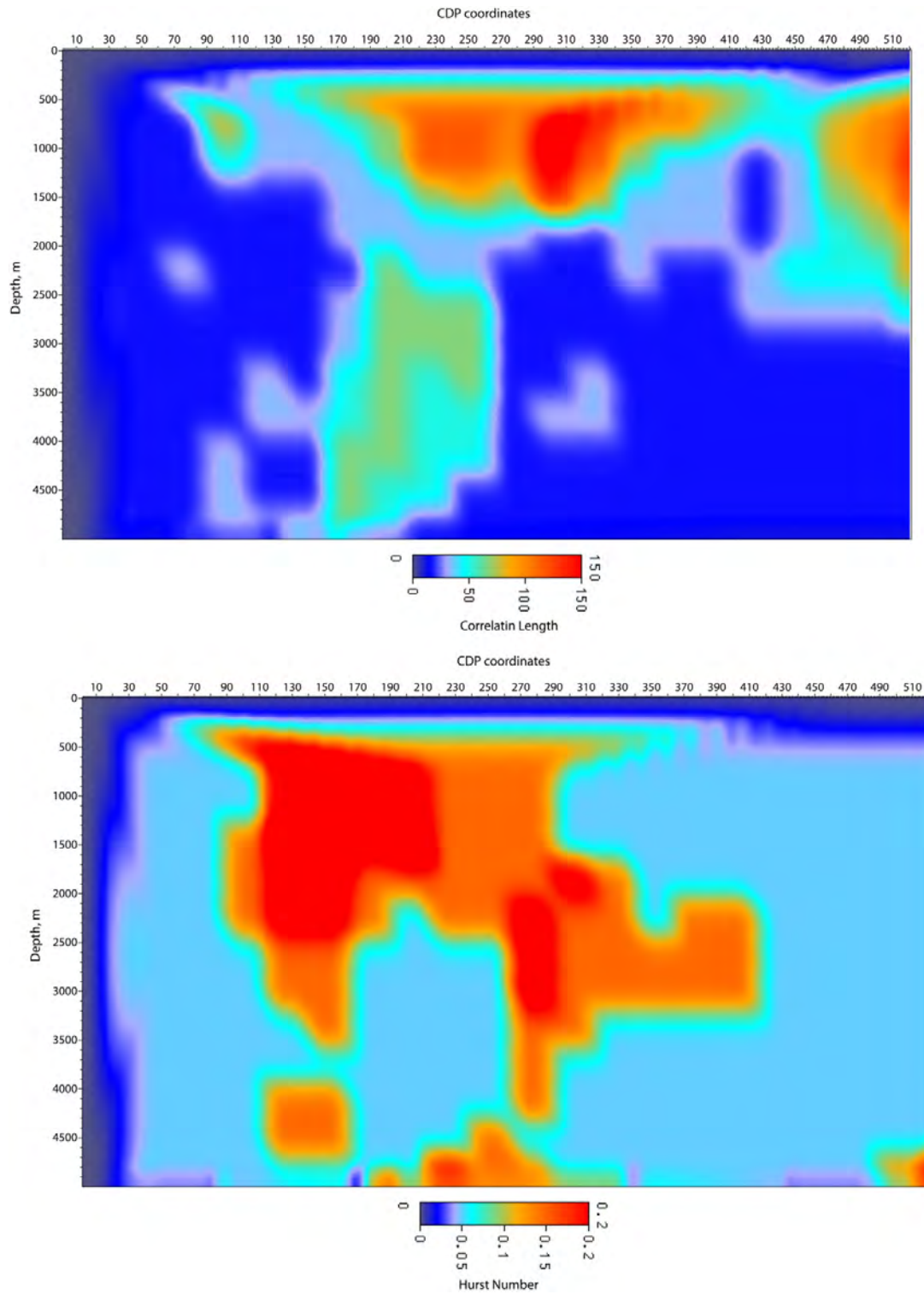
Figure 30: Results from stochastic analysis of Line 4. Figure shows correlation length at the top and Hurst number at the bottom.
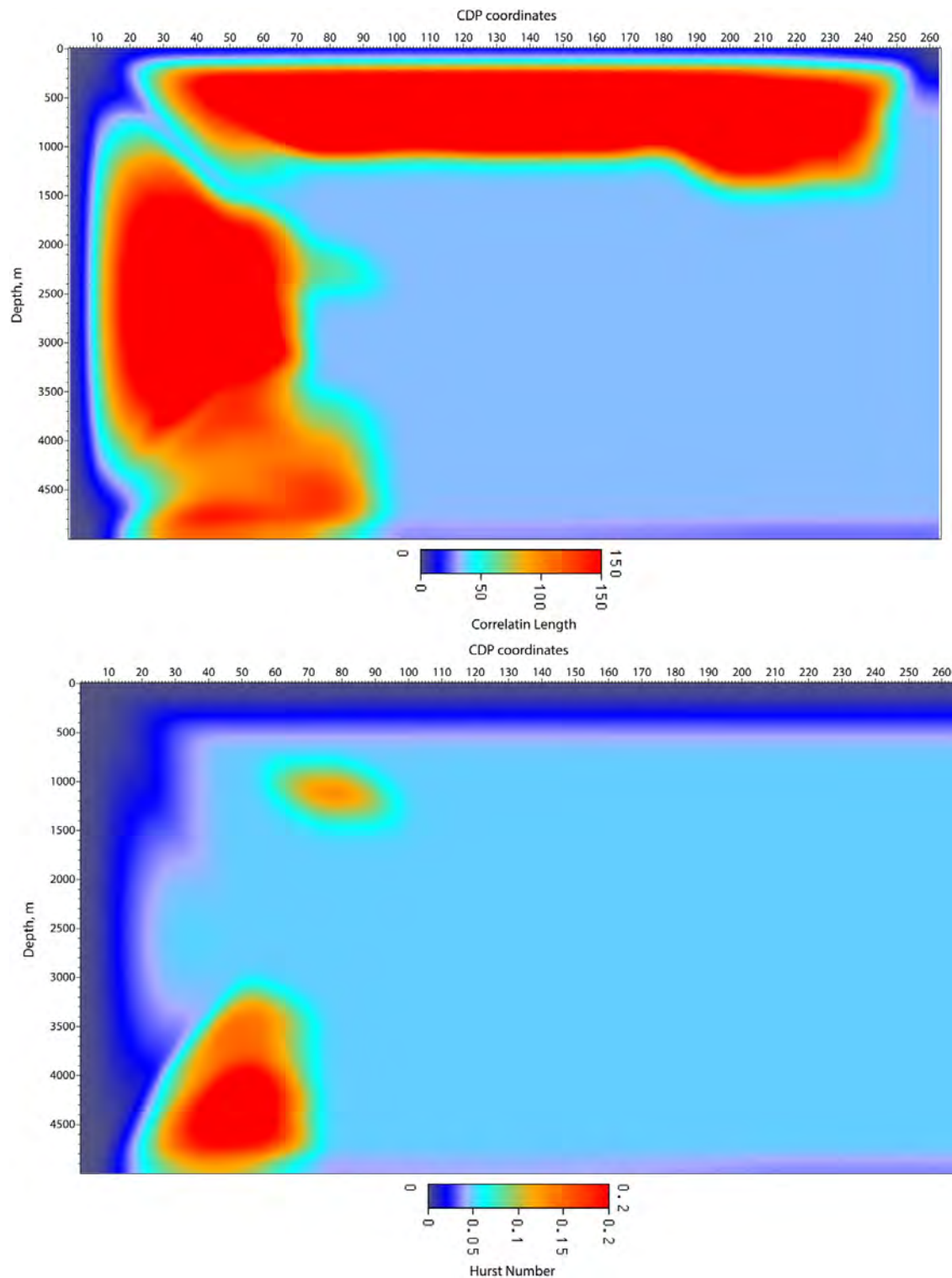
Figure 31: Results from stochastic analysis of Line 5. Figure shows correlation length at the top and Hurst number at the bottom.
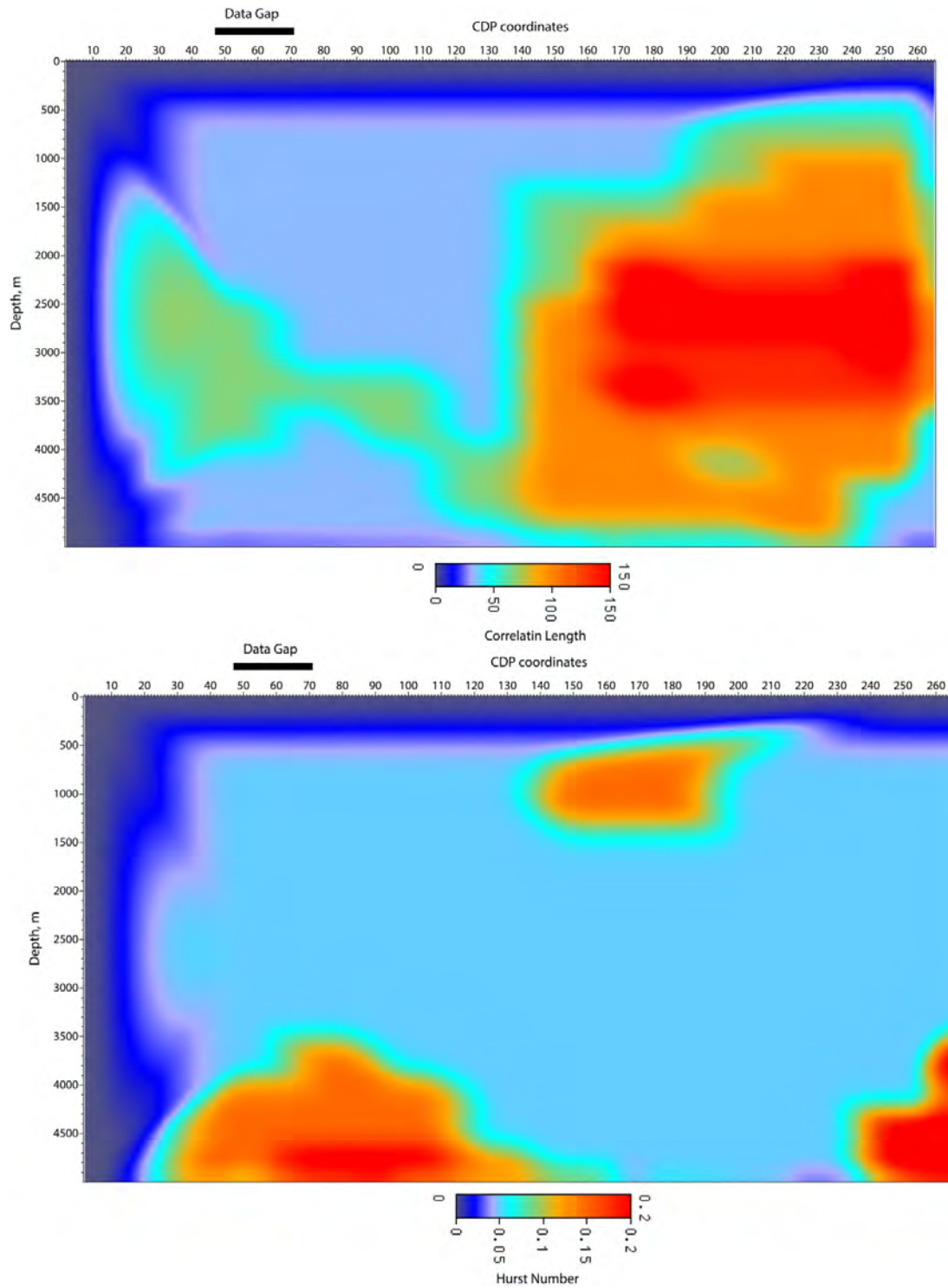
Figure 32: Results from stochastic analysis of Line 6. Figure shows correlation length at the top and Hurst number at the bottom.

Figures 33 to 37 show the stochastic parameters superimposed on the depth migrated sections along with the fault interpretations (see Figures 16, 18, 20, 22 and 24). In general the high correlation length (orange colors) matches the horizontal and sub-horizontal reflectors while the dipping and incoherent reflectors have a low correlation length (blue). The high Hurst numbers (orange) mark areas of broken reflectors that could signify areas of hydrothermal alteration or heavily fractured or faulted zones.
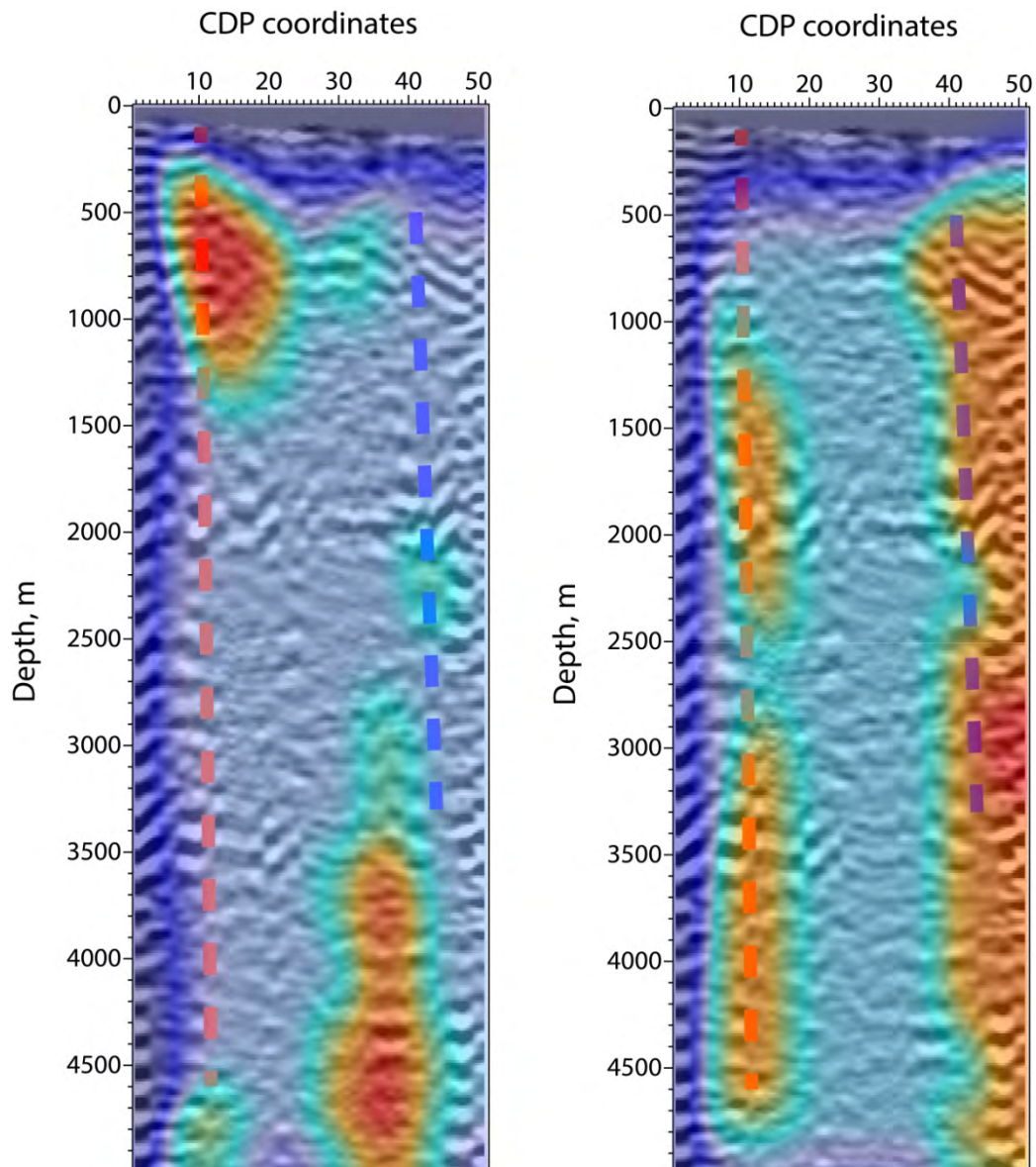
Figure 33: Overlay of correlation length (left) and Hurst number (right) parameters on the depth migrated images along Line 2. Note how the high Hurst number zones (orange) show high degree of correlation with the interpreted Range Front and Piedmont Fault zones. These areas also show smaller correlation lengths (blue).
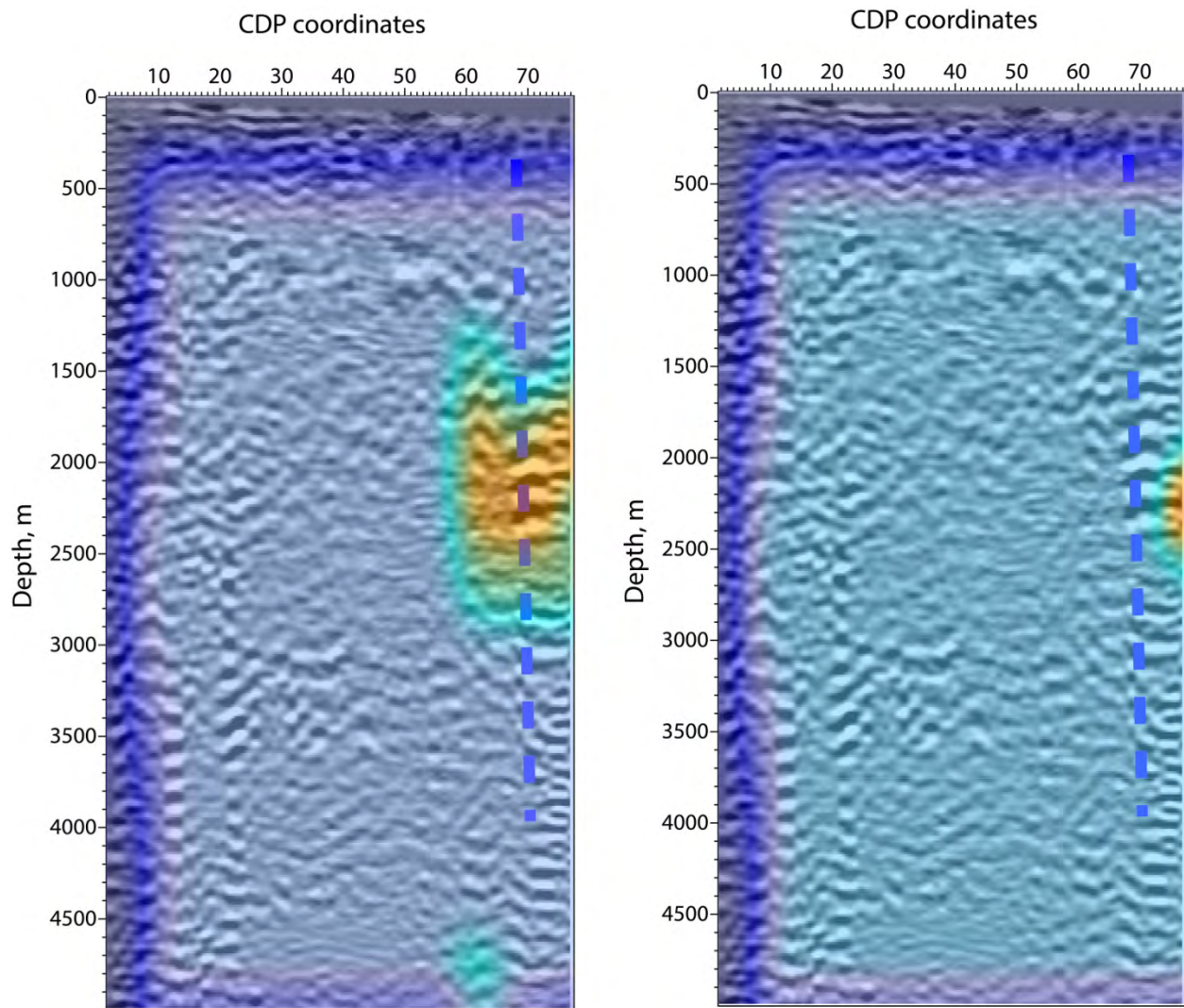
Figure 34: Overlay of correlation length (left) and Hurst number (right) parameters on the depth migrated images along Line 3. Most areas have low values for both stochastic parameters but you do see region of high Hurst number (orange) that correlates to the interpreted Piedmont fault zone.
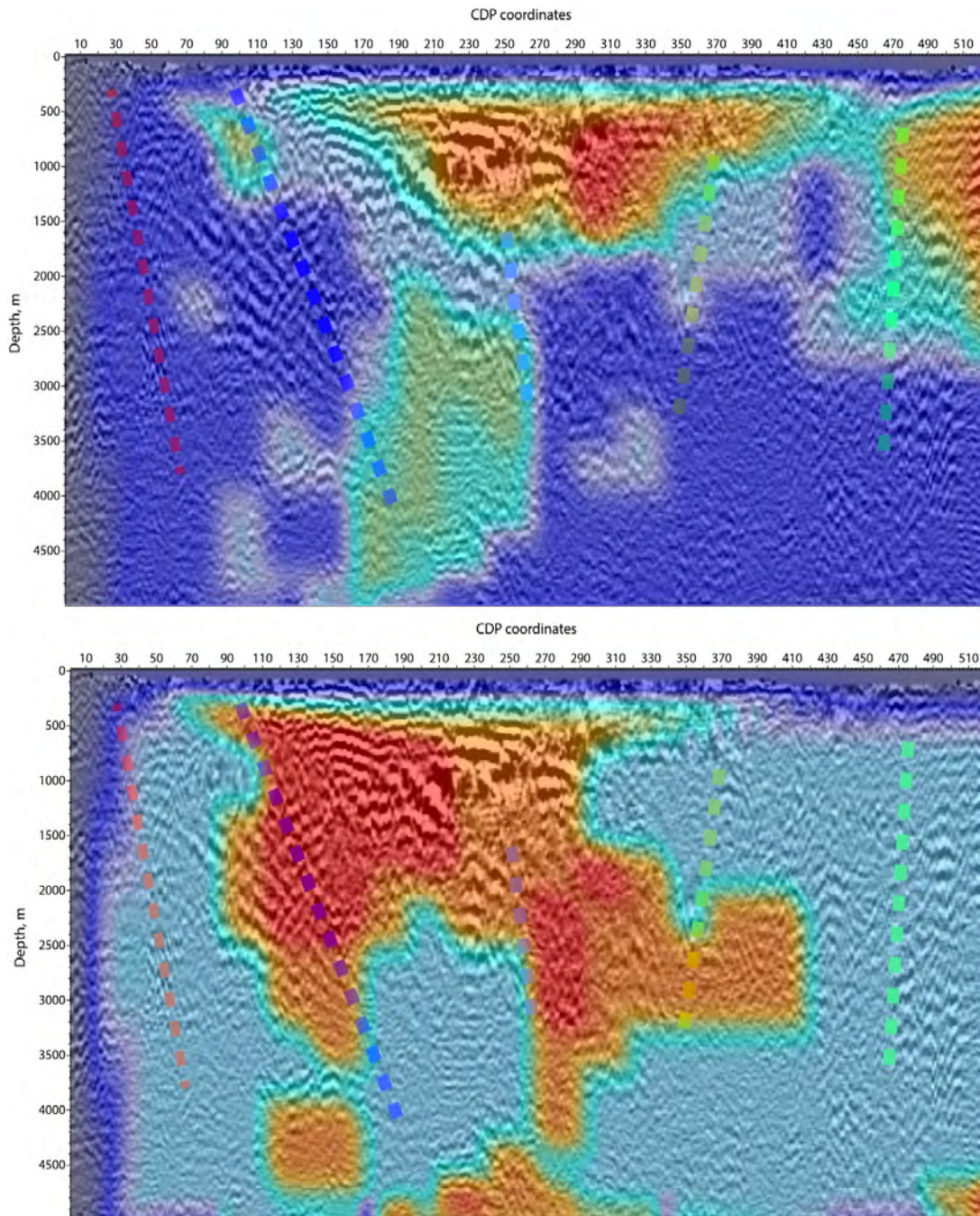
Figure 35: Overlay of correlation length (top) and Hurst number (bottom) parameters on the depth migrated images along Line 4. High Hurst number areas (orange) map out the zone between the interpreted Piedmont fault and the intra basin strike slip faults. The Range Front fault on the west (left hand side) seem to be characterized by small correlation lengths (blue) while the interpreted dipping Buckbrush fault on the right has high correlation lengths associated with it.
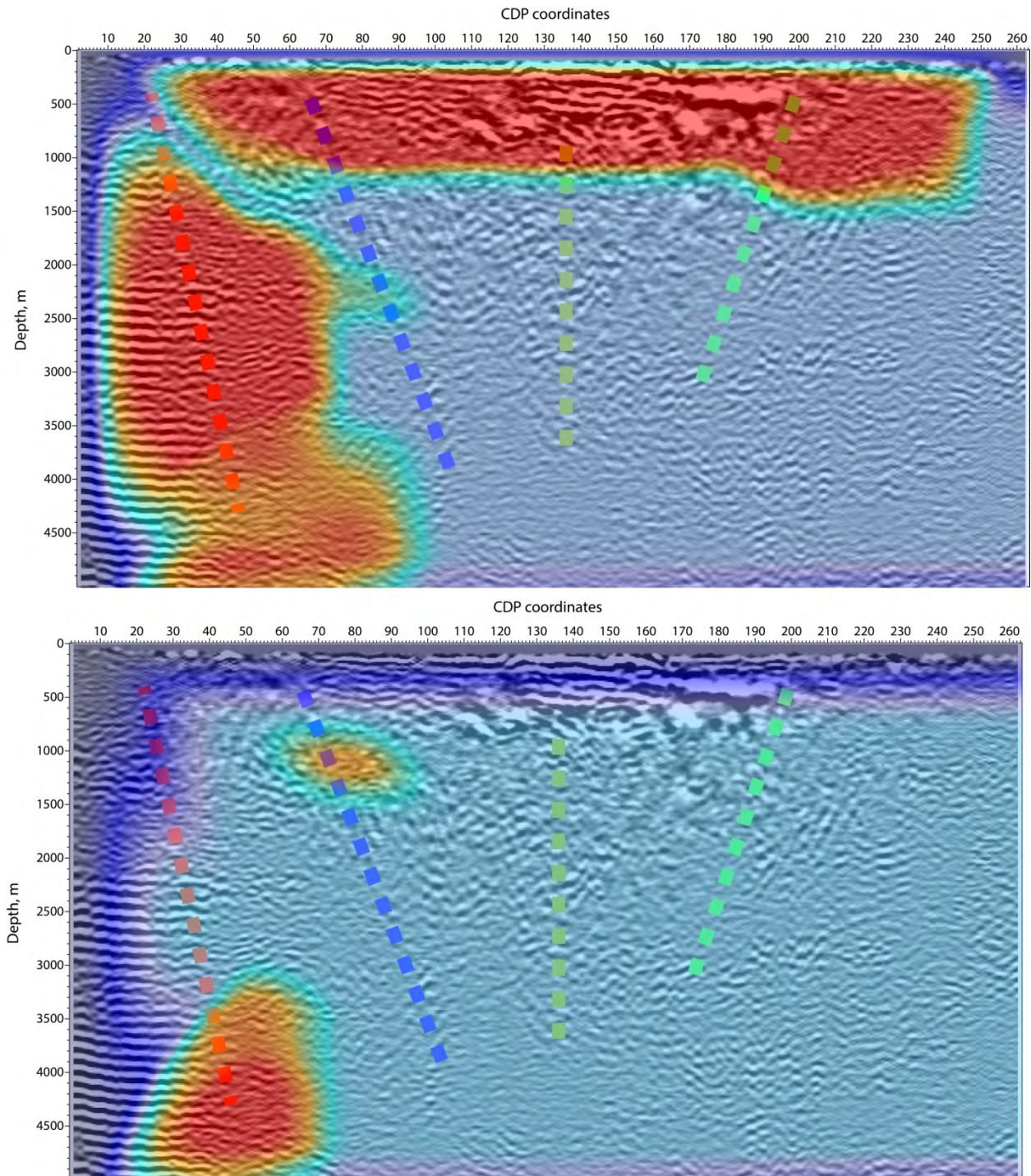
Figure 36: Overlay of correlation length (top) and Hurst number (bottom) parameters on the depth migrated images along Line 5. High Hurst number areas (orange) map out isolated zones along the Range Front fault (left hand side) and Piedmont fault zone. The shallow sub-horizontal reflectors result in a shallow broad high-correlation length zone. The flat reflectors truncating against the Range Front result in another broad zone of high correlation length (orange) zone.
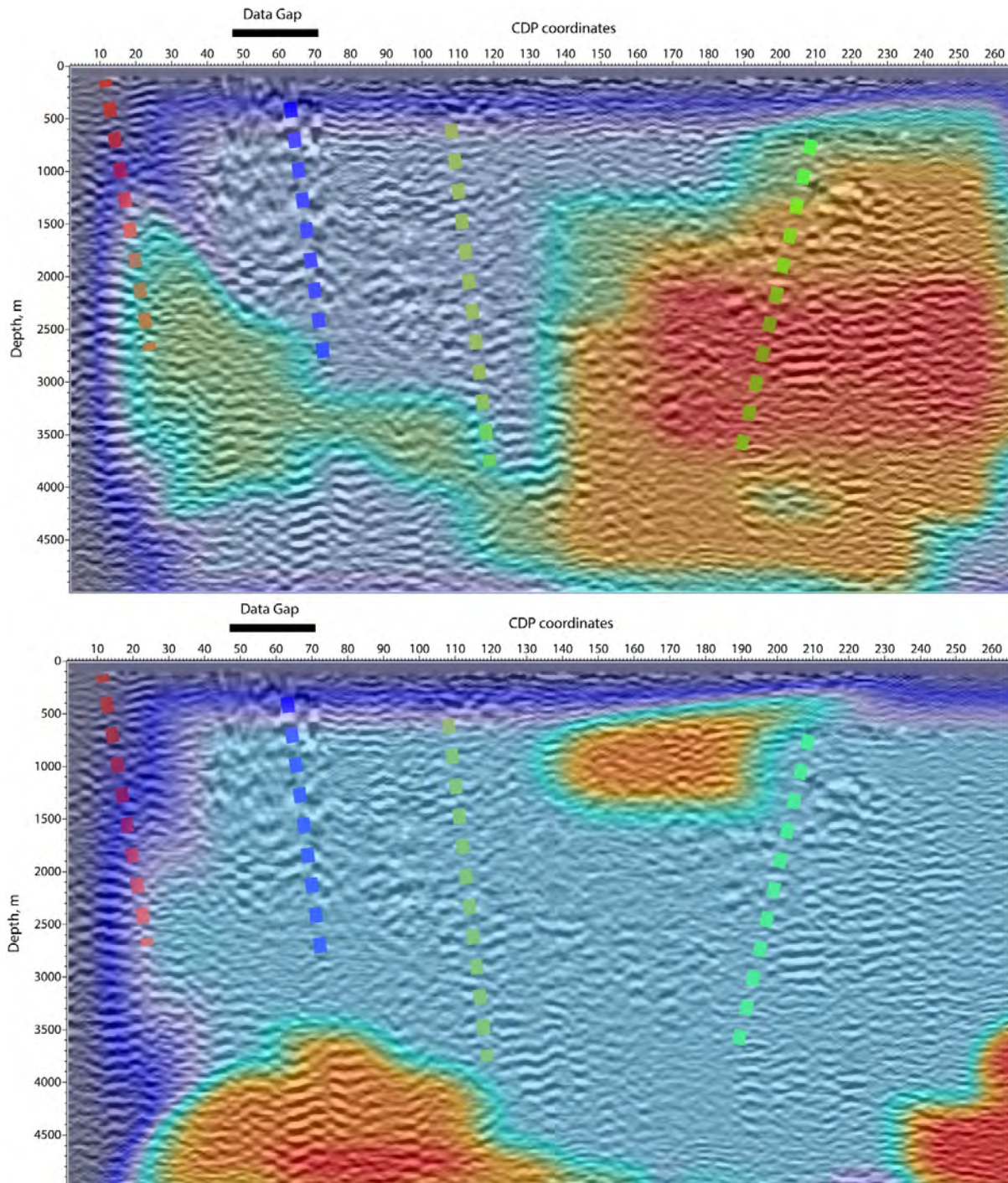
Figure 37: Overlay of correlation length (top) and Hurst number (bottom) parameters on the depth migrated images along Line 6. A zone of high Hurst numbers (orange) extend from the dipping Buckbrush fault zone to the intra basin strike slip faults on this line. Relatively high Hurst numbers are also associated with interpreted Range Front fault zone on the left and to a lesser extent with the Piedmont fault at depth. The correlation lengths do not show any definitive pattern.

In general the Hurst number variations seem to correlate well with the fault zones interpreted from the depth migrations along each line. Along Line 2, the high Hurst number zones (orange) show high degree of correlation with the interpreted Range Front and Piedmont Fault zones. Line 3 shows the least variation but the isolated high Hurst number zone is associated with the Piedmont fault interpretation. Along Line 4, high Hurst number areas map out the zone between the interpreted Piedmont fault and the intra basin strike slip faults. For Line 5, the high Hurst number areas are confined to isolated zones along the Range Front fault and Piedmont fault zone. The zone of high Hurst numbers for Line 6 extends from the Buckbrush fault zone on the east to the intra basin strike slip faults to the west. Relatively high Hurst numbers are also associated with interpreted Range Front fault zone on the and to a lesser extent with the Piedmont fault at depth.

6.0 APPENDIX 4 REFERENCES

Blackwell, D.D., Bergman, S., Goff, F., Kennedy, B.M., McKenna, J.R., Richards, M.C.,Smith, R.P., Waibel, A.F., Wannamaker, P., 2005. Description, synthesis, and interpretation of the thermal regime, geology, geochemistry and geophysics of the Dixie Valley, Nevada Geothermal System. In: Blackwell, D.D., Smith, R.P. (Eds.), unpublished DRAFT DOE Technical Report, 195pp.

Carpentier, S.F.A., K. Roy-Chowdhury, C. A. Hurich, Mapping correlation lengths of lower crustal heterogeneities together with their Bayesian uncertainty estimates, 2010, ftp://ftp.geo.uu.nl/pub/people/kabir/DSS-08/DSS_LITHO.pdf

Goff, J.A. and T.H. Jordan (1988), Stochastic modeling of seafloor-morphology: Inversion of seabeam data for second order statistics. J. Geophys. Res., 93(6):13,589–13,608.

Hurich, C. (2003). *Heterogeneity in the crust and upper mantle: nature, scaling, and seismic properties*, chapter The Nature of Crustal Seismic Heterogeneity: A Case Study From the Grenville Province, pages 299.320. Kluwer Academic Publishers, New York, U.S.A.

Iovenitti, J., Blackwell, D., Sainsbury, J., Tibuleac, I., Waibel, A., Cladouhos, T., Karlin, Isaaks, E., Clyne, M., Ibser, F.H., Callahan, O., Kennedy, B.M., Wannamaker, P., 2012, Towards developing a calibrated EGS Exploration Methodology using the Dixie Valley Geothermal System, Nevada. In: Proceedings 37th Eighth Workshop on Geothermal Reservoir Engineering Stanford University, Stanford, California, January 30–February 1, SGP-TR-194, 15pp.

Louie, J.N., and Qin, J., 1991, Subsurface imaging of the Garlock fault, Cantil Valley, California: Journal of Geophysical Research, B., Solid Earth and Planets, v. 96, p. 14,461-14,479.

Pullammanappallil, S. K., and J. N. Louie, 1997, A combined first-arrival travel time-reflection coherency optimization approach to velocity estimation: Geophysical Research Letters, 24, 511-514.

Tibuleac, I.M., Pullammanappallil, S., von Seggern, D. H., Pancha, A., and Louie, J. N., 2010, Retrieval of Earth's reflection response from ambient seismic noise - a Nevada experiment, American Geophysical Union Fall Meeting, abstract #S33A-2071.

Tibuleac, I.M., von Seggern, D.H., Anderson, J.G., and Louie, J.N., 2011, Computing Green's Functions from Ambient Noise Recorded by Narrow-Band Seismometers, Accelerometers, and Analog Seismometers, doi: 10.1785/gssrl.82.5.661 Seismological Research Letters, September/October, v. 82, no. 5, p. 661-675.

Unruh, J.R., Monastero, F.C. and Pullammanappallil, S.K., 2008, The Nascent Coso Metamorphic Core Complex, East-Central California: Brittle Upper Plate Structure Revealed by Reflection Seismic Data - International Geology Review, 50, 1–25

TABLE 1: LINE 2 CDP LOCATIONS WITH INFERRED FAULT LOCATIONS HIGHLIGHTED IN YELLOW

CDP #	Easting, m	Northing, m	Elevation, m	Distance from NW, m
1	416189	4419218	1123.66	33.53
2	416215	4419196	1113.17	67.58
3	416241	4419174	1104.24	101.64
4	416267	4419152	1100.74	135.70
5	416293	4419130	1097.69	169.76
6	416318	4419108	1096.36	203.06
7	416344	4419086	1094.98	237.12
8	416370	4419064	1091.94	271.18
9	416396	4419042	1088.91	305.24
10	416422	4419020	1085.9	339.30 (DVRF)
11	416448	4418998	1082.97	373.36
12	416474	4418976	1081.97	407.41
13	416500	4418954	1081.02	441.47
14	416526	4418932	1081.52	475.53
15	416551	4418910	1081.98	508.83
16	416577	4418888	1080.98	542.89
17	416603	4418866	1079.86	576.95
18	416629	4418843	1071.6	611.66
19	416655	4418821	1063.93	645.72
20	416681	4418799	1062.93	679.78
21	416707	4418777	1062.16	713.84
22	416733	4418755	1064.67	747.90
23	416759	4418733	1066.74	781.96
24	416785	4418711	1063.06	816.02
25	416810	4418689	1059.47	849.32
26	416836	4418667	1057.69	883.38
27	416862	4418645	1056.19	917.44
28	416888	4418623	1057.32	951.50
29	416914	4418601	1058.82	985.55
30	416940	4418579	1056.35	1019.61
31	416966	4418557	1053.35	1053.67
32	416992	4418535	1049.87	1087.73
33	417018	4418513	1046.32	1121.79
34	417043	4418491	1046	1155.09

35	417069	4418469	1046	1189.15
36	417095	4418447	1045.11	1223.21
37	417121	4418425	1044.11	1257.27
38	417147	4418403	1039.97	1291.33
39	417173	4418381	1036.25	1325.38
40	417199	4418359	1038.25	1359.44 (Piedomnt)
41	417225	4418337	1039.83	1393.50
42	417251	4418315	1038.44	1427.56
43	417277	4418293	1037.07	1461.62
44	417302	4418271	1037.47	1494.92
45	417328	4418249	1037.97	1528.98
46	417354	4418227	1035.21	1563.04
47	417380	4418205	1032.23	1597.10
48	417406	4418182	1030.57	1631.81
49	417432	4418160	1029.06	1665.87
50	417458	4418138	1029.49	1699.93
51	417484	4418116	1029.99	1733.99

TABLE 2: LINE 2 STATION LOCATIONS WITH INFERRED FAULT LOCATIONS HIGHLIGHTED IN YELLOW

Station #	Easting, m	Northing, m	Elevation, m	Distance from NW, m
2001	416163	4419239	1134	0.00
2003	416239	4419182	1105	94.85
2005	416290	4419137	1098	162.68
2007	416349	4419092	1095	237.19
2009	416400	4419047	1089	305.02 (DVRF)
2011	416451	4419002	1083	372.85 (DVRF)
2013	416501	4418958	1081	440.68
2015	416552	4418913	1082	508.51
2017	416603	4418868	1080	576.35
2019	416654	4418823	1064	644.18
2021	416705	4418778	1062	712.01
2023	416755	4418733	1067	779.85
2025	416815	4418688	1059	854.35
2027	416866	4418643	1056	922.18
2029	416916	4418598	1059	990.02

2031	416967	4418553	1053	1057.85
2033	417018	4418508	1046	1125.69
2035	417069	4418463	1046	1193.52
2037	417120	4418418	1044	1261.35
2039	417171	4418384	1036	1322.50 (Piedmont)
2041	417221	4418339	1040	1390.34 (Piedmont)
2043	417281	4418294	1037	1464.85
2045	417331	4418249	1038	1532.68
2047	417380	4418201	1032	1600.99
2049	417433	4418159	1029	1668.51
2051	417484	4418114	1030	1736.35

TABLE 3: LINE 3 CDP LOCATIONS WITH INFERRED FAULT LOCATIONS HIGHLIGHTED IN YELLOW

CDP #	Easting, m	Northing, m	Elevaton, m	Distance from NW, m
1	417532	4421133	1155	35.91
2	417554	4421111	1150	67.29
3	417580	4421089	1147	101.35
4	417606	4421067	1145	135.41
5	417632	4421045	1143	169.46
6	417658	4421023	1139	203.52
7	417683	4421000	1135	237.49
8	417709	4420978	1136	271.55
9	417735	4420956	1138	305.61
10	417761	4420934	1133	339.67
11	417787	4420912	1127	373.73
12	417813	4420890	1123	407.79
13	417839	4420868	1119	441.85
14	417865	4420845	1115	476.56
15	417890	4420823	1111	509.86
16	417916	4420801	1107	543.92
17	417942	4420779	1103	577.98
18	417968	4420757	1104	612.04
19	417994	4420735	1106	646.10
20	418020	4420713	1102	680.15
21	418046	4420690	1097	714.87

22	418071	4420668	1095	748.17
23	418097	4420646	1093	782.23
24	418123	4420624	1091	816.29
25	418149	4420602	1089	850.35
26	418175	4420580	1088	884.40
27	418201	4420558	1086	918.46
28	418227	4420535	1084	953.18
29	418253	4420513	1082	987.24
30	418278	4420491	1079	1020.54
31	418304	4420469	1076	1054.60
32	418330	4420447	1076	1088.65
33	418356	4420425	1076	1122.71
34	418382	4420403	1075	1156.77
35	418408	4420380	1073	1191.49
36	418434	4420358	1074	1225.54
37	418459	4420336	1074	1258.85
38	418485	4420314	1075	1292.90
39	418511	4420292	1077	1326.96
40	418537	4420270	1077	1361.02
41	418563	4420248	1076	1395.08
42	418589	4420225	1073	1429.79
43	418615	4420203	1070	1463.85
44	418641	4420181	1069	1497.91
45	418666	4420159	1068	1531.21
46	418692	4420137	1067	1565.27
47	418718	4420115	1066	1599.33
48	418744	4420093	1065	1633.39
49	418770	4420070	1064	1668.10
50	418796	4420048	1061	1702.16
51	418822	4420026	1057	1736.22
52	418847	4420004	1056	1769.52
53	418873	4419982	1055	1803.58
54	418899	4419960	1054	1837.64
55	418925	4419938	1053	1871.70
56	418951	4419915	1052	1906.41
57	418977	4419893	1051	1940.47
58	419003	4419871	1050	1974.53
59	419029	4419849	1049	2008.59

60	419054	4419827	1046	2041.89
61	419080	4419805	1043	2075.95
62	419106	4419783	1044	2110.01
63	419132	4419760	1045	2144.72
64	419158	4419738	1045	2178.78
65	419184	4419716	1044	2212.84
66	419210	4419694	1043	2246.90
67	419235	4419672	1043	2280.20
68	419261	4419650	1041	2314.26
69	419287	4419628	1039	2348.32
70	419313	4419605	1038	2383.03 (Piedmont)
71	419339	4419583	1038	2417.09
72	419365	4419561	1039	2451.15
73	419391	4419539	1040	2485.20
74	419417	4419517	1042	2519.26
75	419442	4419495	1043	2552.56
76	419468	4419473	1041	2586.62
77	419494	4419450	1038	2621.34
78	419520	4419426	1036	2657.31
79	419546	4419406	1034	2689.54

TABLE 4: LINE 3 STATION LOCATIONS WITH INFERRED FAULT LOCATIONS HIGHLIGHTED IN YELLOW

Station#	Easting, m	Northing, m	Elevation, m	Distance from NW, m
3001	417504	4421155	1155	0.00
3003	417581	4421089	1147	102.11
3005	417633	4421045	1143	170.17
3007	417685	4421000	1135	238.24
3009	417736	4420956	1138	306.32
3011	417788	4420912	1127	374.38
3013	417840	4420868	1119	442.46
3015	417891	4420823	1111	510.53
3017	417943	4420779	1103	578.60
3019	417995	4420735	1106	646.67
3021	418046	4420691	1097	714.74
3023	418098	4420646	1093.3	782.82
3025	418150	4420602	1089.7	850.88

3027	418202	4420558	1086	918.96
3029	418253	4420513	1082	987.03
3031	418305	4420469	1076	1055.11
3033	418357	4420425	1076	1123.18
3035	418408	4420381	1073	1191.25
3037	418460	4420336	1074	1259.33
3039	418512	4420292	1077	1327.40
3041	418564	4420248	1076	1395.47
3043	418615	4420204	1070	1463.55
3045	418667	4420159	1068	1531.62
3047	418719	4420115	1066	1599.70
3049	418770	4420071	1064	1667.77
3051	418822	4420026	1057	1735.85
3053	418874	4419982	1055	1803.92
3055	418926	4419938	1053	1872.00
3057	418977	4419894	1051	1940.07
3059	419029	4419849	1049	2008.15
3061	419081	4419805	1043	2076.22
3063	419132	4419761	1045	2144.30
3065	419184	4419717	1044	2212.38
3067	419236	4419672	1043	2280.45
3069	419288	4419628	1039	2348.53 (Piedmont)
3071	419339	4419584	1038	2416.61 (Piedmont)
3073	419391	4419540	1040	2484.69
3075	419443	4419495	1043	2552.76

TABLE 5: LINE 4 CDP LOCATIONS WITH INFERRED FAULT LOCATIONS HIGHLIGHTED IN YELLOW

CDP #	Easting, m	Northing, m	Elevation, m	Distance from NW, m
1	422210	4423381	1141	19.67
2	422221	4423370	1141	35.42
3	422232	4423357	1142	52.45
4	422244	4423345	1142	69.42
5	422255	4423332	1141	86.45
6	422266	4423320	1140	102.73
7	422278	4423307	1138	120.42
8	422289	4423295	1137	136.70
9	422301	4423282	1136	154.39

10	422312	4423270	1135	170.67
11	422324	4423257	1133	188.36
12	422335	4423245	1130	204.64
13	422347	4423232	1129	222.33
14	422358	4423220	1127	238.61
15	422370	4423207	1125	256.31
16	422381	4423195	1122	272.58
17	422393	4423182	1119	290.28
18	422404	4423170	1116	306.55
19	422416	4423157	1114	324.25
20	422427	4423145	1111	340.53
21	422439	4423132	1106	358.22
22	422450	4423120	1100	374.50
23	422462	4423107	1102	392.19
24	422473	4423095	1104	408.47
25	422485	4423082	1103	426.16
26	422496	4423070	1102	442.44
27	422508	4423057	1101	460.13
28	422519	4423045	1099	476.41
29	422531	4423032	1098	494.10
30	422542	4423020	1097	510.38 (DVRF)
31	422554	4423007	1094	528.07
32	422565	4422995	1090	544.35
33	422577	4422982	1091	562.04
34	422588	4422970	1092	578.32
35	422600	4422957	1091	596.01
36	422611	4422945	1090	612.29
37	422623	4422932	1089	629.98
38	422634	4422920	1087	646.26
39	422646	4422907	1086	663.95
40	422657	4422895	1084	680.23
41	422669	4422882	1083	697.92
42	422680	4422870	1081	714.20
43	422692	4422857	1080	731.89
44	422703	4422845	1079	748.17
45	422715	4422832	1075	765.86
46	422726	4422820	1071	782.14
47	422738	4422807	1071	799.84

48	422749	4422795	1073	816.11
49	422761	4422782	1072	833.81
50	422772	4422770	1071	850.08
51	422784	4422757	1070	867.78
52	422795	4422745	1068	884.06
53	422807	4422732	1067	901.75
54	422818	4422720	1065	918.03
55	422830	4422707	1064	935.72
56	422841	4422695	1062	952.00
57	422853	4422682	1061	969.69
58	422864	4422670	1060	985.97
59	422876	4422657	1056	1003.66
60	422887	4422645	1051	1019.94
61	422899	4422632	1052	1037.63
62	422910	4422620	1054	1053.91
63	422922	4422607	1054	1071.60
64	422933	4422595	1053	1087.88
65	422945	4422582	1052	1105.57
66	422956	4422570	1051	1121.85
67	422968	4422557	1050	1139.54
68	422979	4422545	1048	1155.82
69	422991	4422532	1047	1173.51
70	423002	4422520	1046	1189.79
71	423014	4422507	1045	1207.48
72	423025	4422495	1044	1223.76
73	423037	4422482	1043	1241.45
74	423048	4422470	1041	1257.73
75	423060	4422457	1041	1275.42
76	423071	4422445	1043	1291.70
77	423083	4422432	1044	1309.39
78	423094	4422420	1045	1325.67
79	423106	4422407	1045	1343.37
80	423117	4422395	1046	1359.64
81	423129	4422382	1044	1377.34
82	423140	4422370	1041	1393.61
83	423152	4422357	1042	1411.31
84	423163	4422345	1045	1427.59
85	423175	4422332	1044	1445.28

86	423186	4422320	1041	1461.56
87	423197	4422307	1041	1478.59
88	423209	4422295	1042	1495.56
89	423220	4422282	1042	1512.59
90	423232	4422270	1041	1529.56 (Piedmont)
91	423243	4422257	1040	1546.59
92	423255	4422245	1040	1563.56
93	423266	4422232	1039	1580.59
94	423278	4422220	1038	1597.56
95	423289	4422207	1036	1614.59
96	423301	4422195	1032	1631.56
97	423312	4422182	1032	1648.59
98	423324	4422170	1035	1665.56
99	423335	4422157	1034	1682.59
100	423347	4422145	1032	1699.56
101	423358	4422132	1030	1716.59
102	423370	4422120	1030	1733.56
103	423381	4422107	1031	1750.58
104	423393	4422095	1033	1767.56
105	423404	4422082	1034	1784.58
106	423416	4422070	1034	1801.56
107	423427	4422057	1033	1818.58
108	423439	4422045	1031	1835.56
109	423450	4422032	1031	1852.58
110	423462	4422020	1033	1869.56
111	423473	4422007	1034	1886.58
112	423485	4421995	1034	1903.56
113	423496	4421982	1034	1920.58
114	423508	4421970	1033	1937.56
115	423519	4421957	1032	1954.58
116	423531	4421945	1031	1971.56
117	423542	4421932	1031	1988.58
118	423554	4421920	1034	2005.56
119	423565	4421907	1035	2022.58
120	423577	4421895	1032	2039.56
121	423588	4421882	1032	2056.58
122	423600	4421870	1036	2073.56
123	423611	4421857	1038	2090.58

124	423623	4421845	1038	2107.56
125	423634	4421832	1036	2124.58
126	423646	4421820	1032	2141.55
127	423657	4421807	1031	2158.58
128	423669	4421795	1034	2175.55
129	423680	4421782	1034	2192.58
130	423692	4421770	1031	2209.55
131	423703	4421757	1031	2226.58
132	423715	4421745	1033	2243.55
133	423726	4421732	1033	2260.58
134	423738	4421720	1031	2277.55
135	423749	4421707	1031	2294.58
136	423761	4421695	1035	2311.55
137	423772	4421682	1036	2328.58
138	423784	4421670	1032	2345.55
139	423795	4421657	1031	2362.58
140	423807	4421645	1035	2379.55
141	423818	4421632	1038	2396.58
142	423830	4421620	1038	2413.55
143	423841	4421607	1038	2430.58
144	423853	4421595	1037	2447.55
145	423864	4421582	1037	2464.58
146	423876	4421570	1037	2481.55
147	423887	4421557	1037	2498.58
148	423899	4421545	1037	2515.55
149	423910	4421532	1037	2532.58
150	423922	4421520	1036	2549.55
151	423933	4421507	1036	2566.58
152	423945	4421495	1036	2583.55
153	423956	4421482	1036	2600.58
154	423968	4421470	1036	2617.55
155	423979	4421457	1036	2634.58
156	423991	4421445	1036	2651.55
157	424002	4421432	1036	2668.58
158	424014	4421420	1035	2685.55
159	424025	4421407	1034	2702.58
160	424037	4421395	1032	2719.55
161	424048	4421382	1031	2736.58

162	424060	4421370	1033	2753.55
163	424071	4421358	1035	2769.83
164	424083	4421345	1034	2787.52
165	424094	4421333	1034	2803.80
166	424106	4421320	1032	2821.50
167	424117	4421308	1030	2837.77
168	424128	4421295	1032	2854.80
169	424140	4421283	1034	2871.77
170	424151	4421270	1033	2888.80
171	424163	4421258	1033	2905.77
172	424174	4421245	1031	2922.80
173	424186	4421233	1030	2939.77
174	424197	4421220	1032	2956.80
175	424209	4421208	1033	2973.77
176	424220	4421195	1032	2990.80
177	424232	4421183	1032	3007.77
178	424243	4421170	1031	3024.80
179	424255	4421158	1030	3041.77
180	424266	4421145	1031	3058.80
181	424278	4421133	1032	3075.77
182	424289	4421120	1031	3092.80
183	424301	4421108	1031	3109.77
184	424312	4421095	1030	3126.80
185	424324	4421083	1030	3143.77
186	424335	4421070	1031	3160.80
187	424347	4421058	1031	3177.77
188	424358	4421045	1030	3194.80
189	424370	4421033	1030	3211.77
190	424381	4421020	1030	3228.80
191	424393	4421008	1030	3245.77
192	424404	4420995	1031	3262.80
193	424416	4420983	1031	3279.77
194	424427	4420970	1031	3296.80
195	424439	4420958	1031	3313.77
196	424450	4420945	1032	3330.80
197	424462	4420933	1032	3347.77
198	424473	4420920	1032	3364.80
199	424485	4420908	1032	3381.77

200	424496	4420895	1033	3398.80
201	424508	4420883	1033	3415.77
202	424519	4420870	1033	3432.80
203	424531	4420858	1033	3449.77
204	424542	4420845	1034	3466.80
205	424554	4420833	1034	3483.77
206	424565	4420820	1034	3500.80
207	424577	4420808	1034	3517.77
208	424588	4420795	1035	3534.80
209	424600	4420783	1035	3551.77
210	424611	4420770	1035	3568.80
211	424623	4420758	1035	3585.77
212	424634	4420745	1036	3602.80
213	424646	4420733	1036	3619.77
214	424657	4420720	1036	3636.80
215	424669	4420708	1036	3653.77
216	424680	4420695	1036	3670.80
217	424692	4420683	1037	3687.77
218	424703	4420670	1037	3704.80
219	424715	4420658	1038	3721.77
220	424726	4420645	1034	3738.80
221	424738	4420633	1030	3755.77
222	424749	4420620	1034	3772.80
223	424761	4420608	1038	3789.77
224	424772	4420595	1038	3806.80
225	424784	4420583	1038	3823.77
226	424795	4420570	1038	3840.80
227	424807	4420558	1037	3857.77
228	424818	4420545	1037	3874.80
229	424830	4420533	1037	3891.77
230	424841	4420520	1034	3908.80
231	424853	4420508	1030	3925.77
232	424864	4420495	1033	3942.80
233	424876	4420483	1037	3959.77
234	424887	4420470	1037	3976.80
235	424899	4420458	1037	3993.77
236	424910	4420445	1037	4010.80
237	424922	4420433	1036	4027.77

238	424933	4420420	1036	4044.80
239	424945	4420408	1036	4061.77
240	424956	4420395	1033	4078.80 (NS strike slip)
241	424968	4420383	1030	4095.77
242	424979	4420370	1033	4112.80
243	424991	4420358	1036	4129.77
244	425002	4420345	1036	4146.80
245	425014	4420333	1036	4163.77
246	425025	4420320	1036	4180.80
247	425037	4420308	1035	4197.77
248	425048	4420295	1035	4214.80
249	425060	4420283	1035	4231.77
250	425071	4420270	1033	4248.80
251	425082	4420258	1031	4265.08
252	425094	4420245	1032	4282.77
253	425105	4420233	1034	4299.05
254	425117	4420220	1035	4316.74
255	425128	4420208	1035	4333.02
256	425140	4420195	1035	4350.71
257	425151	4420183	1035	4366.99
258	425163	4420170	1035	4384.68
259	425174	4420158	1035	4400.96
260	425186	4420145	1035	4418.65
261	425197	4420133	1035	4434.93
262	425209	4420120	1035	4452.63
263	425220	4420108	1035	4468.90
264	425232	4420095	1035	4486.60
265	425243	4420083	1035	4502.87
266	425255	4420070	1035	4520.57
267	425266	4420058	1035	4536.85
268	425278	4420045	1035	4554.54
269	425289	4420033	1034	4570.82
270	425301	4420020	1034	4588.51
271	425312	4420008	1034	4604.79
272	425324	4419995	1034	4622.48
273	425335	4419983	1034	4638.76
274	425347	4419970	1034	4656.45
275	425358	4419958	1034	4672.73

276	425370	4419945	1034	4690.42
277	425381	4419933	1034	4706.70
278	425393	4419920	1034	4724.39
279	425404	4419908	1034	4740.67
280	425416	4419895	1033	4758.36
281	425427	4419883	1031	4774.64
282	425439	4419870	1031	4792.33
283	425450	4419858	1033	4808.61
284	425462	4419845	1034	4826.30
285	425473	4419833	1034	4842.58
286	425485	4419820	1034	4860.27
287	425496	4419808	1034	4876.55
288	425508	4419795	1034	4894.24
289	425519	4419783	1034	4910.52
290	425531	4419770	1034	4928.21
291	425542	4419758	1034	4944.49
292	425554	4419745	1034	4962.18
293	425565	4419733	1034	4978.46
294	425577	4419720	1034	4996.16
295	425588	4419708	1034	5012.43
296	425600	4419695	1034	5030.13
297	425611	4419683	1034	5046.40
298	425623	4419670	1034	5064.10
299	425634	4419658	1033	5080.38
300	425646	4419645	1033	5098.07
301	425657	4419633	1033	5114.35
302	425669	4419620	1033	5132.04
303	425680	4419608	1033	5148.32
304	425692	4419595	1033	5166.01
305	425703	4419583	1033	5182.29
306	425715	4419570	1033	5199.98
307	425726	4419558	1033	5216.26
308	425738	4419545	1033	5233.95
309	425749	4419533	1033	5250.23
310	425761	4419520	1032	5267.92
311	425772	4419508	1031	5284.20
312	425784	4419495	1031	5301.89
313	425795	4419483	1032	5318.17

314	425807	4419470	1033	5335.86
315	425818	4419458	1034	5352.14
316	425830	4419445	1034	5369.83
317	425841	4419433	1034	5386.11
318	425853	4419420	1033	5403.80
319	425864	4419408	1031	5420.08
320	425876	4419395	1031	5437.77
321	425887	4419383	1033	5454.05
322	425899	4419370	1034	5471.74
323	425910	4419358	1035	5488.02
324	425922	4419345	1035	5505.71
325	425933	4419333	1035	5521.99
326	425945	4419320	1034	5539.69
327	425956	4419308	1032	5555.96
328	425968	4419295	1031	5573.66
329	425979	4419283	1033	5589.93
330	425991	4419270	1035	5607.63
331	426002	4419258	1036	5623.91
332	426013	4419245	1036	5640.93
333	426025	4419233	1036	5657.91
334	426036	4419220	1035	5674.93
335	426048	4419208	1032	5691.91
336	426059	4419195	1030	5708.93
337	426071	4419183	1030	5725.91
338	426082	4419170	1030	5742.93
339	426094	4419158	1030	5759.91
340	426105	4419145	1030	5776.93
341	426117	4419133	1030	5793.91
342	426128	4419120	1028	5810.93
343	426140	4419108	1023	5827.91
344	426151	4419095	1022	5844.93
345	426163	4419083	1027	5861.90
346	426174	4419070	1030	5878.93
347	426186	4419058	1030	5895.90
348	426197	4419045	1030	5912.93
349	426209	4419033	1030	5929.90
350	426220	4419020	1031	5946.93
351	426232	4419008	1033	5963.90

352	426243	4418995	1034	5980.93
353	426255	4418983	1035	5997.90
354	426266	4418970	1035	6014.93
355	426278	4418958	1035	6031.90
356	426289	4418945	1035	6048.93
357	426301	4418933	1035	6065.90
358	426312	4418920	1035	6082.93
359	426324	4418908	1035	6099.90
360	426335	4418895	1035	6116.93
361	426347	4418883	1036	6133.90
362	426358	4418870	1035	6150.93
363	426370	4418858	1032	6167.90
364	426381	4418845	1031	6184.93
365	426393	4418833	1034	6201.90
366	426404	4418820	1036	6218.93
367	426416	4418808	1036	6235.90
368	426427	4418795	1036	6252.93
369	426439	4418783	1035	6269.90
370	426450	4418770	1035	6286.93 (NE-SW Strike Slip)
371	426462	4418758	1035	6303.90
372	426473	4418745	1035	6320.93
373	426485	4418733	1035	6337.90
374	426496	4418720	1035	6354.93
375	426508	4418708	1035	6371.90
376	426519	4418695	1035	6388.93
377	426531	4418683	1034	6405.90
378	426542	4418670	1034	6422.93
379	426554	4418658	1034	6439.90
380	426565	4418645	1034	6456.93
381	426577	4418633	1032	6473.90
382	426588	4418620	1030	6490.93
383	426600	4418608	1032	6507.90
384	426611	4418595	1034	6524.93
385	426623	4418583	1034	6541.90
386	426634	4418570	1034	6558.93
387	426646	4418558	1034	6575.90
388	426657	4418545	1034	6592.93
389	426669	4418533	1035	6609.90

390	426680	4418520	1035	6626.93
391	426692	4418508	1035	6643.90
392	426703	4418495	1035	6660.93
393	426715	4418483	1035	6677.90
394	426726	4418470	1035	6694.93
395	426738	4418458	1035	6711.90
396	426749	4418445	1035	6728.93
397	426761	4418433	1035	6745.90
398	426772	4418420	1035	6762.93
399	426784	4418408	1035	6779.90
400	426795	4418395	1035	6796.93
401	426807	4418383	1035	6813.90
402	426818	4418370	1035	6830.93
403	426830	4418358	1036	6847.90
404	426841	4418345	1036	6864.93
405	426853	4418333	1036	6881.90
406	426864	4418320	1036	6898.93
407	426876	4418308	1036	6915.90
408	426887	4418295	1036	6932.93
409	426899	4418283	1036	6949.90
410	426910	4418270	1036	6966.93
411	426922	4418258	1033	6983.90
412	426933	4418245	1030	7000.93
413	426944	4418233	1033	7017.21
414	426956	4418220	1036	7034.90
415	426967	4418208	1036	7051.18
416	426979	4418195	1036	7068.87
417	426990	4418183	1036	7085.15
418	427002	4418170	1036	7102.84
419	427013	4418158	1036	7119.12
420	427025	4418145	1036	7136.82
421	427036	4418133	1036	7153.09
422	427048	4418120	1036	7170.79
423	427059	4418108	1036	7187.06
424	427071	4418095	1036	7204.76
425	427082	4418083	1036	7221.04
426	427094	4418070	1037	7238.73
427	427105	4418058	1037	7255.01

428	427117	4418045	1037	7272.70
429	427128	4418033	1037	7288.98
430	427140	4418020	1037	7306.67
431	427151	4418008	1037	7322.95
432	427163	4417995	1037	7340.64
433	427174	4417983	1037	7356.92
434	427186	4417970	1037	7374.61
435	427197	4417958	1037	7390.89
436	427209	4417945	1037	7408.58
437	427220	4417933	1037	7424.86
438	427232	4417920	1037	7442.55
439	427243	4417908	1037	7458.83
440	427255	4417895	1037	7476.52
441	427266	4417883	1034	7492.80
442	427278	4417870	1031	7510.49
443	427289	4417858	1033	7526.77
444	427301	4417845	1036	7544.46
445	427312	4417833	1037	7560.74
446	427324	4417820	1037	7578.43
447	427335	4417808	1037	7594.71
448	427347	4417795	1037	7612.40
449	427358	4417783	1037	7628.68
450	427370	4417770	1037	7646.37
451	427381	4417758	1037	7662.65
452	427393	4417745	1037	7680.35
453	427404	4417733	1037	7696.62
454	427416	4417720	1037	7714.32
455	427427	4417708	1037	7730.59
456	427439	4417695	1036	7748.29
457	427450	4417683	1036	7764.57
458	427462	4417670	1036	7782.26
459	427473	4417658	1036	7798.54
460	427485	4417645	1036	7816.23
461	427496	4417633	1036	7832.51
462	427508	4417620	1036	7850.20
463	427519	4417608	1036	7866.48
464	427531	4417595	1036	7884.17
465	427542	4417583	1034	7900.45

466	427554	4417570	1031	7918.14
467	427565	4417558	1032	7934.42
468	427577	4417545	1035	7952.11
469	427588	4417533	1036	7968.39
470	427600	4417520	1037	7986.08
471	427611	4417508	1037	8002.36
472	427623	4417495	1037	8020.05
473	427634	4417483	1035	8036.33
474	427646	4417470	1031	8054.02
475	427657	4417458	1032	8070.30
476	427669	4417445	1036	8087.99
477	427680	4417433	1037	8104.27
478	427692	4417420	1038	8121.96
479	427703	4417408	1038	8138.24
480	427715	4417395	1038	8155.93 (Buckbrush)
481	427726	4417383	1036	8172.21
482	427738	4417370	1031	8189.90
483	427749	4417358	1032	8206.18
484	427761	4417346	1036	8223.15
485	427772	4417333	1038	8240.18
486	427784	4417321	1039	8257.15
487	427795	4417308	1039	8274.18
488	427807	4417296	1039	8291.15
489	427818	4417283	1036	8308.18
490	427830	4417271	1032	8325.15
491	427841	4417258	1032	8342.18
492	427853	4417246	1037	8359.15
493	427864	4417233	1039	8376.18
494	427876	4417221	1040	8393.15
495	427887	4417208	1040	8410.18
496	427898	4417196	1040	8426.46
497	427910	4417183	1040	8444.15
498	427921	4417171	1040	8460.43
499	427933	4417158	1040	8478.12
500	427944	4417146	1041	8494.40
501	427956	4417133	1041	8512.09
502	427967	4417121	1040	8528.37
503	427979	4417108	1040	8546.07

504	427990	4417096	1041	8562.34
505	428002	4417083	1041	8580.04
506	428013	4417071	1042	8596.32
507	428025	4417058	1042	8614.01
508	428036	4417046	1041	8630.29
509	428048	4417033	1040	8647.98
510	428059	4417021	1041	8664.26
511	428071	4417008	1042	8681.95
512	428082	4416996	1043	8698.23
513	428094	4416983	1042	8715.92
514	428105	4416971	1041	8732.20
515	428117	4416958	1041	8749.89
516	428128	4416946	1042	8766.17
517	428140	4416933	1043	8783.86
518	428151	4416921	1044	8800.14
519	428163	4416908	1044	8817.83
520	428174	4416896	1044	8834.11
521	428186	4416883	1044	8851.80

TABLE 6: LINE 4 STATION LOCATIONS WITH INFERRED FAULT LOCATIONS HIGHLIGHTED IN YELLOW

Station #	Easting. m	Northing, m	Elevation, m	Distance from NW, m
4001	422197	4423396	1145	0.00
4002	422243	4423345	1142	68.68
4003	422266	4423320	1140	102.65
4004	422289	4423295	1137	136.62
4005	422312	4423270	1135	170.59
4006	422336	4423245	1132	205.25
4007	422359	4423220	1127	239.22
4008	422382	4423195	1122	273.19
4009	422405	4423169	1116	307.90
4010	422428	4423144	1111	341.87
4011	422451	4423119	1106	375.84
4012	422474	4423094	1104	409.81
4013	422497	4423069	1102	443.78
4014	422520	4423044	1099	477.75
4015	422543	4423019	1097	511.73 (DVRF)
4016	422566	4422994	1095	545.70 (DVRF)

4017	422590	4422968	1092	581.08
4018	422613	4422943	1090	615.05
4019	422636	4422918	1087	649.02
4020	422659	4422893	1084	682.99
4021	422682	4422868	1081	716.96
4022	422705	4422843	1079	750.93
4023	422728	4422818	1076	784.90
4024	422751	4422792	1073	819.62
4025	422774	4422767	1071	853.59
4026	422797	4422742	1068	887.56
4027	422820	4422717	1065	921.53
4028	422844	4422692	1062	956.18
4029	422867	4422667	1060	990.15
4030	422890	4422642	1057	1024.12
4031	422913	4422617	1055	1058.09
4032	422936	4422591	1053	1092.81
4033	422959	4422566	1051	1126.78
4034	422982	4422541	1048	1160.75
4035	423005	4422516	1046	1194.72
4036	423028	4422491	1044	1228.69
4037	423051	4422466	1042	1262.66
4038	423074	4422441	1043	1296.63
4039	423097	4422415	1045	1331.34
4040	423121	4422390	1046	1366.00
4041	423144	4422365	1047	1399.97
4042	423167	4422340	1046	1433.94
4043	423190	4422315	1044	1467.91
4044	423213	4422290	1043	1501.88 (Piedmont)
4045	423236	4422265	1041	1535.85 (Piedmont)
4046	423259	4422240	1040	1569.82
4047	423282	4422214	1038	1604.54
4048	423305	4422189	1037	1638.51
4049	423328	4422164	1036	1672.48
4050	423354	4422138	1030	1709.25
4051	423375	4422114	1033	1741.14
4052	423398	4422089	1034	1775.11
4053	423421	4422064	1034	1809.08
4054	423444	4422038	1035	1843.79

4055	423467	4422013	1034	1877.76
4056	423490	4421988	1034	1911.73
4057	423513	4421963	1033	1945.70
4058	423536	4421938	1032	1979.67
4059	423559	4421913	1036	2013.64
4060	423582	4421888	1039	2047.62
4061	423606	4421863	1038	2082.27
4062	423629	4421837	1038	2116.98
4063	423652	4421812	1037	2150.95
4064	423675	4421787	1035	2184.93
4065	423698	4421762	1032	2218.90
4066	423721	4421737	1034	2252.87
4067	423744	4421712	1035	2286.84
4068	423767	4421687	1037	2320.81
4069	423790	4421662	1038	2354.78
4070	423813	4421636	1038	2389.49
4071	423837	4421611	1037	2424.15
4072	423860	4421586	1037	2458.12
4073	423883	4421561	1037	2492.09
4074	423906	4421536	1037	2526.06
4075	423929	4421511	1036	2560.03
4076	423952	4421486	1036	2594.00
4077	423975	4421460	1036	2628.71
4078	423998	4421435	1036	2662.68
4079	424021	4421410	1035	2696.65
4080	424044	4421385	1035	2730.62
4081	424067	4421360	1035	2764.59
4082	424091	4421335	1034	2799.25
4084	424137	4421285	1034	2867.19
4085	424160	4421259	1033	2901.90
4086	424183	4421234	1033	2935.88
4087	424206	4421209	1033	2969.85
4088	424229	4421184	1032	3003.82
4089	424252	4421159	1032	3037.79
4090	424275	4421134	1032	3071.76
4091	424298	4421109	1031	3105.73
4092	424322	4421084	1031	3140.38
4093	424345	4421058	1031	3175.10

4094	424368	4421033	1030	3209.07
4095	424391	4421008	1030	3243.04
4096	424414	4420983	1031	3277.01
4097	424437	4420958	1031	3310.98
4098	424460	4420933	1032	3344.95
4099	424483	4420908	1032	3378.92
4100	424506	4420883	1033	3412.89
4101	424529	4420857	1033	3447.60
4102	424553	4420832	1034	3482.26
4103	424576	4420807	1034	3516.23
4104	424599	4420782	1035	3550.20
4105	424622	4420757	1035	3584.17
4106	424645	4420732	1036	3618.14
4107	424668	4420707	1036	3652.11
4108	424691	4420682	1037	3686.08
4109	424714	4420656	1037	3720.80
4110	424737	4420631	1038	3754.77
4111	424760	4420606	1038	3788.74
4112	424784	4420581	1038	3823.39
4113	424807	4420556	1037	3857.36
4114	424830	4420531	1037	3891.33
4115	424853	4420506	1037	3925.30
4116	424876	4420481	1037	3959.27
4117	424899	4420455	1037	3993.99
4118	424922	4420430	1036	4027.96
4119	424945	4420405	1036	4061.93 (NS Strike Slip)
4120	424968	4420380	1036	4095.90 (NS Strike Slip)
4121	424992	4420355	1036	4130.55
4122	425015	4420330	1036	4164.53
4123	425038	4420305	1035	4198.50
4124	425061	4420279	1035	4233.21
4125	425084	4420254	1035	4267.18
4126	425107	4420229	1035	4301.15
4127	425130	4420204	1035	4335.12
4128	425153	4420179	1035	4369.09
4129	425176	4420154	1035	4403.06
4130	425199	4420129	1035	4437.03
4131	425223	4420104	1035	4471.69

4132	425246	4420078	1035	4506.40
4133	425269	4420053	1034	4540.37
4134	425292	4420028	1034	4574.34
4135	425315	4420003	1034	4608.31
4136	425338	4419978	1034	4642.28
4137	425361	4419953	1034	4676.25
4138	425384	4419928	1034	4710.22
4139	425407	4419903	1034	4744.20
4140	425431	4419877	1034	4779.58
4141	425454	4419852	1034	4813.55
4142	425477	4419827	1034	4847.52
4143	425500	4419802	1034	4881.49
4144	425523	4419777	1034	4915.46
4145	425546	4419752	1034	4949.43
4146	425569	4419727	1034	4983.40
4147	425592	4419702	1034	5017.37
4148	425615	4419676	1033	5052.09
4149	425639	4419651	1033	5086.74
4150	425662	4419626	1033	5120.71
4151	425685	4419601	1033	5154.68
4152	425708	4419576	1033	5188.65
4153	425731	4419551	1033	5222.62
4154	425754	4419526	1033	5256.59
4155	425777	4419501	1033	5290.56
4156	425800	4419475	1033	5325.28
4157	425823	4419450	1034	5359.25
4158	425846	4419425	1034	5393.22
4159	425870	4419400	1034	5427.87
4160	425893	4419375	1034	5461.85
4161	425916	4419350	1035	5495.82
4162	425939	4419325	1035	5529.79
4163	425962	4419300	1035	5563.76
4164	425985	4419275	1035	5597.73
4165	426008	4419249	1036	5632.44
4166	426031	4419224	1036	5666.41
4167	426054	4419199	1036	5700.38
4168	426078	4419174	1034	5735.04
4169	426101	4419149	1032	5769.01

4170	426124	4419124	1030	5802.98
4171	426147	4419099	1028	5836.95
4172	426170	4419074	1030	5870.92
4173	426193	4419048	1032	5905.63
4174	426216	4419023	1034	5939.60
4175	426239	4418998	1034	5973.57
4176	426262	4418973	1035	6007.54
4177	426286	4418948	1035	6042.20
4178	426309	4418923	1035	6076.17
4179	426332	4418898	1035	6110.14
4180	426355	4418873	1036	6144.11
4181	426378	4418847	1036	6178.82
4182	426401	4418822	1036	6212.80
4183	426424	4418797	1036	6246.77
4184	426447	4418772	1035	6280.74 (NE-SW Strike Slip)
4185	426471	4418747	1035	6315.39 (NE-SW Strike Slip)
4186	426494	4418722	1035	6349.36
4187	426517	4418697	1035	6383.33
4188	426540	4418672	1034	6417.30
4189	426563	4418646	1034	6452.02
4190	426586	4418621	1034	6485.99
4191	426609	4418596	1034	6519.96
4192	426632	4418571	1034	6553.93
4193	426655	4418546	1034	6587.90
4194	426679	4418521	1035	6622.55
4195	426702	4418496	1035	6656.52
4196	426725	4418471	1035	6690.50
4197	426748	4418445	1035	6725.21
4198	426771	4418420	1035	6759.18
4199	426794	4418395	1035	6793.15
4200	426817	4418370	1035	6827.12
4201	426840	4418345	1035	6861.09
4202	426863	4418320	1036	6895.06
4203	426887	4418295	1036	6929.72
4204	426910	4418270	1036	6963.69
4205	426933	4418245	1036	6997.66
4206	426956	4418219	1036	7032.37
4207	426979	4418194	1036	7066.34

4208	427002	4418169	1036	7100.31
4209	427025	4418144	1036	7134.28
4210	427048	4418119	1036	7168.25
4211	427072	4418094	1036	7202.91
4212	427095	4418069	1036	7236.88
4213	427118	4418044	1037	7270.85
4214	427141	4418018	1037	7305.56
4215	427164	4417993	1037	7339.53
4216	427187	4417968	1037	7373.50
4217	427210	4417943	1037	7407.47
4218	427233	4417918	1037	7441.45
4219	427256	4417893	1037	7475.42
4220	427280	4417868	1037	7510.07
4221	427303	4417843	1037	7544.04
4222	427326	4417817	1037	7578.76
4223	427349	4417792	1037	7612.73
4224	427372	4417767	1037	7646.70
4225	427395	4417742	1037	7680.67
4226	427418	4417717	1037	7714.64
4227	427441	4417692	1036	7748.61
4228	427465	4417667	1036	7783.26
4229	427488	4417642	1036	7817.23
4230	427511	4417617	1036	7851.20
4231	427534	4417591	1036	7885.92
4232	427557	4417566	1036	7919.89
4233	427580	4417541	1036	7953.86
4234	427603	4417516	1037	7987.83
4235	427626	4417491	1037	8021.80
4236	427650	4417466	1037	8056.46
4237	427673	4417441	1037	8090.43
4238	427696	4417416	1038	8124.40
4239	427719	4417390	1038	8159.11 (Buckbrush)
4240	427742	4417365	1038	8193.08 (Buckbrush)
4241	427765	4417340	1038	8227.05
4242	427788	4417315	1039	8261.02
4243	427811	4417290	1039	8294.99
4244	427835	4417265	1039	8329.65
4245	427858	4417240	1039	8363.62

4246	427881	4417215	1040	8397.59
4247	427904	4417190	1040	8431.56
4248	427927	4417164	1040	8466.27
4249	427950	4417139	1041	8500.24
4250	427973	4417114	1041	8534.21
4251	427996	4417089	1041	8568.18
4252	428019	4417064	1042	8602.15
4253	428043	4417039	1042	8636.81
4254	428066	4417014	1042	8670.78
4255	428089	4416989	1043	8704.75
4256	428112	4416963	1043	8739.46
4257	428135	4416938	1043	8773.44
4258	428158	4416913	1044	8807.41
4259	428181	4416888	1044	8841.38

TABLE 7: LINE 5 CDP LOCATIONS WITH INFERRED FAULT LOCATIONS HIGHLIGHTED IN YELLOW

CDP #	Easting, m	Northing, m	Elevation, m	Distance from NW, m
1	424425	4424738	1157	34.89
2	424444	4424713	1154	66.49
3	424467	4424687	1150	101.21
4	424489	4424662	1145	134.51
5	424511	4424636	1140	168.57
6	424533	4424610	1135	202.62
7	424555	4424584	1130	236.68
8	424578	4424558	1125	271.40
9	424600	4424532	1120	305.46
10	424622	4424507	1115	338.76
11	424644	4424481	1110	372.82
12	424666	4424455	1110	406.87
13	424689	4424429	1111	441.59
14	424711	4424403	1110	475.65
15	424733	4424378	1108	508.95
16	424755	4424352	1107	543.01
17	424777	4424326	1105	577.07
18	424800	4424300	1104	611.78
19	424822	4424274	1102	645.84
20	424844	4424248	1096	679.90 (DVRF)

21	424866	4424223	1090	713.20
22	424888	4424197	1090	747.26
23	424911	4424171	1090	781.97
24	424933	4424145	1090	816.03
25	424955	4424119	1090	850.09
26	424977	4424094	1090	883.39
27	424999	4424068	1090	917.45
28	425022	4424042	1090	952.16
29	425044	4424016	1090	986.22
30	425066	4423990	1085	1020.28
31	425088	4423965	1080	1053.58
32	425110	4423939	1083	1087.64
33	425133	4423913	1086	1122.35
34	425155	4423887	1085	1156.41
35	425177	4423861	1084	1190.47
36	425199	4423835	1083	1224.53
37	425221	4423810	1082	1257.83
38	425244	4423784	1081	1292.54
39	425266	4423758	1080	1326.60
40	425288	4423732	1075	1360.66
41	425310	4423706	1070	1394.72
42	425332	4423681	1072	1428.02
43	425355	4423655	1075	1462.73
44	425377	4423629	1074	1496.79
45	425399	4423603	1072	1530.85
46	425421	4423577	1071	1564.91
47	425443	4423551	1069	1598.97
48	425466	4423526	1068	1632.94
49	425488	4423500	1066	1667.00
50	425510	4423474	1065	1701.06
51	425532	4423448	1063	1735.12
52	425554	4423422	1062	1769.18
53	425577	4423397	1060	1803.15
54	425599	4423371	1060	1837.20
55	425621	4423345	1061	1871.26
56	425643	4423319	1061	1905.32
57	425665	4423293	1061	1939.38
58	425688	4423267	1061	1974.09

59	425710	4423242	1060	2007.40
60	425732	4423216	1060	2041.45
61	425754	4423190	1060	2075.51
62	425776	4423164	1055	2109.57
63	425799	4423138	1050	2144.29
64	425821	4423113	1053	2177.59 (Piedmont)
65	425843	4423087	1057	2211.65
66	425865	4423061	1054	2245.70
67	425887	4423035	1050	2279.76
68	425910	4423009	1052	2314.48
69	425932	4422983	1054	2348.53
70	425954	4422958	1052	2381.84
71	425976	4422932	1050	2415.90
72	425998	4422906	1050	2449.95
73	426021	4422880	1051	2484.67
74	426043	4422854	1051	2518.73
75	426065	4422829	1050	2552.03
76	426087	4422803	1050	2586.09
77	426109	4422777	1049	2620.15
78	426132	4422751	1049	2654.86
79	426154	4422725	1048	2688.92
80	426176	4422699	1048	2722.98
81	426198	4422674	1047	2756.28
82	426220	4422648	1044	2790.34
83	426243	4422622	1040	2825.05
84	426265	4422596	1043	2859.11
85	426287	4422570	1046	2893.17
86	426309	4422545	1046	2926.47
87	426331	4422519	1045	2960.53
88	426354	4422493	1045	2995.24
89	426376	4422467	1044	3029.30
90	426398	4422441	1042	3063.36
91	426420	4422415	1040	3097.42
92	426442	4422390	1041	3130.72
93	426465	4422364	1043	3165.43
94	426487	4422338	1043	3199.49
95	426509	4422312	1043	3233.55
96	426531	4422286	1043	3267.61

97	426553	4422261	1043	3300.91
98	426576	4422235	1043	3335.62
99	426598	4422209	1043	3369.68
100	426620	4422183	1043	3403.74
101	426642	4422157	1042	3437.80
102	426664	4422131	1042	3471.86
103	426687	4422106	1042	3505.83
104	426709	4422080	1042	3539.89
105	426731	4422054	1042	3573.95
106	426753	4422028	1042	3608.00
107	426775	4422002	1042	3642.06
108	426798	4421977	1041	3676.03
109	426820	4421951	1040	3710.09
110	426842	4421925	1041	3744.15
111	426864	4421899	1042	3778.21
112	426886	4421873	1042	3812.27
113	426909	4421847	1042	3846.98
114	426931	4421822	1042	3880.28
115	426953	4421796	1042	3914.34
116	426975	4421770	1042	3948.40
117	426997	4421744	1042	3982.46
118	427020	4421718	1042	4017.17
119	427042	4421693	1042	4050.47
120	427064	4421667	1042	4084.53
121	427086	4421641	1042	4118.59
122	427108	4421615	1042	4152.65
123	427131	4421589	1042	4187.36
124	427153	4421564	1041	4220.67
125	427175	4421538	1040	4254.72
126	427197	4421512	1040	4288.78
127	427219	4421486	1040	4322.84
128	427242	4421460	1040	4357.56
129	427264	4421434	1040	4391.61
130	427286	4421409	1040	4424.92
131	427308	4421383	1040	4458.97
132	427330	4421357	1035	4493.03
133	427353	4421331	1030	4527.75
134	427375	4421305	1034	4561.81

135	427397	4421280	1038	4595.11 (NE-SW Strike Slip)
136	427419	4421254	1039	4629.17
137	427441	4421228	1040	4663.22
138	427464	4421202	1040	4697.94
139	427486	4421176	1040	4732.00
140	427508	4421150	1035	4766.06
141	427530	4421125	1030	4799.36
142	427552	4421099	1030	4833.42
143	427575	4421073	1030	4868.13
144	427597	4421047	1032	4902.19
145	427619	4421021	1035	4936.25
146	427641	4420996	1036	4969.55
147	427664	4420970	1037	5004.26
148	427686	4420944	1038	5038.32
149	427708	4420918	1040	5072.38
150	427730	4420892	1041	5106.44
151	427752	4420866	1042	5140.50
152	427775	4420841	1042	5174.47
153	427797	4420815	1042	5208.53
154	427819	4420789	1042	5242.58
155	427841	4420763	1042	5276.64
156	427863	4420737	1042	5310.70
157	427886	4420712	1042	5344.67
158	427908	4420686	1042	5378.73
159	427930	4420660	1042	5412.79
160	427952	4420634	1042	5446.85
161	427974	4420608	1042	5480.91
162	427997	4420582	1042	5515.62
163	428019	4420557	1042	5548.92
164	428041	4420531	1042	5582.98
165	428063	4420505	1042	5617.04
166	428085	4420479	1041	5651.10
167	428108	4420453	1040	5685.81
168	428130	4420428	1041	5719.11
169	428152	4420402	1042	5753.17
170	428174	4420376	1042	5787.23
171	428196	4420350	1042	5821.29
172	428219	4420324	1042	5856.00

173	428241	4420298	1042	5890.06
174	428263	4420273	1042	5923.36
175	428285	4420247	1042	5957.42
176	428307	4420221	1042	5991.48
177	428330	4420195	1042	6026.19
178	428352	4420169	1042	6060.25
179	428374	4420144	1042	6093.55
180	428396	4420118	1042	6127.61
181	428418	4420092	1042	6161.67
182	428441	4420066	1041	6196.38
183	428463	4420040	1040	6230.44
184	428485	4420014	1041	6264.50
185	428507	4419989	1042	6297.80
186	428529	4419963	1041	6331.86
187	428552	4419937	1040	6366.58
188	428574	4419911	1041	6400.63
189	428596	4419885	1041	6434.69
190	428618	4419860	1041	6468.00
191	428640	4419834	1040	6502.05
192	428663	4419808	1041	6536.77
193	428685	4419782	1042	6570.83
194	428707	4419756	1043	6604.88
195	428729	4419730	1043	6638.94
196	428751	4419705	1043	6672.24
197	428774	4419679	1044	6706.96
198	428796	4419653	1044	6741.02
199	428818	4419627	1045	6775.08
200	428840	4419601	1043	6809.13 (Buckbrush)
201	428862	4419576	1040	6842.44
202	428885	4419550	1042	6877.15
203	428907	4419524	1044	6911.21
204	428929	4419498	1042	6945.27
205	428951	4419472	1040	6979.33
206	428973	4419446	1041	7013.38
207	428996	4419421	1042	7047.35
208	429018	4419395	1041	7081.41
209	429040	4419369	1040	7115.47
210	429062	4419343	1041	7149.53

211	429084	4419317	1043	7183.59
212	429107	4419292	1042	7217.56
213	429129	4419266	1040	7251.62
214	429151	4419240	1042	7285.68
215	429173	4419214	1044	7319.74
216	429195	4419188	1042	7353.80
217	429218	4419163	1040	7387.77
218	429240	4419137	1042	7421.82
219	429262	4419111	1045	7455.88
220	429284	4419085	1043	7489.94
221	429306	4419059	1040	7524.00
222	429329	4419033	1043	7558.71
223	429351	4419008	1046	7592.02
224	429373	4418982	1046	7626.07
225	429395	4418956	1046	7660.13
226	429417	4418930	1046	7694.19
227	429440	4418904	1047	7728.91
228	429462	4418879	1047	7762.21
229	429484	4418853	1047	7796.27
230	429506	4418827	1044	7830.32
231	429528	4418801	1040	7864.38
232	429551	4418775	1040	7899.10
233	429573	4418749	1040	7933.16
234	429595	4418724	1042	7966.46
235	429617	4418698	1045	8000.52
236	429639	4418672	1043	8034.57
237	429662	4418646	1040	8069.29
238	429684	4418620	1043	8103.35
239	429706	4418595	1047	8136.65
240	429728	4418569	1047	8170.71
241	429750	4418543	1047	8204.77
242	429773	4418517	1044	8239.48
243	429795	4418491	1040	8273.54
244	429817	4418465	1043	8307.60
245	429839	4418440	1046	8340.90
246	429861	4418414	1046	8374.96
247	429884	4418388	1046	8409.67
248	429906	4418362	1043	8443.73

249	429928	4418336	1040	8477.79
250	429950	4418311	1044	8511.09
251	429972	4418285	1048	8545.15
252	429995	4418259	1049	8579.86
253	430017	4418233	1051	8613.92
254	430039	4418207	1051	8647.98
255	430061	4418181	1050	8682.04
256	430083	4418156	1050	8715.34
257	430106	4418130	1050	8750.05
258	430128	4418104	1050	8784.11
259	430150	4418078	1050	8818.17
260	430172	4418052	1050	8852.23
261	430194	4418027	1050	8885.53
262	430217	4418001	1050	8920.24
263	430239	4417975	1050	8954.30

TABLE 8: LINE 5 STATION LOCATIONS WITH INFERRED FAULT LOCATIONS HIGHLIGHTED IN YELLOW

Station #	Easting. m	Northing, m	Elevation, m	Distance from NW, m
5001	424403	4424765	1160	0.00
5003	424469	4424687	1150	102.13
5005	424513	4424636	1140	170.21
5007	424558	4424584	1130	238.29
5009	424602	4424533	1120	306.38
5011	424646	4424481	1110	374.46
5013	424691	4424429	1111.8	442.54
5015	424735	4424378	1108.6	510.62
5017	424780	4424326	1105.4	578.71
5019	424824	4424274	1102.2	646.79 (DVRF)
5021	424868	4424223	1090	714.88 (DVRF)
5023	424913	4424171	1090	782.96
5025	424957	4424119	1090	851.05
5027	425001	4424068	1090	919.13
5029	425046	4424016	1090	987.22
5031	425090	4423964	1080	1055.30
5033	425134	4423913	1086.8	1123.39
5035	425179	4423861	1084.6	1191.48

5037	425223	4423809	1082.4	1259.56
5039	425268	4423758	1080.2	1327.65
5041	425312	4423706	1070	1395.74
5043	425356	4423654	1075.2	1463.82
5045	425401	4423603	1072.3	1531.91
5047	425445	4423551	1069.5	1600.00
5049	425489	4423500	1066.7	1668.08
5051	425534	4423448	1063.8	1736.17
5053	425578	4423396	1060	1804.26
5055	425622	4423345	1061.3	1872.35
5057	425667	4423293	1061.7	1940.43
5059	425711	4423241	1060	2008.52
5061	425756	4423190	1060.5	2076.61
5063	425800	4423138	1050	2144.70 (Piedmont)
5065	425844	4423086	1057.5	2212.79 (Piedmont)
5067	425889	4423035	1050	2280.88
5069	425933	4422983	1054.5	2348.96
5071	425977	4422931	1050	2417.06
5073	426022	4422880	1051.5	2485.15
5075	426066	4422828	1050	2553.23
5077	426111	4422777	1049.3	2621.32
5079	426155	4422725	1048.5	2689.42
5081	426199	4422673	1047.7	2757.51
5083	426244	4422622	1040	2825.59
5085	426288	4422570	1046.2	2893.68
5087	426332	4422518	1045.5	2961.78
5089	426377	4422467	1044.8	3029.87
5091	426421	4422415	1040	3097.96
5093	426466	4422363	1043.8	3166.05
5095	426510	4422312	1043.6	3234.14
5097	426554	4422260	1043.3	3302.23
5099	426599	4422208	1043.1	3370.32
5101	426643	4422157	1042.9	3438.42
5103	426688	4422105	1042.7	3506.51
5105	426732	4422054	1042.4	3574.60
5107	426776	4422002	1042.2	3642.69
5109	426821	4421950	1040	3710.79
5111	426865	4421899	1042.1	3778.88

5113	426909	4421847	1042.2	3846.97
5115	426954	4421795	1042.4	3915.07
5117	426998	4421744	1042.5	3983.17
5119	427043	4421692	1042.6	4051.26
5121	427087	4421640	1042.8	4119.35
5123	427131	4421589	1042.9	4187.44
5125	427176	4421537	1040	4255.54
5127	427220	4421486	1040	4323.64
5129	427265	4421434	1040	4391.73
5131	427309	4421382	1040	4459.82
5133	427353	4421331	1030	4527.92
5135	427398	4421279	1038.7	4596.02 (NE-SW Strike Slip)
5137	427442	4421227	1040.3	4664.11 (NE-SW Strike Slip)
5139	427487	4421176	1040	4732.20
5141	427531	4421124	1030	4800.30
5143	427575	4421072	1030	4868.40
5145	427620	4421021	1035.7	4936.49
5147	427665	4420971	1037.85	5004.24
5149	427709	4420918	1040	5072.74
5151	427753	4420866	1042.9	5140.83
5153	427797	4420814	1042.8	5208.93
5155	427842	4420763	1042.7	5277.02
5157	427886	4420711	1042.6	5345.13
5159	427931	4420659	1042.4	5413.22
5161	427975	4420608	1042.3	5481.32
5163	428019	4420556	1042.2	5549.42
5165	428064	4420505	1042.1	5617.52
5167	428108	4420453	1040	5685.61
5169	428153	4420401	1042.1	5753.71
5171	428197	4420350	1042.2	5821.82
5173	428241	4420298	1042.4	5889.91
5175	428286	4420246	1042.5	5958.01
5177	428330	4420195	1042.6	6026.11
5179	428375	4420143	1042.8	6094.21
5181	428419	4420092	1042.9	6162.31
5183	428463	4420040	1040	6230.41
5185	428508	4419988	1042.5	6298.51
5187	428552	4419937	1040	6366.61

5189	428597	4419885	1041.5	6434.71
5191	428641	4419833	1040	6502.81
5193	428686	4419782	1042.2	6570.91
5195	428730	4419730	1043.4	6639.02
5197	428774	4419679	1044.6	6707.11
5199	428819	4419627	1045.8	6775.21 (Buckbrush)
5201	428863	4419575	1040	6843.32 (Buckbrush)
5203	428908	4419524	1044.5	6911.42
5205	428952	4419472	1040	6979.52
5207	428996	4419420	1042.5	7047.62
5209	429041	4419369	1040	7115.72
5211	429085	4419317	1043.5	7183.83
5213	429130	4419266	1040	7251.93
5215	429174	4419214	1044.5	7320.04
5217	429219	4419162	1040	7388.14
5219	429263	4419111	1045.5	7456.24
5221	429307	4419059	1040	7524.34
5223	429352	4419007	1046.4	7592.45
5225	429396	4418956	1046.8	7660.55
5227	429441	4418904	1047.2	7728.66
5229	429485	4418853	1047.6	7796.76
5231	429529	4418801	1040	7864.87
5233	429574	4418749	1040	7932.97
5235	429618	4418698	1045.5	8001.08
5237	429663	4418646	1040	8069.18
5239	429707	4418594	1047.7	8137.29
5241	429752	4418543	1047.3	8205.39
5243	429796	4418491	1040	8273.50
5245	429840	4418440	1046.7	8341.60
5247	429885	4418388	1046.3	8409.71
5249	429929	4418336	1040	8477.82
5251	429974	4418285	1048.7	8545.92
5253	430018	4418233	1051.3	8614.03
5255	430063	4418181	1050	8682.13
5257	430107	4418130	1050	8750.24
5259	430151	4418078	1050	8818.35
5261	430196	4418027	1050	8886.46
5263	430240	4417975	1050	8954.56

TABLE 9: LINE 6 CDP LOCATIONS WITH INFERRED FAULT LOCATIONS HIGHLIGHTED IN YELLOW

CDP #	Easting, m	Northing, m	Elevation, m	Distance from NW, m
1	425765	4425822	1125	36.53
2	425784	4425798	1120	67.04
3	425806	4425772	1116	101.10
4	425829	4425747	1110	135.07
5	425851	4425721	1104	169.13
6	425874	4425695	1100	203.84
7	425896	4425670	1096	237.14
8	425918	4425644	1093	271.20
9	425941	4425619	1090	305.17
10	425963	4425593	1090	339.23 (DVRF)
11	425985	4425567	1090	373.29 (DVRF)
12	426008	4425542	1091	407.26
13	426030	4425516	1092	441.32
14	426052	4425491	1090	474.62
15	426075	4425465	1088	509.33
16	426097	4425439	1087	543.39
17	426120	4425414	1085	577.36
18	426142	4425388	1085	611.42
19	426164	4425362	1084	645.48
20	426187	4425337	1083	679.45
21	426209	4425311	1081	713.51
22	426231	4425286	1081	746.81
23	426254	4425260	1080	781.53
24	426276	4425234	1080	815.58
25	426299	4425209	1079	849.56
26	426321	4425183	1075	883.61
27	426343	4425158	1071	916.92
28	426366	4425132	1071	951.63
29	426388	4425106	1071	985.69
30	426410	4425081	1071	1018.99
31	426433	4425055	1071	1053.70
32	426455	4425030	1070	1087.00
33	426478	4425004	1069	1121.72
34	426500	4424978	1068	1155.78
35	426522	4424953	1067	1189.08

36	426545	4424927	1067	1223.79
37	426567	4424902	1067	1257.09
38	426589	4424876	1066	1291.15
39	426612	4424850	1065	1325.86
40	426634	4424825	1064	1359.17
41	426657	4424799	1063	1393.88
42	426679	4424774	1061	1427.18
43	426701	4424748	1058	1461.24
44	426724	4424722	1059	1495.95
45	426746	4424697	1062	1529.25
46	426768	4424671	1061	1563.31
47	426791	4424646	1060	1597.28
48	426813	4424620	1060	1631.34
49	426836	4424594	1060	1666.06
50	426858	4424569	1060	1699.36
51	426880	4424543	1060	1733.42
52	426903	4424518	1059	1767.39
53	426925	4424492	1058	1801.44
54	426947	4424466	1058	1835.50
55	426970	4424441	1058	1869.47
56	426992	4424415	1057	1903.53
57	427015	4424390	1056	1937.50
58	427037	4424364	1056	1971.56
59	427059	4424338	1056	2005.62
60	427082	4424313	1056	2039.59
61	427104	4424287	1056	2073.65 (Piedmont)
62	427126	4424262	1055	2106.95 (Piedmont)
63	427149	4424236	1053	2141.67
64	427171	4424210	1053	2175.72
65	427193	4424185	1052	2209.03
66	427216	4424159	1052	2243.74
67	427238	4424134	1051	2277.04
68	427261	4424108	1051	2311.75
69	427283	4424082	1050	2345.81
70	427305	4424057	1050	2379.11
71	427328	4424031	1049	2413.83
72	427350	4424006	1049	2447.13
73	427372	4423980	1049	2481.19

74	427395	4423954	1049	2515.90
75	427417	4423929	1050	2549.20
76	427440	4423903	1050	2583.92
77	427462	4423878	1051	2617.22
78	427484	4423852	1050	2651.28
79	427507	4423826	1048	2685.99
80	427529	4423801	1047	2719.29
81	427551	4423775	1048	2753.35
82	427574	4423750	1048	2787.32
83	427596	4423724	1047	2821.38
84	427619	4423698	1047	2856.09
85	427641	4423673	1046	2889.39
86	427663	4423647	1046	2923.45
87	427686	4423622	1045	2957.42
88	427708	4423596	1045	2991.48
89	427730	4423570	1044	3025.54
90	427753	4423545	1044	3059.51
91	427775	4423519	1043	3093.57
92	427798	4423494	1043	3127.54
93	427820	4423468	1042	3161.60
94	427842	4423442	1042	3195.66
95	427865	4423417	1042	3229.63
96	427887	4423391	1042	3263.69
97	427909	4423366	1042	3296.99
98	427932	4423340	1041	3331.70
99	427954	4423314	1039	3365.76
100	427977	4423289	1040	3399.73
101	427999	4423263	1044	3433.79
102	428021	4423238	1046	3467.09
103	428044	4423212	1045	3501.80
104	428066	4423186	1045	3535.86
105	428088	4423161	1044	3569.17
106	428111	4423135	1044	3603.88
107	428133	4423110	1043	3637.18
108	428156	4423084	1043	3671.89 (NE-SW Strike Slip)
109	428178	4423058	1043	3705.95 NE-SW Strike Slip)
110	428200	4423033	1044	3739.25
111	428223	4423007	1045	3773.97

112	428245	4422982	1047	3807.27
113	428267	4422956	1048	3841.33
114	428290	4422930	1048	3876.04
115	428312	4422905	1047	3909.34
116	428334	4422879	1047	3943.40
117	428357	4422853	1046	3978.11
118	428379	4422828	1045	4011.42
119	428402	4422802	1044	4046.13
120	428424	4422777	1044	4079.43
121	428446	4422751	1043	4113.49
122	428469	4422725	1044	4148.20
123	428491	4422700	1046	4181.50
124	428513	4422674	1047	4215.56
125	428536	4422649	1047	4249.53
126	428558	4422623	1047	4283.59
127	428581	4422597	1047	4318.30
128	428603	4422572	1047	4351.61
129	428625	4422546	1047	4385.67
130	428648	4422521	1047	4419.64
131	428670	4422495	1047	4453.69
132	428692	4422469	1047	4487.75
133	428715	4422444	1047	4521.72
134	428737	4422418	1047	4555.78
135	428760	4422393	1047	4589.75
136	428782	4422367	1047	4623.81
137	428804	4422341	1047	4657.87
138	428827	4422316	1047	4691.84
139	428849	4422290	1047	4725.90
140	428871	4422265	1047	4759.20
141	428894	4422239	1048	4793.91
142	428916	4422213	1047	4827.97
143	428939	4422188	1046	4861.94
144	428961	4422162	1046	4896.00
145	428983	4422137	1047	4929.30
146	429006	4422111	1048	4964.02
147	429028	4422085	1048	4998.08
148	429050	4422060	1048	5031.38
149	429073	4422034	1048	5066.09

150	429095	4422009	1048	5099.39
151	429118	4421983	1048	5134.11
152	429140	4421957	1048	5168.16
153	429162	4421932	1048	5201.47
154	429185	4421906	1048	5236.18
155	429207	4421881	1048	5269.48
156	429229	4421855	1048	5303.54
157	429252	4421829	1048	5338.25
158	429274	4421804	1048	5371.55
159	429297	4421778	1048	5406.27
160	429319	4421753	1048	5439.57
161	429341	4421727	1048	5473.63
162	429364	4421701	1048	5508.34
163	429386	4421676	1049	5541.64
164	429408	4421650	1049	5575.70
165	429431	4421625	1049	5609.67
166	429453	4421599	1049	5643.73
167	429475	4421573	1049	5677.79
168	429498	4421548	1049	5711.76
169	429520	4421522	1049	5745.82
170	429543	4421497	1049	5779.79
171	429565	4421471	1049	5813.85
172	429587	4421445	1049	5847.91
173	429610	4421420	1049	5881.88
174	429632	4421394	1049	5915.94
175	429654	4421369	1049	5949.24
176	429677	4421343	1049	5983.95
177	429699	4421317	1049	6018.01
178	429722	4421292	1049	6051.98
179	429744	4421266	1050	6086.04
180	429766	4421241	1050	6119.34
181	429789	4421215	1050	6154.05
182	429811	4421189	1050	6188.11
183	429833	4421164	1050	6221.41
184	429856	4421138	1050	6256.13
185	429878	4421113	1050	6289.43
186	429901	4421087	1050	6324.14
187	429923	4421061	1050	6358.20

188	429945	4421036	1050	6391.50
189	429968	4421010	1050	6426.22
190	429990	4420985	1050	6459.52
191	430012	4420959	1050	6493.58
192	430035	4420933	1050	6528.29
193	430057	4420908	1048	6561.59
194	430080	4420882	1046	6596.30
195	430102	4420857	1047	6629.61
196	430124	4420831	1048	6663.67
197	430147	4420805	1050	6698.38
198	430169	4420780	1051	6731.68
199	430191	4420754	1053	6765.74
200	430214	4420729	1054	6799.71
201	430236	4420703	1053	6833.77
202	430259	4420677	1053	6868.48
203	430281	4420652	1053	6901.78
204	430303	4420626	1053	6935.84
205	430326	4420601	1054	6969.81
206	430348	4420575	1054	7003.87
207	430370	4420549	1055	7037.93
208	430393	4420524	1055	7071.90
209	430415	4420498	1055	7105.96
210	430438	4420472	1055	7140.67 (Buckbrush)
211	430460	4420447	1054	7173.97 (Buckbrush)
212	430482	4420421	1053	7208.03
213	430505	4420396	1052	7242.00
214	430527	4420370	1051	7276.06
215	430549	4420344	1052	7310.12
216	430572	4420319	1052	7344.09
217	430594	4420293	1053	7378.15
218	430616	4420268	1053	7411.45
219	430639	4420242	1054	7446.16
220	430661	4420216	1054	7480.22
221	430684	4420191	1055	7514.19
222	430706	4420165	1055	7548.25
223	430728	4420140	1054	7581.55
224	430751	4420114	1054	7616.27
225	430773	4420088	1053	7650.33

226	430795	4420063	1053	7683.63
227	430818	4420037	1052	7718.34
228	430840	4420012	1052	7751.64
229	430863	4419986	1053	7786.36
230	430885	4419960	1053	7820.41
231	430907	4419935	1054	7853.72
232	430930	4419909	1055	7888.43
233	430952	4419884	1056	7921.73
234	430974	4419858	1057	7955.79
235	430997	4419832	1055	7990.50
236	431019	4419807	1054	8023.80
237	431042	4419781	1052	8058.52
238	431064	4419756	1051	8091.82
239	431086	4419730	1051	8125.88
240	431109	4419704	1051	8160.59
241	431131	4419679	1052	8193.89
242	431153	4419653	1052	8227.95
243	431176	4419628	1053	8261.92
244	431198	4419602	1053	8295.98
245	431221	4419576	1054	8330.69
246	431243	4419551	1054	8364.00
247	431265	4419525	1055	8398.05
248	431288	4419500	1055	8432.03
249	431310	4419474	1056	8466.08
250	431332	4419448	1056	8500.14
251	431355	4419423	1057	8534.11
252	431377	4419397	1057	8568.17
253	431400	4419372	1057	8602.14
254	431422	4419346	1057	8636.20
255	431444	4419320	1054	8670.26
256	431467	4419295	1050	8704.23
257	431489	4419269	1053	8738.29
258	431511	4419244	1057	8771.59
259	431534	4419218	1057	8806.30
260	431556	4419192	1058	8840.36
261	431579	4419167	1058	8874.33
262	431601	4419141	1058	8908.39
263	431623	4419116	1058	8941.69

264	431646	4419090	1058	8976.41
265	431668	4419064	1059	9010.47

TABLE 10: LINE 6 STATION LOCATIONS WITH INFERRED FAULT LOCATIONS HIGHLIGHTED IN YELLOW

Station #	Easting, m	Northing, m	Elevation, m	Distance from NW, m
6001	425741	4425849	1129	0.00
6003	425808	4425772	1116	102.38
6005	425853	4425721	1104	170.63
6007	425898	4425669	1096	238.89
6009	425943	4425618	1090	307.14 (DVRF)
6011	425988	4425567	1090	375.39 (DVRF)
6013	426033	4425515	1092	443.65
6015	426078	4425464	1088	511.90
6017	426122	4425412	1085	580.15
6019	426167	4425361	1084	648.41
6021	426212	4425309	1081	716.66
6023	426257	4425258	1080	784.92
6025	426302	4425207	1079	853.17
6027	426347	4425155	1071	921.43
6029	426392	4425104	1071	989.68
6031	426437	4425052	1071	1057.94
6033	426482	4425001	1069	1126.19
6035	426526	4424949	1067	1194.45
6037	426571	4424898	1067	1262.71
6039	426616	4424847	1065	1330.96
6041	426661	4424795	1063	1399.22
6043	426706	4424744	1057	1467.48
6045	426751	4424692	1062	1535.73
6047	426795	4424644	1060	1601.49
6049	426840	4424593	1060	1669.65
6051	426885	4424542	1060	1737.69
6053	426930	4424490	1058	1805.59
6055	426974	4424438	1058	1873.69
6057	427019	4424388	1056	1941.46
6059	427064	4424337	1056	2009.64
6061	427109	4424286	1056	2077.61 (Piedmont)

6063	427153	4424235	1053	2145.34 (Piedmont)
6065	427198	4424184	1052	2213.02
6067	427243	4424133	1051	2281.16
6069	427288	4424082	1050	2349.12
6071	427334	4424024	1049	2423.21
6073	427379	4423973	1050	2491.47
6075	427424	4423921	1050	2559.72
6077	427469	4423870	1051	2627.99
6079	427514	4423818	1047	2696.24
6081	427559	4423767	1048	2764.51
6083	427604	4423716	1047	2832.77
6085	427649	4423664	1046	2901.03
6087	427694	4423613	1045	2969.29
6089	427739	4423561	1045	3037.55
6091	427784	4423510	1044	3105.81
6093	427828	4423458	1043	3174.07
6095	427873	4423407	1042	3242.33
6097	427918	4423356	1042	3310.60
6099	427963	4423304	1038	3378.86
6101	428008	4423253	1046	3447.12
6103	428053	4423201	1045	3515.38
6105	428098	4423150	1045	3583.64
6107	428143	4423099	1044	3651.91 (NE-SW Strike Slip)
6109	428188	4423047	1043	3720.17 NE-SW Strike Slip)
6111	428233	4422996	1046	3788.43
6113	428278	4422944	1049	3856.70
6115	428322	4422897	1048	3921.59
6117	428367	4422842	1046	3993.35
6119	428412	4422790	1045	4061.61
6121	428457	4422739	1043	4129.87
6123	428502	4422687	1047	4198.14
6125	428547	4422636	1047	4266.40
6127	428592	4422584	1047	4334.67
6129	428637	4422533	1047	4402.93
6131	428682	4422482	1047	4471.20
6133	428727	4422430	1047	4539.47
6135	428772	4422379	1047	4607.73
6137	428817	4422327	1047	4676.00

6139	428861	4422276	1048	4744.27
6141	428906	4422225	1048	4812.53
6143	428951	4422173	1045	4880.80
6145	428996	4422122	1048	4949.07
6147	429041	4422070	1048	5017.33
6149	429086	4422019	1048	5085.60
6151	429131	4421968	1048	5153.87
6153	429176	4421916	1048	5222.13
6155	429221	4421865	1049	5290.40
6157	429266	4421813	1049	5358.67
6159	429311	4421762	1049	5426.94
6161	429356	4421711	1049	5495.20
6163	429401	4421659	1049	5563.47
6165	429445	4421608	1049	5631.74
6167	429490	4421556	1049	5700.01
6169	429535	4421505	1049	5768.28
6171	429580	4421454	1050	5836.55
6173	429625	4421402	1050	5904.82
6175	429670	4421351	1050	5973.09
6177	429715	4421299	1050	6041.36
6179	429760	4421248	1050	6109.63
6181	429805	4421197	1050	6177.89
6183	429850	4421145	1050	6246.17
6185	429895	4421094	1050	6314.44
6187	429940	4421042	1050	6382.71
6189	429985	4420991	1050	6450.98
6191	430030	4420940	1050	6519.25
6193	430074	4420888	1046	6587.52
6195	430119	4420837	1049	6655.79
6197	430164	4420785	1051	6724.06
6199	430209	4420734	1054	6792.33
6201	430254	4420683	1054	6860.61
6203	430299	4420631	1053	6928.88
6205	430344	4420580	1054	6997.15
6207	430389	4420528	1055	7065.42 (Buckbrush)
6209	430434	4420477	1055	7133.70 (Buckbrush)
6211	430479	4420426	1053	7201.97
6213	430524	4420374	1051	7270.24

6215	430569	4420323	1052	7338.52
6217	430614	4420271	1053	7406.79
6219	430659	4420220	1054	7475.06
6221	430704	4420169	1055	7543.34
6223	430748	4420122	1054	7607.32
6225	430794	4420066	1053	7679.97
6227	430838	4420015	1052	7748.25
6229	430883	4419963	1053	7816.52
6231	430928	4419912	1055	7884.80
6233	430973	4419860	1057	7953.07
6235	431018	4419809	1054	8021.35
6237	431063	4419758	1051	8089.62
6239	431108	4419706	1052	8157.90
6241	431153	4419655	1053	8226.17
6243	431198	4419603	1054	8294.45
6245	431243	4419552	1054	8362.73
6247	431288	4419501	1055	8431.00
6249	431333	4419449	1056	8499.28
6251	431378	4419398	1057	8567.56
6253	431423	4419346	1057	8635.83
6255	431471	4419297	1050	8704.87
6257	431513	4419244	1058	8772.56
6259	431558	4419192	1058	8840.84
6261	431603	4419141	1058	8909.12
6263	431648	4419089	1059	8977.40
6265	431670	4419064	1059	9011.53